

University of
Strathclyde
Science

**GLUT4 Dispersal at the Plasma Membrane:
A Molecular and Microscopy-Based Journey
From Single Cells to Intact Tissues**

Angéline Geiser

A thesis submitted in fulfilment of the requirements for
the degree of Doctor of Philosophy

2024

Abstract

The regulation of glucose uptake in adipocytes and muscle cells fundamentally depends on the glucose transporter GLUT4, which is critical in maintaining glucose homeostasis. GLUT4 is known to undergo translocation from intracellular compartments to the plasma membrane in response to insulin, facilitating glucose entry into cells. While GLUT4 translocation to the plasma membrane has been well-studied since its discovery in 1988, the finer details of GLUT4 behaviour at the plasma membrane have only recently been uncovered. In adipocytes, advances in light microscopy have shed light on GLUT4's ability to transition from a clustered formation into dispersed monomers upon insulin stimulation. This dispersal process is thought to enhance glucose uptake efficiency, and recent evidence has suggested a correlation between impaired GLUT4 dispersal and insulin resistance, a key characteristic of type 2 diabetes.

To deepen the understanding of GLUT4's dynamics at the cell surface, this thesis first focuses on two newly identified regulatory proteins at the plasma membrane, EFR3a and PI4K-III α , hypothesised to drive GLUT4 dispersal in adipocytes. This thesis aims to investigate how these proteins regulate GLUT4 behaviour at the single-cell level using molecular and microscopy-based techniques. Facing the limitations inherent to super-resolution microscopy, it seeks to develop a DNA-PAINT imaging system for enhanced single-GLUT4 localisation accuracy at the plasma membrane.

Additionally, this thesis extends beyond adipose tissues to explore the often-overlooked GLUT4 machinery in cardiac muscle tissues, addressing the challenges associated with cardiovascular research, both at the cellular

level and within intact hearts. Significantly, we present here a novel optical mesoscopy approach that, using the imaging capability of the Mesolens, allows for precise measurement of the spatial location of GFP-tagged GLUT4 within specific anatomical structures across the myocardium in ultrathick sections (5 mm × 5 mm × 3 mm) of intact mouse hearts.

Overall, this research offers new tools for high-resolution imaging, advances our understanding of GLUT4 dispersal machinery in adipocytes and contributes to improved methodologies for studying cardiovascular metabolism.

Declaration of Authenticity and Author's Right

This thesis is the result of the author's original research. It has been composed by the author and has not been previously submitted for examination which has led to the award of a degree.

The copyright of this thesis belongs to the author under the terms of the United Kingdom Copyright Acts as qualified by the University of Strathclyde Regulation 3.50. Due acknowledgement must always be made of the use of any material contained in, or derived from, this thesis.

Signed: 

Date: 24/08/2024

Statement of Inclusion of Published Material

This thesis includes material from the following published papers:

GLUT4 Dispersal at the Plasma Membrane of Adipocytes:

A Super-Resolved Journey

Angeline Geiser, Shannan Foylan, Peter W. Tinning, Nia J. Bryant
and Gwyn W. Gould

Bioscience Reports

Portland Press

October 2023

DOI: 10.1042/BSR20230946

Link to Published Article: <https://doi.org/10.1042/BSR20230946>

Sections in Thesis:

- 1.3.2.2 GLUT4-Vesicular Trafficking
- 1.4 GLUT4 Dynamics Near and Within the Plasma Membrane
- 3.1 Chapter 3 - Introduction
- 4.1.1 GLUT4 Dispersal and Clustering:
Size of Clusters and Effects on Activity

Permission: This article is included, in part, in this thesis with permission from Portland Press. The original source has been attributed as required by the publisher.

*A Novel 3D Imaging Approach for Quantification of GLUT4 Levels
Across the Intact Myocardium*

Angeline Geiser, Susan Currie, Hadi Al-Hasani, Alexandra Chadt, Gail McConnell
and Gwyn W. Gould

Journal of Cell Science
The Company of Biologists
June 2024

DOI: 10.1242/jcs.262146

Link to Published Article: <https://doi.org/10.1242/jcs.262146>

Sections in Thesis:

- 5.1 Chapter 5 - Introduction
- 5.3.1 A Novel 3D Imaging Approach for Quantification of GLUT4 Levels across the Intact Myocardium
 - Materials and Methods associated with section 5.3.1, except for section 2.2.5.6
- 5.4.1 Expanding Mesoscopy Applications
- 7.5 A Novel 3D Imaging Approach for Quantification of GLUT4 Levels across the Intact Myocardium: Supplementary Information

Permission: This article is included in this thesis with permission from The Company of Biologists. The original source is attributed as required by the publisher, including a DOI citation and a link to the published article on the journal website.

The materials from these papers are integrated into the thesis sections specified above. The primary author of these publications (i.e., myself) contributed significantly to the conception, design, execution, and writing of the studies. Co-authors provided essential support in various aspects of the research, including supervision, validation, and funding, as defined in the author contributions statements of these papers and as acknowledged in this thesis.

It is confirmed that this material represents original work and has been duly acknowledged by the regulations of the University of Strathclyde's Code of Practice for Postgraduate Research Students.

Signed: 

Date: 24/08/2024

Acknowledgement

Thank you. Merci.

First and foremost, I am profoundly grateful to my supervisor, Prof. Gwyn W. Gould. Gwyn introduced me to the field of GLUT4 biology eight years ago. Since then, he has continuously provided me with opportunities to advance my career, from the summer internship that started it all to our final EASD workshop in Oxford. I am deeply grateful for your unwavering guidance and support throughout my PhD journey and beyond. Your encouragement and insight have been invaluable. You have undeniably strengthened my ambitions to pursue research. I cannot thank you enough.

I have been lucky to have worked with an amazing group of people throughout my PhD. A big thank you to everyone in the Gould Lab, from Glasgow to Strathclyde. I want to express my special gratitude to Laura, Justin, Rod, Peter, Shannan, Shaun, and Holly. I truly appreciate your support and encouragement and the peaceful and helpful environment you have provided. Long live powdered custard!

Thank you to Dr. Peter W. Tinning for teaching me about optical physics and super-resolution microscopy. Working with you has been a highlight of this journey.

Thank you to Prof. Gail McConnell and her group for introducing me to the world of mesoscopy and a (potentially real) Mesolens. This experience further showed me just how exciting and impactful interdisciplinary research can be!

I am also deeply appreciative of Susan Currie, my second supervisor, for her guidance in cardiovascular research. Her insights and unwavering support have been incredibly valuable and will undoubtedly influence my future career direction.

I would also like to thank everyone I met at SIPBS, with a special shoutout to everyone on the 5th floor. Your camaraderie and support have made a big difference throughout this PhD experience. It's been great getting to know you all.

To all the friends I made along the way, to my Frenchies in Glasgow, and most importantly, to my favourite tramps, thank you. Without you, these past eight years would have been undeniably less fun and entertaining. I love you all!

To my oldest friends and flatmates, Marc, Maxence, and Tanguy, you were always there to annoy me when I needed it.

Un grand merci à ma famille, sans qui je ne serais pas là aujourd'hui. Maman, papa, tout cela, c'est grâce à vous. Merci de m'avoir laissé partir à 18 ans, de m'avoir soutenu.e émotionnellement et financièrement, de m'avoir poussé.e à donner le meilleur de moi-même et de soutenir mes ambitions de carrière sans vraiment comprendre ce que je faisais. À ma sœur, Mathilde, bizarrement, les mots me manquent un peu pour toi, mais mes émotions sont les plus intenses. Je t'aime fort. Et surtout, une très grande pensée à mes deux grands-pères: merci pour tout.

Une pensée pour mes cousins, ma famille lyonnaise, et la famille et les amis qui sont toujours là pour me soutenir, même quand je pars vivre dans le nord (semper robur).

Merci aussi à Monica pour ses petits mots et son attention qui mettent toujours du baume au cœur.

Last but not least, the biggest thank you to my partner, Nico. Thank you for supporting and loving me through the highs and lows of this journey. I know we joke about it sometimes, but you truly are a ray of light in my life. Thank you for moving to Brussels with me. I cannot wait to start this new chapter with you. Je t'aime.

Table of Contents

<u>Abstract</u>	<u>2</u>
<u>Declaration of Authenticity and Author's Right</u>	<u>4</u>
<u>Statement of Inclusion of Published Material</u>	<u>5</u>
<u>Acknowledgement</u>	<u>8</u>
<u>Table of Contents</u>	<u>11</u>
<u>List of Tables</u>	<u>22</u>
<u>List of Figures</u>	<u>23</u>
<u>List of Abbreviations</u>	<u>29</u>
<u>Introduction</u>	<u>33</u>
1.1 Diabetes Mellitus	33
1.1.1 Causes	35
1.1.2 Complications	35
1.1.2.1 Microvascular Complications	37
1.1.2.2 Macrovascular Complications	38
1.1.3 Diabetes as a Growing Healthcare Burden	40
1.2 Glucose Homeostasis	41
1.2.1 Glucose Management in Health	41
1.2.2 Energy Substrates and Management in the Heart	43
1.3 Glucose Transport in Adipose and Muscle Tissues	46
1.3.1 Introduction to GLUT4	47
1.3.2 GLUT4 in Adipocytes: A Reference	50
1.3.2.1 Insulin Signalling	50

1.3.2.2 GLUT4-Vesicular Trafficking	54
1.3.3 GLUT4 in Muscle Cells	56
1.3.3.1 Insulin Signalling	56
1.3.3.1.1 Impaired Insulin Signalling in Diabetic Cardiomyopathy	58
1.3.3.2 GLUT4-Vesicular Trafficking:	60
Insulin-Dependent and -Independent Trigger	60
1.4 GLUT4 Dynamics Near and Within the Plasma Membrane	62
1.4.1 GLUT4 Trafficking Revealed	62
using Microscopy-Based Approaches	62
1.4.1.1 Meaning and Importance of Spatial Resolution	63
1.4.1.2 A Super-Resolved Journey	66
1.4.1.2.1 Super-Resolution Microscopy: Shaped Illumination	67
1.4.1.2.2 Super-Resolution Microscopy: Localisation-Based	70
1.4.1.2.3 Super-Resolution Microscopy: One Big Family	76
1.4.2 Insulin-Stimulated GLUT4-Vesicles near the Plasma Membrane	76
1.4.3 Insulin-Stimulated GLUT4-Dispersal	77
within the Plasma Membrane	77
1.4.3.1 Impaired GLUT4 Dispersal in Insulin Resistance	81
1.5 Aims	82
<u>Materials and Methods</u>	<u>84</u>
2.1 Materials: Recipes and Antibodies	84
2.1.1 Buffers and Solutions Recipes	84
2.1.2 Antibodies and NanoBodies	87
2.1.2.1 Primary Antibodies and Nanobodies	87

2.1.2.2 Secondary Antibodies and NanoBodies	88
2.2 Methods	89
2.2.1 Cell Culture	89
2.2.1.1 3T3-L1 Fibroblasts Growth and Maintenance	89
2.2.1.2 3T3-L1 Adipocyte Differentiation	90
2.2.1.3 Insulin Stimulation of 3T3-L1 Adipocytes	91
2.2.1.4 Insulin Stimulation, PI4K-III α Pharmacological Inhibition, and Glucose Uptake Assay in 3T3-L1 Adipocytes	91
2.2.1.5 siRNA-Mediated Gene Knockdown in 3T3-L1 Adipocytes	92
2.2.1.6 CRISPR/Cas9-Mediated Gene Knockout in 3T3-L1 Fibroblasts	94
2.2.1.6.1 CRISPR/Cas9 System Delivery using Ribonucleoprotein	94
2.2.1.6.2 CRISPR/Cas9 System Delivery using Plasmid DNA	95
2.2.1.6.3 Puromycin Selection	96
2.2.1.6.4 Single-Cell Expansion by Dilution Plating	96
2.2.1.7 HEK295 Cells Growth, Maintenance, and Insulin Stimulation	98
2.2.1.8 Plasmid DNA Transfection in HEK295 Cells	98
2.2.1.9 Generation of ALFA-GLUT4 Stable HEK293 Cell Lines: G418 Selection and Clone Isolation	99
2.2.2 Animal Work	100
2.2.2.1 Mice	100
2.2.2.2 High-Fat Diet-Feeding, Weighing, and Blood Glucose Measurement in Mice	100
2.2.2.3 Heart Collection and Dissection	101
2.2.2.3.1 Mouse Heart Collection for Mesolens Imaging	101

2.2.2.3.2 Mouse and Rat Heart Collection and Sectioned for Quantitative Immunoblotting	102 102
2.2.2.4 Cardiomyocyte Isolation	103
2.2.2.4.1 Buffer and Surgical Area Preparation	103
2.2.2.4.2 Primary Adult Mouse Cardiomyocyte Langendorff-Free and Enzymatic Dissociation-Based Isolation	105 105
2.2.2.4.3 Cardiomyocyte Collection and Calcium Reintroduction	107
2.2.2.4.4 Insulin Stimulation of Primary Adult Isolated Cardiomyocytes	108 108
2.2.3 Cell Lysates and Tissue Homogenates	108
2.2.3.1 Sectioned Cardiac Tissue Homogenisation	108
2.2.3.2 Primary Adult Isolated Cardiomyocytes Lysate	109
2.2.3.3 3T3-L1 and HEK295 Whole Cells Lysate	109
2.2.4 Cellular Methods	110
2.2.4.1 Sub-Cellular Fractionation of 3T3-L1 Adipocytes and HEK295 Cells	110 110
2.2.4.2 Lipid Raft Fractionation of 3T3-L1 Adipocytes	112
2.2.5 Protein-Specific Assays	112
2.2.5.1 Bicinchoninic Acid Assay and Sample Preparation for Immunoblotting	113 113
2.2.5.2 SDS-PAGE	113
2.2.5.3 Wet Transfer	114
2.2.5.4 Dot Blot Sample Preparation	115
2.2.5.5 Immunoblotting	115

2.2.5.6 PNGase F-Mediated Protein De-Glycosylation	116
2.2.6 Molecular Methods	116
2.2.6.1 Polymerase Chain Reaction (PCR)	117
2.2.6.2 Agarose Gel Electrophoresis	118
2.2.6.3 Surveyor® Nuclease Assay for Gene Modification	118
2.2.7 Microscopy	121
2.2.7.1 Sample Preparation	121
2.2.7.1.1 Cellular Fixation, Immunofluorescent, and Permanent DNA-PAINT Staining	121
2.2.7.1.2 Primary Isolated Mouse Cardiomyocytes Fixation and Immunofluorescent Staining	123
2.2.7.1.3 Single-Molecule Surfaces for DNA-PAINT Imaging	124
2.2.7.1.4 Mouse Heart Optical Clearing	125
2.2.7.2 Imaging Setups and Data Acquisition	126
2.2.7.2.1 STEDYCON (STED and Confocal) Microscope	126
2.2.7.2.2 Perfusion Syringe System and pH Measurement Experiment	126
2.2.7.2.3 Single-Molecule Localisation Microscope	128
2.2.7.2.4 Confocal Microscope	129
2.2.7.2.5 The Mesolens	129
2.2.8 Data and Statistical Analyses	131
2.2.8.1 Densitometry	131
2.2.8.2 Quantitative Analysis of PI4P Distribution within 3T3-L1 Adipocytes expressing HA-GLUT4-GFP	132

2.2.8.3 DNA-PAINT Data Analysis	135
2.2.8.4 Mesolens-Acquired Data Processing and Analysis	136
2.2.8.4.1 Analysis of Global Regional Fluorescence	137
2.2.8.4.2 Analysis of Transmural Fluorescence	137
2.2.8.4.3 Analysis of Lumen Size	139
2.2.8.4.4 Visualisation and Presentation	139
2.2.8.5 Statistical Analysis	140
<u>Chapter 3 - GLUT4 Dispersal at the Plasma Membrane:</u>	<u>141</u>
<u>Deciphering the Role of EFR3a and PI4K-IIIα in Adipocytes</u>	<u>141</u>
3.1 Chapter 3 - Introduction	141
3.1.1 EFR3 and PI4K-III α	141
3.1.2 EFR3a Regulate GLUT4 Dispersal in Adipocyte: Evidence and Hypothesis	144
3.1.3 Chapter 3 - Aims	146
3.2 Chapter 3 - List of Methods	148
3.3 Chapter 3 - Results	150
3.3.1 Targeting the EFR3a/PI4K-III α Machinery in 3T3-L1 Adipocytes	150
3.3.1.1 siRNA-Mediated Gene Knockdown of Efr3a or Pi4ka in 3T3-L1 Adipocytes	150
3.3.1.2 Pharmacological Inhibition of PI4K-III α in 3T3-L1 Adipocytes	156
3.3.2 Characterisation of the EFR3a/PI4K-III α Machinery in 3T3-L1 Adipocytes	157
3.3.2.1 EFR3a and PI4K-III α Localisation at the Plasma Membrane is Increased in Insulin-Stimulated 3T3-L1 Adipocytes	157

3.3.2.2 EFR3a Localisation in Lipid Raft in 3T3-L1 Adipocytes	164
3.3.2.3 PI4P Localisation at the Plasma Membrane is Increased in Insulin-Stimulated 3T3-L1 Adipocytes	167
3.3.3 CRISPR-Cas9-Mediated Efr3a Gene Knockout as a Permanent Alternative to siRNA-Mediated Knockdown	173
3.3.3.1 Ribonucleoprotein-Mediated CRISPR-Cas9 Genome Editing	173
3.3.3.2 Plasmid DNA-Mediated CRISPR-Cas9 Genome Editing	179
3.4 Chapter 3 - Discussion and Future Work	186
3.4.1 EFR3a and PI4K-III α : The Premise of a Newly Identified GLUT4 Dispersal Machinery	186
3.4.2 A Need for Standardisation of CRISPR/Cas9 Genome Editing Protocols	188
<u>Chapter 4 - Optimising Single-Molecule Localisation Microscopy for Advanced Analysis of GLUT4 Dispersal at the Plasma Membrane</u>	<u>192</u>
4.1 Chapter 4 - Introduction	192
4.1.1 GLUT4 Dispersal and Clustering: Size of Clusters and Effects on Activity	192
4.1.2 Exchange-PAINT: The True Power of DNA-PAINT	194
4.1.3 Super-Resolution Microscopy: An Open-Source Hardware Initiative	196
4.1.4 The Labelling Linkage Issue in Single-Molecule Localisation Microscopy	199
4.1.5 The HA-Tag: Success, Limitations, and Alternative	201
4.1.6 Chapter 4 - Aims	203

4.2 Chapter 4 - List of Methods	205
4.3 Chapter 4 - Results	207
4.3.1 A Journey Toward Exchange-PAINT	207
4.3.1.1 Fluid Transfer Accuracy of a Homemade Perfusion System	207
4.3.1.2 Automatised DNA-PAINT Imaging	209
using a Homemade Perfusion System	209
4.3.2 A New Probe for GLUT4 Imaging at the Plasma Membrane:	212
Reducing the Labelling Linkage Error	212
4.3.2.1 Identification and Characterisation of an HA-Tag Nanobody:	212
Redemption of the HA-GLUT4-GFP Construct?	212
4.3.2.2 Characterisation of the ALFA-GLUT4 Construct as a New	215
Probe for GLUT4 Imaging at the Plasma Membrane	215
4.3.2.2.1 Insulin-Stimulated Translocation of ALFA-GLUT4	215
in Transiently Transfected HEK293 Cells	215
4.3.2.2.2 Generation and Characterisation of an	219
ALFA-GLUT4 Stable HEK293 Cell Line	219
4.4 Chapter 4 - Discussion and Future Work	225
4.4.1 Exchange-PAINT: Project Focus Adjustment and Future Work	225
4.4.2 The ALFA-GLUT4 Construct: Potential for Success	226
<u>Chapter 5 - GLUT4 in the Heart: From Whole Tissue to Single Cell</u>	<u>229</u>
5.1 Chapter 5 - Introduction	229
5.1.1 Cardiac Metabolic Disturbance in Diabetes	229
5.1.2 Cardiac Regional Heterogeneity	231
5.1.3 The Challenges of Cardiovascular Research	233

5.1.4 Optical Mesoscopy: Introduction to the Mesolens	235
5.1.5 Chapter 5 - Aims	237
5.2 Chapter 5 - List of Methods	239
5.3 Chapter 5 - Results	241
5.3.1 A Novel 3D Imaging Approach for Quantification of GLUT4 Levels across the Intact Myocardium	241
5.3.1.1 Axial Imaging Depth with and without Organ Perfusion	241
5.3.1.2 Quantitative Analysis of GLUT4 Levels and Distribution within Intact Ventricular Cardiac Sections	244
5.3.1.2.1 Global Regional GLUT4 Expression Levels	246
5.3.1.2.2 Transmural Fluorescence: GLUT4 Distribution Across Cardiac Walls	251
5.3.1.2.3 Sex-Specific Impact of a High-Fat Diet	255
5.3.1.3 Anatomical Parameters of Cardiac Structure	257
5.3.2 Optimisation of a Langendorff-Free Isolation Method for Viable Primary Adult Cardiomyocytes	259
5.3.2.1 Ensuring Cell Survival	259
5.3.2.2 Immunostaining of Langendorff-Free Isolated Cardiomyocytes	262
5.3.2.3 Insulin Stimulation of Langendorff-Free Isolated Cardiomyocytes	264
5.4 Chapter 5 - Discussion and Future Work	270
5.4.1 Expanding Mesoscopy Applications	270
5.4.2 Deciphering the Role of GLUT4 N-Glycosylation	273

5.4.3 Isolation of Adult Rodent Cardiomyocytes:	275
To Langendorff, or Not to Langendorff?	275
<u>Final Conclusion and Future Perspectives</u>	<u>277</u>
<u>Appendices</u>	<u>281</u>
7.1. Effectiveness of siRNA-Mediated Efr3a and Pi4ka	281
Knockdown in 3T3-L1 Adipocytes	281
7.2 gRNA, Plasmid DNA, and Primers	282
7.2.1 CRISPR/Cas9 gRNA and Associated Primers	282
7.2.1.1 CRISPR/Cas9 gRNA/Primers Set #1	283
7.2.1.2 CRISPR/Cas9 gRNA/Primers Set #1 Targeting the Efr3a gene	284
(Exon 1)	284
7.2.1.3 CRISPR/Cas9 gRNA/Primers Set #2	285
7.2.1.4 CRISPR/Cas9 gRNA/Primers Set #2 Targeting the Efr3a gene	286
(Exon 6)	286
7.2.2 Plasmid DNA and Associated Primers	288
7.2.2.1 CRISPR/Cas9 Plasmid DNA and Associated Primers	288
7.2.2.1.1 CRISPR/Cas9 Plasmid DNA Map:	288
pRP[CRISPR]-Puro-hCas9-U6>mEfr3a[gRNA#5786]	288
7.2.2.1.2 CRISPR/Cas9 Plasmid DNA-Associated gRNA/Primers	290
7.2.2.1.3 CRISPR/Cas9 Plasmid DNA-Associated gRNA/Primers	291
Targeting the Efr3a gene (Exon 17)	291
7.2.2.2 ALFA-GLUT4 Plasmid DNA Map	293
7.2.2.3 HA-GLUT4-GFP Plasmid DNA Map	294
7.3. Plasmid DNA Transfection Optimisation in 3T3-L1 Fibroblasts	295

using Xfect™ Transfection Reagent	295
7.4. Automated DNA-PAINT Imaging Strand Perfusion:	297
Homemade Perfusion Syringe System G-code	297
7.5. A Novel 3D Imaging Approach for Quantification of	299
GLUT4 Levels across the Intact Myocardium:	299
Supplementary Information	299
7.5.1 Illustrative Movies	299
7.5.1.1 Illustrative Movies of 3D Render of GLUT4-GFP	299
in Ultrathick Sections of Cleared Mouse Heart.	299
7.5.1.2 Illustrative Movies of Sequential Render of GLUT4-GFP	299
in Ultrathick Sections of Cleared Mouse Heart.	299
7.5.2 Impact of High-Fat Diet-Feeding on Body Weights and	300
Blood Glucose Levels, and Summary of Isolated Hearts.	300
7.5.3 Impact of High-Fat Diet-Feeding on GLUT4-GFP Fluorescence	301
in the Septum and RV of Male and Female Mouse Hearts	301
7.5.4 Quantification of Gross Anatomical Features	303
<u>Bibliography</u>	<u>304</u>

List of Tables

Table 2.1. Transfection Mixture for siRNA-Mediated Gene Knockdown using TransIT-X2® Dynamic Delivery System.	94
Table 2.2. PCR Reaction Setup.	117
Table 2.3. PCR Thermocycling Conditions.	118
Table 2.4. pH Measurements Reaction Setup.	128
Appendix Table 7.1. CRISPR/Cas9 gRNA/Primers Set #1 Specificities.	283
Appendix Table 7.2. CRISPR/Cas9 gRNA/Primers Set #2 Specificities.	285
Appendix Table 7.3. CRISPR/Cas9 Plasmid DNA gRNA/Primers Specificities.	290

List of Figures

Figure 1.1. Schematic of Glucose Homeostasis.	43
Figure 1.2. Simplified Schematic of the Randle Cycle.	46
Figure 1.3. Schematic of the Insulin Signalling Cascade in Adipocytes.	54
Figure 1.4. Model of GLUT4 Trafficking to the Plasma Membrane in Adipocytes.	56
Figure 1.5. Diffraction-Limited Resolution of Light (Optical) Microscopy.	66
Figure 1.6. Schematic of Total Internal Reflection Fluorescence (TIRF) Microscopy.	69
Figure 1.7. Principle of Classical Single-Molecule Localization Microscopy and DNA-PAINT.	73
Figure 1.8. Localisation Precision in Single-Molecule Localisation Microscopy.	75
Figure 1.9. Model of GLUT4 Fusion to, and Dispersal within, the Plasma Membrane of Adipocytes.	81
Figure 2.1. Photographic Images of the Surgical Area for a Langendorff-Free and Enzymatic Dissociation-Based Cardiomyocytes Isolation Procedure.	105
Figure 2.2. Schematic Representation of Mutations Detection by Surveyor® Nuclease Assay.	121
Figure 2.3. Schematic diagram of point-scanning confocal Mesolens for imaging of GLUT4-GFP in ultrathick sections of cleared mouse heart.	131
Figure 2.4. The Kurtosis Principal in Descriptive Statistics.	135

Figure 3.1. Hypothetical Model of EFR3a/PI4K-III α -Regulated GLUT4 Dispersal within the Plasma Membrane of Adipocytes.	146
Figure 3.2. Efr3a Knockdown and its Effect on Adipogenesis and Insulin Action in Differentiated 3T3-L1 Adipocytes.	153
Figure 3.3. Pi4ka Knockdown and its Effect on Adipogenesis and Insulin Action in Differentiated 3T3-L1 Adipocytes.	154
Figure 3.4. Efr3a and Pi4ka Double Knockdown and its Effect on Adipogenesis and Insulin Action in Differentiated 3T3-L1 Adipocytes.	155
Figure 3.5. Inhibition of PI4K-III α impairs insulin-stimulated 2-deoxy-D- glucose uptake in 3T3-L1 adipocytes.	157
Figure 3.6. EFR3a Localisation in Insulin-Stimulated WT, EFR3a KD, PI4K-III α KD, and EFR3a KD and PI4K-III α KD 3T3-L1 Adipocytes.	160
Figure 3.7. PI4K-III α Localisation in Insulin-Stimulated WT, EFR3a KD, PI4K- III α KD, and EFR3a KD and PI4K-III α KD 3T3-L1 Adipocytes.	162
Figure 3.8. GLUT4 Localisation in Insulin-Stimulated WT, EFR3a KD, PI4K-III α KD, and EFR3a KD and PI4K-III α KD 3T3-L1 Adipocytes.	164
Figure 3.9. GLUT4, EFR3a, and PI4K-III α Lipid Raft Association in Insulin- Stimulated WT 3T3-L1 Adipocytes.	167
Figure 3.10. PI4P Localisation in Insulin-Stimulated WT, EFR3a KD, PI4K-III α KD, and EFR3a KD and PI4K-III α KD 3T3-L1 Adipocytes.	169
Figure 3.11. Representative Immunofluorescence Staining of PI4P and Quantification of PI4P and GLUT4 Distribution in WT and EFR3a KD 3T3-L1 HA-GLUT4-GFP Adipocytes.	172
Figure 3.12. Excess Kurtosis Values of GLUT4-GFP and PI4P Fluorescence Intensity Profiles in Insulin-Stimulated WT and EFR3a KD 3T3-L1	

Adipocytes.	173
Figure 3.13. Optimisation and Validation of Primer Design for CRISPR/Cas9-Mediated Gene Knockout of Efr3a using Ribonucleoprotein.	178
Figure 3.14. Validation of CRISPR/Cas9-Mediated Efr3a Knockout in 3T3-L1 Fibroblasts using Ribonucleoprotein.	179
Figure 3.15. Optimisation and Validation of Primer Design for CRISPR/Cas9-Mediated Gene Knockout of Efr3a using Plasmid DNA.	181
Figure 3.16. Validation of CRISPR/Cas9-Mediated Efr3a Knockout in 3T3-L1 Fibroblasts using Plasmid DNA.	183
Figure 3.17. Characterisation of Plasmid DNA-Mediated CRISPR/Cas9 Efr3a Knockout 3T3-L1 Clones.	185
Figure 4.1. pH Measurements Accuracy between Homemade Perfusion Syringe System and Manual Pipetting.	209
Figure 4.2. Blinking Event Profiles Under Automated DNA-PAINT Imaging Strand Perfusion Using a Homemade Perfusion Syringe System.	211
Figure 4.3. Representative Immunofluorescence and DNA-PAINT Staining of the HA-Tag using Different Labelling Strategies in 3T3-L1 HA-GLUT4-GFP Adipocytes.	215
Figure 4.4. Characterisation of ALFA-GLUT4 Insulin-Stimulated Trafficking to the Plasma Membrane in Transiently Transfected HEK293 Cells.	219
Figure 4.5. Confirmation of ALFA-GLUT4 Expression in Stably Transfected HEK293 Clones.	221
Figure 4.6. Characterisation of ALFA-GLUT4 Insulin-Stimulated Trafficking to the Plasma Membrane in Stably Transfected HEK293 Cells.	222
Figure 4.7. ALFA-GLUT4 Localisation in Insulin-Stimulated Stably Transfected HEK293 Cells.	224

Figure 5.1. Visualisation of GLUT4-GFP in Ultrathick Sections of Cleared Mouse Hearts and Characterisation of Axial Imaging Depth with and without Organ Perfusion.	244
Figure 5.2. Summarised Flowchart of the Analysis Pipeline for Quantification of GLUT4-GFP Levels in Ultrathick Sections of Cleared Mouse Hearts.	246
Figure 5.3. Representative Axial Projections of GLUT4-GFP Fluorescence and Quantification of Global Regional GLUT4 Expression Levels in Control and HFD Hearts.	250
Figure 5.4. GLUT4 N-Glycosylation Cardiac Regional Heterogeneity in Mouse, Rat, and Rabbit.	251
Figure 5.5. Quantification of Transmural GLUT4-GFP Fluorescence in Control and HFD Hearts.	255
Figure 5.6. Quantification of Transmural GLUT4-GFP Fluorescence in Male and Female Hearts and the Impact of HFD in Females.	257
Figure 5.7. Protocol Optimisation for High Yields of Langendorff-Free Isolated Rod-Shaped Adult Mouse Cardiomyocytes.	261
Figure 5.8. Optimisation of HA-Tagged GLUT4 Immunofluorescent Staining in Adult Mouse Isolated Cardiomyocytes.	264
Figure 5.9. Insulin Stimulation of Adult Mouse Langendorff-Free Isolated Cardiomyocytes.	266
Figure 5.10. Insulin Stimulation of Adult Rat Cardiomyocytes Isolated using a Langendorff Perfusion System.	269
Figure 6.1. Updated Model of EFR3a/PI4K-III α -Regulated GLUT4 Dispersal in Adipocytes and Methodological Advancement for the Study of GLUT4 Spatial Organisation within the Plasma Membrane.	278

Appendix Figure 7.1. Effectiveness of siRNA-Mediated Efr3a and Pi4ka Knockdown in 3T3-L1 Adipocytes.	281
Appendix Figure 7.2. Schematic of CRISPR/Cas9 gRNA/Primers Set #1 Targeting Exon 1 of the Efr3a Gene.	284
Appendix Figure 7.3. Schematic of CRISPR/Cas9 gRNA/Primers Set #2 Targeting Exon 6 of the Efr3a Gene.	287
Appendix Figure 7.4. CRISPR/Cas9 DNA Plasmid Vector Map of pRP[CRISPR]-Puro-hCas9-U6>mEfr3a[gRNA#5786].	289
Appendix Figure 7.5. Schematic of CRISPR/Cas9 Plasmid DNA-Associated gRNA/Primers Targeting Exon 17 of the Efr3a Gene.	292
Appendix Figure 7.6. DNA Plasmid Vector Map of pcDNA3.1 (+) ALFA-GLUT4.	293
Appendix Figure 7.7. DNA Plasmid Vector Map of pcDNA3.1 (+) HA-GLUT4-GFP.	294
Appendix Figure 7.8. Optimisation of the Transient Transfection Protocol of pEGFP-C1-P4M-SidMx1 Plasmid DNA in 3T3-L1 Fibroblasts using Xfect™ Transfection Reagent.	296
Appendix Figure 7.9. Automated DNA-PAINT Imaging Strand Perfusion: Homemade Perfusion Syringe System G-code.	298
Appendix Figure 7.10. Illustrative Movies of 3D Render of GLUT4-GFP in Ultrathick Sections of Cleared Mouse Heart.	299
Appendix Figure 7.11. Illustrative Movies of Sequential Render of GLUT4-GFP in Ultrathick Sections of Cleared Mouse Heart.	299
Appendix Figure 7.12. Impact of High-Fat Diet-Feeding on Body Weight and Final Blood Glucose Levels in Mice, and Summary of Isolated Hearts Specifications.	300

Appendix Figure 7.13. Impact of HFD on GLUT4-GFP Fluorescent Signal in the Septum and RV of Male and Female Hearts and Quantification of Lateral Position of Maximum GLUT4-GFP Fluorescence Along the Breadth of Male and Female Cardiac Walls.	302
Appendix Figure 7.14. Quantification of Gross Anatomical Features in Imaged Myocardium.	303

List of Abbreviations

2DG	2-Deoxy-D-Glucose
31P-MRS	31P-Magnetic Resonance Spectroscopy
3D	Three-Dimensional
ACC	Acetyl-CoA Carboxylase
AMPK	AMP-activated protein Kinase
APS	Adapter protein with a Pleckstrin homology and an SH2 domain
BDM	2,3-ButaneDione Monoxime
BSA	Bovine Serum Albumin
CAP	c-Cbl-Associated Protein
c-Cbl	Casitas b-lineage lymphoma
CHD	Coronary Heart Disease
CIP4	Cdc42-Interacting Protein 4
CoA	Coenzyme A
CPT	Carnitine PalmitoylTransferase
CVD	CardioVascular Disease
DCM	Diabetic CardioMyopathy
DIY	Do-It-Yourself
DKA	Diabetic KetoAcidosis
DM	Diabetes Mellitus
DMEM	Dulbecco's Modified Eagle Medium
DNA-PAINT	DNA-Point Accumulation In Nanoscale Topography
DNe	Diabetic Nephropathy
DNu	Diabetic Neuropathy
DR	Diabetic Retinopathy
DSB	Double-Strand Break
dSTORM	diract Stochastic Optical Reconstruction Microscopy

EC	Endothelial Cell
FA	Fatty Acid
FAS	FA Synthase
FBS	Fetal Bovine Serum
FDM	Fused Deposition Modelling
FOV	Field Of View
FOXO1	FORKhead boX O1
GFP	Green Fluorescent Protein
GLUT	Glucose Transporter
gRNA	guide RNA
GS	Glycogen Synthase
GSC	GLUT4 Storage Compartments
GSK3	Glycogen Synthase Kinase 3
HA	HemAgglutinin
HDM	High-Density Microsomes
HF	Heart Failure
HFD	High-Fat Diet
HFpEF	HF with preserved Ejection Fraction
HFrEF	HF with reduced Ejection Fraction
HHS	Hyperglycaemia Hyperosmolar State
HMIT	H ⁺ -Driven Myoinositol Transporter
IR	Insulin Receptor
IRS	IR Substrate
IRV	Insulin-Responsive Vesicle
KD	KnockDown
KO	KnockOut
KRP	Krebs-Ringer-Phosphate
LA	Left Atrium
LDM	Low-Density Microsomes

LP	Localisation Precision
LSB	Laemmli Sample Buffer
LV	Left Ventricle
MODY	Maturity-Onset Diabetes of the Young
mTORC1	mammalian Target Of Rapamycin Complex 1
NA	Numerical Aperture of the imaging lens
NHEJ	Non-Homologous End Joining
NO	Nitric Oxide
PALM	Photo-Activated Localisation Microscopy
PDH	Pyruvate DeHydrogenase
PDK1	Phosphoinositide-Dependent Kinase 1
PET	Positron Emission Tomography
PFK	PhosphoFructoKinase
PI	PhosphoInositide
PI3K	Phosphatidylinositol 3-Kinase
PI4K-III α	Phosphatidylinositol 4-Kinase type III α
PI4P	Phosphatidylinositol 4-Phosphate
PIP2	Phosphatidylinositol 4,5-bisPhosphate
PIP3	Phosphatidylinositol 3,4,5-trisPhosphate
PTPase	Protein Tyrosine Phosphatase
PM	Plasma Membrane
PTEN	Phosphatase and TENsin homolog
RA	Right Atrium
RabGAP	Rab GTPase Activating Protein
RNP	RiboNucleoProtein
ROI	Region Of Interest
RV	Right Ventricle
SCAMP	Secretory Carrier-Associated Membrane Protein
siRNA	small-interfering RNA

SMLM	Single-Molecule Localisation Microscopy
SP	Soluble Protein
SREBP-1c	Sterol Regulatory Element-Binding Protein 1c
SRM	Super-Resolution Microscopy
STED	STimulated Emission Depletion
T1D	Type 1 Diabetes
T2D	Type 2 Diabetes
Ta	Annealing Temperature
TGN	Trans-Golgi Network
TIR	Total Internal Reflection
TIRF	TIR Fluorescence
Tm	Melting Temperature
TPS	Total Protein Stain
TTC7	TetraTriCopeptide repeat domain 7
v/v	Units volume per Unit volume
Vps10p	Vacuolar protein sorting 10 protein
w/v	Units weight per Unit volume
WCL	Whole Cell Lysate
WT	Wild-Type
Δ hxt	Depletion of Hexose Transporters

Introduction

1.1 Diabetes Mellitus

Diabetes mellitus (DM) encompasses various subtypes, including type 1 (T1D; autoimmune), type 2 (T2D; insulin resistance), maturity-onset diabetes of the young (MODY; genetic mutation), and gestational diabetes (pregnancy-related), all primarily characterised by a sustained elevation in blood glucose concentration. DM is typically diagnosed upon the detection of fasting blood glucose equal to or higher than 7.0 mM. Circulating glycated haemoglobin (HbA1c) above 6.5% can also be an accurate marker (Ampofo and Boateng, 2020; Antar et al., 2023; Atkinson et al., 2014). Such a chronic state of hyperglycaemia arises from defects in glucose uptake, primarily in adipose and muscle tissues, with the underlying mechanisms defining each DM subtype.

T1D and T2D are the two most common types of DM. T1D is an autoimmune disease characterised by the destruction of β -cells, resulting in little to no insulin production. Although T1D is generally defined by such loss of insulin production, there are rarer variants, such as idiopathic and fulminant T1D, that are not driven by autoimmunity. Both of these subtypes are associated with episodic ketoacidosis (see section [1.1.2](#)). While idiopathic T1D is more common in individuals of Asian or African heritage, fulminant T1D, also characterised by rapid β -cell destruction, is particularly present in East Asian populations (Antar et al., 2023; Atkinson et al., 2014). On the other hand, T2D, which affects 90% of the diabetic population, is defined by the inability of the body to use the insulin it effectively

produces. In T2D, defective glucose uptake primarily results from a combination of insulin resistance and progressive loss of β -cell insulin secretion (Saisho, 2014). Insulin resistance is characterised by a progressive lowering of the response to insulin in muscle, adipose, and liver cells. Higher amounts of insulin are therefore required by these cells to sustain proper glucose uptake. As a result, the pancreas responds by increasing its production of insulin. As long as enough insulin is produced to overcome the cells' increasing demands, blood glucose levels will remain stable and in the appropriate range. However, progressive insulin resistance worsening can eventually reach absolute resistance and lead to pancreatic β -cells failure (Artasensi et al., 2020).

Interestingly, hybrid forms of DM combine features of both T1D and T2D. Latent autoimmune diabetes in adults initially presents with insulin resistance but progresses to β -cell failure more rapidly than typical T2D. Ketosis-prone T2D, another hybrid form, begins with severe insulin deficiency and ketosis but can enter remission, requiring no long-term insulin therapy. These forms highlight the complex interaction between insulin resistance, autoimmunity, and β -cell dysfunction (Antar et al., 2023).

Specific genetic mutations can also cause DM. For example, MODY is a monogenic form of DM caused by genetic mutations that impair β -cell function, leading to reduced insulin production. MODY typically appears at a young age and differs from T1D and T2D as it does not involve autoimmunity or insulin resistance. Each MODY subtype is linked to specific gene mutations, affecting how the pancreas produces insulin (Antar et al., 2023).

Finally, gestational diabetes is primarily due to hyperglycemia during pregnancy. Unlike other types of DM, gestational diabetes is temporary, usually resolving after childbirth. Nevertheless, it increases the mother's risk of developing T2D later in life (Antar et al., 2023).

1.1.1 *Causes*

T1D remains a disease primarily attributed to genetic factors and an autoimmune response in which a T cell-mediated attack culminates in the loss of β -islet cells, affecting otherwise healthy individuals (Todd, 2010). In contrast, although the development of T2D often involves underlying genetic components, lifestyle factors such as lack of physical activity, diets rich in saturated fatty acids (FA) and high glycaemic index carbohydrates, stress, and smoking habits are recognised as strong environmental risk factors for T2D (Dendup et al., 2018; Kolb and Martin, 2017; Uusitupa, 2002). Characterised by a body mass index equal to or above 30 kg/m², obesity is observed in around 60% of individuals with T2D. While for the past 50 years, obesity was mainly identified as an important societal issue in high-income countries, its prevalence has recently tripled in lower-income countries. Given the relationship between obesity and diabetes, the prevalence of diabetes is, therefore, projected to significantly increase by 2030 (Ampofo and Boateng, 2020; Chatterjee et al., 2017).

1.1.2 *Complications*

Diabetic ketoacidosis (DKA) and hyperglycaemia hyperosmolar state (HHS) represent two extremes in the spectrum of DM physiological

consequences, as well as distinct markers for subtypes of DM. Both DKA and HHS result from the insulin imbalance and elevated glucose levels observed in individuals with untreated DM (Gosmanov et al., 2000). DKA is characterised by the body shifting into a primarily catabolic state where an increase in glycogenolysis and triglyceride hydrolysis is observed in adipose tissues, and a switch from protein synthesis to proteolysis is triggered in muscle tissues (Kitabchi and Nyenwe, 2006). As a result, the latter substrates released from peripheral tissues stimulate the liver to produce glucose and ketone bodies, which accumulate in the blood. This metabolic decompensation then leads to a decrease in blood pH, which can result in hypotension, shock, and death (Foster and McGarry, 1983; Miles et al., 1980). HHS is another consequence of sustained hyperglycaemia. High blood glucose levels lead to increased blood osmolarity and, therefore, water loss, causing dehydration and an electrolyte imbalance (Kitabchi et al., 2009). If left untreated, DKA and HHS can cause unconsciousness, also known as diabetic coma, and lead to numerous complications, including renal disease, retinopathy, neuropathy, and, most importantly, cardiovascular diseases (CVD).

Under normal physiological conditions, endothelial cells (EC) mediate vascular tone, cell adhesion, and clotting homeostasis, ensuring blood fluidity (Popov, 2010). For instance, in healthy EC, the phosphatidylinositol 3-kinase (PI3K)-dependent insulin signalling pathway (see section [1.3.2.1](#)) stimulates the activation of endothelial nitric oxide (NO) synthase, releasing NO that subsequently promotes vasorelaxation and activates anti-inflammatory and anti-atherosclerotic mechanisms. However, when impaired, this system is shown to contribute to the development of numerous DM-related complications (Riehle and Abel, 2016; Symons and

Abel, 2013). Exposure to high blood glucose levels disturbs numerous intracellular signalling pathways and induces a phenotypic switch of EC that acquires, amongst others, inflammatory, proliferative, apoptotic, or even senescent properties (Popov, 2010). Over time, the intensification of these cells' metabolic activity and biochemical imbalance leads to a modification of the cellular structures, damaging both EC and vascular walls. As a result, severe damage to both large and small blood vessels, such as arterioles and capillaries, can be observed (Popov, 2010). The vascular consequences of hyperglycaemia are generally categorised into macro- and microvascular complications, depending on the size of the injured vessels (Fowler, 2008; Popov, 2010).

1.1.2.1 Microvascular Complications

In smaller vessels, the blood flow will initially slow down, reducing oxygen and nutrient supply and causing structural damage within vascular walls. Two of the most common microvascular complications are diabetic retinopathy (DR) and diabetic nephropathy (DNe). DR is diagnosed upon the apparition of retinal haemorrhages, microaneurysms, microvascular abnormalities, and venous calibre changes. From visual impairment to blindness, DR affects around 100 million people worldwide (Duh et al., 2017; Teo et al., 2021). Meanwhile, DNe is defined by the chronic loss of renal functions that, over the years, can culminate in kidney failure. While it can take up to 15-20 years for kidney failure to develop, DR can be difficult to diagnose as it often requires invasive interventions to confirm and, therefore, be properly treated in the early stages (Haller et al., 2017).

As for DR and DNe, the risk of developing diabetic neuropathy (DNe) depends on the magnitude and duration of hyperglycaemic events, causing more or less injuries to the peripheral nerves. The most common manifestation of DNe is sensory neuropathy. While some individuals can experience pain in their extremities, others can experience simple numbness. Because up to 50% of peripheral DNe can be asymptomatic, in the absence of preventive care, patients are at risk of unnoticed injuries and infections, such as painless foot ulceration, which can lead to amputation (Fowler, 2008; Pop-Busui et al., 2017).

1.1.2.2 Macrovascular Complications

Among macrovascular complications, CVD are the most critical and common long-term complications. Being the leading cause of death in people with DM, the close link between DM, more specifically T2D, and CVD has long been established (Haffner et al., 1998; Laakso, 2011). At the centre of macrovascular complications is the development of atherosclerosis, characterised by the excessive accumulation of lipids in the endothelial wall of arteries, infiltration and proliferation of inflammatory cells, which in turn induce the proliferation and accumulation of smooth muscle and collagen, respectively, and finally the formation of a lipid-rich atherosclerotic lesion. As a result, atherosclerosis leads to the narrowing of arterial walls in both the peripheral and coronary vascular systems (Boyle, 2007). Over 80% of CVD-associated deaths and injuries are associated with atherosclerosis (Funk et al., 2012).

Further highlighting the complex relationship between CVD and DM, in 1974, the Framingham Heart Study reported that in individuals with T2D,

the incidence of heart failure (HF) was increased by 2.4-fold and 5-fold in men and women, respectively (Kannel et al., 1974). In 2004, it was measured that in the United States, 44% of patients with chronic HF had DM (Adams et al., 2005). Equally, coronary heart disease (CHD) was shown to increase by 2- to 4-fold in T2D (Haffner et al., 1998; Kannel and McGee, 1979).

Another example of CVD is diabetic cardiomyopathy (DCM). While less common, DCM was discovered after post-mortem examinations of four patients with T2D. This diagnosis helped explain why symptoms of HF were observed in these patients without any signs of CHD or other valvular diseases (Rubler et al., 1972). Known to affect approximately 12% of individuals with T2D, DCM is a clinical condition that is first defined by the dilatation and hypertrophy of the heart and the presence of diastolic and/or systolic dysfunction (increase in ventricular stiffness, left ventricle (LV) end-diastolic pressure, and left atrial enlargement). As the disease progresses, chronic hyperglycaemia and insulin resistance cause metabolic alterations. This includes an increase in collagen formation, the activation of mitogen-activated protein kinase and calcium signalling pathways, which increase the volume of cardiomyocytes and finally lead to cell death. As a result, these molecular changes culminate in left ventricular hypertrophy, cardiac remodelling, reduced contractile capacity, advanced diastolic dysfunctions, and the emergence of clinical symptoms of HF (Bernardo et al., 2010; Trachanas et al., 2014; Westermeier et al., 2016). Consequently, anatomic and physiological modifications appear in the myocardium, affecting both cardiac functions and performance, eventually leading to HF (Trachanas et al., 2014).

Considering the impact of CVD in T2D, the heart will be a major focus of this thesis (see [Chapter 5](#)).

1.1.3 *Diabetes as a Growing Healthcare Burden*

Diabetes has emerged as a fundamental physiological and economic burden for society. Diabetes affects ~415 million individuals worldwide and caused ~5 million deaths in 2015, incurring a global health expenditure estimated at \$673 billion. These figures are estimated to reach \$802 billion and 642 million affected individuals by 2040. Worryingly, studies have shown increasing rates in low- and middle-income countries (Ogurtsova et al., 2017).

In the UK, about 7% of the population is estimated to live with diabetes, including 40,000 children and 1 million people with undiagnosed T2D. About one-third of people with T2D already have microvascular complications at the time of their diagnosis. In 2019, the NHS spent ~£27 million a day on diabetes and recorded 530 myocardial infarctions and 175 amputations every week as consequences of the disease (Whicher et al., 2020).

Diabetes, therefore, represents a significant societal and economic healthcare problem. While changes toward a more active and balanced lifestyle have been shown to effectively prevent, improve, or even reverse T2D (Lean et al., 2018), medication options such as Metformin remain the first line of therapy for patients with T2D (Chatterjee et al., 2017). However, while these medications can treat the symptoms of T2D, no cure is currently available. A better understanding of glucose management mechanisms in

both normoglycemic and diabetic individuals is therefore of central importance to reduce diabetes prevalence and enhance treatment options.

1.2 Glucose Homeostasis

1.2.1 *Glucose Management in Health*

Glucose is an essential source of energy. While plants are autotrophic organisms capable of producing glucose by photosynthesis from carbon dioxide and water, animals absorb glucose from their diet. Glucose is then either metabolised, used for lipid synthesis, or stored as glycogen by different tissues around the body. When metabolised, the chemical energy of glucose is converted into ATP by an oxidative process called cellular respiration. Glycolysis is a metabolic pathway and the first step of cellular respiration. It takes place in the cytosol and involves the enzymatic breakdown of glucose into pyruvate. Upon entry into mitochondria, pyruvate molecules are converted into acetyl-coenzyme A (CoA) and proceed to the citric acid cycle, otherwise known as the Krebs cycle, the second primary step of cellular respiration. Finally, the electrons and protons produced during glycolysis and the citric acid cycle are fed into an electron transport chain, ultimately ending in oxidative phosphorylation and the production of ATP (Campbell et al., 2017).

In normoglycemic individuals, circulating blood glucose levels are typically maintained between 4 and 6 mM. While several mechanisms exist to help regulate these levels, glucose homeostasis is primarily achieved by insulin and glucagon, two peptide hormones with opposing actions produced by specialised cells in the islets of Langerhans of the pancreas (**Figure 1.1**).

When blood glucose levels drop below normal range, glucagon is released from α -cells. It primarily promotes hepatic glycogenolysis, a catabolic process which converts stored glycogen into glucose. During prolonged fasting, glucagon also stimulates both hepatic and renal gluconeogenesis, allowing the synthesis of additional glucose (**Figure 1.1**). In contrast, rising blood glucose levels stimulate pancreatic β -cells to produce insulin after meals. Upon docking to its receptor, known as the tyrosine kinase insulin receptor (IR), insulin primarily triggers the uptake of excess glucose from the bloodstream into muscle and adipose tissues. In muscle cells, glucose is either used immediately to produce ATP or stored as glycogen, which can then be converted back to glucose when required. In adipocytes, glucose is mainly converted into triglycerides for storage. By regulating their release of free FA from stored triglycerides, adipose tissues can also influence insulin sensitivity in the liver and muscle tissues. Finally, while hepatic glucose uptake is insulin-independent, the latter hormone was found to help hepatic storage of absorbed glucose into glycogen through glycogenesis (**Figure 1.1**) (Röder et al., 2016).

In a normoglycemic individual, the well-functioning interplay of the pancreas with all the involved tissues ensures glucose homeostasis. However, impairment in the production and/or sensitivity to insulin often results in metabolic diseases, such as T2D.

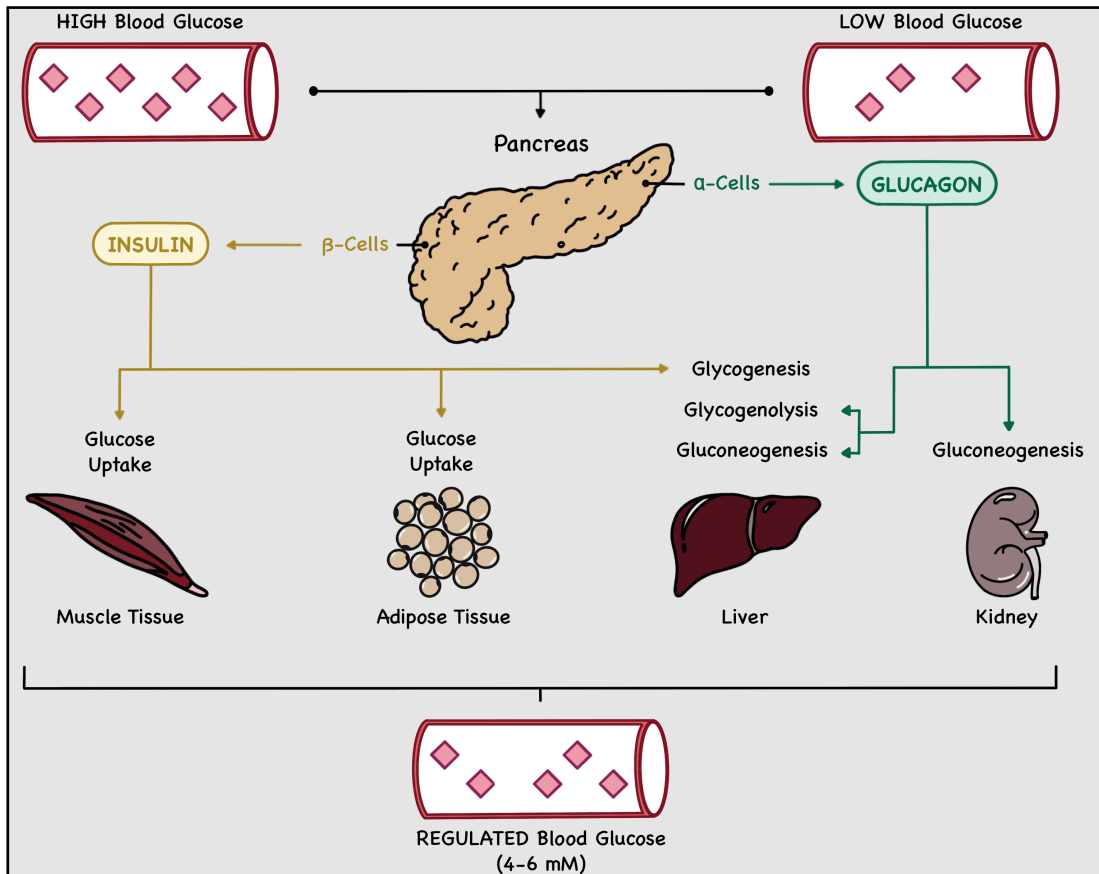


Figure 1.1. Schematic of Glucose Homeostasis.

Blood glucose levels are regulated by glucagon and insulin produced by the pancreatic α - and β -cells, respectively. Detection of low blood glucose levels triggers the secretion of glucagon (green), which promotes the production of endogenous glucose through hepatic glycogenolysis, as well as both hepatic and renal gluconeogenesis. When blood glucose levels rise above the normal range, insulin (yellow) is produced to promote glucose uptake into muscle and adipose tissues and stimulate hepatic glycogenesis. Inspired by Röder et al. (2016).

1.2.2 Energy Substrates and Management in the Heart

The heart is the most energy-demanding tissue in the body. While it has a relatively low ATP content, its ATP hydrolysis rate is high, leading to a complete turnover of myocardial ATP every 10 seconds at rest. To accommodate this, the heart can generate energy from lipids,

carbohydrates, lactate, amino acids, and ketone bodies, depending on the prevailing metabolic milieu.

Primarily relying on mitochondrial oxidative phosphorylation, a healthy heart preferentially uses lipids as its main source of energy, with around 60 to 90% of produced ATP coming from the oxidation of FA, whereas 10 to 40% of ATP is derived from the oxidation of pyruvate, obtained from glycolysis and lactate oxidation (Stanley et al., 2005). In 1963, Randle et al. proposed a “glucose-fatty acid cycle” to explain this metabolic asymmetry. As confirmed by numerous studies over the years, the “Randle cycle” describes the ability of high circulating levels of FA to inhibit glucose utilisation and vice-versa (**Figure 1.2**) (Randle et al., 1963). More complex than initially revealed, the intricate relationship between glucose and FA metabolism is controlled by the degree of expression of numerous vital metabolic enzymes and transporters, as well as regulation through a series of allosteric alterations, changes in the concentration of specific metabolites, and translocation of key proteins to their site of function. Briefly, FA oxidation was revealed to reduce glucose utilisation via allosteric inhibitions of glycolytic enzymes phosphofructokinase (PFK)-1 and pyruvate dehydrogenase (PDH). Inhibition first occurs upon increased mitochondrial acetyl-CoA concentration upon FA oxidation, inhibiting PDH activity. Subsequently, the Krebs cycle intermediate citrate accumulation, in turn, inhibits PFK-1 (**Figure 1.2**) (Hue and Taegtmeyer, 2009; Randle et al., 1963).

Interestingly, changes in the expression and activity of these metabolic proteins can happen without affecting overall ATP production, allowing rapid adaptation in response to stressful events such as exercise or

ischemia (Stanley et al., 2005). Indeed, while the main biochemical consequence of the Randle cycle's glucose-sparing side is conserving glucose for the brain during starvation, the capacity to increase glucose utilisation by decreasing FA oxidation is also necessary for the heart to recover from pathophysiological metabolic stresses. It was demonstrated that increased production of malonyl-CoA, a lipogenic intermediate from glucose oxidation, plays a key role in lowering FA oxidation by inhibiting carnitine palmitoyltransferase (CPT)-1, which controls the entry of FA into the mitochondria (**Figure 1.2**) (Hue and Taegtmeyer, 2009; Randle et al., 1963).

Ketone bodies provide D-beta-hydroxybutyrate, an alternative substrate for oxidative phosphorylation, produced by the liver from the incomplete oxidation of FA and released from adipose tissues. While metabolised by the heart, amino acids only represent a minor energy source (Stanley et al., 2005). Ultimately, the relative contribution of different substrates to produce ATP in the heart will change depending on the energy demand and substrate availability. For instance, exercise induces a switch from FA to glucose oxidation (Bertero and Maack, 2018).

This ability to adapt and shift between different substrates, ensuring a continuous energy supply, has earned the heart the name of “metabolic omnivore” (Taegtmeyer, 1985).

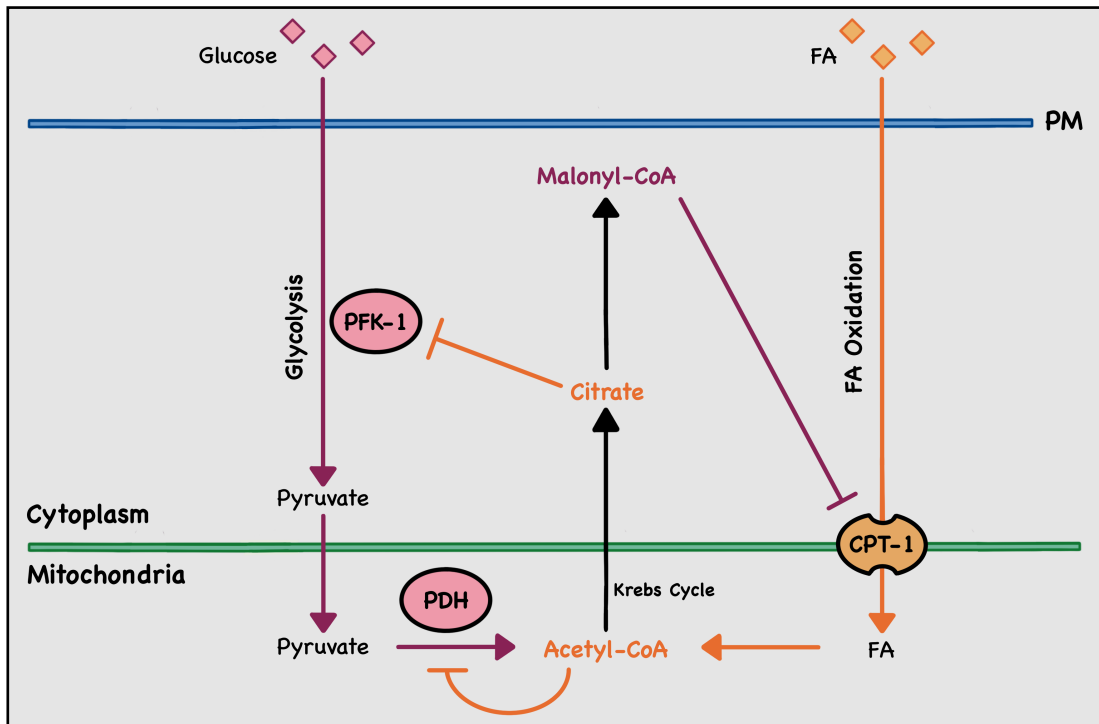


Figure 1.2. Simplified Schematic of the Randle Cycle.

The Randle Cycle describes the ability of high circulating levels of fatty acids (FA) to inhibit glucose utilisation and vice-versa through a series of allosteric alterations, changes in the concentration of specific metabolites, and translocation of key proteins to their site of function. Mechanisms of inhibition of glucose utilisation by FA oxidation are highlighted in orange in this figure. Inhibition first occurs upon increased mitochondrial acetyl-CoA concentration upon FA oxidation, inhibiting pyruvate dehydrogenase (PDH) activity. Subsequently, the Krebs cycle intermediate citrate accumulation inhibits phosphofructokinase (PFK)-1. On the other hand, mechanisms of inhibition of FA oxidation by glucose are highlighted in purple in this figure. Increased production of malonyl-CoA, a lipogenic intermediate from glucose oxidation, inhibits carnitine palmitoyltransferase (CPT)-1, which controls the entry of FA into the mitochondria, ultimately lowering overall FA oxidation. PM; Plasma Membrane. Inspired by Hue and Taegtmeyer (2009).

1.3 Glucose Transport in Adipose and Muscle Tissues

1.3.1 Introduction to GLUT4

The transport of glucose from the bloodstream into cells across the plasma membrane (PM) relies on a family of 14 glucose transporters, known as GLUTs, that are expressed in a tissue-specific manner (Mueckler and Thorens, 2013). Following the isolation of GLUT1 cDNA in 1985 (Mueckler et al., 1985), a further 13 members of the GLUT family were identified: GLUT2 to 12, HMIT (H⁺-driven myoinositol transporter or GLUT13), and GLUT14 (Bell et al., 1990; James et al., 1988; Joost and Thorens, 2001; Kayano et al., 1990; Mueckler and Thorens, 2013; Wu and Freeze, 2002).

Many organs, such as the brain, have a constitutive requirement of high glucose. In these organs, GLUTs are constitutively targeted to the cell surface (e.g., GLUT3) to allow sufficient glucose uptake. Unlike other GLUT, GLUT4 depends on specialised insulin- and/or exercise-stimulated regulatory mechanisms to prevent large variations in blood glucose levels. In 1939, Einar Lundsgaard was the first to observe an insulin-mediated increase in glucose uptake into cat skeletal muscle (Kruhøffer and Crone, 1972; Lundsgaard, 1939). This phenomenon was subsequently shown, first in adipocytes (Cushman and Wardzala, 1980; Suzuki and Kono, 1980; Wardzala et al., 1978) and later in muscle cells (Klip et al., 1987; Wardzala and Jeanrenaud, 1981), to rely on a specific trafficking system that involves the insulin-dependent translocation of GLUT4 from intracellular compartments, now defined collectively as GLUT4 storage compartments (GSC) (Bryant et al., 2002), to the PM. A few years later, GLUT4 was cloned and defined as the main glucose transporter to undergo insulin-stimulated translocation in adipose and muscle tissues (Charron et al., 1989;

Fukumoto et al., 1989; Garcia de Herreros and Birnbaum, 1989; James et al., 1988; Kaestner et al., 1989).

In the early 2000s, Barbara Kahn's laboratory then significantly advanced our understanding of GLUT4's tissue-specific roles by generating knockout (KO) mouse models where GLUT4 was selectively deleted in either skeletal muscle or adipose tissue. These models revealed surprising insights. Mice lacking GLUT4 in skeletal muscle developed significant insulin resistance and glucose intolerance within the muscle, yet exhibited relatively normal systemic glucose levels due to maintained GLUT4 expression and compensatory insulin sensitivity in adipose and liver tissues. However, these mice still presented with fasting hyperglycemia and hyperinsulinemia, highlighting the importance of muscle GLUT4 in maintaining glucose balance and demonstrating that its absence directly contributes to the development of T2D's features (Zisman et al., 2000). Mice lacking GLUT4 in adipose tissue displayed systemic insulin resistance and glucose intolerance. The absence of GLUT4 in adipose tissue led to dysregulated lipid metabolism, increased circulating free fatty acids, and disrupted adipokine secretion, contributing to insulin resistance in muscle and liver despite GLUT4 expression remaining unchanged in these tissues. This study underscored that GLUT4 in adipose tissue is essential for maintaining insulin sensitivity throughout the body, and highlighted a communication mechanism between adipose tissue and other metabolic organs like muscle and liver (Abel et al., 2001). Kahn's findings had profound implications for understanding the pathogenesis of insulin resistance and T2D, first suggesting that defects in GLUT4 function in either tissue can contribute to systemic metabolic dysfunction (Abel et al., 2001; Zisman et al., 2000).

Structurally, GLUT consist of 12 transmembrane α -helices, with an exofacial and cytoplasmic loop, as well as both amino- and carboxyl-termini located in the cytosol (Mueckler et al., 1985). More specifically, the fourteen GLUT mentioned above are categorised into three classes based on sequence similarity. Class 1 (GLUT 1 to 4 and 14) and Class 2 (GLUT 5, 7, 9 and 11) are structurally distinguishable from Class 3 (GLUT 6, 8, 10, 12 and 13) proteins. This distinction lies in the location of their sites of amino-linked glycosylation, which reside in the first exofacial linker domains for Class 1 and 2 GLUT and in the fifth exofacial linker domains for Class 3 proteins (Mueckler and Thorens, 2013). While sharing basic similarities with other GLUT, GLUT4 possesses unique amino acid sequences relating to its specific functions and kinetics during endo- and exocytosis. These include a double leucine and an acidic motif in the carboxyl-terminal, which regulate the intracellular distribution of GLUT4 (Corvera et al., 1994; Shewan et al., 2000). An FQQI motif located at the amino-terminus allows the interaction of GLUT4 with specific adaptor proteins, essential for endosomal sorting and GLUT4 targeting to proper intracellular locations (Bernhardt et al., 2009).

Over the years, studies have shown that GLUT4 translocation to the PM mainly depends on two mechanisms, namely insulin signalling (see section [1.3.2.1](#)) and vesicular trafficking (see section [1.3.2.2](#)). While GLUT4 is primarily expressed in both adipose and muscle tissues, details about these molecular pathways rapidly emerged at the centre of numerous investigations using adipocytes, considered then and now as a more amenable model than myocytes (see [Chapter 5](#)). Over the years,

adipocytes have become a reference model for studying GLUT4 trafficking machinery.

1.3.2 *GLUT4 in Adipocytes: A Reference*

1.3.2.1 Insulin Signalling

As previously explained, when blood glucose levels rise above the normal range in a healthy individual, insulin is secreted into the bloodstream from pancreatic β -cells (see section [1.2.1](#)). Although the existence of a cell-surface IR was identified in 1971 (Freychet et al., 1971), it was in 1985 that the IR was determined to contain a transmembrane domain, as well as an intrinsic tyrosine kinase domain with multiple tyrosine auto-phosphorylation sites (Ebina et al., 1985). Upon insulin binding, the IR, therefore, activates itself before phosphorylating IR substrate (IRS) proteins, such as IRS-1, which then act as docking proteins to recruit other signal-transducing molecules to the PM (Kasuga et al., 1982; Sun et al., 1991). One of these, PI3K, leads to the formation of phosphatidylinositol 3,4,5-trisphosphate (PIP₃) from phosphatidylinositol 4,5-bisphosphate (PIP₂) at the inner leaflet of the PM. PIP₃ subsequently recruits phosphoinositide-dependent kinase 1 (PDK1) and Akt, also known as protein kinase B, to the PM, where PDK1 phosphorylates and activates Akt (Kohn et al., 1996). In 2003, Sano et al. showed that the subsequent activation of the Akt-signalling pathway plays a major role in the regulation of GLUT4 trafficking and, therefore, glucose uptake (Sano et al., 2003). Targeted by Akt, TBC1D4 (also known as AS160) was identified as a Rab GTPase activating protein (RabGAP). RabGAP's primary function are to regulate intracellular vesicle

trafficking by recruiting small effector G proteins, known as Rabs, when in an active GTP-bound form. Inactivation of RabGAP occurs upon GTP hydrolysis to GDP by their GAP domain. Akt phosphorylation of TBC1D4 was observed to inhibit its GAP activity, allowing GTP loading and the recruitment of Rabs. Overall, while studies are still exploring the various regulation mechanisms of TBC1D4, the subsequent activation of both TBC1D4 and Rabs was found to be essential in the fusion of GLUT4-containing insulin-responsive vesicles (IRV) with the PM (**Figure 1.3**) (Klip et al., 2019; Sano et al., 2003).

In addition to its role in GLUT4 translocation, Akt also regulates glycogen synthesis by inactivating glycogen synthase kinase 3 (GSK3), and *de novo* lipogenesis by regulating the activity of the mammalian target of rapamycin complex 1 (mTORC1) and forkhead box O1 (FOXO1) (**Figure 1.3**). GSK3 phosphorylates and inhibits glycogen synthase (GS), the enzyme responsible for converting glucose into glycogen. Upon insulin stimulation, Akt phosphorylates GSK3, rendering it inactive. This disinhibition of glycogen synthase allows GS to remain active, promoting glycogen synthesis from glucose (Oreña et al., 2000). While glycogen synthase is regulated by insulin, its activity in adipocytes is less developed compared to other tissues like the liver and muscle. Most of the glucose taken up by adipocytes is directed toward *de novo* lipogenesis, which contributes to the synthesis of triglycerides for fat storage rather than being stored as glycogen. Indeed, under insulin stimulation, Akt activates mTORC1, which promotes lipogenesis by enhancing the expression of sterol regulatory element-binding protein 1c (SREBP-1c). This transcription factor upregulates lipogenic enzymes such as acetyl-CoA carboxylase (ACC). ACC is the enzyme that converts acetyl-CoA into malonyl-CoA, a

crucial substrate for lipogenesis from glucose-derived substrates. Concurrently, insulin signalling leads to the phosphorylation and inactivation of FOXO1, a transcription factor that promotes gluconeogenesis and fatty acid oxidation. The inactivation of FOXO1 by Akt prevents the expression of gluconeogenic genes, effectively shifting glucose utilisation toward lipogenesis instead of glucose production (Savova et al., 2023).

Overall, this coordinated action of Akt ensures that insulin effectively facilitates both glucose uptake (via GLUT4) and metabolism (via GSK3, mTORC1 and FOXO1) (**Figure 1.3**), contributing to overall glucose homeostasis.

In parallel, while less characterised, multiple studies have also observed the presence of a second signalling branch involved in GLUT4 trafficking in 3T3-L1 adipocytes (Isakoff et al., 1995). Upon insulin stimulation, the phosphorylation of adapter proteins with a pleckstrin homology and an SH2 domain (AP5) by the IR was shown to induce the subsequent activation of proto-oncogene Casitas b-lineage lymphoma (c-Cbl). c-Cbl then recruits c-Cbl-associated proteins (CAP), ultimately activating the GTPase known as TC10. Finally, TC10 binds to Cdc42-interacting protein 4 (CIP4), stimulating GLUT4 translocation in a PI3K-independent manner (**Figure 1.3**) (Chang et al., 2007; Liu et al., 2002).

Finally, the inhibition of insulin action is also crucial for maintaining glucose homeostasis, allowing for a precise and efficient on/off response to insulin. After insulin dissociates from its receptor, the phosphorylation of the IR and its substrates is rapidly reversed by protein tyrosine phosphatases (PTPase).

PTP1B and phosphatase and tensin homolog (PTEN) are two key proteins involved in this regulatory process. While PTP1B inhibits autophosphorylation of the IR and IRS-1, PTEN inhibits insulin signalling by dephosphorylating PIP₃ (**Figure 1.3**). Both PTPases reduce downstream Akt activation and dampen insulin's effects on glucose uptake and metabolism (Delibegović et al., 2024; Nakashima et al., 2000).

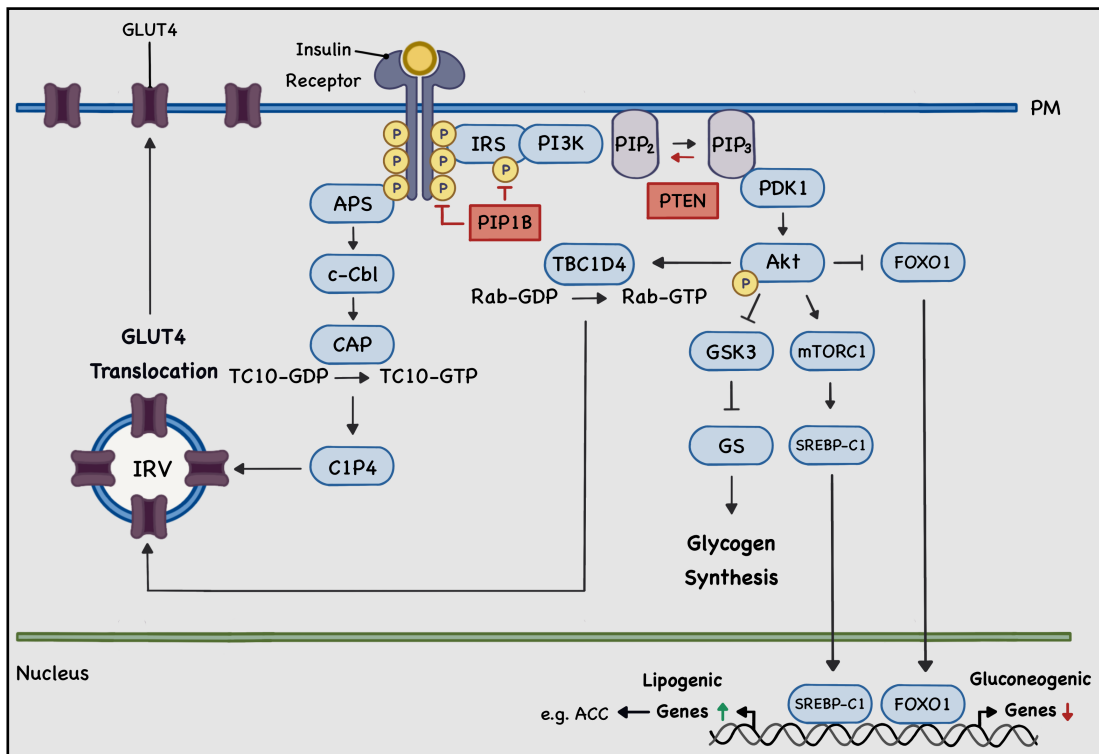


Figure 1.3. Schematic of the Insulin Signalling Cascade in Adipocytes.

Upon insulin docking, insulin receptors (IR) are auto-phosphorylated, leading to the phosphorylation and activation of IR substrate (IRS) proteins and adapter proteins with a pleckstrin homology and an SH2 domain (APS). On one side, IRS activates phosphatidylinositol 3-kinase (PI3K) to produce phosphatidylinositol 3,4,5-trisphosphate (PIP₃) from phosphatidylinositol 4,5-bisphosphate (PIP₂), and recruits phosphoinositide-dependent kinase 1 (PDK1) and Akt to the plasma membrane (PM). Activated by PDK1, Akt then phosphorylates and inactivates the GAP domain of TBC1D4. Once in its active GTP-bound form, TBC1D4 recruits Rabs and stimulates the translocation of GLUT4-containing insulin-responsive vesicles (IRV) to the PM. In parallel, APS-activated proto-oncogene Casitas b-lineage lymphoma (c-Cbl) and c-CBL-associated protein (CAP) stimulate the recruitment of TC10, which binds to Cdc42-interacting protein 4 (CIP4) to promote GLUT4 translocation to the PM. Akt also regulates glycogen synthesis and lipogenesis. Akt phosphorylation and inactivation of glycogen synthase kinase 3 (GSK3) allows glycogen synthase (GS) to promote glycogen synthesis from glucose. However, in adipocytes, glucose primarily undergoes *de novo* lipogenesis, driven by Akt activation of mTORC1 and the expression of SREBP-1c, which upregulates lipogenic enzymes like acetyl-CoA carboxylase (ACC). Simultaneously, Akt phosphorylates and inactivates forkhead box O1 (FOXO1), inhibiting gluconeogenic gene expression. The termination of insulin signalling is regulated by protein tyrosine phosphatases such as PTP1B and (phosphatase and tensin homolog) PTEN reversing IR, IRS, and PIP₃ phosphorylation, thereby reducing Akt activation and diminishing insulin's metabolic effects.

1.3.2.2 GLUT4-Vesicular Trafficking

In parallel to the above discoveries, the study of GLUT4-vesicular trafficking to the PM also became a major focus of investigation. In adipocytes, it is now established that in the absence of insulin, 95% of cellular GLUT4 transporters were shown to accumulate in GSC, which include the *trans*-Golgi network (TGN), endosomes, and IRV (Gould et al., 2020; Klip et al.,

2019; Slot et al., 1991b). Upon insulin stimulation, up to 70% of the sequestered GLUT4 undergoes exocytosis to the PM (Malide et al., 2000; Slot et al., 1991a; Slot et al., 1991b). From the TGN, IRV are transported along cytoskeletal elements, facilitating their final tethering, docking, and fusion to the PM. In parallel, insulin also inhibits GLUT4 endocytosis from the PM. As a result, GLUT4 levels at the PM increase with a concomitant increase in glucose entry into the cells (Bogan, 2012; Gould et al., 2020; Klip et al., 2019; Saltiel, 2021). Upon insulin removal, most of the PM-localised GLUT4 are re-internalised and recycled back into IRV, where they once again accumulate (**Figure 1.4**) (Bogan, 2012).

Failure of GLUT4 to undergo insulin-stimulated translocation to the PM represents a major manifestation of insulin resistance in T2D (Bogan, 2012). This has, in turn, driven extensive efforts to understand the itinerary of GLUT4 trafficking within cells and how its delivery to and from the PM is regulated. The complexity of GLUT4 trafficking is exemplified by the number of proteins identified as regulators of different aspects of intracellular GLUT4 storage, the levels of many changes in T2D, and the difficulties in unravelling the pathways involved in its endocytotic trafficking (Bernhardt et al., 2009; Livingstone et al., 2022).

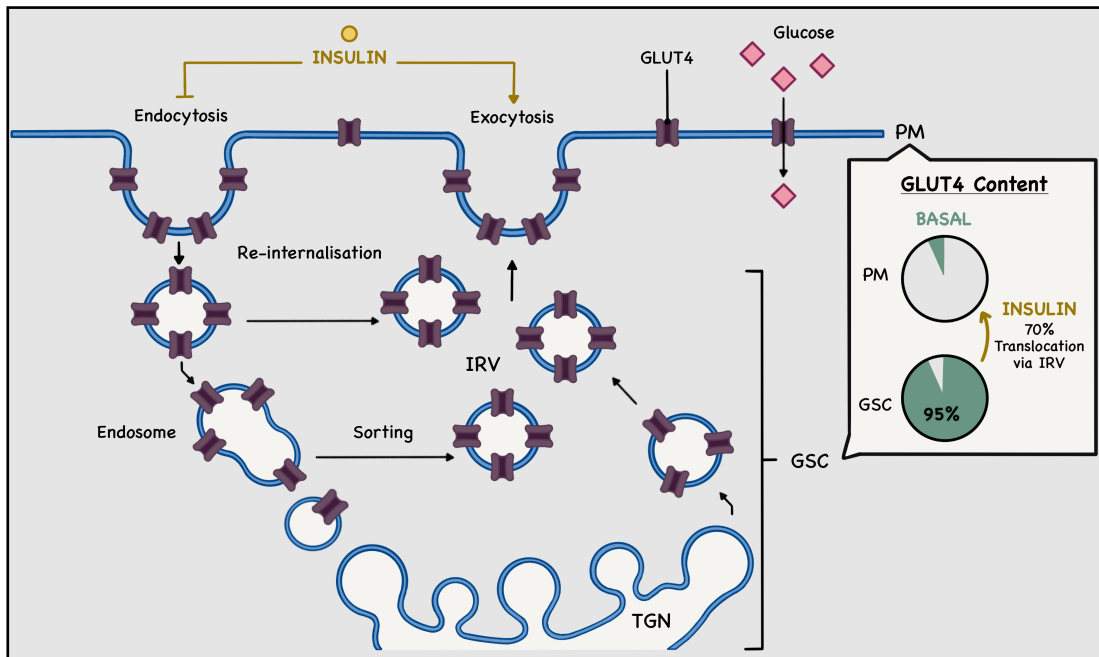


Figure 1.4. Model of GLUT4 Trafficking to the Plasma Membrane in Adipocytes.

In adipocytes, insulin regulates GLUT4 translocation to, and dispersal within, the plasma membrane (PM). Under basal conditions, 95% of cellular GLUT4 transporters (shown as purple structures) accumulate in GLUT4 storage compartments (GSC), including the trans-Golgi network (TGN), endosomes, and insulin-responsive vesicles (IRV). Upon insulin stimulation, up to 70% of the sequestered GLUT4, primarily in IRV, translocates to and fuse with the PM (exocytosis), leading to glucose (pink) uptake into the cell. In parallel, insulin also inhibits GLUT4 endocytosis from the PM. GLUT4 molecules are re-internalised upon insulin removal and recycled back into the GSC. Adapted from Geiser et al. (2023).

1.3.3 GLUT4 in Muscle Cells

1.3.3.1 Insulin Signalling

Compared to adipocytes, fewer studies have been performed in skeletal muscle cells and only a few in cardiomyocytes. This reflects the differences in cell morphology and the difficulty in obtaining isolated, viable cells from muscle tissues to study (see [Chapter 5](#)). Nevertheless, studies have

suggested that muscles possess a similar PI3K-dependent insulin-signalling pathway to adipocytes (**Figure 1.3**), with only a few differences. For instance, while in adipocytes, the key Rab targeted by TBC1D4 is Rab10, Rab8 and Rab13 have been identified as the main Rabs in skeletal muscle cells (Klip et al., 2019; Sun et al., 2010). A TBC1D4 paralog, named TBC1D1, has also been identified and found to be highly expressed in skeletal muscle while absent in both adipocytes or cardiomyocytes. Unlike TBC1D4, TBC1D1 is involved in insulin-stimulated and contraction-induced GLUT4 translocation (see section [1.3.3.2](#)) (Taylor et al., 2008). Although different, the insulin- and contraction-induced molecular pathways often converge, involving numerous similar signalling molecules. In skeletal muscles, incorporated glucose is then converted to glycogen for storage in a GSK3/GS-dependent manner (**Figure 1.3**) or enters the glycolytic pathway, where it is oxidised for energy production (Cross et al., 1995; Ijuin et al., 2015). Increased protein synthesis upon insulin signalling is also mediated via FOXO and mTORC1 (Ueda-Wakagi et al., 2018).

In cardiomyocytes, insulin modulates numerous cellular processes, from metabolism to cell growth and survival. Similarly to adipocytes and skeletal muscle cells, insulin stimulates GLUT4 translocation to the PM in a PI3K/Akt-dependent manner. In contrast, Akt1 and Akt2 have been identified as two of the most abundant Akt isoforms in cardiomyocytes while appearing to regulate myocardial metabolism differentially. In isolated mice cardiomyocytes, only Akt2 is required for insulin-mediated glucose uptake, whereas Akt1 appears to govern cellular somatic growth. For instance, the deletion of Akt2, but not Akt1, in mice showed a reduction in insulin-stimulated glucose uptake in the heart and ischemia tolerance (Bae et al., 2003; DeBosch et al., 2006; Riehle and Abel, 2016). Equally, further down

this insulin-signalling cascade, only Rab11 has been consistently observed in the myocardium (Uhlir et al., 2005).

Finally, while GLUT4 and GLUT1 are the most widely studied GLUT in all mammalian tissues, including the heart, GLUT3, GLUT8, GLUT10, and GLUT12 have also been detected in cardiac tissues (Abel, 2004; Dawson et al., 2001b; Doege et al., 2000; Grover-McKay et al., 1999; Macheda et al., 2002). Interestingly, GLUT8 and GLUT12 have also been identified as insulin-responsive. GLUT8 was found to mediate glucose uptake in blastocysts upon insulin stimulation. GLUT12, while primarily located at the cell surface, was shown to improve insulin sensitivity in mice when over-expressed (Carayannopoulos et al., 2000; Purcell et al., 2011). It is also worth noting that insulin also targets the endocardium in the heart. For instance, a central downstream mediator of insulin action in EC, phosphorylated by Akt, endothelial NO synthase generates NO, promotes vasorelaxation and activates anti-inflammatory and anti-atherosclerotic mechanisms (Zeng et al., 2000).

1.3.3.1.1 Impaired Insulin Signalling in Diabetic Cardiomyopathy

While less is known about cardiomyocytes, defective insulin signalling has been defined as a critical component in the development of DCM. Myocardial biopsies from individuals with T2D have reported decreased insulin signalling and defective GLUT4 trafficking and expression (Cook et al., 2010). In 2012, mice with cardiomyocytes-restricted deletion of the IR were found to display symptoms similar to those of T2D models with DCM and cardiac insulin resistance. The latter symptoms included a decrease in

cardiac glucose uptake, an increase in cardiac reactive oxygen species production, as well as mitochondrial dysfunction (Bugger and Abel, 2014).

It is well known that insulin resistance impairs the PI3K/Akt signalling pathway, inhibiting GLUT4 recruitment to the PM, which reduces glucose uptake. In the heart, reduction in glucose oxidation decreases calcium ATPase activity and moves calcium back into the sarcoplasmic reticulum, increasing intracellular ion levels (Lebeche et al., 2008). Since Akt can also activate endothelial NO synthase, the production of NO also decreases upon insulin resistance, further increasing intracellular calcium levels and cardiomyocyte calcium sensitisation via the cGMP/PKG signalling pathway (Jia et al., 2016; Stuhlinger et al., 2002). Interestingly, the PI3K/Akt signalling pathway also regulates the isoform composition of the giant elastic protein called titin, whose primary function is to adjust passive myocardial stiffness in the perinatal heart and chronic heart disease. Such impairment in insulin signalling increases the proportion of stiff N2B-titin isoforms, reducing cardiomyocyte distensibility (Kruger et al., 2010). As a result, all these abnormalities promote cardiac hypertrophy and diastolic dysfunctions.

These discoveries highlight the importance of further studies investigating the impact of different pathophysiological processes in the myocardium, both at a structural and biomolecular level. However, linking the two, and more specifically, linking them to distinct metabolic changes, is challenging as there remains an unmet need for an imaging modality that can provide detailed molecular and cellular insight on the mesoscale (i.e., within distinct three-dimensional (3D) structures of intact hearts) (see [Chapter 5](#)).

1.3.3.2 GLUT4-Vesicular Trafficking:

Insulin-Dependent and -Independent Trigger

Far less is known about the molecular machinery behind GLUT4 trafficking to the PM of muscles. Nevertheless, with some minor exceptions, studies have shown that overall GLUT4-vesicular trafficking in cardiomyocytes is similar to those observed in skeletal muscle cells.

Myocytes are composed of a specific PM, known as the sarcolemma, which contains invaginations, namely T-tubules, allowing the PM to reach deep into the muscle fibre. Similarly to adipocytes (see section [1.3.2.2](#)), insulin was shown to increase GLUT4 translocation to the PM through exocytosis and to decrease GLUT4 endocytosis in L6 myocytes, as well as in human and rat muscle cells (Fazakerley et al., 2010; Foley et al., 2011; Karlsson et al., 2009; Yang and Holman, 2005). Unlike adipocytes, exercise also mediates GLUT4 translocation to the PM in muscle cells, using distinct mechanisms from those stimulated by insulin (Douen et al., 1990; Yang and Holman, 2005). In skeletal muscle, AMP-activated protein kinase (AMPK) activation has been shown to regulate GLUT4 trafficking during muscle contraction (Winder and Hardie, 1996). Similarly, while debated (Beauloye et al., 2002), AMPK activity was also studied to increase in the heart, mediating the effect of increased workload during exercise (Coven et al., 2003). It is also worth noting that catecholamines can induce glucose uptake in cardiomyocytes through α - and β -adrenergic stimulation, independent of changes in contraction (Fischer et al., 1996; Rattigan et al., 1991).

Insulin- and exercise-induced glucose uptake signalling mechanisms both result in GLUT4 translocation from intracellular GSC to the sarcolemma and T-tubules. Under basal conditions, GLUT4 transporters are predominantly stored in intracellular GSC; however, unlike adipocytes, two distinct GLUT4 populations have been identified within these compartments. In skeletal muscles, GLUT4 translocation to the PM was found to occur primarily in T-tubules. Using immuno-gold labelling in transgenic mice over-expressing GLUT4, it was observed that 90% of insulin-stimulated GLUT4 transporters were found to accumulate in T-tubules (Wang et al., 1996). While insulin mediates an increase in GLUT4 of 7-fold in the sarcolemma and 15-fold in T-tubules, muscle contraction promotes a slightly higher increase of 9-fold in the sarcolemma and 20-fold in T-tubules. Interestingly, a total increase in GLUT4 of 14-fold in the sarcolemma and 30-fold in T-tubules suggested an additive effect of both stimuli (Ploug et al., 1998). As such, it was hypothesised that in skeletal muscles, each mechanism, either insulin- or contraction-dependent, affects two distinct pools of GLUT4 transporters (Lauritzen, 2013).

Similarly, in cardiomyocytes, two populations of GLUT4 were identified. The first population was found to be predominantly composed of GLUT4, low levels of GLUT1, and secretory carrier-associated membrane proteins (SCAMP). On the other hand, GLUT1 and SCAMP were found primarily in the second population, with only a few GLUT4. Both populations were depleted from their intracellular components upon insulin stimulation, and a 40-fold increase in GLUT4 at the PM of cardiomyocytes was observed. (Fischer et al., 1997; Slot et al., 1991a). As in skeletal muscle cells, kinetic experiments have further confirmed the existence of two intracellular pools of GLUT4 transporters in cardiomyocytes, where each pool is selectively

recruited by either insulin or contraction (Becker et al., 2001; Sevilla et al., 1997). Interestingly, these two pools were found to correlate with the two populations described above by Fischer et al. (Fischer et al., 1997).

However, the unusual architecture of muscle cells presents multiple problems for further analysis of the latter phenomenon, including difficulties in sub-cellular fractionation, imaging over a large field of views and the inter-related nature of cells within the intact tissue. While most studies have been performed on rodents, multiple studies have also observed a similar effect of insulin and contraction stimulation on GLUT4 trafficking in human skeletal muscle (Guma et al., 1995; Kennedy et al., 1999). Nevertheless, these studies, and more specifically in the field of cardiovascular research, remain challenging to perform in humans due to technical and ethical constraints.

1.4 GLUT4 Dynamics Near and Within the Plasma Membrane

1.4.1 GLUT4 Trafficking Revealed using Microscopy-Based Approaches

The discovery and subsequent use of green fluorescent proteins (GFP) as localisation markers for subcellular structures fundamentally altered the scope of questions that cell biologists could address (Shimomura et al., 1962; Tsien, 1998). In 1996, GLUT4-GFP was expressed in 3T3-L1 adipocytes, allowing for the first time real-time observation of GLUT4 insulin-mediated translocation to the PM (Dobson et al., 1996). Subsequently, a hemagglutinin (HA)-tag was added to the first exofacial

loop of the GLUT4-GFP construct and expressed in primary rat adipocytes. Confocal microscopy allowed the distinction between intracellular and PM-fused GLUT4 populations (Dawson et al., 2001a). These studies laid the foundations for many future projects using fluorescence microscopy to investigate GLUT4 trafficking to the PM, and the HA-GLUT4-GFP construct became widely used in studies of GLUT4 behaviour within the PM.

The main site of GLUT4 function is at the PM. While the steps of GLUT4 trafficking to the PM have been dissected and insulin established as the main regulator, less is known about the dynamics of GLUT4 within the PM. 30% of human genes encode membrane proteins (Fagerberg et al., 2010) and given that one of the most fundamental functions of the PM is the transport of materials/signals into and out of the cell, complex cellular mechanisms likely regulate the activity and location of membrane proteins such as GLUT4. To study the behaviour and regulatory mechanisms of individuals or groups of molecules within the PM, structural and dynamic information is required on length scales below the resolving power of traditional light (optical) microscopy.

1.4.1.1 Meaning and Importance of Spatial Resolution

As first described in 1873 by Ernst Karl Abbe, the ability of optical microscopes to distinguish individual structures from one another is physically limited (Abbe, 1873). This phenomenon is often referred to as the diffraction barrier of light microscopy. Due to its wave nature, the light collected through an objective lens aperture which emanates from a single point source, such as a fluorophore, ultimately produces an image that is broadened into a central spot (diffraction disk) surrounded by a series of

concentric rings (diffraction rings), overall lacking the sharpness of the original details within the illuminated target (**Figure 1.5**). Together, these diffraction patterns are called an Airy disk, whose diameter is defined by the wavelength of light (λ) and the numerical aperture of the imaging lens (NA). More specifically, NA is defined as $n \cdot \sin\theta$, where n is the refractive index of the medium in which the light propagates between the point source and the objective (Air: $n = 1$, Immersion oil: $n = 1.52$) and θ is the half-angle of the maximum cone of light that can enter the objective lens aperture (**Figure 1.5**) (Murphy, 2002).

Abbe's work initially established that the spatial resolution of a light microscope is limited to $\lambda/2NA$ laterally (x,y) and $2\lambda/2NA^2$ axially (z). In the lateral direction, this theory was later refined by Rayleigh's criterion, which quantitates the measure of separation necessary between two Airy disks to be $0.61\lambda/NA$ for them to be distinguished as separate entities (Inoué, 2006; Murphy, 2002). Accordingly, the only way to increase the resolving power of an imaging system is through some combination of reducing λ , increasing NA, and using an imaging medium with a high refractive index, all of which have physical limitations. For instance, under optimal conditions, the spatial resolution of a conventional light microscope is limited to around 250 nm laterally (x,y) and 550 nm in the axial (z) direction (Galbraith and Galbraith, 2011). This signifies that, if positioned at a lower distance from each other than 250 nm, closely labelled proteins will appear as a single fluorescent entity when viewed through a microscope, with overlapping intensity profiles and leaving their precise localisation undetectable (**Figure 1.5**).

Any optical microscopy technique that overcomes the diffraction barrier of conventional light microscopes by at least 2-fold is considered a super-resolution technique (Galbraith and Galbraith, 2011).

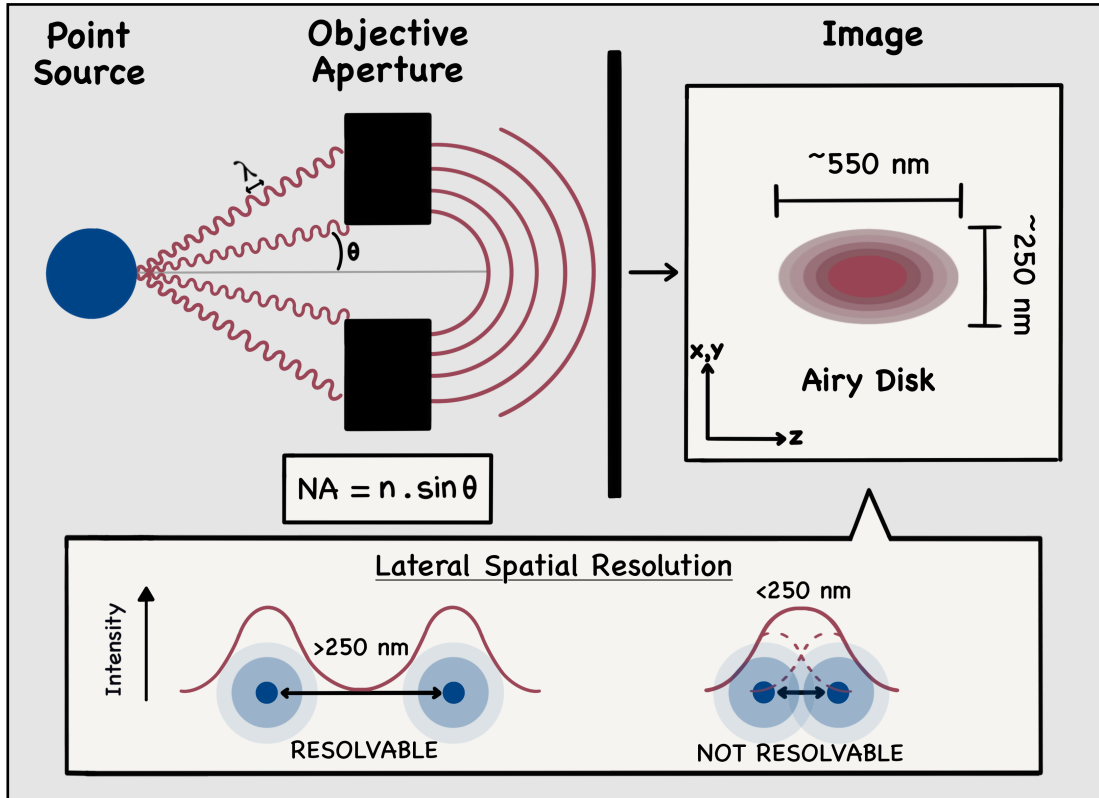


Figure 1.5. Diffraction-Limited Resolution of Light (Optical) Microscopy.

As it passes through the objective aperture, the emitted light emanating from a single point source (blue) is diffracted into a series of concentric rings, ultimately producing an image that is broadened and lacks the sharpness of the original illuminated details, known as an Airy disk. Using a conventional light microscope with a high numerical aperture (NA), the spatial resolution of the image point source is limited to approximately 250 nm laterally (x,y) and 550 nm axially (z), depending on the used wavelength (λ). If positioned at a lower distance from each other than 250 nm, closely labelled proteins will appear as a single fluorescent entity when viewed through a microscope, with overlapping intensity profiles and leaving their precise localisation undetectable (unresolved). $NA = n \cdot \sin\theta$, where n is the refraction rate between the point source and the objective (Air: $n = 1$, Immersion oil: $n = 1.52$) and θ is the half-angle of the maximum cone of light that can enter the objective lens aperture. Adapted from Geiser et al. (2023).

1.4.1.2 A Super-Resolved Journey

Microscopy techniques that do not rely on illumination with light, such as electron or atomic force microscopy, do not suffer from the limits in spatial resolution outlined above (see section [1.4.1.1](#)). However, while these methods can offer molecular and atomic resolution (Malide et al., 2000), the need for rigorous and often destructive sample preparation means that biologists still favour fluorescence microscopy despite the limit on resolution. In the past 30 years, there has been a concerted effort to surpass the diffraction barrier of light, resulting in a new family of fluorescence imaging techniques known as super-resolution microscopy (SRM) or nanoscopy (Galbraith and Galbraith, 2011; Huang et al., 2009; Jacquemet et al., 2020; Liu et al., 2022; Schermelleh et al., 2019; Valli et al., 2021). The range of optical techniques that fall under the umbrella of SRM is extensive and ever-growing. Therefore, in this section, we will highlight

approaches that have impacted the field of GLUT4 research and have been further applied throughout this project.

SRM utilises phenomena in optical physics and molecular chemistry to bypass the diffraction barrier imposed by light's physical properties. Broadly, the field of SRM can be divided into two categories: techniques that rely on shaped illumination (see section [1.4.1.2.1](#)) and localisation-based methods (see section [1.4.1.2.2](#)).

1.4.1.2.1 Super-Resolution Microscopy: Shaped Illumination

The first category includes techniques that alter the excitation beam path of the microscope and, therefore, how it is projected onto the studied sample. The oldest approach within this family is total internal reflection fluorescence (TIRF) microscopy. This technique improves the axial resolution of diffraction-limited systems by applying the principle that diverse mediums, such as glass, air, or water, can reflect light differently. Travelling at a certain angle from one medium to another, with different refractive indices (n), a portion or all of the light can be confined to the higher-index medium (Air: $n = 1$, Glass: $n = 1.5$). The complete confinement of the light beam into the higher-index medium is defined as total internal reflection (TIR) (**Figure 1.6**). This concept was first applied by Ambrose in 1951, followed by Axelrod in 1981, leading to the invention of TIRF microscopy (Ambrose, 1956; Axelrod, 1981).

In a conventional fluorescence microscope, such as a confocal microscope, the excitation light is focused through an objective onto the sample (e.g., cells), where it illuminates both the focal planes and out-of-focus planes of

the studied specimen, consequently, exciting fluorophores in all illuminated planes (**Figure 1.6**). However, in TIRF microscopy, the excitation beam is projected onto the sample at an oblique angle so that it can experience TIR off the specimen's surface. As a result, the evanescent byproduct of the laser beam undergoing TIR excites exclusively fluorophores within a few 100 nm of the specimen-substrate interface. (**Figure 1.6**) (Fish, 2009). As previously mentioned, the lowest axial spatial resolution that can be achieved using a conventional optical microscope is approximately 550 nm (see section [1.4.1.1](#)).

TIR behaviour is governed by Snell's law, given as $n(1) \times \sin\theta(1) = n(2) \times \sin\theta(2)$, where $n(1)$ and $n(2)$ equal the higher and lower refractive indices of the used mediums, respectively. The angle of the projected incident beam is defined as $\theta(1)$, while the refracted beam angle within the lower-index medium is given by $\theta(2)$. When the refracted ray of light becomes parallel to the interface ($\theta(2)=90^\circ$), $\theta(1)$ becomes $\theta(c)$, defined as the critical angle. For TIR to occur, with $n(1)$ greater than $n(2)$, $\theta(1)$, therefore, needs to exceed $\theta(c)$ (**Figure 1.6**) (Axelrod et al., 1984; Martin-Fernandez et al., 2013).

Applied to a typical biological investigation of the cell membrane, $n(1)$ would represent the coverglass's higher refractive index, while $n(2)$ would be the refractive index of the cell cytosol. As discussed below, TIRF microscopy is widely used to study GLUT4 dynamics near and within the PM (see sections [1.4.2](#) and [1.4.3](#)).

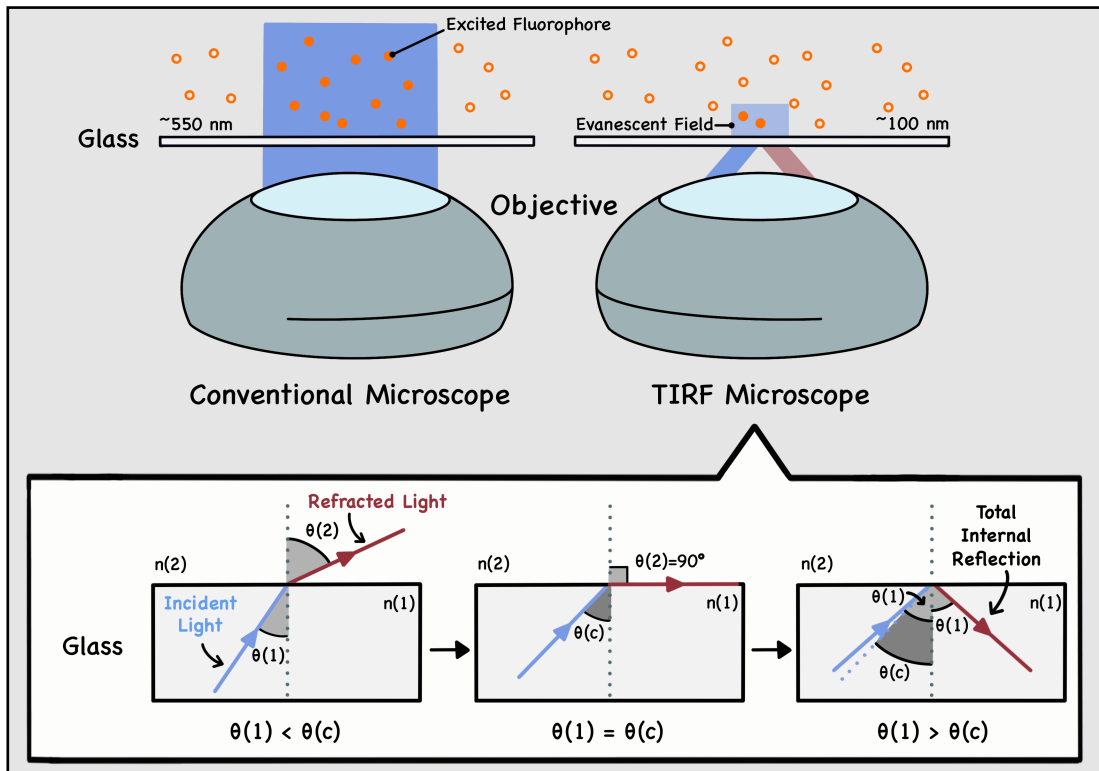


Figure 1.6. Schematic of Total Internal Reflection Fluorescence (TIRF) Microscopy.

In conventional fluorescence microscopy (top left), the excitation light is focused through an objective onto both the sample's focal and out-of-focus planes, exciting fluorophores (shown as filled-orange structures) in all illuminated planes. The lowest achievable axial spatial resolution using such microscopes is approximately 550 nm. In total internal reflection fluorescence (TIRF) microscopy (top right), the excitation beam (blue) is projected onto the sample at an oblique angle in such a way that the light is reflected (red) off the coverglass surface. This phenomenon, known as total internal reflection (TIR), results in the evanescent byproduct of the laser beam only exciting fluorophores within a few 100 nm of the surface. TIR behaviour (bottom) is governed by Snell's law, given as $n(1) \times \sin\theta(1) = n(2) \times \sin\theta(2)$, where $n(1)$ and $n(2)$ equal the coverglass's higher refractive index and the refractive index of the studied sample (e.g., aqueous solution or cell cytosol), respectively. The angle of the projected incident beam (blue) is defined as $\theta(1)$, while the angle of the refracted light (red) is given by $\theta(2)$. When the refracted ray of light becomes parallel to the coverglass interface ($\theta(2)=90^\circ$), $\theta(1)$ becomes $\theta(c)$, termed the critical angle. For TIR to occur, $\theta(1)$ needs to exceed $\theta(c)$.

A further technique is stimulated emission depletion (STED) microscopy, allowing for a much improved lateral spatial resolution on the order of 30-50 nm (Hell and Wichmann, 1994; Willig et al., 2007). This method relies on having two laser sources, a conventional Gaussian excitation beam and a longer wavelength masked 'doughnut-shaped' depletion beam, which overlap and force emitting fluorophores within the profile of the depletion beam into a dark ground state. Therefore, only fluorophores within the unmasked region of the excitation beam are detected, giving rise to sub-diffraction limit resolution.

1.4.1.2.2 Super-Resolution Microscopy: Localisation-Based

As previously explained (see section [1.4.1.1](#)), the diffraction limit of light affects the size and intensity distribution of a fluorophore when viewed under a microscope, causing the acquired image of the illuminated target to appear larger than its actual size. This phenomenon consequently limits the spatial resolution of a conventional light microscope with a high NA to around 250 nm laterally and 550 nm in the axial direction (**Figure 1.5**) (Galbraith and Galbraith, 2011). The second family of SRM, namely single-molecule localisation microscopy (SMLM) methods, therefore, classically approaches visualising structures below the diffraction limit by iteratively switching on and off fluorophores, such that only a sparse population of single molecules is detected at any one time. Ultimately, imaging single isolated signals over several thousand frames in SMLM allows for the reconstitution of super-resolved images (**Figure 1.7A**).

The first methods for achieving SMLM were shown with photo-activated localisation microscopy (PALM) and stochastic optical reconstruction

microscopy (STORM). While PALM is based on the activation and subsequent photo-bleaching of fluorescent proteins present within a studied specimen through depth (Betzig et al., 2006), STORM uses pairs of photo-switchable fluorophores (activator and reporter) to target and image single molecules (Rust et al., 2006). Subsequently, the use of conventional cyanine dyes, along with blinking-inducing specialised buffer solutions, became increasingly popular (Herdly et al., 2023). This technique came to be known as direct STORM (dSTORM), the direct nature coming from the fact that *pairs* of photo-switchable fluorophores are not required (Heilemann et al., 2008; van de Linde et al., 2011).

More recently, fluorescent transiently-binding single DNA strands have re-emerged as a versatile tool, allowing for improved single-molecule localisation with the development of point accumulation in nanoscale topography (DNA-PAINT) (Jungmann et al., 2010; Schnitzbauer et al., 2017). While dSTORM uses antibodies conjugated with photoswitchable fluorophore to label its target, DNA-PAINT employs designed pairs of oligonucleotides, where fluorescently conjugated imaging strands transiently binds selected protein targets previously labelled with complementary docking strands. During imaging, upon hybridisation of an imaging strand to a docking strand, the fluorophore labelled to the imaging strand will become momentarily immobilised (ON-state), with τ_b representing the duration of these binding events. In contrast, if the imaging strand is dissociated from the docking strand, no fluorescence is observed in the focal plane, resembling a fluorescent OFF-state where τ_d is the time during which an imaging strand remains unbound. In summary, the transient binding of imaging strands represents a behaviour similar to

the single-molecule blinking of fluorophore that occurs in dSTORM, which can be recorded over time (**Figure 1.7B**) (Schnitzbauer et al., 2017).

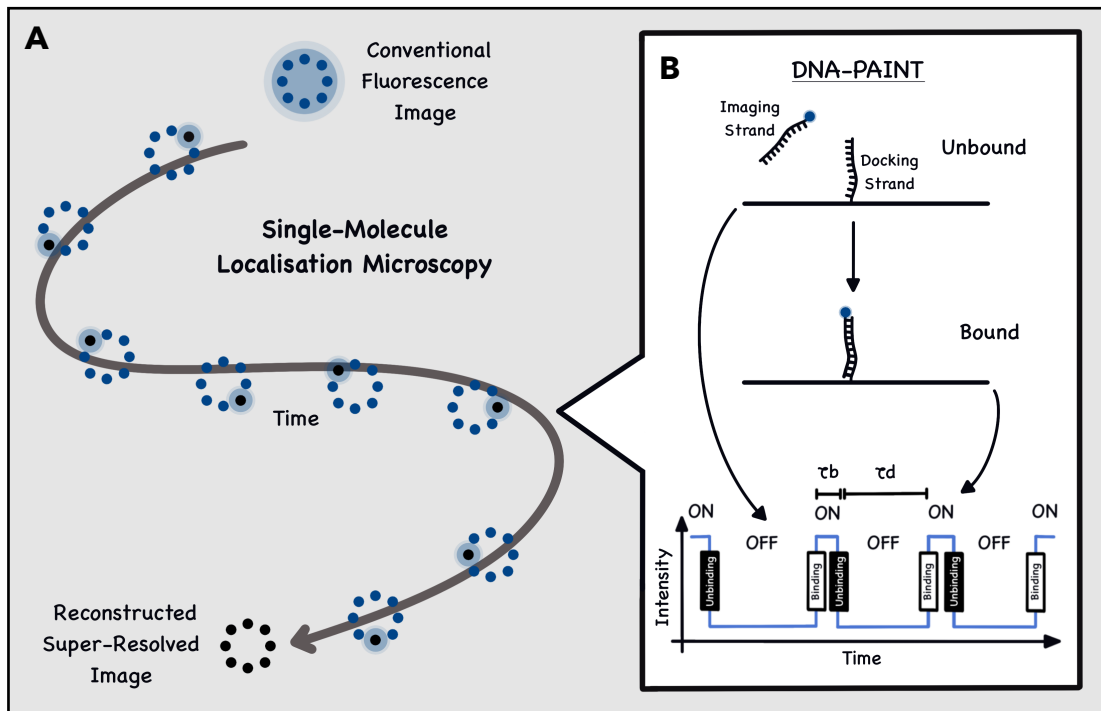


Figure 1.7. Principle of Classical Single-Molecule Localization Microscopy and DNA-PAINT.

(A) The diffraction limit of light does not allow for closely labelled structures to be resolved using conventional light microscopy, which will be detected as a single fluorescent entity. Classical single-molecule localisation microscopy (SMLM), such as dSTORM, is based on switching on and off fluorescent emitters so that only a sparse population of single molecules is detected at any one time. This allows to localise the position of single, non-overlapping blinking events with high precision over several thousand frames over time, from which a final super-resolved image can then be reconstituted. (B) DNA-PAINT is an SMLM technique that works without fluorescent photoswitching; instead, it uses pairs of oligonucleotides. Fluorescently conjugated imaging strands transiently bind with complementary docking strands. Without the binding of the imaging strand (unbound), no fluorescence is observed, resembling a fluorescent OFF-state. Upon the transient binding of an imaging strand to the docking strand, a fluorescent blinking event is observed (ON-state). A typical intensity vs. time trace will, therefore, show a switch between low fluorescence upon unbinding of the imager strand, with τ_d being the time for the unbound state, and high fluorescence upon binding of the imager strand, where τ_b is the time for the bound state. Inspired by Jungmann et al. (2010).

SMLM image reconstruction is achieved by fitting the intensity distribution of each recorded single-molecule emission to a 2D Gaussian function. With the peak of the latter distribution being directly linked to the localisation of where the most photons are emitted, the 'precise' position of each detected fluorophore within the imaged field of view is, therefore, revealed (**Figure 1.8**). Concurrently, the precision of this measurement is also linked to the number of photons detected. In simple terms, the more photons detected, the higher the localisation precision.

It is important to understand that at this point of the reconstruction process, the obtained localisation coordinates for each detected signal within each

frame only correspond to the position of the fluorescent emitter and not to those of the molecular target it is labelled to. The application of labelling technologies to connect a target of interest to a fluorescent emitter automatically introduces a localisation offset between the studied target and the imaged fluorophore. This physical separation is a phenomenon known as the labelling linkage error, which we will further investigate in [Chapter 4](#). It is only by overlapping multiple localisations of the same target, obtained from multiple blinking events of the same emitter recorded throughout several frames, that the 'true' position of the molecular target it is attached to can then be extrapolated. In SMLM, the precision with which single molecular targets can be localised is known as the localisation precision (LP; **Figure 1.8**), which typically equals the standard deviation of the Gaussian fit obtained from the overlay of multiple localisations from an individual target (Lelek et al., 2021).

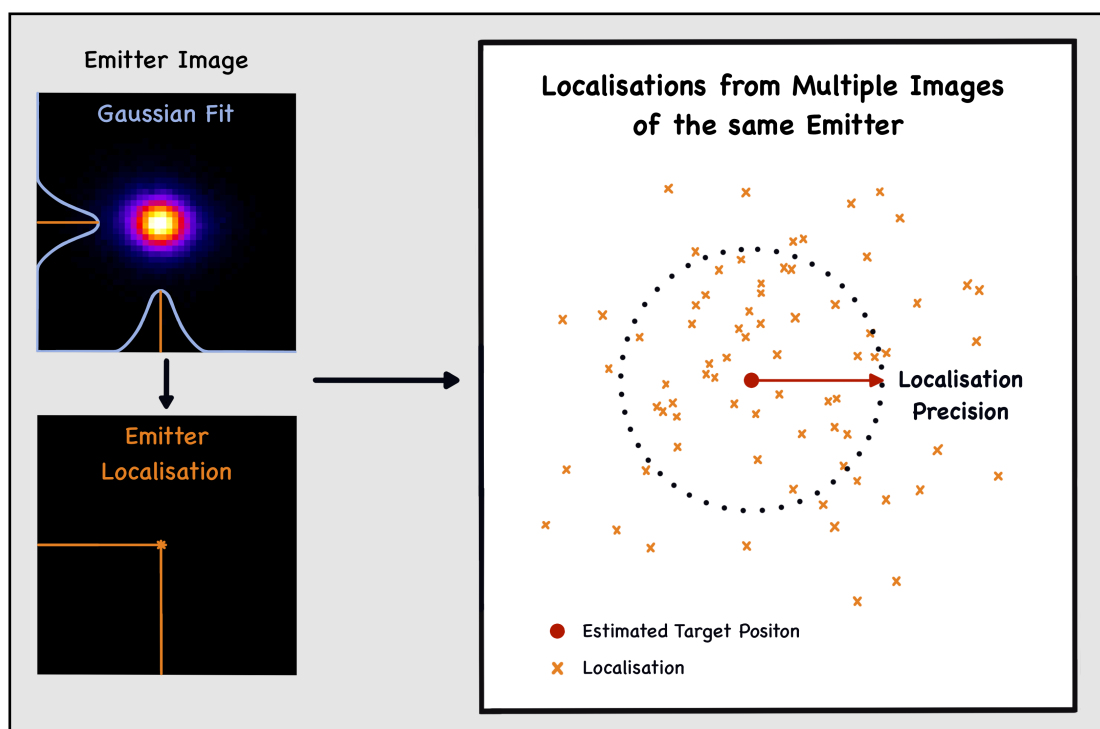


Figure 1.8. Localisation Precision in Single-Molecule Localisation Microscopy.

In SMLM, the reconstruction of a super-resolved image is achieved by mapping the intensity of each recorded emission (top left; emitter image colour-coded by fluorescent intensity using the “fire” lookup table) to a Gaussian function, with the peak of these functions providing the localisation of the detected emitters (bottom left; orange). Due to the distance that separates a molecular interest from the fluorescent emitter it is labelled to, a localisation offset between the two exists. Therefore, to obtain an estimated position of the molecular target (red dot), multiple localisations of the same emitter (orange cross), obtained from multiple blinking events recorded throughout several frames, are overlaid. The precision with which a single molecular target can be localised is known as the localisation precision (red arrow).

For clarity, we want to emphasise the distinction between spatial resolution and LP. While spatial resolution relates to a system's ability to distinguish two separated point-like objects from each other, the LP of a system refers to the precision with which an object's position can be defined. To put it simply, spatial resolution is about separating and identifying two distinct targets as individual entities rather than blurring them into a single image (**Figure 1.5**), whereas LP is about pinpointing the position of a single object within the system's imaging field. As described above, LP does not necessarily relate to distinguishing two separate objects but focuses instead on the ability to define the exact location of a single object with high precision (**Figure 1.8**), even if that object is within the bounds of the system's spatial resolution. Even when two objects cannot be resolved separately (due to the diffraction barrier of light), their positions might still be localised with high accuracy using specific microscopy techniques (i.e., SMLM).

1.4.1.2.3 Super-Resolution Microscopy: One Big Family

Truly, both super-resolution families do not have to remain separate entities. The concurrent use of shaped illumination methods has been demonstrated to effectively improve the LP of SMLM techniques. In particular, TIRF microscopy has lent itself well as the most popular illumination method for SMLM (Lelek et al., 2021). In DNA-PAINT, for instance, since single-molecule fluorescence from the focal plane of the microscope is recorded when transient binding occurs, any out-of-focus fluorescence from unbound imaging strands must be diminished. As a result, DNA-PAINT is usually performed in TIRF mode (Jungmann et al., 2010). Its thin, tunable depth optical range significantly reduces background fluorescence, thus allowing for increased SMLM super-resolved image reconstruction accuracy.

The search for better detection methods to achieve improved spatial resolution is an ongoing quest (see [Chapter 4](#)), which has opened the range of structures and biological processes that can be studied and further the study of GLUT4 behaviour near (approaching and adjacent to the PM) (see section [1.4.2](#)) and within the PM (i.e., post-fusion) (see section [1.4.3](#)).

1.4.2 *Insulin-Stimulated GLUT4-Vesicles near the Plasma Membrane*

Over the years, insulin has been widely reported to regulate GLUT4 trafficking in several ways, and it has become indisputable that the main site for GLUT4 function and recycling is at the PM (Bai et al., 2007). In 2004,

using EGFP-fused GLUT4, Li et al. first applied TIRF microscopy to investigate the 3D mobility of GLUT4 approaching the PM in live 3T3-L1 adipocytes. Tracking GLUT4 behaviour using TIRF and single-particle analysis revealed that the movement of GLUT4-vesicles was restricted within a mean radius of 160 nm from the PM under insulin stimulation, suggesting the presence of an intracellular tethering matrix. In addition, GLUT4-vesicles were found to exhibit a continuum of 3D diffusional coefficients, indicating that despite there being several potential routes for GLUT4-vesicles to reach the PM, they appear to be organised in a continuous range of mobility (Li et al., 2004).

The use of a dual-coloured probe to follow GLUT4 trafficking in TIRF mode has also allowed for the quantification of fusion events as well as vesicular location. Insulin was observed to induce a 40-fold increase from basal conditions in the fusion of GLUT4-vesicles to the PM in 3T3-L1 adipocytes. Interestingly, it was observed that a fraction (~15%) of vesicular fusion to the PM exhibited a fusion-with-retention or “kiss-and-run” type event, where PM-fused GLUT4 molecules are retained at their sites of fusion before being re-internalised from the PM (**Figure 1.9**) (Jiang et al., 2008). Lizunov et al. also showed that insulin regulates immobilisation, tethering, and fusion of GLUT4-containing vesicles with the PM in live isolated rat adipocytes using TIRF microscopy (Lizunov et al., 2009).

1.4.3 Insulin-Stimulated GLUT4-Dispersal within the Plasma Membrane

In 2010, it was suggested that insulin also impacts the spatial distribution of GLUT4 within the PM. Using multi-colour TIRF microscopy, the existence of

GLUT4 molecules present as stationary 'clusters' at the cell surface of isolated rat adipocytes was revealed. It was further suggested that a portion of GLUT4 in the PM existed as monomers (Stenkula et al., 2010). Stenkula et al. posited that these monomers derived from the exocytosis of GLUT4 involved in fusion-with-release type events, where GLUT4 transporters are shown to rapidly spread out into the PM, away from their fusion sites. Experimentally, the authors showed that in the basal state, fusion-with-retention events represent 95% of all fusion events (**Figure 1.9**). At this point, the amounts of clustered and monomeric GLUT4 at the PM were found to be broadly similar. On the other hand, insulin was observed to increase the total fusion rate of GLUT4-vesicles with the PM from 0.03 events/ $\mu\text{m}^2/\text{min}$ to 0.15 events/ $\mu\text{m}^2/\text{min}$ after only 2 min of stimulation. This increase was shown to be the result of the differential stimulation of both previously described modes of exocytosis (see section [1.4.2](#)) (Jiang et al., 2008), with a 60-fold increase in the number of fusion-with-release events against a 2-fold rise in fusion-with-retention. These boosts in fusion events could account for observed increases in both total PM-fused GLUT4 as well as clustered and dispersed GLUT4, respectively. Consequently, this suggests that in the basal state, fusion-with-retention is the primary GLUT4 provider of the PM in the form of clusters. Insulin stimulation triggers fusion-with-release events where a significant amount of GLUT4 is delivered to and dispersed into the PM. These observations demonstrated that GLUT4 proteins are distributed non-homogeneously within the PM. Nevertheless, it was established that upon insulin stimulation, the total amount of translocated GLUT4 corresponded broadly to a cellular increase in glucose uptake, suggesting that both GLUT4 populations at the PM are functional glucose transporters (Stenkula et al., 2010).

Considering the above data, Stenkula et al. proposed a new kinetic model to explain GLUT4 behaviour among GSC and the PM, which they based on the inclusion of specific parameters. The first is that, at the PM, insulin only affects the dispersal of GLUT4 (i.e., not its activity), and the second is that the amount of GLUT4 in all GSC, apart from IRV, remains relatively constant upon insulin stimulation. This extends previous models (Holman et al., 1994) by adding GLUT4 clusters as a new quasi-compartment. Under basal conditions, PM-fused GLUT4 are mostly found to localise in this compartment, which functions as an intermediate hub between GLUT4 exocytosis and re-internalisation. Upon insulin stimulation, this model considers a rapid increase in GLUT4 monomers at the PM primarily due to an increase in GLUT4-vesicle fusion, specifically fusion-with-release events (**Figure 1.9**). Based on this new kinetic model, Stenkula et al. provided evidence for a hitherto unidentified step in the GLUT4 trafficking system: insulin increases GLUT4 dispersal within the PM from clusters to monomers, and glucose uptake becomes more efficient (Stenkula et al., 2010).

The GLUT4 dispersal model is readily amenable to probes using SRM, and different techniques have been developed to further investigate its dynamics within the PM in the presence of insulin. By transfecting adipocytes with an HA-GLUT4-EOS probe and using a TIRF-PALM microscopy system, Lizunov et al. confirmed that insulin contributes to the transfer of GLUT4 from a cluster to a monomeric state (**Figure 1.9**). Insulin increases GLUT4 monomer dissociation from clusters and decreases the rate of GLUT4 endocytosis (Lizunov et al., 2013). The spatial arrangement of HA-GLUT4-GFP within the PM of 3T3-L1 adipocytes has also been

studied at a single molecule level using dSTORM (Gao et al., 2017; Koester et al., 2022b). The studies reinforced the idea that insulin stimulates GLUT4 dispersal within the PM post-fusion, highlighting a novel facet of GLUT4 biology with potentially significant consequences.

Further, while adipocytes remain the prime cellular model in GLUT4 research, GLUT4 dispersal was also shown to operate in other cell types. Using ectopically expressed HA-GLUT4-GFP in either induced pluripotent stem cell-derived cardiomyocytes or HeLa cells, insulin-stimulated GLUT4 dispersal was identified in both cell types (Koester et al., 2022a).

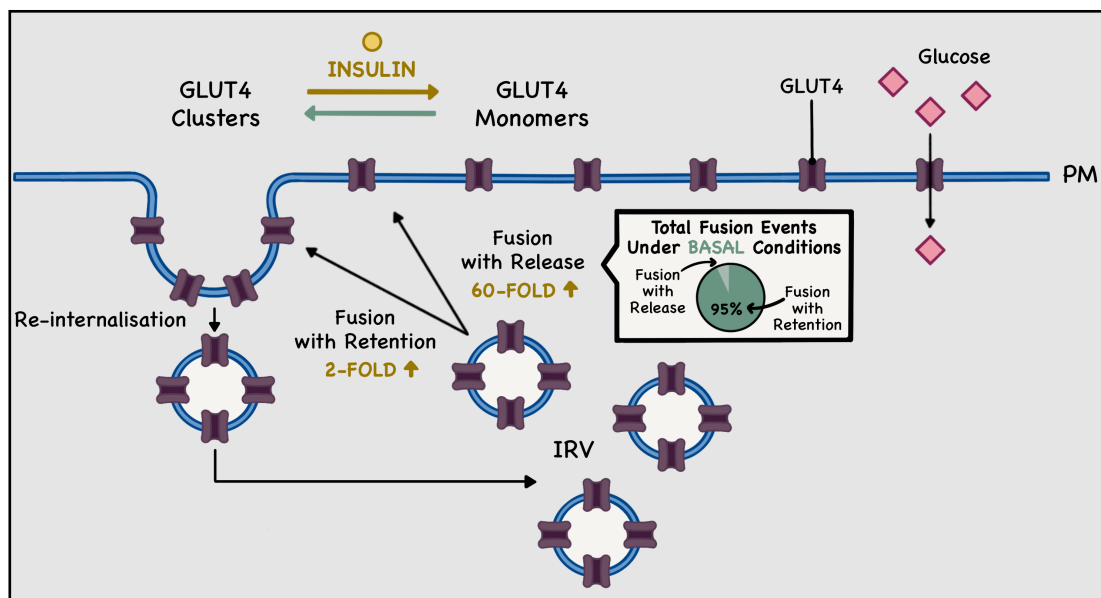


Figure 1.9. Model of GLUT4 Fusion to, and Dispersal within, the Plasma Membrane of Adipocytes.

In adipocytes, insulin regulates GLUT4 fusion to, and dispersal within, the plasma membrane (PM). In the basal state, 95% of all fusion events happen in a fusion-with-retention manner, upon which PM-fused GLUT4 molecules (shown as purple structures) are retained at their site of fusion, forming clusters which function as intermediate hubs between GLUT4 exocytosis and re-internalisation. In the presence of insulin, the number of fusion-with-retention events increased by 2-fold, while fusion-with-release events increased by 60-fold. GLUT4 transporters, therefore, primarily undergo exocytosis through the fusion of IRV and release into the PM as monomers, leading to increased and more efficient glucose (pink) uptake into the cell. Adapted from Geiser et al. (2023).

1.4.3.1 Impaired GLUT4 Dispersal in Insulin Resistance

In 2017, Gao et al. used dSTORM to image HA-GLUT4-GFP at the PM of basal and maximally insulin-stimulated 3T3-L1 adipocytes. Consistent with data from TIRF microscopy, in the presence of insulin, the authors observed a shift in the distribution of GLUT4 at the PM to a more dispersed configuration. Interestingly, experimental insulin resistance was also observed to increase GLUT4 clustering, suggesting a link between the clustering ability of GLUT4 and insulin sensitivity (Gao et al., 2017). This link was further revealed when considering how GLUT4 dispersal is correlated with cell size (Koester et al., 2022a; Wollman et al., 2022). Adipocytes of different sizes have been shown to exhibit distinct metabolic properties: larger adipocytes exhibit reduced insulin-stimulated glucose transport compared to smaller cells and are associated with adverse metabolic outcomes (Stenkula and Erlanson-Albertsson, 2018). Strikingly, Koester et al. observed that GLUT4 dispersal is reduced in larger cells (Koester et al., 2022a), supporting the hypothesis that larger adipocytes are refractory to

insulin challenge and further suggesting that GLUT4 dispersal (**Figure 1.9**) is an integral facet of the cellular insulin response. Such studies emphasise a need to understand the mechanism(s) that underpin this dispersal.

1.5 Aims

The discovery of insulin-responsive GLUT4 in 1988 (James et al., 1988) has not only sparked a multitude of cellular mechanistic studies but also revolutionised our understanding of how insulin regulates glucose uptake into both adipose and muscle tissues, as well as highlighted the implications of GLUT4 in the development of T2D. As previously mentioned, T2D, the most prevalent form of DM, is characterised by insulin resistance in hepatic and peripheral tissues. The defective expression or translocation of GLUT4 to the PM of adipocyte and muscle cells in individuals with T2D significantly impairs glucose entry into cells, leading to inadequate energy production and storage. In addition to drug treatments, implementing a more active and balanced lifestyle, including appropriate diet and/or exercise, has been shown to effectively prevent, improve, or even reverse T2D (Lean et al., 2018). Nevertheless, T2D is currently a metabolic disorder that knows no cure, with a strong relationship with CVD, being its leading cause of death, and which prevalence is globally on the rise (see section [1.1](#)).

Therefore, this thesis employs molecular- and microscopy-based approaches to investigate the evolving understanding of the mechanism behind GLUT4 trafficking and dispersal at the PM of adipocytes. It also aims to determine, both at a cellular level and on the mesoscale, the neglected

mechanics of GLUT4 machinery in cardiac muscle tissues, addressing the tissue and cellular isolation challenges that arise in cardiovascular research.

Aims and hypotheses will be further detailed in each chapter.

Materials and Methods

2.1 **Materials: Recipes and Antibodies**

2.1.1 *Buffers and Solutions Recipes*

- *2x Laemmli Sample Buffer (LSB)*

100 mM Tris, HCl; pH 6.8, 4% (w/v) SDS, 20% (v/v) Glycerol, 0.2% (w/v) Bromophenol Blue, 100 mM DTT (added on the day of the experiment).

- *Blocking Buffer*

3% (w/v) Bovine Serum Albumin (BSA), 1% (v/v) Goat Serum in PBS.

- *Calcium Reintroduction Solutions*

Perfusion Buffer supplemented with either (see section [5.3.2.1](#)):

Initial Concentrations:

100 μ M, 200 μ M, 500 μ M, 1 mM, or 1.8 mM CaCl₂.

Final Concentration: 500 μ M or 1.8 mM CaCl₂.

- *DNA-PAINT Solution*

500 mM NaCl in PBS; pH 7.4

- *EDTA Buffer*

130 mM NaCl, 5 mM KCl, 500 μ M NaH₂PO₄, 10 mM HEPES, 5 mM EDTA, 5 mM Na-Pyruvate (C₃H₃NaO₃), 10 mM 2,3-Butanedione monoxime (BDM; Sigma-Aldrich P/N B0753) in ultrapure 18.2 M Ω .cm H₂O; pH 7.4 (autoclave before use). 5 mM Glucose was added on the day of the experiment.

- *Enzyme Buffer*

Perfusion Buffer supplemented with 1.66 mg/mL BSA, 0.5 mg/mL Collagenase Type I (from *Clostridium histolyticum*; Sigma-Aldrich, P/N C0130), 0.4 mg/mL Protease Type XIV (from *Streptomyces griseus*; Sigma-Aldrich, P/N P5147).

- *Fixation Solution*

4% (w/v) PFA in PBS.

- *HE Buffer*

20mM HEPES, 1mM EDTA in dH₂O; pH 7.4.

- *HES Buffer*

20 mM HEPES, 1mM EDTA, 250mM Sucrose in dH₂O; pH 7.4, supplemented with 1x Pierce™ Protease Inhibitor Tablet (ThermoFisher Scientific, P/N A32963), 1:100 Phosphatase Inhibitor Cocktail Set II (Sigma-Aldrich, P/N 524625) when required.

- *HES/Sucrose Buffer*

HES Buffer supplemented with 1.12M Sucrose.

- *Homogenisation Buffer*

250mM Tris-HCl; pH 7.4, 1x Pierce™ Protease Inhibitor Tablet, 1:100 Phosphatase Inhibitor Cocktail Set II.

- *Krebs-Ringer-Phosphate (KRP) Buffer*

136 mM NaCl, 5 mM Sodium Phosphate Buffer ($\text{NaH}_2\text{PO}_4\text{-Na}_2\text{HPO}_4\cdot 7\text{H}_2\text{O}$), 4.7 mM KCl, 1.25 mM MgSO_4 , 1.25 mM CaCl_2 ; pH 7.4.

- *Lysis Buffer*

50 mM Tris-HCl, 50 mM NaF, 1 mM $\text{Na}_4\text{P}_2\text{O}_7$, 1 mM EDTA, 1 mM EGTA, 1% (v/v) Triton X-100, 250 mM Mannitol, 1 mM DTT; pH 7.4, 1x Pierce™ Protease Inhibitor Tablet, 1:100 Phosphatase Inhibitor Cocktail Set II.

- *MES Buffer*

25mM MES, 150mM NaCl in dH_2O ; pH 6.5, supplemented with 1% (v/v) Triton X-100, 1x Pierce™ Protease Inhibitor Tablet, 1:100 Phosphatase Inhibitor Cocktail Set II when required.

- *PBS*

137 mM NaCl, 2.7 mM KCl, 10 mM Na_2HPO_4 , 1.8 mM KH_2HPO_4 in dH_2O ; pH 7.4.

- *PBS-T*

PBS supplemented with 0.1% (v/v) Tween-20.

- *Perfusion Buffer*

135 mM NaCl, 5 mM KCl, 330 μM NaH_2PO_4 , 10 mM HEPES, 5 mM Na-Pyruvate, 10 mM BDM (Sigma-Aldrich P/N B0753), 1 mM MgCl in ultrapure 18.2 $\text{M}\Omega\cdot\text{cm}$ H_2O ; pH 7.4 (autoclave before use). 5 mM Glucose was added on the day of the experiment.

- *Permeabilisation Buffer*

3% (w/v) BSA, 1% (v/v) Goat Serum, 0.5% (w/v) Saponin in PBS.

- *Quenching Buffer*

50 mM NH₄Cl in PBS.

- *SDS-PAGE Running Buffer*

25 mM Tris, 190 mM Glycine, 0.1% (w/v) SDS in dH₂O.

- *STOP Buffer*

Perfusion Buffer supplemented with 5% Fetal Bovine Serum (FBS).

- *TAE Buffer*

40 mM Tris-HCl, 1 mM EDTA in dH₂O; pH 7.4.

- *Wet Transfer Buffer*

25 mM Tris-HCl, 192 mM Glycine, 20% (v/v) Ethanol in dH₂O.

2.1.2 Antibodies and NanoBodies

2.1.2.1 Primary Antibodies and Nanobodies

Antigen	Dilution	Description	Source
ACC	1:1,000 (WB)	Rabbit Monoclonal	Cell Signaling (P/N 3676)
ALFA-Tag	1:500 (WB) 1:500 (IF)	Rabbit Polyclonal Serum	Nanotag Biotechnologies (P/N N1580)
Caveolin-1	1:1000 (WB)	Rabbit Polyclonal	Abcam (P/N ab2910)

Antigen	Dilution	Description	Source
EFR3a	1:100 (WB)	Rabbit Polyclonal	Thermo Fisher Scientific (P/N PA554694)
FAS	1:1,000 (WB)	Rabbit Monoclonal	Cell Signaling (P/N 3180)
GAPDH	1:1,000 (WB)	Mouse Monoclonal	Invitrogen (P/N AM4300)
GLUT4 Carboxy-terminal (14 amino acids)	1:500 (WB) 1:500 (IF)	Rabbit Polyclonal	Homemade
GLUT4 Amino-terminal (14 amino acids)	1:500 (WB) 1:500 (IF)	Rabbit Polyclonal	Homemade
HA-Tag	1:1000 (IF)	Mouse Monoclonal	BioLegend (P/N 901515)
HA-Tag (Biotinylated)	1:1000 (IF)	Mouse Monoclonal	BioLegend (P/N 901505)
HA-Tag (Nanobody, Biotinylated)	1:50 (IF)	Alpaca Monoclonal	ABclonal (P/N AE117, Discontinued; Beads P/N AE108)
Phospho-AKT (S473)	1:500 (WB)	Rabbit Monoclonal	Cell Signaling (P/N 4058)
PI4K-III α	1:500 (WB)	Rabbit Polyclonal	Thermo Fisher Scientific (P/N PA528570)
PI4P	1:100 (WB) 1:100 (IF)	Mouse Monoclonal	Echelon Biosciences (P/N Z-P004)
Syntaxin4	1:1,000 (WB)	Mouse Monoclonal	Synaptic Systems (P/N 110 041)
Total-AKT	1:1,000 (WB)	Mouse Monoclonal	Cell Signaling (P/N 2920)

2.1.2.2 Secondary Antibodies and NanoBodies

Antigen	Dilution	Description	Source
Mouse IgG	1:200 (IF)	Alpaca Alexa Fluor® 647 AffiniPure-VHH™ Fragment	Jackson ImmunoResearch (P/N 615-604-214)
Mouse IgG	1:1000 (IF)	Goat Alexa Fluor™ 647	Invitrogen (P/N A21235)
Mouse IgG	1:10,000 (WB)	Donkey IRDye 680LT	LI-COR Biosciences (P/N 926 68022)
Rabbit IgG	1:1000 (IF)	Goat Alexa Fluor™ 488	Invitrogen (P/N A11008)
Rabbit IgG	1:10,000 (WB)	Donkey IRDye 800CW	LI-COR Biosciences (P/N 926 32213)

2.2 Methods

2.2.1 Cell Culture

2.2.1.1 3T3-L1 Fibroblasts Growth and Maintenance

3T3-L1 is a sub-clonal cell line derived from the original 3T3 Swiss albino cell line isolated from mouse embryos (Green and Meuth, 1974; Todaro and Green, 1963).

3T3-L1 fibroblasts, wild-type (WT; American Tissue Culture Collection, P/N CCL-92.1, RRID:CVCL_0123) or stably expressing HA-GLUT4-GFP (Morris et al., 2020), were cultured in Dulbecco's Modified Eagle Medium (DMEM) supplemented with 10% (v/v) Newborn Calf Serum, 1% (v/v) L-Glutamine, and 1% (v/v) Penicillin-Streptomycin. Fibroblasts were incubated in Corning T-75 tissue culture flasks (75 cm²; Corning Incorporated, P/N 430641U) in a 10% CO₂ humidified tissue culture incubator at 37°C, and the culture medium was changed every second day. When cells reached 70% confluency, passaging was performed by washing and detaching the cells from the plastic surface of the flask with PBS and TrypLE™ Express Enzyme (ThermoFisher Scientific, P/N 12604013), respectively. TrypLE™ was quenched with culture medium (see above), and cells were diluted to the desired concentration and seeded onto appropriate fresh plastic ware.

2.2.1.2 3T3-L1 Adipocyte Differentiation

3T3-L1 fibroblasts (WT or stably expressing HA-GLUT4-GFP) were grown and maintained as described in section [2.2.1.1](#). 48 h post-confluency, fibroblasts were differentiated into adipocytes. On Day 0 of differentiation, the medium was replaced by DMEM containing 10% (v/v) FBS, 1% (v/v) L-Glutamine, 1% (v/v) Penicillin-Streptomycin, and filtered after the addition of 0.5 mM 3-isobutyl-1-methylxanthine, 1 μM insulin (Sigma-Aldrich, P/N I5523), 0.25 μM dexamethasone, and 1 nM troglitazone. Three days post-differentiation, the medium was changed to DMEM/FBS-based medium (see above), this time supplemented with 1 μM insulin and 1 nM troglitazone, and filtered. On Day 6 of differentiation, the medium was replaced with an un-supplemented DMEM/FBS-based medium. After Day 6 of differentiation, the medium was replaced with an un-supplemented

DMEM/FBS, which was changed every second day. Cells were fully differentiated and ready to use between days 8 and 12 of differentiation.

2.2.1.3 Insulin Stimulation of 3T3-L1 Adipocytes

Cells were cultured and differentiated as described in sections [2.2.1.1](#) and [2.2.1.2](#) and rendered quiescent (basal state) for 2 h in serum-free medium (DMEM supplemented with 1% (v/v) L-Glutamine, and 1% (v/v) Penicillin-Streptomycin). 100 nM insulin (Sigma-Aldrich, P/N I5523) was then added to the culture medium and cells were incubated at 37°C and 10% CO₂ for 20 min.

2.2.1.4 Insulin Stimulation, PI4K-III α Pharmacological Inhibition, and Glucose Uptake Assay in 3T3-L1 Adipocytes

For each biological replicate, glucose uptake assays were performed with 3 technical replicates per each condition.

Cells were cultured, differentiated, and rendered quiescent onto a 12-well plate (Corning Incorporated, P/N 3513) as described in sections [2.2.1.1](#), [2.2.1.2](#), and [2.2.1.3](#). The serum-free medium was then removed, and cells were washed 2x with pre-warmed KRP Buffer (see section [2.1.1](#)).

Subsequently, 0 nM or 200 nM of the phosphatidylinositol 4-kinase type III α (PI4K-III α) inhibitor C7 (Ximbio, P/N 153579) (Waring et al., 2014) was added to the KRP Buffer for 20 min. Cells were then subjected to either 0 nM or 100 nM insulin and incubated at 37°C and 10% CO₂ for 15 min. 0.25 uCi of 2-deoxy-D-glucose (2DG) in KRP Buffer was added in each well (final

concentration of 50 μM) and incubated at 37 °C and 10% CO_2 for 4 min. Half of the samples were incubated with 10 μM of cytochalasin B, a mycotoxin inhibiting facilitative glucose uptake in cells and serving as a background for this assay's background. After that, the cells were rinsed 3x with ice-cold PBS, air dried and lysed with 1% (v/v) Triton X-100 (1 mL/well). The radioactivity in the sample was measured using liquid scintillation counting.

Prof. Gwyn W. Gould kindly performed all glucose uptake assays in this thesis.

2.2.1.5 siRNA-Mediated Gene Knockdown in 3T3-L1 Adipocytes

3T3-L1 fibroblasts (WT) were plated onto 10-cm dishes (Scientific Laboratory Supplies, P/N 353003), cultured, and differentiated as described in sections [2.2.1.1](#) and [2.2.1.2](#). On Day 6 or 7 of differentiation, cells were simultaneously transfected with small-interfering RNAs (siRNA) of interest and transferred onto either 6-well plates (1x initial 10-cm dish per 1x 6-well plate; Corning Incorporated, P/N 3516) for the generation of cell lysates (see section [2.2.3.3](#)), or fresh 10-cm dishes for sub-cellular and lipid raft fractionation experiments (see sections [2.2.4.1](#) and [2.2.4.2](#)).

siRNAs of interest were transfected using the *TransIT-X2*[®] Dynamic Delivery System (Cambridge Bioscience, P/N MIR6004), as described below.

Transfection reagents for 1x 6-well plate or 1x 10-cm dish (**Table 2.1**) were first added in an Eppendorf tube and incubated at room temperature for 30 min. Optimal *Efr3a* and *Pi4ka* siRNA concentrations were estimated from

an initial titration experiment (see Appendix [7.1](#)) based on previous work in our laboratory (Koester et al., 2022b).

Meanwhile, differentiating adipocytes (Day 6 or 7) were washed and detached from the plastic surface of 10-cm dishes using PBS and TrypLE™ Express Enzyme, respectively. TrypLE™ was then quenched with DMEM/FBS-based medium (see section [2.2.1.1](#)), and cell suspensions were transferred in 15 mL centrifuge tubes to be spun at 200 x g for 5 min. Supernatants were aspirated and pelleted cells were resuspended in 11.2 mL DMEM/FBS-based medium. 800 µL of transfection mixture was added and gently mixed with the cells in suspension. Final *Efr3a* and *Pi4ka* siRNA concentrations were 50 nM and 100 nM, respectively, in a total volume of 12 mL. 2 mL or the full 12 mL of cell suspension plus transfection mixture were added per one well of a 6-well plate or into a 10-cm dish, respectively. Finally, cells were incubated with transfection reagents at 37°C and 10% CO₂ for 24 h before switching back to a DMEM/FBS-based culture medium. Cells were then insulin-stimulated, if required, and lysed 96 h post-transfection (see sections [2.2.1.3](#) and [2.2.3.3](#)). *Efr3a* and *Pi4ka* (double) knockdown (KD) cells were generated by mixing both siRNAs targeting the latter genes within a single transfection mixture. For each siRNA KD condition, non-targeting siRNA was added to the negative control transfection mixture, matching the total targeting-siRNA final concentration.

Opti-MEM	siRNA*				Final Volume
	<i>TransIT-X2</i> [®]	<i>Efr3a</i>	<i>Pi4Ka</i>	Negative Control	
Final Volume - (<i>TransIT-X2</i> [®] + siRNA)	32 μ L	0.75 μ M	1.5 μ M	Match Total Targeting-siRNA Concentration	800 μ L

Table 2.1. Transfection Mixture for siRNA-Mediated Gene Knockdown using *TransIT-X2*[®] Dynamic Delivery System.

Volumes were calculated for transfection in 1x 6-well plate or 1x 10-cm dish. Optimal *Efr3a* and *Pi4ka* siRNA concentrations were estimated from an initial titration experiment (see Appendix 7.1). * Silencer™ Select Pre-Designed siRNA (Ambion™, P/N 4390815; *Efr3a* ID: s94606 for KD of EFR3a, *Pi4ka* ID: s104706 for KD of PI4K-III α) and Silencer™ Select Negative Control #1 siRNA (Ambion™, P/N 4390844) for negative control non-targeting siRNA.

2.2.1.6 CRISPR/Cas9-Mediated Gene Knockout in 3T3-L1 Fibroblasts

2.2.1.6.1 CRISPR/Cas9 System Delivery using Ribonucleoprotein

Low-passage 3T3-L1 fibroblasts (WT) were first plated and maintained on a 12-well plate as described in section 2.2.1.1. When 50-70% confluent, cells were then transfected with ribonucleoproteins (RNP), composed of Cas9 protein and guide RNA (gRNA), using Xfect™ Transfection Reagent (TaKaRa bio, P/N 631318), which utilise cell-penetrating peptide to bind and transport active proteins into the cell. The transfection mixture was prepared as follows per 1x 12-well plate (1x 12-well plate per condition), as previously performed in our laboratory (Bremner et al., 2022): 500 μ L Opti-MEM was first added in an Eppendorf tube, followed by 100 μ L Xfect™

Reaction Buffer, 600 ng gRNA of interest (see Appendix [7.2.1](#)) with 2 μ g Cas9 protein (Sigma-Aldrich, P/N CAS9PROT) to generate RNPs, and 1.5 μ L Xfect™ Polymer. The final mix was then briefly vortexed, incubated at room temperature for 10 min, and spun down once again for 1 sec. Finally, the entire solution was equally spread through each well, drop-wise directly onto the cells. Passage-matched cells were also transfected with Cas9 alone to be used as negative controls. All cells were then incubated with the transfection mixtures at 37°C and 10% CO₂ for 4 h to overnight before the medium was switched back to normal maintenance medium (see section [2.2.1.1](#)). Cells were then incubated for another 48 h (until at least 70% confluent) before being transferred into 96-well plates (Corning Incorporated, P/N 3596) from single-cell colony expansion.

2.2.1.6.2 CRISPR/Cas9 System Delivery using Plasmid DNA

Low-passage 3T3-L1 fibroblasts (WT) were first plated and maintained on 10-cm dishes as described in section [2.2.1.1](#). When 50-70% confluent, cells were then transfected with a plasmid DNA containing the sequences for Cas9, the gRNA, and a puromycin resistance gene (pRP[CRISPR]-Puro-hCas9-U6>mEfr3a[gRNA#5786]; see Appendix [7.2.2](#)), using Xfect™ Transfection Reagent. The transfection mixture was prepared as follows per 1x 10-cm dish (1x 10-cm dish per condition): 500 μ L Opti-MEM was first added in an Eppendorf tube, followed by 100 μ L Xfect™ Reaction Buffer, 160 μ g plasmid DNA, and 48 μ L Xfect™ Polymer (0.3 μ L per 1 μ g DNA). Optimal plasmid DNA and Xfect™ Polymer concentrations were determined from an initial titration experiment (see Appendix [7.3](#)). The final mix was then briefly vortexed, incubated at room temperature for 10 min, and spun down once again for 1 sec. Finally, the entire solution was added

to the 10-cm dish, drop-wise directly onto the cells. Passage-matched cells were also transfected with either a puromycin-resistant plasmid DNA lacking gRNA as non-targeting controls or no plasmid DNA to be used as negative controls for the puromycin selection (see section [2.2.1.6.3](#)). All cells were then incubated with the transfection mixtures at 37°C and 10% CO₂ for 4 h to overnight before the medium was switched back to normal maintenance medium (see section [2.2.1.1](#)). Cells were then incubated for another 48 h (until at least 70% confluent) before being subjected to a puromycin selection.

2.2.1.6.3 Puromycin Selection

Puromycin selection was performed on cells transfected with the pRP[CRISPR]-Puro-hCas9-U6>mEfr3a[gRNA#5786] plasmid (see Appendix [7.2.2](#)) and negative control cells (see section [2.2.1.6.2](#)), using 1.5 µg/mL puromycin (Sigma-Aldrich, P/N P8833). Optimal puromycin concentration was determined from initial titration experiments performed on 3T3-L1 fibroblast (WT; data not shown). Cells were incubated with puromycin for 10 days, changing the medium every second day, before being transferred into 96-well plates from single-cell colony expansion.

2.2.1.6.4 Single-Cell Expansion by Dilution Plating

RNP (see section [2.2.1.6.1](#)) or plasmid DNA (see section [2.2.1.6.2](#)) -transfected cells were washed and detached from wells or dishes using PBS and TrypLE™, which was subsequently quenched using culture medium (see section [2.2.1.1](#)). Total cell numbers were acquired using a

hemocytometer for both transfected and control cell conditions. Cell suspensions were then diluted to 45 cells per well (2-3x 96-well plates were seeded for CRISPR/Cas9-treated cell conditions and 1x 96-well plate for control cells) using a 1:1 mixture of fresh medium and conditioned medium that was left 3T3-L1 fibroblasts for 24 to 48 h. 96-well plates were then incubated at 37°C and 10% CO₂, and medium was changed every second day.

The genomic DNA from the remaining cells was extracted using QuickExtract™ DNA Extraction Solution (Cambio, P/N QE0905T), and a Surveyor® nuclease assay was performed to confirm genome modification using the Surveyor® Mutation Detection Kit for Standard Gel Electrophoresis (Integrated DNA Technologies, P/N 706020; see section [2.2.6.3](#)). Genomic DNA from untreated WT 3T3-L1 fibroblasts was also extracted, as described above, from the validation of designed primer pairs (**Figures 3.13 and 3.15**).

After 1 week, all wells were checked and marked when containing a single colony. When reaching confluency, these colonies were sub-passaged as described above and transferred into larger plastic wares (1x colony per well/flask; 24-well (Corning Incorporated, P/N 3524), 12-well, 6-well plates, T-25 (Corning Incorporated, P/N 3289), and T-75 flasks). Upon confluency in T-75 flasks, the genomic DNA of each clone and control cells was extracted. PCR reactions were performed using the extracted DNA (see section [2.2.6.1](#)), and products were sequenced by DNA Sequencing & Services (MRC I PPU, School of Life Sciences, University of Dundee, Scotland, www.dnaseq.co.uk) using Applied Biosystems Big-Dye Ver 3.1 chemistry on an Applied Biosystems Model 3730 automated capillary DNA

sequencer. For both the Surveyor® nuclease assay and sequencing, primers (see Appendix [7.2](#)) were designed around the studied gRNA target sequence and purchased from Sigma-Aldrich.

2.2.1.7 HEK295 Cells Growth, Maintenance, and Insulin Stimulation

HEK295 cells (American Tissue Culture Collection, P/N CRL-3216 RRID:CVCL_0063) were cultured in DMEM supplemented with 10% (v/v) FBS, 1% (v/v) L-Glutamine, and 1% (v/v) Penicillin-Streptomycin. Cells were cultured in Corning T-75 tissue culture flasks in a 5% CO₂ humidified tissue culture incubator at 37°C, and the culture medium was changed every second day. When cells reached 70% confluency, passaging was performed by washing and detaching the cells from the plastic surface of the flask with PBS and TrypLE™ Express Enzyme, respectively. TrypLE™ was quenched with culture medium (see above), and cells were diluted to the desired concentration and seeded onto appropriate, fresh plastic ware.

Insulin stimulation was performed first by rendering the cells quiescent (basal state) for 2 h in serum-free medium (DMEM supplemented with 1% (v/v) L-Glutamine and 1% (v/v) Penicillin-Streptomycin). 100 nM insulin was then added to the culture medium and cells were incubated at 37°C and 10% CO₂ for 15 min.

2.2.1.8 Plasmid DNA Transfection in HEK295 Cells

HEK 293 cells were first plated and maintained on 12-well plates as described in section [2.2.1.7](#). When 50-70% confluent, cells were

transfected with DNA plasmids of choice (see Appendices [7.2.2.2](#) and [7.2.2.3](#); custom-synthesised by Genscript) using Xfect™ Transfection Reagent. The transfection mixture was prepared as follows per 1x well: 100 µL Xfect™ Reaction Buffer, 7 µg plasmid DNA, and 2.1 µL Xfect™ Polymer (0.3 µL per 1 µg DNA). Optimal plasmid DNA and Xfect™ Polymer concentrations were determined from an initial titration experiment (data not shown). The final mix was then briefly vortexed, incubated at room temperature for 10 min, and spun down once again for 1 sec. Cells were washed with Penicillin-Streptomycin-free HEK295 growth medium and fed with 1 mL per well of the same medium before adding the transfection solution drop-wise into the well. Cells were incubated with the mixture at 37°C and 5% CO₂ for 4 h to overnight before switching back to normal maintenance medium (see section [2.2.1.7](#)) or an antibiotic selection medium to generate stable cell lines (see section [2.2.1.9](#)). Finally, cells were incubated for another 48 h (until at least 70% confluent) before further use.

2.2.1.9 Generation of ALFA-GLUT4 Stable HEK293 Cell Lines: G418 Selection and Clone Isolation

Initial G418 selection was performed on cells transfected with the ALFA-GLUT4 DNA plasmid (see Appendix [7.2.2.2](#)), as described in section [2.2.1.8](#), using HEK293 growth medium (section [2.2.1.7](#)) supplemented with 0.5 µg/mL G418 (Cole-Palmer, P/N 108321-42-2). Optimal G418 concentration was determined from initial titration experiments (data not shown). Cells were incubated with G418, changing the medium every second day until visible individual colonies were observed (10-14 days). Cells were then detached from plastic surfaces as described in section

2.2.1.7 and seeded into T-75 tissue culture flasks at limiting dilution (monoclonal cell population) and as a pooled polyclonal population. Expanded cells were maintained in the presence of 0.1 mg/mL G418 until further use.

2.2.2 *Animal Work*

All animal work was performed under the Home Office Project Licence (UK) PP5059943 and establishment licence X56B4FB08.

2.2.2.1 Mice

HA-GLUT4-GFP transgenic mice were obtained from the German Diabetes Foundation, Düsseldorf, Germany. These animals (RRID: IMSR_JAX:027496) express GLUT4 containing an HA-tag within the exofacial loop and a GFP-tag fused to its carboxyl terminus under the control of the muscle creatinine kinase promoter. HA-GLUT4-GFP trafficking translocation to the PM of cardiomyocytes isolated from these mice has been reported and studied (Fazakerley et al., 2009; Lizunov et al., 2012).

2.2.2.2 High-Fat Diet-Feeding, Weighing, and Blood Glucose Measurement in Mice

A total of 14 mice (see section 2.2.2.1) were used in the experiments described in section 5.3.1, including 7 males and 7 females, and were fed with a standard chow diet (pelleted; 10% kcal% fat; DMB Scotland Ltd, P/N 824050) up to 5 weeks of age. At 5 weeks, mice were randomised to either

control or high-fat diet (HFD) groups. Thereafter, mice in the Control group were kept on a standard diet, while HFD mice were switched to a diet with higher fat content (not pelleted; 60% kcal% fat; DMB Scotland Ltd, P/N 824054) up to the end of the study (20 weeks). Mice were provided with unrestricted access to food and water. Food was only removed for 12h (9 am-9 pm), pre-blood glucose measurements on weeks 14, 16, and 18. Mice were housed at a constant temperature ($21 \pm 2^\circ\text{C}$) and humidity of 45-65%, with a 12-h-light-12-h-dark cycle.

Following the start of the experiment (week 1), mice were weighed every week (see Appendix [7.5.2](#)). Blood glucose measurements were first performed 4 weeks after switching diets and repeated every 2 weeks. Blood glucose measurements on weeks 14, 16, and 18 were performed following an overnight fast (9 pm-9 am). Blood glucose measurements were performed using the Alphatrak2 glucometer (Zoetis; see Appendix [7.5.2](#)).

2.2.2.3 Heart Collection and Dissection

2.2.2.3.1 Mouse Heart Collection for Mesolens Imaging

Mice (see sections [2.2.2.1](#) and [2.2.2.2](#)) were euthanised using 200 mg/mL Dolethal containing sodium pentobarbital. Hearts with the lungs still attached were removed by cutting the ascending aorta and superior vena cava behind the thymus. All tissues were then submerged in BDM-free Perfusion Buffer (see section [2.1.1](#)), where the lungs, thymus, and any remaining connective tissues were carefully excised. Hearts were then

gently pressed down using the back side of curved tweezers, removing as much blood as possible. Finally, hearts were set on an upside-down Eppendorf lid within a clean petri dish, where the aorta was cannulated and clamped. Hearts were then slowly perfused with 20 mL BDM-free Perfusion Buffer, followed by 20 mL of Fixation Solution (see section [2.1.1](#)). The cannula was then carefully removed, and final heart sections were dissected to an appropriate size for Mesolens imaging (maximum 3 mm thickness; see section [2.2.7.2.5](#)) using sharp-end scissors. For all hearts, 1 mm was measured from the apex before measuring and trimming the 3 mm-thick required section. Specimens were then transferred into a Fixation Solution-filled Eppendorf and fixed overnight at 4°C, in the dark, with gentle agitation before optical clearing (see section [2.2.7.1.4](#)).

In section [5.3.1](#), we use the term intact when referring to final isolated heart sections, where the core structure remains untouched and individual cardiac chambers undissected, as described above, conversely to sectioned and homogenised hearts used for quantitative immunoblotting analysis (see sections [2.2.2.3.2](#) and [2.2.3.1](#)).

2.2.2.3.2 Mouse and Rat Heart Collection and Sectioned for Quantitative Immunoblotting

Mice (36 weeks old; see section [2.2.2.1](#)) or rats (16 weeks old; Sprague Dawley) were euthanised using 200 mg/mL Dolethal, which contains sodium pentobarbital (sex is specified in figure legends). Hearts with the lungs still attached were removed by cutting the ascending aorta and superior vena cava behind the thymus. All tissues were then submerged in BDM-free Perfusion Buffer (see section [2.1.1](#)), where the lungs, thymus, and

any remaining connective tissues were carefully excised. Hearts were then gently pressed down using the back side of curved tweezers, removing as much blood as possible. Subsequently, hearts were carefully dissected to isolate the right atrium (RA), left atrium (LA), right ventricle (RV), LV, and the septum. Hearts were placed in fresh BDM-free Perfusion Buffer (just enough so hearts do not float) and placed under a magnifying lamp. Deflated RV were then located, pinched with curved tweezers, and cut at the top using sharp-end scissors to properly expose RA, which were then excised, followed by the LA. RV were subsequently further opened and entirely removed. Finally, the septum was separated from the remaining LV. Each section was kept on ice and homogenised as described in section [2.2.3.1](#). If blood clots were identified during the process, they were carefully removed using tweezers.

2.2.2.4 Cardiomyocyte Isolation

2.2.2.4.1 Buffer and Surgical Area Preparation

A single mouse heart extraction for cardiomyocyte isolation required roughly 50 mL of Perfusion Buffer, 50 mL of EDTA Buffer, 100 mL of Enzyme Buffer, and 10 mL of STOP Buffer (see section [2.1.1](#)). To increase enzymatic digestion efficiency and cell viability, Collagenase Type I and Protease Type XIV were added just before isolation experiments, and all solutions were first warmed up to 37°C using a water bath before use.

Before isolation, buffers were first aliquoted as 1x 7 mL and 1x 10 mL sterile syringes of EDTA Buffer, 1x 7 mL syringe of Perfusion Buffer, and 5x 10 mL

syringes of Enzyme Buffer. 27 G needles were attached to each syringe, and it was ensured that no air bubbles existed in either the syringes or needles. Using a heat lamp, all syringes were kept warm close to the surgical area at around 37°C. A 1 mL plastic pipette and 15 mL centrifuge tube for the collection of tissue-cell suspension were also placed under the heat lamp. 3x 10-cm and 1x 60-mm (Scientific Laboratory Supplies, P/N 353002) sterile dishes were prepared, respectively, containing around 30 mL EDTA, 30 mL Perfusion, 30 mL Enzyme, and 3 mL Enzyme Buffer. A single P1000 pipette and a timer were then placed close to the dishes. Finally, the surgical instruments, including 1x blunt-end scissors, 1x sharp-end scissors, 1x curved hemostatic forceps, and 1x curved tweezers, were cleaned using 70% ethanol and arranged next to the dissection platform (Figure 2.1).

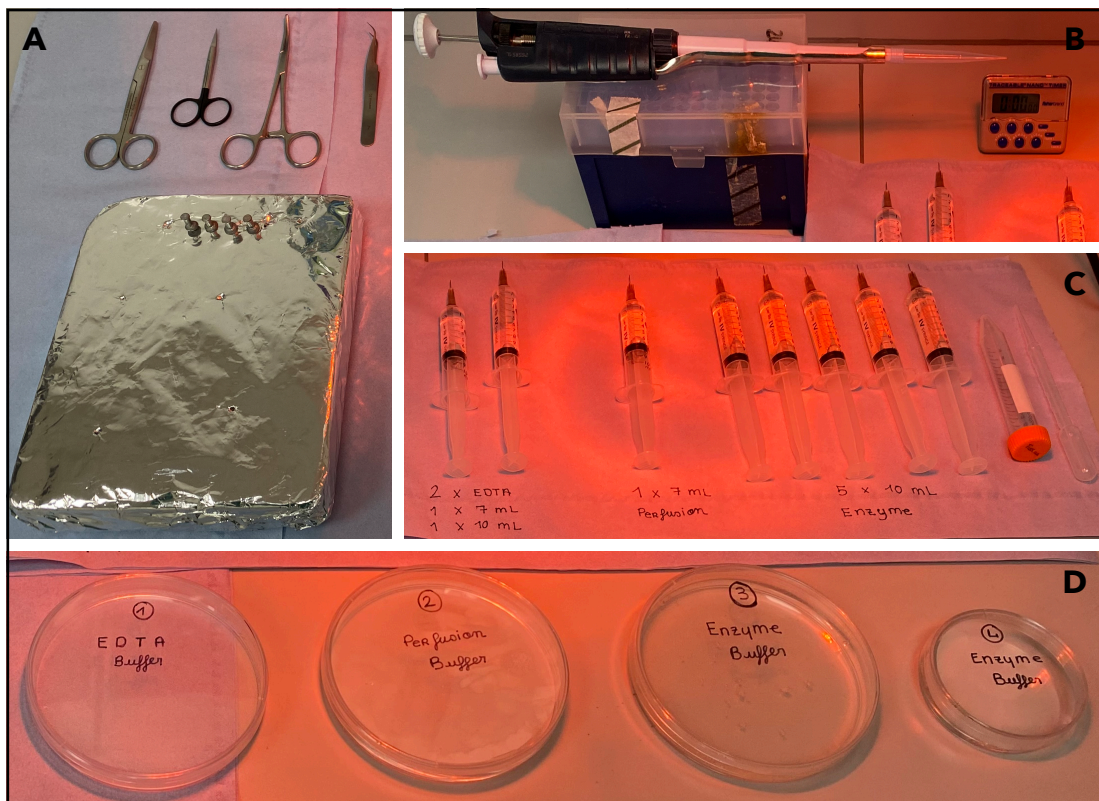


Figure 2.1. Photographic Images of the Surgical Area for a Langendorff-Free and Enzymatic Dissociation-Based Cardiomyocytes Isolation Procedure.

All required equipment was set up optimally to ensure a rapid and fluid progression throughout the procedure. (A) Surgical instruments were placed next to the dissection platform, including 1x blunt-end scissors, 1x sharp-end scissors, 1x curved hemostatic forceps, and 1x curved tweezers. (B) A single P1000 pipette and a timer were placed close to the surgical area. (C) 1x 7 mL and 1x 10 mL syringes of EDTA Buffer, 1x 7 mL syringe of Perfusion Buffer, and 5x 10 mL syringes of Enzyme Buffer were aligned, in this order, under a heat lamp. A 1 mL plastic pipette and 15 mL centrifuge tube for the collection of tissue-cell suspension were also placed under the heat lamp. (D) 3x 10-cm and 1x 60-mm sterile dishes were aligned, respectively, containing around 30 mL EDTA, 30 mL Perfusion, 30 mL Enzyme, and 3ml Enzyme Buffer. All buffers were prepared as described in section [2.1.1](#).

2.2.2.4.2 Primary Adult Mouse Cardiomyocyte Langendorff-Free and Enzymatic Dissociation-Based Isolation

An optimised Langendorff-free and enzymatic dissociation-based method based on the work of Ackers-Johnson et al. (Ackers-Johnson et al., 2016) was used to isolate cardiomyocytes from adult transgenic mice expressing HA-GLUT4-GFP (see section [2.2.2.1](#)).

Mice of approximately 12 weeks old (sex is specified in figure legends) were euthanised using 200 mg/mL Dolethal, which contains sodium pentobarbital. The skin below the diaphragm was cut horizontally using blunt-end scissors and lifted using curved tweezers. Sharp-end scissors were used to cut through the diaphragm, exposing the heart. Lungs were then removed using sharp-end scissors and curved tweezers to reveal the inferior vena cava and descending aorta, which were subsequently cut. Blood within the heart was flushed out by injection of 7 mL EDTA Buffer

into the RV within 1 min, at which point the heart lightened in colour. The needle was pushed no more than a few mm into the heart for optimal perfusion. Curved hemostatic forceps were then used to clamp the ascending aorta and vena cava superior to the heart, which was removed by cutting the latter vessels above the forceps.

Clamped hearts were submerged in EDTA Buffer and injected through the LV within 1 min of 10 mL EDTA Buffer. Hearts were then transferred into Perfusion Buffer and similarly injected with 7 mL of Perfusion Buffer, when possible, via the perforation left by the previous injection. Hearts were next transferred into 10 mL of Enzyme Buffer and once again injected into the LV with 5x 10 mL syringes of Enzyme Buffer. For optimal digestion at the chosen enzyme concentration (see section [2.1.1](#)), the injection rate was set at roughly 10 mL per 1.5 min. However, the volume of Enzyme Buffer required for complete digestion can vary between hearts. Reduction in resistance to injection pressure, loss of rigidity, and holes and/or extensive pale and fluffy appearance at the heart surface were considered signs of complete digestion. For larger and older hearts, digestion sometimes requires more than 50 mL of Enzyme Buffer, necessitating the re-cycling of buffer through recollection from the dish and re-use of the buffer using a new syringe and 27 G needle.

Once digestion was completed, hearts were released from the hemostatic forceps and any remaining connective tissues were carefully removed using sharp-end scissors and tweezers. Hearts were then transferred into 3 mL of Enzyme Buffer and, using sharp scissors, gently chopped apart into as many small pieces as possible. A 1 mL pipette was used to dissociate tissues further for around 1.5 min until the solution became blurry. While

this may vary depending on the size of the heart, it was observed that the optimal total digestion time was between 8 and 10 min (see section [5.3.2.1](#)). Finally, to inhibit any further enzymatic reaction, 5 mL of STOP Buffer was added to the final cell-tissue suspensions using a P1000 pipette and carefully mixed using a 1 mL plastic pipette. The presence of rod-shaped cardiomyocytes in suspension was confirmed by microscopy. Suspensions were then transferred into 15 mL centrifuge tubes, which were kept on their side at room temperature until further use.

2.2.2.4.3 Cardiomyocyte Collection and Calcium Reintroduction

Consecutive processing of tissue-cell suspensions was undertaken in a 37°C water bath. Tissue pieces in suspension were first allowed to quickly gravity settle, and the cell-containing supernatant was carefully transferred in a new tube using a P1000 pipette with a wide-cut tip to avoid shear stress. Cell suspensions were then allowed to gravity settle for 20 min, during which cardiomyocytes would settle faster than dying hypercontractive cells, creating an enriched rod-shaped myocyte pellet. After 20 min, non-myocytes and debris in suspension were gently removed, and viable pelleted cardiomyocytes underwent sequential rounds of gravity settling, using 5 or 2 intermediate Calcium Reintroduction Solutions (see sections [5.3.2.1](#) and [2.1.1](#)) to gradually restore extracellular calcium concentration to 1.8 mM (supraphysiological in mouse) (Schaeffer et al., 2009).

Finally, for each experiment and before any treatments (see section [2.2.2.4.4](#)), the total number of collected cells, including both viable rod-

shaped cardiomyocytes and non-viable hypercontractive cells, was determined using a hemocytometer.

2.2.2.4.4 Insulin Stimulation of Primary Adult Isolated Cardiomyocytes

Primary mouse cardiomyocytes expressing HA-GLUT4-GFP were isolated and reintroduced to physiological extracellular calcium levels as described in sections [2.2.2.4.1](#), [2.2.2.4.2](#), and [2.2.2.4.3](#). Prof. Susan Currie and Zainab Olatunji from the Strathclyde Institute of Pharmacy & Biomedical Sciences, University of Strathclyde, UK, kindly provided primary Langendorff-isolated rat cardiomyocytes from Sprague Dawley rats of approximately 12 weeks old (sex is specified in figure legends) post-calcium reintroduction.

When required, isolated cardiomyocytes were transferred into Eppendorf tubes using a P1000 pipette and a wide-cut tip and resuspended in serum-free medium (DMEM supplemented with 1% (v/v) L-Glutamine, 1% (v/v) Penicillin-Streptomycin, and 10 mM BDM) for either 1 h or 1 h 30 at 37°C in a water bath. 100 nM insulin was then added to the medium and cells were left to gravity settle for 20 min at 37°C.

2.2.3 *Cell Lysates and Tissue Homogenates*

2.2.3.1 Sectioned Cardiac Tissue Homogenisation

Rabbit tissues were kindly gifted by Prof. Godfrey Smith from the Institute of Cardiovascular and Medical Sciences, University of Glasgow, UK.

Isolated and sectioned cardiac tissues (see section [2.2.2.3.2](#)) were placed on ice and weighed. Specimens were submerged in 100 μ L Homogenisation Buffer (see section [2.1.1](#)) per 10 mg of tissue. Samples were then chopped apart using sharp scissors, transferred into centrifuge tubes of appropriate size, and homogenised using a T8 basic ULTRA-TURRAX® (IKA) disperser homogeniser. Before and between each sample, the tissue grinder was washed in water, followed by methanol to help loosen connective tissues if present. The grinding was repeated at least twice, depending on the amount of tissue. Samples were then aliquoted and stored at -80°C until further use (see sections [2.2.5.2](#) and [2.2.5.6](#)).

2.2.3.2 Primary Adult Isolated Cardiomyocytes Lysate

Isolated cardiomyocyte-containing suspensions were allowed to gravity settle for 20 min at 37°C in a water bath. Supernatants were then removed using a P1000 pipette. The cell pellet was placed on ice, and Lysis Buffer (see section [2.1.1](#)) was added to the cells (1 mL buffer per 10⁶ cells). Cells were incubated on a roller at 4°C for 30 min and centrifuged at 18,500 x g at 4°C for 10 min. Finally, lysate supernatants were aliquoted, subjected to a BCA assay, and prepared for immunoblotting as described in section [2.2.5.1](#). Samples were stored at -80 °C until use.

2.2.3.3 3T3-L1 and HEK295 Whole Cells Lysate

Cell-containing culture plates were placed on ice and washed 3x with ice-cold PBS. For 6-well plates, 300 μ L Lysis Buffer (see section [2.1.1](#)) was

applied to each well. Cells were then scraped off the plate surface and left to incubate for 20 min in wells on ice. Cell suspensions were then transferred into Eppendorf tubes using a P100 pipette and centrifuged at $18,500 \times g$ for 10 min at 4 °C. Finally, supernatants (lysate) were aliquoted, subjected to a BCA assay, and prepared for immunoblotting as described in section [2.2.5.1](#). Samples were stored at -20 °C until use.

2.2.4 Cellular Methods

2.2.4.1 Sub-Cellular Fractionation of 3T3-L1 Adipocytes and HEK295 Cells

Sub-cellular fractionation experiments, isolating PM, high-and low-density microsomes (HDM and LDM), and soluble protein (SP) fractions, were performed using a well-characterised procedure (Simpson et al., 1983).

Cells (WT 3T3-L1 adipocytes or HEK295 cells) were first plated onto 10-cm dishes, cultured, differentiated and insulin-stimulated when required, as described in sections [2.2.1.1](#), [2.2.1.2](#), [2.2.1.3](#), and [2.2.1.7](#). Upon confluency, cells were washed 3x with ice-cold HES Buffer and scraped off in the same buffer supplemented with protease and phosphatase inhibitors (see section [2.1.1](#)). Cells were then transferred in 15 mL centrifuge tubes and spun at $200 \times g$ for 5 min. The supernatant was aspirated, and pellets were resuspended in 1 mL HES Buffer (per 2x dishes). Cell suspensions were transferred into Eppendorf tubes and homogenised by passing through a 23 G needle 10 times.

Homogenates were then centrifuged at $3500 \times g$ for 20 min (Rotor ID: TLA-100.4; from this stage on, all centrifugations were performed in a Beckman Bench-top Optima™ MAX-XP Ultracentrifuge at 4°C). The supernatant (containing HDM and LDM) was retrieved and set on ice. The pellet from this spin was resuspended in 1 mL HES Buffer, layered onto a 1 mL HES/sucrose cushion (see section [2.1.1](#)), and centrifuged at $53,500 \times g$ for 1 h (Rotor ID: TLS-55). Using a 23 G needle, the PM was collected from the interface of the sucrose cushion and the supernatant, diluted 1:5 in HE Buffer (see section [2.1.1](#)), and placed on ice. The initial supernatant (HDM and LDM) was centrifuged at $13,800 \times g$ for 20 min (Rotor ID: TLA-100.4), yielding a HDM pellet, which was resuspended in 100 μ L HES Buffer. The supernatant and the diluted PM were then re-centrifuged at $195,000 \times g$ for 1 h (Rotor ID: TLA-100.4), yielding the final pellets of LDM and PM, respectively. Both pellets were resuspended in 100 μ L HES Buffer, and PM, HDM, and LDM fractions were subjected to a BCA assay and prepared for immunoblotting as described in section [2.2.5.1](#). Samples were stored at -80 °C until use.

Finally, the supernatant from the latest LDM-isolation spin was collected in an Eppendorf tube for the isolation of SP fractions. For 1 mL of collected supernatant, 200 μ L of 10% trichloroacetic acid was carefully mixed into the sample, which was subsequently incubated on ice for 10 min and centrifuged at $18,500 \times g$ for another 10 min. Trichloroacetic precipitates smeared down the side of the Eppendorf tube were then resuspended into 100 μ L 1x LSB (see section [2.1.1](#)) per 1 mL of original supernatant. If the sample became yellow (acidic), pH was adjusted by adding a few microlitres of saturated Tris until the solution turned blue again. Samples were then stored at -80 °C until further use.

2.2.4.2 Lipid Raft Fractionation of 3T3-L1 Adipocytes

3T3-L1 fibroblasts (WT) were plated onto 10-cm dishes, cultured, differentiated, and insulin-stimulated, as described in sections [2.2.1.1](#), [2.2.1.2](#) and [2.2.1.3](#). On ice, cells were washed 3x with ice-cold MES Buffer and scraped off in 1 mL (per dish) of the same buffer supplemented with Triton X-100, protease and phosphatase inhibitors (see section [2.1.1](#)). Cells were then transferred into Eppendorf tubes, incubated at 4 °C for 20 min with end-over-end rotation, and homogenised with 10 strokes of a Dounce homogeniser.

Lipid raft fractionation was subsequently performed as described by Chamberlain and Gould (2002). Homogenates were mixed to an equal volume of 80% (w/v) sucrose in MES Buffer. 1 mL of the solubilised cells was then transferred in a thin-wall polypropylene ultracentrifuge tube (Beckman Coulter; P/N 326819) and successively overlaid with 1.5 mL of 30% sucrose and 0.5 mL of 5% sucrose (in MES Buffer). Samples were then centrifuged at 4 °C at $148,500 \times g$ for 18 h in a swinging-bucket rotor (ID: SW55Ti) using the Beckman Optima™ L-100 XP Ultracentrifuge. Finally, 250 µL fractions were retrieved from the top (fraction number 1) to the bottom (fraction number 12) of the sucrose gradient (Fractions 1-5 = 5% Sucrose Layer, Fractions 6-9 = 30% Sucrose, and Fractions 10-12 = 80% Sucrose). Fractions were stored at -80 °C until use.

2.2.5 Protein-Specific Assays

2.2.5.1 Bicinchoninic Acid Assay and Sample Preparation for Immunoblotting

When required, a Bicinchoninic acid (BCA) assay (ThermoFisher Scientific, P/N 23225) was performed to measure the protein concentration of specific samples. A range of BSA standards, from 0 to 10 mg/mL, were made up by mixing 10 mg/mL BSA stock in dH₂O. Unknown protein samples were then diluted 1:5 with dH₂O. In duplicate, 10 µL of each unknown protein sample and BSA standard were combined with 200 µL of the supplier's BCA assay reagent mix in a 96-well plate. Lysis or homogenisation buffers (see section [2.1.1](#)) were also tested for each experiment. Finally, the plate was incubated at 37°C for 30 min, and the absorbance was measured at 570 nm using a micro-plate reader. For western blotting analysis, 1 mg/mL stocks of measured samples were prepared with 2x LSB (see section [2.1.1](#)). Samples were then stored at -20°C until use.

2.2.5.2 SDS-PAGE

Sodium dodecyl sulfate-polyacrylamide gel electrophoresis (SDS-PAGE) was carried out using the Bio-Rad Mini-PROTEAN Tetra cell gel apparatus (Bio-Rad Laboratories Ltd). Gels were prepared with 12% (v/v) acrylamide resolving gel (for 10 mL: 3.3 mL H₂O, 4 mL 30% acrylamide, 2.5 mL 1.5 M Tris (pH 8.8), 100 µL 10% SDS, 100 µL 10% ammonium persulfate, and 4 µL TEMED) and 5% stacking gel (for 10 mL: 6.8 mL H₂O, 1.7 mL 30% acrylamide, 1.25 mL 1 M Tris (pH 6.8), 100 µL 10% SDS, 100 µL 10% ammonium persulfate, and 10 µL TEMED). Protein samples prepared as

described in section [2.2.5.1](#) were thawed and, when probing for GLUT4, heated for 10 min at 65°C instead of the conventional 95°C. Samples were then appropriately loaded into each well. Whole-cell lysates (see sections [2.2.3.2](#) and [2.2.3.3](#)), tissue homogenates (see section [2.2.3.1](#)), and PM, HDM, and LDM fractions (see section [2.2.4.1](#)) were subjected to a BCA assay to quantify total protein concentrations (see section [2.2.5.1](#)), subsequently loading equal protein amounts into each well (typically 10 µg). For SP fractions (see section [2.2.4.1](#)), recovery is assumed to be the same in all fractions; as such, equal amounts of each fraction were loaded by volume (20 µL). For lipid raft fractions (see section [2.2.4.2](#)), equal amounts of each fraction were also loaded by volume (10 µL). Finally, gels were run in Running Buffer (see section [2.1.1](#)) at 100 V for approximately 2 h. The Blue Prestained Protein Standard (New England BioLabs, P/N P7718) was loaded as a molecular weight ladder for each gel.

2.2.5.3 Wet Transfer

Proteins were transferred from SDS-PAGE gels onto nitrocellulose membranes by wet transfer using a Trans-Blot® Turbo™ Transfer System. 0.2 µm nitrocellulose membranes, transfer filter papers, and transfer buffer were purchased within the Trans-Blot Turbo RTA Mini 0.2 µm Nitrocellulose Transfer Kit (Bio-Rad, P/N 1704270). In the transfer cassettes, gel, membrane, and filter paper were sandwiched together and submerged in the provided transfer buffer, following the instructions of the latter transfer kit. A cassette filled with 1 mini gel would then be run into the Trans-Blot® Turbo™ transfer machine using the Bio-Rad HIGH MW programme at 1.3 A, up to 25 V, for 10 min.

2.2.5.4 Dot Blot Sample Preparation

First, 1 x 1 cm grids were carefully drawn onto 0.2 µm nitrocellulose membranes using a pencil. Then, using a narrow-mouth pipette tip, a few microliters of samples were slowly spotted at the centre of a square onto the gridded membranes. Equal protein amounts of PM fractions (see section [2.2.4.2](#)), previously subjected to a BCA assay (see section [2.2.5.1](#)), were pipetted onto the membranes (typically 2 µg). Subsequently, membranes were let to dry and blocked in 5% (w/v) milk powder in PBS-T (see section [2.1.1](#)) for 45 min without shaking. Immunoblotting was then performed as described in section [2.2.5.5](#).

2.2.5.5 Immunoblotting

Prior to immunoblotting, transfer efficiency was checked using a total protein stain (TPS) kit (LI-COR, P/N 926-11010) or Ponceau S (Sigma-Aldrich, P/N P3504). Membranes were then blocked in 5% (w/v) milk powder (or 5% (w/v) BSA when using anti-PI4K-III α primary antibody; see section [2.1.2.1](#)) in PBS-T (see section [2.1.1](#)) for 30 min, with shaking. Primary antibodies (see section [2.1.2.1](#)) were diluted to the appropriate concentration in 3% (w/v) milk (or 3% (w/v) BSA when using anti-PI4K-III α primary antibody) in PBS-T. When blotting for GLUT4, carboxy- and amino-terminal homemade antibodies were mixed together at the provided concentrations (see section [2.1.2.1](#)). Membranes were subsequently incubated with the appropriate primary antibody solution for 1 h at room temperature, with shaking. Membranes were then washed 3x with PBS-T for 5 min. For 1 h at room temperature, membranes were subsequently

incubated with secondary antibodies (see section [2.1.2.2](#)), diluted beforehand at a concentration of 1:10,000 in 3% (w/v) milk (or 3% (w/v) BSA when using anti-PI4K-III α primary antibody) in PBS-T, with shaking. Once again, membranes were washed 3x with PBS-T for 5 min to remove residual antibodies. Blots were then visualised at 800 or 700 nm (see section [2.1.2.2](#)) using a LI-COR Odyssey SA Infrared Imaging System at a resolution of 169 μ m. High-quality composite images of both channels were obtained and analysed with ImageStudioLite (Version 5.2) (see section [2.2.8.1](#)).

2.2.5.6 PNGase F-Mediated Protein De-Glycosylation

Purchased from New England BioLabs (P/N P0704), Peptide:*N*-Glycosidase F (PNGase F) catalyses the removal of amino-linked oligosaccharides from glycoproteins. This enzyme was used to de-glycosylate glycoproteins in cardiac tissue homogenates (see section [2.2.3.1](#)). As advised by the supplier, 20 μ g of glycoprotein and 1 μ L of 10X Glycoprotein Denaturing Buffer were mixed in dH₂O for a total reaction volume of 20 μ L. Samples were then desaturated at 65°C for 10 min, chilled on ice, and briefly centrifuged (10 sec). Subsequently, the reaction volume was doubled by adding 4 μ L of 10X GlycoBuffer 2, 4 μ L 10% NP-40, and 12 μ L dH₂O. PNGase F was added at a concentration of 1:20 to the studied samples, which were then incubated at 37°C overnight. Finally, the extent of de-glycosylation was assessed by mobility shifts of the glycoprotein of interest (GLUT4) on SDS-PAGE gels (see sections [2.2.5.2](#), [2.2.5.3](#) and [2.2.5.5](#)).

2.2.6 *Molecular Methods*

2.2.6.1 Polymerase Chain Reaction (PCR)

PCR reactions were prepared in thin-walled PCR tubes on ice, as shown in **Table 2.2**. Nuclease-free water was used to increase the final volume to 50 μL . PCR tubes were then transferred in an Applied Biosystems MiniAmp Thermo Cycler. Reactions were carried out as shown in **Table 2.3**. Finally, PCR products were visualised using agarose gel electrophoresis (see section [2.2.6.2](#)).

Component	Final Concentration
5X GoTaq [®] Reaction Buffer (Promega, P/N M791A)	1X (1.5 mM MgCl_2)
Deoxynucleotide (dNTP) Sotultion Mix (New England BioLabs, P/N N0447S), 10 mM each dNTP	0.2 mM each dNTP
GoTaq [®] G2 DNA Polymerase (Promega, P/N M784A), 5U/ μL	2.5U/50 μL
Forward and Reverse Primers (Merck, Gillingham, UK; see Appendix 7.2), 100 μM each primer	0.25 μM each primer
Template DNA (see section 2.2.1.6 and Appendix 7.2)	< 0.5 μg /50 μL

Table 2.2. PCR Reaction Setup.

Step	Temperature	Time
Initial Denaturation	95°C	4 min
40 Cycles:		
Denaturation	95°C	30 sec
Annealing	55-65°C*	1 min
Final Extension	72°C	5 min
Hold	4°C	∞

Table 2.3. PCR Thermocycling Conditions.

* Annealing temperature (Ta) was calculated from the melting temperature (Tm) of the primers and must be determined for each primer pair used in PCR (see Appendix [7.2](#)).

2.2.6.2 Agarose Gel Electrophoresis

Agarose gels were prepared with 0.8-2% (based on the size of the studied products) of agarose (w/v) in Tris-Acetate-EDTA (TAE) Buffer (see section [2.1.1](#)) and 0.2 µg/mL Ethidium Bromide. Gel loading dye (6x) from New England BioLabs (P/N B7024S) was added at a dilution of 1:5 to each DNA sample. DNA ladder was made up as suggested by the supplier by mixing 4 µL dH₂O, 1 µL gel loading dye (6x), and 1 µL 100 bp DNA ladder (New England BioLabs, P/N N3231 and N3232, respectively). Gels were then loaded with DNA ladder (1.2 and 2.4 µL) and DNA samples (2-5 µL for PCR products; see section [2.2.6.1](#)) and electrophoresed in TAE Buffer at a constant voltage of 80 V for 30 min. Gels were visualised under UV light using a Syngene Gel Documentation System.

2.2.6.3 Surveyor® Nuclease Assay for Gene Modification

To confirm genome modifications following CRISPR/Cas9-mediated genome editing (see section [2.2.1.6](#)), the Surveyor® Mutation Detection Kit for Standard Gel Electrophoresis from Integrated DNA Technologies was used on heterogeneous DNA populations extracted from pools of CRISPR/Cas9-treated cells collected before single-cell colony expansion (see section [2.2.1.6.4](#)). Along with the provided Control G and Control C plasmid DNA, the targeted locus (see Appendix [7.2](#)) in both CRISPR/Cas9-treated and negative control DNA were first amplified by PCR (see section [2.2.6.1](#)).

CRISPR/Cas9-treated and control PCR products were then separately added into thin-walled PCR tubes. Each tube contained 500 ng total DNA in a total volume of 30 µL. Control G and Control C PCR products were prepared in a similar manner, and an equal amount of Control C and G products (250 ng each) were also mixed together as a positive control. All samples were then desaturated at 95°C for 10 min and left to slowly cool down at room temperature, allowing for re-annealing and the formation of two types of DNA duplexes (i.e., either homoduplexes or heteroduplexes). Whether DNA sequences are WT or mutated, homoduplexes consist of perfectly paired double-stranded DNA sequences. On the other hand, heteroduplexes contain unpaired/mismatched DNA regions (insertions and/or deletions), with one DNA strand being mutated (**Figure 2.2**).

From this assay, the targeting efficiency achieved during CRISPR/Cas9-mediated genome editing experiments can be estimated. To do so, DNA duplex samples are treated with Surveyor® nuclease, as described by the supplier. The enzyme recognises all base mutations and cleaves the 3' side of mismatched sites in both DNA strands of heteroduplexes (**Figure 2.2**).

DNA products are then visualised by agarose gel electrophoresis (see section [2.2.6.2](#)) and analysed for the presence or absence of cleaved products. By definition, no heteroduplexes can be formed in the absence of mutations, and therefore, the Surveyor® nuclease will not produce any cleaved products. However, if cleaved products are observed, accounting that a CRISPR/Cas9-mediated mutation has occurred. In this case, using ImageStudioLite (Version 5.2), each band intensity is determined similarly as described in section [2.2.8.1](#). Gene modification levels are then estimated using the following equation: % gene modification = $100 * (1 - \sqrt{1 - x})$, where x is the sum of the cleavage products' band intensities divided by the sum of the cleavage products and parental band intensities (**Figure 2.2**).

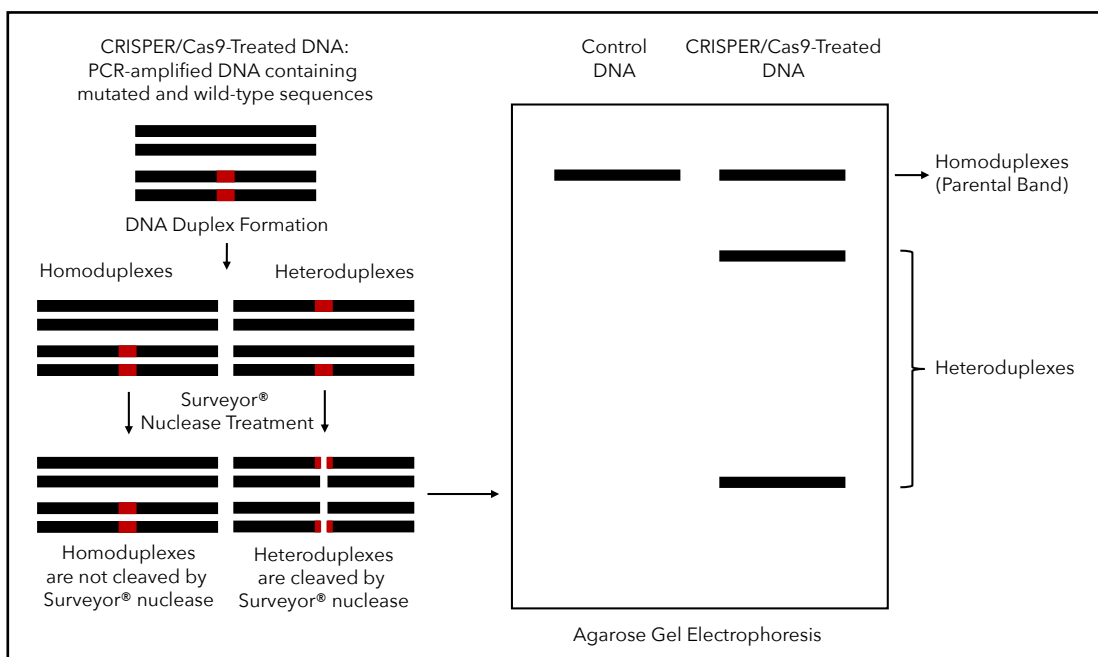


Figure 2.2. Schematic Representation of Mutations Detection by Surveyor® Nuclease Assay.

The genomic locus containing the expected mutation site (in red) in a heterogeneous DNA population extracted from a pool of CRISPR/Cas9-treated cells is amplified by PCR and subjected to denaturation at 95°C and subsequent re-annealiation to form homoduplexes and heteroduplexes. DNA duplexes are then cleaved by the Surveyor® nuclease enzyme and visualised by agarose gel electrophoresis either as an uncleaved (homoduplex) parental band or specific cleavage product (heteroduplex) bands. Control DNA represents an untargeted WT reference.

2.2.7 Microscopy

2.2.7.1 Sample Preparation

2.2.7.1.1 Cellular Fixation, Immunofluorescent, and Permanent DNA-PAINT Staining

Cells were cultured and insulin-stimulated when required onto 13 mm glass coverslips in 12-well plates. On ice, cells were then washed 3x with ice-cold PBS and incubated in Fixation Solution (see section [2.1.1](#)) at room temperature for 30 min. Subsequently, cells were washed 3x with PBS, submerged in Quenching Buffer at room temperature for 40 min (see section [2.1.1](#)), and subjected to a third PBS wash.

For immunostaining of PM-specific phosphatidylinositol 4-phosphate (PI4P), all steps from this point on were performed on ice. Additionally, for both PI4P and GLUT4 staining, coverslips were first incubated in Permeabilisation Buffer (see section [2.1.1](#)) for 5 min prior to blocking.

The cells were then blocked in Blocking Buffer (see section [2.1.1](#)) at room temperature for 45 min. Primary antibodies or nanobodies were diluted to the appropriate concentration (see section [2.1.2.1](#)) in Blocking Buffer, and staining was carried out by pipetting 50 μ L of the latter primary antibody solution on a clean Parafilm-coated surface. Coverslips were removed from wells, inverted, and placed onto the antibody solution using fine tweezers incubated for 1 h at room temperature. Coverslips were returned to wells and washed 3x with Blocking Buffer.

For immunofluorescent staining, secondary antibody (see section [2.1.2.2](#)) staining was then performed in the same manner as for primary antibodies for 45 min in the dark at room temperature. For permanent DNA-PAINT staining, coverslips were incubated in wells for 20 min at RT with 0.1 mg/mL NeutrAvidin (Thermo Fisher Scientific, P/N 31000) in Blocking Buffer and subsequently rinsed 3x with Blocking Buffer. Biotinylated-docking and imaging double-stranded complexes DNA, incubated together in DNA-PAINT Solution (see section [2.1.1](#)) overnight at 4°C 24 h prior to staining, were then added onto the coverslips for 5 min at RT (Docking: 4 nM, Biotin-5'-GGGAATGCGAATCAAGTAATATAATCAGGC-3'; Imaging: 2 nM, 5'-GCCTGAT-ATTO655-ATATTACTTGATTTCGCATTCCC-3'; Eurogentec). Both immunofluorescent and DNA-PAINT coverslips were then again washed 3x with Blocking Buffer, and cells were stained in the dark with 1 μ g/mL DAPI (4',6-diamidino-2-phenylindole) in PBS for 10 min at room temperature following the same process as for antibody staining.

Finally, a drop of ProLong™ Glass Antifade Mountant (Invitrogen, P/N P36980) was applied to a glass microscope slide. Coverslips were carefully

placed on the montant droplet with cells facing down. The slides were covered and left to dry overnight.

2.2.7.1.2 Primary Isolated Mouse Cardiomyocytes Fixation and Immunofluorescent Staining

In Eppendorf tubes, isolated cardiomyocytes (see section [2.2.2.4](#)) were resuspended and incubated in Fixation Solution (see section [2.1.1](#)) at room temperature for 20 min. Subsequently, once cells had gravity settled, Fixation Solution was carefully removed, and cells were resuspended in Quenching Buffer at room temperature for 20 min (see section [2.1.1](#)).

Primary Langendorff-isolated rat cardiomyocytes from Wistar rats of approximately 8 weeks old (sex is specified in figure legends) were kindly gifted by Prof. Luc Bertrand and Dr. Laurent Bultot from the Institut de Recherche Expérimentale et Clinique, Université Catholique de Louvain, Belgium. Cells were transfected with the HA-GLUT4-GFP construct, insulin-stimulated as described in [2.2.2.4.4](#), and provided post-fixation.

Through the same gravity-settling-resuspension process described above, cells were subsequently washed with 200 μ L PBS for 15 min and blocked in 200 μ L Blocking Buffer (see section [2.1.1](#)) for 30 min. If required, cells were first incubated in Permeabilisation Buffer (see section [2.1.1](#)) for 15 min prior to blocking. Anti-HA-tag primary antibodies were then diluted to the appropriate concentration (non-biotinylated; see section [2.1.2.1](#)) in Blocking Buffer, and staining was carried out by incubating the cells in 200 μ L primary antibody solution for 1 h at room temperature or overnight at 4 °C (see section [5.3.2.2](#)), in the dark and with end-over-end rotation.

Cardiomyocytes were then washed in Blocking Buffer for 15 min, and secondary antibody (see section [2.1.2.2](#)) staining was then performed in the same manner as for primary antibodies for 1 h at room temperature, in the dark. Finally, cells were washed once again with Blocking Buffer and stained in the dark with 1 $\mu\text{g}/\text{mL}$ DAPI in PBS for 15 min in the same manner as for primary and secondary antibodies. The stained cardiomyocytes were then stored in PBS in the dark at 4°C. On the day of imaging, 1 drop of resuspended cardiomyocytes in PBS was added to a glass microscope slide and covered with an 18-mm coverslip.

2.2.7.1.3 Single-Molecule Surfaces for DNA-PAINT Imaging

Nunc Lab-Tek™ II chambered coverglasses (#1.5, 8 Wells; Thermo Fisher Scientific, P/N 155409PK) were cleaned as follows; LabTek™ chambers were first incubated in 3% (w/v) Decon 90 in dH₂O for 15 min, washed 3x with dH₂O, submerged in 1M KOH for 30 min and finally rinsed 3x with dH₂O.

Single-molecule surfaces were prepared by incubating LabTek™ chambers overnight at 4°C with 200 μL of 10 mg/mL BSA and 0.1 mg/mL biotinylated-BSA (Merck, P/N A8549) in PBS. The next day, LabTek™ chambers were rinsed 3x with PBS and incubated for 20 min at RT with 200 μL of 0.2 mg/mL NeutrAvidin (Thermo Fisher Scientific, P/N 31000) in PBS. Chambers were once again rinsed 3x with PBS, incubated for 5 min at RT with 200 μL of 50 nM docking DNA strand (Biotin-5'-GGGAATGCGAATCAAGTAATATAATCAGGC-3'; Eurogentec) in PBS, and finally washed for the last time 3x with PBS.

For imaging (see sections [4.3.1.2](#) and [2.2.7.2.3](#)), different concentrations of ATTO655-labelled imaging docking strands (5'-CTGAT-ATTO655-AT-3'; Eurogentec) in DNA-PAINT Solution (see section [2.1.1](#)) were perfused onto single-molecule surfaces (see section [2.2.7.2.2](#)). For imaging of the 0 to 100% pulse profile, 0% corresponded to 0 nM of the imaging strand, and 100% corresponded to 0.3 nM. Three pulses were measured throughout 15,000 frames (see Appendix [7.4](#)). For the stepwise increase and decrease profile, the concentration of the imaging strand was initially increased stepwise from 0 to 0.1, then to 0.2, and finally to 0.3 nM, followed by a reverse stepwise decrease throughout 15,000 frames (see Appendix [7.4](#)).

2.2.7.1.4 Mouse Heart Optical Clearing

Following fixation collected hearts (see section [2.2.2.3.1](#)) were optically cleared using the iDISCO method (Renier et al., 2014). Hearts were washed 3x in PBS for 30 min at room temperature on a rotator and were subsequently dehydrated through a series of methanol solutions, starting with a 20% methanol in dH₂O, for 1 hour with no agitation. This was repeated in 40%, 60%, 80%, and 100% methanol solutions. Specimens were left overnight at room temperature in a final 100% methanol solution without agitation. Dichloromethane (Sigma-Aldrich P/N 270997) was then introduced by placing the specimens in a 1:2 methanol to dichloromethane mixture for 3 hours, followed by two washes of 15 min in 100% dichloromethane at room temperature on a rotator. Finally, the hearts were transferred in an opaque Eppendorf tube and submerged in dibenzyl ether (Sigma-Aldrich P/N 108014) until becoming visually transparent

(**Figure 5.1**), at which point specimens were mounted for imaging with the Mesolens (see section [2.2.7.2.5](#)).

2.2.7.2 Imaging Setups and Data Acquisition

2.2.7.2.1 STEDYCON (STED and Confocal) Microscope

Samples imaged using the STEDYCON system were acquired using an NA 1.45, 100× oil immersion objective (UPLXAPO100XO, Olympus). Confocal images were acquired using 488 nm (pulsed; GLUT4-GFP) and 405 nm (continuous wave; DAPI) excitation laser lines. STED images were acquired from a 775 nm (immunostained PI4P) pulsed STED laser. Images from the corresponding STEDYCON software were stored in the OsmAnd Binary Maps.OBF format and processed using Fiji (Schindelin et al., 2012), Excel (Version 16.82), and GraphPad Prism 10 software, as described in section [2.2.8.2](#).

2.2.7.2.2 Perfusion Syringe System and pH Measurement Experiment

Dr Peter W. Tinning custom-built the perfusion syringe system, based on the work of Baas and Saggiomo and Schnitzbauer (Baas and Saggiomo, 2021; Schnitzbauer et al., 2017), using a Creality Ender-3 V2 3D printer at a total cost of £180. The system was programmed using G-code and composed of two syringe channels. Channel Y and X, respectively, allow for the perfusion of imaging strands and DNA-PAINT Solution (see section

2.1.1). Fluid removal was performed using a peristaltic pump (Farnell, P/N ADAFRUIT 1150) to reduce shaking and noise.

The pH experiment (see section 4.3.1.1) was performed using dSTORM photoswitching buffer according to the work of Herdly et al. (Herdly et al., 2023). Photoswitching buffer was prepared according to previously published protocols (Herdly et al., 2021; Herdly et al., 2023). Briefly, the final enzymatic oxygen scavenger system consisted of 10% (w/v) Glucose, 10 U/mL Glucose Oxidase, and 200 U/mL Catalase in PBS.

Mercaptoethylamine was added to the solution at a final concentration of 50 mM. Initial 6.3 and 8.4 pH solutions were adjusted by adding HCl and KOH, respectively, until desired pH were reached. Both perfusion system and manual dilutions were performed simultaneously and set to mix specific volumes of 6.3 and 8.4 pH solutions throughout 21 measurements (**Table 2.4**). The final solutions were collected, and their pH was measured using an Oakton 700 pH meter.

Volume of 6.3 pH Solution (mL)	Volume of 8.4 pH Solution (mL)
2	0
1.9	0.1
1.8	0.2
1.7	0.3
1.6	0.4
1.5	0.5
1.4	0.6
1.3	0.7
1.2	0.8
1.1	0.9
1	1
0.9	1.1
0.8	1.2
0.7	1.3
0.6	1.4
0.5	1.5
0.4	1.6
0.3	1.7
0.2	1.8
0.1	1.9
0	2

Table 2.4. pH Measurements Reaction Setup.

2.2.7.2.3 Single-Molecule Localisation Microscope

DNA-PAINT measurements (see section [2.2.7.1.3](#)) were performed using a SMLM system, as previously described (Herdly et al., 2021; Herdly et al., 2023). This system comprises a single-molecule-sensitive, wide-field microscope body (IX73, Olympus). It uses an NA 1.49, 60× oil immersion objective (APON60XOTIRF, Olympus), a diode laser (iBeam Smart, 641 nm, Toptica or 642 nm Fibre Laser, MPB communications) for excitation, and an EMCCD camera (iXon Life 888, Andor) with a pixel size of 122 nm. All

measurements were performed with a confirmed tiff imaging modality at a laser output power of 500 mW. 15,000 frames were acquired at 10 Hz.

2.2.7.2.4 Confocal Microscope

Samples imaged were acquired using a Leica TCS SP8 multi-photon confocal microscope and corresponding software. The objective magnification used is specified in figure legends. Images were processed using Fiji.

2.2.7.2.5 The Mesolens

Individual specimens were secured in custom-designed mounts for long-term imaging with the Mesolens, as described by Clapperton et al. (Clapperton et al., 2024).

A full report detailing the specification and performance of the Mesolens instrument has been published by McConnell et al. (McConnell et al., 2016). Here, we provide an overview of the Mesolens, along with modifications tailored specifically for imaging of clarified sections of mouse hearts.

Figure 2.3 illustrates a schematic of the multimodal setup employed by the Mesolens. An illumination source consisting of a 488 nm laser (Cairn Research, Multiline Laserbank) was utilised for the excitation of the GFP fluorescence (HA-GLUT4-GFP) of the specimens. A total laser power of 4 mW at the specimen plane was maintained during imaging.

The Mesolens was used as a point-scanning confocal laser scanning instrument for imaging of all specimens. A 5 mm × 5 mm lateral field of view (FOV) was scanned with a sampling rate of 1 pixel per micron. The pixel dwell time was set to 0.5 μs, giving an acquisition time of approximately 50 seconds per single optical section of the full 5 mm × 5 mm field. Residual back-scattered 488 nm laser excitation was rejected in the detection path using a dichroic mirror (Thorlabs, P/N DMLP505R) that transmitted wavelengths longer than 505 nm. A bandpass filter (Thorlabs, P/N MF525-39) was placed before the detector to allow only the 525 ± 19.5 nm fluorescence signal to be detected using a photomultiplier tube (PMT) (Senstech, P/N P30-01), for 16-bit detection.

Specimens were moved along the optical axis for imaging at discrete z-planes using the confocal method with a computer-controlled z-positioning system (Prior Scientific, Optiscan II). The z-step size was set to 5 μm to minimise data acquisition time. The system was controlled using an in-house laser scanning software package, 'Mesoscan', designed to handle scanned images. Images were stored in the Open Microscopy Environment OME.TIFF format and processed using Fiji, Excel, and GraphPad Prism 10 software as described in section [2.2.8.4](#).

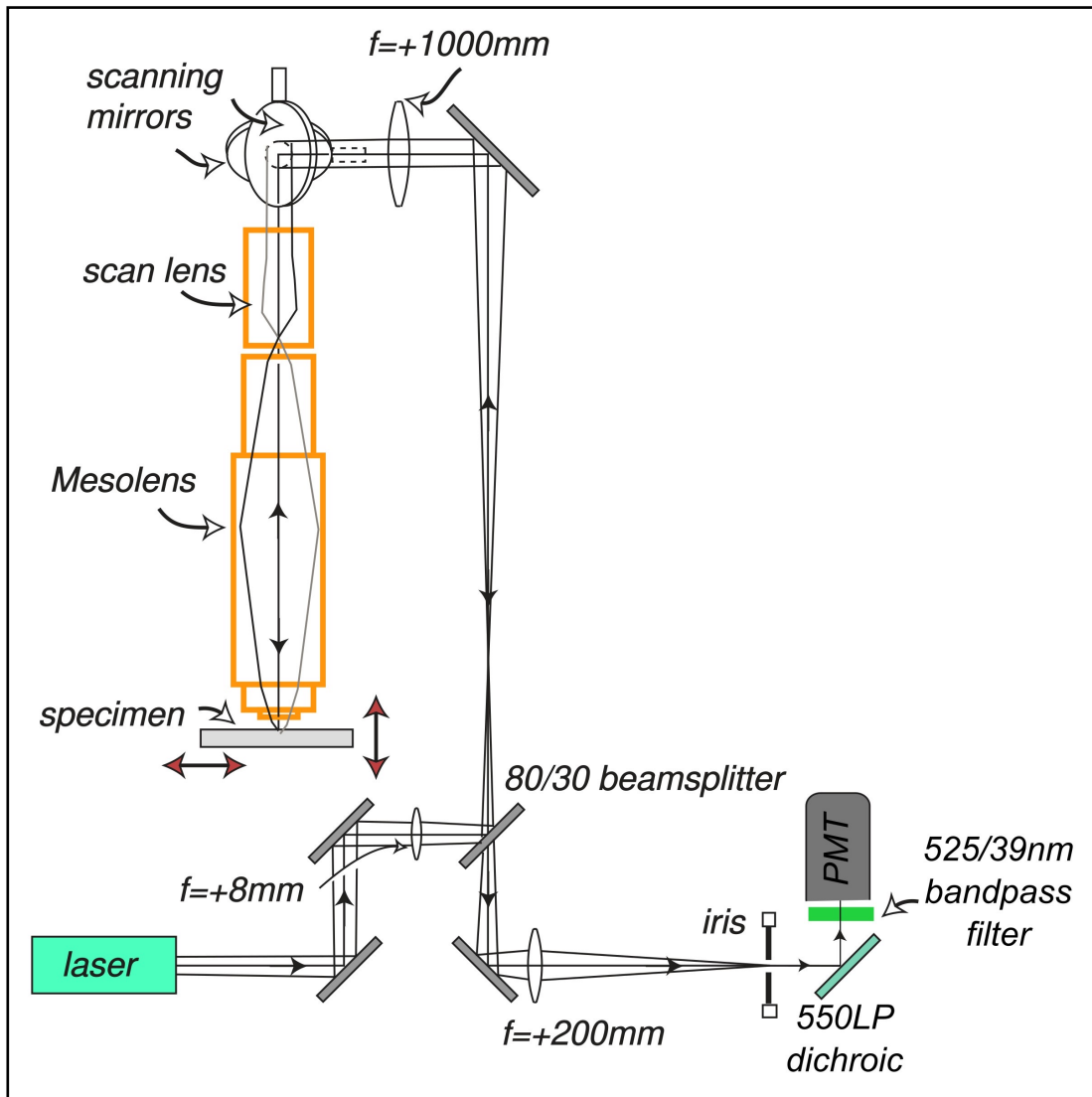


Figure 2.3. Schematic diagram of point-scanning confocal Mesolens for imaging of GLUT4-GFP in ultrathick sections of cleared mouse heart.

A 488 nm laser was used to excite fluorescence from GLUT4-GFP. A single confocal iris was used in the detection path. A single photomultiplier (PMT) was used to detect the fluorescence contrast, together with a 550LP dichroic and a 525/39 nm bandpass filter to minimise backscattered laser light and transmit only fluorescence from GLUT4-GFP.

Published in Geiser et al. (2024).

2.2.8 Data and Statistical Analyses

2.2.8.1 Densitometry

Immuno-stained nitrocellulose membranes were visualised as described in section [2.2.5.5](#). High-quality composite images were then analysed using ImageStudioLite (Version 5.2). In the analysis window, a box was drawn around each protein band of interest, and the automatically background-corrected mean pixel intensity was measured. Mean pixel intensities of proteins of interest were normalised against either GAPDH protein intensities or a TPS to adjust values for the loaded protein amounts.

2.2.8.2 Quantitative Analysis of PI4P Distribution

within 3T3-L1 Adipocytes expressing HA-GLUT4-GFP

Following the acquisition, raw STEDYCON data were processed using Fiji image processing software (Schindelin et al., 2012). Experiments were performed three times ($n = 3$) for each condition, and for each biological replicate, analysis was applied to three cells (i.e., a total of nine cells per condition). No smoothing was applied to the data.

For each wavelength, 488 nm (GLUT4-GFP) and 647 nm (PI4P), the Plot Profile tool (Analyse > Plot Profile) was used to generate fluorescence intensity profiles across the cell width (x-axis). For each cell, the line selection tool was used with a linewidth set at 1 pixel and intensity plot regions of interest (ROI) was manually segmented by drawing a line from one side of the cell to the other, PM to PM passing through the nucleus when possible (**Figure 3.11**) so that the final line width equalled 40 μm . Our rationale for using this diameter was based on previous studies showing that larger adipocytes (greater than 10,000 μm^2) exhibit reduced

insulin-stimulated GLUT4 translocation to and dispersal within the PM. 3T3-L1 adipocytes typically show a range in diameter from 10 to 150 μm ; we therefore arbitrarily selected 40 μm for our study (Koester et al., 2022a; Wollman et al., 2022).

Plot profiles were displayed as 2D line graphs, with the x-axis representing the distance along the drawn line (from 0 to 40 μm) and the y-axis representing the vertically averaged pixel grey value. Datasets were extracted as CSV files from Fiji and subsequently processed in Excel. Fluorescent signal values were first expressed relative to the highest intensity values within each extracted plot and resampled to obtain a fixed number of 100 data points for each profile. The measured intensity values (y-axis) from each extracted profile were redistributed between a given range of measurement intervals (i.e., a redefined x-axis range controlled by an increment value). For each profile, the increment value was calculated as follows: final minus first-row number with y-axis value divided by 99. Mean fluorescence intensity profiles were then obtained by averaging y-axis resampled values for each condition ($n = 9$). That said, mean fluorescence intensity profiles were only used for data visualisation purposes (**Figure 3.11**). Further Kurtosis values were extracted from individual isolated intensity profiles using GraphPad Prism 10 software (Analyse > Descriptive Statistics).

Kurtosis is a descriptive statistic used to measure how data are dispersed between a distribution's centre and tails. By definition, Kurtosis quantifies whether the tails of the data distribution match those of a Gaussian distribution (Kurtosis = 3 a.u). The Kurtosis value that the GraphPad Prism 10 software reports for a Gaussian distribution is 0. This value (after

subtracting 3) is known as the excess Kurtosis. While a distribution with fewer values in the tails than a Gaussian distribution will yield a negative Kurtosis value, a distribution with more values in the tails or values further out in the tails than in a Gaussian distribution will have a positive Kurtosis (**Figure 2.4**). It is important to note that Kurtosis is always computed by applying a normal distribution onto the datasets it is given, ignoring any non-central additional peaks in its final fit. Therefore, in our case, the detection of fluorescent signal toward the PM, as well as at the centre of a cell, is expected to be fitted as a distribution with values further out in the tails rather than to have larger Gaussian-like tails, also yielding a positive Kurtosis value (**Figure 2.4**). Statistical analyses on all extracted Kurtosis values were also performed using GraphPad Prism 10 software (see section [2.2.8.5](#)).

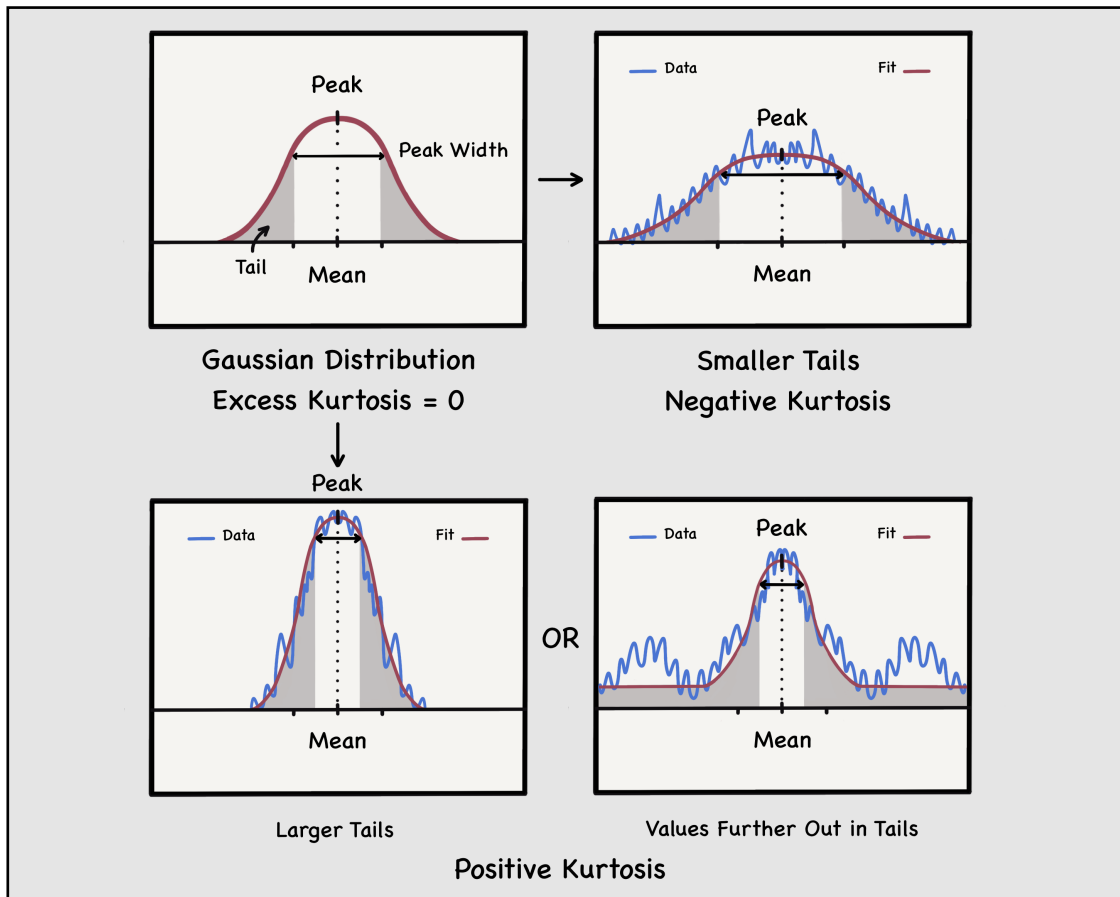


Figure 2.4. The Kurtosis Principal in Descriptive Statistics.

Kurtosis is a descriptive statistic used to measure how data are dispersed between a distribution's centre and tails. Kurtosis quantifies whether the tails of the data distribution match those of a Gaussian distribution (Excess Kurtosis = 0 a.u; Top Left). Therefore, when a distribution of data points has fewer values in the tails than a Gaussian distribution (smaller tails), the Kurtosis value of the dataset will be negative (Top Right). On the other hand, a distribution with either more values in the tails (larger tails; Bottom Left) or values further out in the tails (Bottom Right) than in a Gaussian distribution will have a positive Kurtosis. It is important to note that Kurtosis is always computed by applying a normal distribution onto the datasets it is given, ignoring any non-central additional peaks in its final fit. The presence of additional peaks will lead to a fitted distribution with values further out in the tails (Bottom Right). Blue, Experimental Data Distribution. Red, Kurtosis Fit.

2.2.8.3 DNA-PAINT Data Analysis

DNA-PAINT data were processed using the freely available Fiji plugin ThunderSTORM (Ovesný et al., 2014). Briefly, imaged filtering was performed using a pre-detection wavelet filter (B-spline), initial detection of blinking events was achieved using a local maximum finder, and sub-pixel localisation was extracted using an integrated form of a symmetric 2D Gaussian function. All parameters were set to default settings. The camera pixel size after optical magnification was 122 nm (see section [2.2.7.2.3](#)).

Extracted values were then plotted as histograms. The x-axis was divided into bins of 850 frames each, starting from frame one and ending at the last frame of the experiment. Each bin represents the number of blinking events recorded within its 850-frame interval. The y-axis shows the count of blinking events per bin.

2.2.8.4 Mesolens-Acquired Data Processing and Analysis

The analysis pipeline of image processing, visualisation and quantification of GLUT4-GFP fluorescent signals described below is summarised in **Figure 5.2**. Following acquisition, raw Mesolens data were processed using Fiji image processing software. The individual optical sectioned images were used for each specimen to reconstruct 3D heart structures. With a z-step size of 5 μm , the average imaging depth was 2.06 ± 0.33 mm (**Figure 5.1C**). No smoothing was applied to the data. 3D volumes were then displayed as 2D images by performing an average intensity axial projection (**Figure 5.2A**; Image > Stacks > Z Project > Average Intensity).

Heart no. 9 (see Appendix [7.5.2](#)) was excluded from the analysis process as anatomical structures were visibly damaged.

2.2.8.4.1 Analysis of Global Regional Fluorescence

The polygon selection tool was then used to manually segment each heart ROI, namely the LV, septum and RV. Each ROI was saved in the ROI Manager (Analyse > Tools > ROI Manager...), and the area, as well as fluorescent signals, was measured (**Figure 5.2B**). Fluorescent signals, also defined as mean grey values in Fiji, were calculated from the sum of the grey values of all pixels within the ROI divided by the area of the ROI. Extracted values were then processed using GraphPad Prism 10 (see section [2.2.8.5](#)).

2.2.8.4.2 Analysis of Transmural Fluorescence

Subsequently, the Plot Profile tool (Analyse > Plot Profile) was used to generate fluorescence intensity profiles across the width (x-axis) of the left ventricular, septal and right ventricular walls from average intensity axial projections of Mesolens-acquired 3D reconstructed ventricular volumes (**Figure 5.2C**). We refer to the fluorescence extracted from these profiles as transmural fluorescence. For each heart, the line selection tool was used with a linewidth set at 300 pixels and intensity plot ROI were manually segmented by drawing a line from the LV to the RV, crossing the septum and passing between LV papillary muscles. Our rationale for using this approach was to mirror one of the most common cross-sectional views of the heart (parasternal short axis) used for assessing cardiac wall parameters

and contractile function during in vivo ultrasound imaging (Benavides-Vallve et al., 2012; Franchi et al., 2013).

Plot profiles were displayed as 2D line graphs where the x-axis represented the distance along the drawn line and the y-axis was the vertically averaged pixel grey value. All intensity profiles are displayed as the LV, septum and RV, in this order, from left to right along the x-axis. Transmural fluorescence datasets were extracted as Fiji CSV files and processed in Excel. Individual left ventricular, septal and right ventricular transmural fluorescence profiles were isolated from each extracted fluorescence profile by cutting y-axis datasets at the minimum intensity data point between the LV and the septum and the septum and the RV. The widths of the septal and both ventricular walls (see Appendix [7.5.4](#)) were then extracted from obtained x-axis distances of isolated transmural fluorescence profiles.

Mean transmural fluorescence profiles (**Figures 5.5A and 5.6A**) were obtained by averaging the y-axis values of each condition for each heart region, aligning the first y-axis intensity data point of all curves with each other. Although misalignments inevitably remained toward the right-hand side of each mean profile due to individual differences in wall width among specimens, note that mean transmural fluorescence profiles, as displayed in **figures 5.5A and 5.6A**, were only used for data visualisation purposes and that all further analysis was performed using individual isolated transmural profiles. GLUT4-GFP fluorescence signals from individual transmural fluorescence profiles (**Figures 5.5B and 5.6B,C**; see Appendix [7.5.3](#)) were calculated from the area under the curve using GraphPad Prism 10 software. This analysis also provided information on the position of where GLUT4-GFP fluorescence peaked along the x-axis of each

transmural profile (**Figures 5.5C,D**; see Appendix [7.5.3](#)). The latter values, displayed as 'Peak X' in GraphPad Prism 10, were then normalised relative to total ventricular or septal wall width (see Appendix [7.5.4](#)) and labelled as 'lateral position of maximum fluorescence'. Statistical analyses on all extracted values were then performed using GraphPad Prism 10 software (see section [2.2.8.5](#)).

2.2.8.4.3 Analysis of Lumen Size

To isolate and quantify the surface area of the lumen within each heart, average-intensity axial-projected datasets were subjected to thresholding (**Figure 5.2D**). Images were first colour-inverted using the Invert LUT lookup table (Image > Lookup Tables > Invert LUT), and threshold segmentations were performed using the Default mode and Red display mode (Image > Adjust > Threshold). Threshold ranges were manually set within each inverted image so that the lumen edges were fully uncovered. The options 'Dark Background' and 'Don't Reset Range' were selected, and threshold was applied. Selection of the lumen as an ROI was obtained using the Analyze Particles tool (Analyze > Analyze Particles...) with the following settings: Size (μm^2) = 0-Infinty, Circularity = 0.00-1.00, Show = Masks. The lumen ROI was then selected amongst resulting isolated particles within the ROI Manager, and its area was measured. Extracted values were then processed using GraphPad Prism 10 (see section [2.2.8.5](#)).

2.2.8.4.4 Visualisation and Presentation

For visualisation and presentation purposes, axial-projected images were colour-coded by fluorescent intensity using Fiji's "fire" lookup table (**Figure 5.2E**).

2.2.8.5 Statistical Analysis

All statistical analyses were performed with GraphPad Prism 10 software. n values and statistical analysis are stated in figure legends. *, **, ***, ****, and ns represent $P \leq 0.05$, $P \leq 0.01$, $P \leq 0.001$, $P \leq 0.0001$, and not significant, respectively, throughout.

All analyses presented in section [5.3.1](#) were performed while unaware of the experimental conditions, and no statistics were used to determine sample size as we had no evidence base on which to project power calculations.

Chapter 3 - GLUT4 Dispersal at the Plasma Membrane:
Deciphering the Role of EFR3a and PI4K-IIIa in Adipocytes

3.1 Chapter 3 - Introduction

3.1.1 *EFR3 and PI4K-IIIa*

It is now well established that many molecular mechanisms that regulate membrane traffic are conserved through evolution, from single-cell organisms such as yeast to metazoans, and that many seminal findings in the GLUT4 field have initially been made using genetically tractable systems such as *Saccharomyces cerevisiae*, *Drosophila melanogaster* and *Caenorhabditis elegans*. When heterologously expressed in *S. cerevisiae*, human GLUT4 is sequestered intracellularly, as observed in adipose and muscle cells (Shewan et al., 2013). Such observations confirmed that the pathway followed by GLUT4 in insulin-sensitive cells is conserved through evolution from yeast to mammals, allowing the use of yeast as a model system to study GLUT4 trafficking and thus potentially identify key genes involved in aspects of GLUT4 biology.

In 2003, Wieczorke et al. used a strain of *S. cerevisiae* deficient in hexose transporters. In this temperature-sensitive strain, hexoses are depleted (Δ hxt) at a restrictive growth temperature of 30°C or above, preventing growth on media supplemented with hexoses as a carbon source. Interestingly, the expression of mammalian (rat and human) GLUT4 in this mutant did not rescue growth on glucose (Wieczorke et al., 2003). When heterogeneously expressed in Δ hxt *S. cerevisiae*, rat GLUT4 is retained

intracellularly and does not contribute to glucose uptake (Kasahara and Kasahara, 1997). However, Wiczorke et al. observed a clear redistribution of ectopically expressed human GLUT4 toward the PM in their Δ hxt yeast strain (Wiczorke et al., 2003), supporting the idea that the regulatory machinery of GLUT4 within the PM may play an essential role in glucose cellular uptake. A genetic screen to generate mutants of the Δ hxt strain that enable the expressed GLUT4 to support glucose uptake identified the recessive mutant *fgy1-1* allele (Schmidl et al., 2020; Wiczorke et al., 2003). This allele encodes a mutant version of Efr3.

Efr3 is a membrane protein essential for the assembly of Stt4-containing patches at the PM. Stt4 is the yeast ortholog of the human PI4K-III α , which catalyses the synthesis of PI4P, an essential signalling lipid at the PM (Baird et al., 2008; Nakatsu et al., 2012). EFR3 has two paralogs in mammals, EFR3a and EFR3b, which are evolutionarily conserved from mammals to yeast, sharing a 62% sequence identity. Both proteins contain an amino-terminal cysteine-rich region that encodes palmitoylation sites, allowing anchoring to the PM. Adjacent, armadillo repeats have been identified to permit protein-protein interactions. As of present, neither EFR3 isoforms have been shown to be expressed in a tissue-specific manner (Bojjireddy et al., 2015). As in yeast, mammalian EFR3 is responsible for the PM localisation of PI4K-III α , where it is known to generate PI4P (Chung et al., 2015; Koester et al., 2022b).

Phosphoinositides (PI) are one of the phospholipid families that build the lipid membrane bilayer of eukaryotic cells. The basic structure of PI, also known as phosphatidylinositol, consists of a six-carbon inositol ring attached by a phosphodiester bond to a diacylglycerol, which possesses

two FA tails that anchor PI into membrane structures. Phosphatidylinositols are the initial substrate of numerous kinases that phosphorylate hydroxyl groups along the inositol ring. Once phosphorylated, phosphatidylinositol comes to be referred to as PI. Phosphatidylinositols can be phosphorylated in seven combinations at the 3-, 4-, and 5-hydroxyl groups, generating mono- or poly-PI isomers that can directly alter numerous cellular processes (Di Paolo and De Camilli, 2006). This allows for diversity in the location of each PI across cellular membranes and their role and interaction with proteins that have specific functions in these respective membranes (Bairstow et al., 2004; Di Paolo and De Camilli, 2006). For instance, PI3K generates at the PM PIP_3 from PIP_2 , allowing the recruitment and activation of PDK1 and Akt at the PM (see section [1.3.2.1](#)) (Kohn et al., 1996). As for PI4P, it is one of the most abundant members of the PI family, which has been identified in numerous mammalian tissues and categorised into four distinct kinases, type II- α or - β and type III- α or - β , based on the enzymatic properties of the protein (Balla and Balla, 2006; Carpenter and Cantley, 1996; Pike, 1992).

As previously mentioned, the yeast ortholog of Stt4 is the PM-localised protein known as PI4K-III α , which generates PI4P at the PM of mammalian cells. PI4K-III α localises at the PM as part of an evolutionarily conserved complex composed of two main adaptor proteins, namely EFR3 and tetratricopeptide repeat domain 7 (TTC7; Ypp1 in yeast). Studies have suggested that EFR3 anchors PI4K-III α to the PM via TTC7 as a scaffold protein (Baird et al., 2008; Nakatsu et al., 2012). Additionally, the regulatory protein FAM126A has also been shown to play a key role within the latter PI4K-III α network, primarily stabilising TTC7 (Baskin et al., 2016). A further transmembrane protein, TMEM150A (Sfk1 in yeast), was identified to form

a complex with EFR3 and PI4K-III α , independently of TTC7, suggesting plasticity among the formed complexes. While it does not bypass the role of EFR3, TMEM150A was demonstrated to positively regulate PI4K-III α (Chung et al., 2015).

Consequently, present studies suggest that two separate PI4K-III α -containing complexes exist: one composed of PI4K-III α , EFR3, TTC7, and FAM126A, which is required for the initial targeting of PI4K-III α to the PM, with TTC7 interacting with both PI4K-III α and EFR3. A second complex comprised of PI4K-III α , EFR3, and TMEM150A is thought to favour PI4P formation at the PM (Chung et al., 2015). Finally, whether either EFR3 paralogues, EFR3a or EFR3b, participate in the formation of either complex specifically is yet to be determined.

3.1.2 *EFR3a Regulate GLUT4 Dispersal in Adipocyte:*

Evidence and Hypothesis

In recent studies, our group first tested the hypothesis that EFR3, more specifically EFR3a, and PI4K-III α played a key role in the insulin-stimulated regulation of GLUT4 at the PM of adipocytes. Koester et al. initially demonstrated that EFR3a exhibited significantly higher expression in 3T3-L1 adipocytes, with mRNA levels over 500-fold greater than EFR3b. As a result, they directed their focus toward EFR3a (Koester et al., 2022b).

Using siRNA to reduce (KD) the expression of EFR3a or PI4K-III α , evidence showed decreased insulin-stimulated glucose transport into 3T3-L1 adipocytes. Additionally, the localisation of both proteins at the PM was

found to increase under insulin stimulation. Based on these findings, it was suggested that EFR3a and PI4K-III α may have a regulatory effect on GLUT4 at the PM. Using 3T3-L1 adipocytes expressing HA-GLUT4-GFP and adopting a dSTORM approach, Koester et al. tested the hypothesis that EFR3a KD impairs GLUT4 dispersal within the PM (see section [1.4.3](#)). Results showed that siRNA-mediated KD of EFR3a significantly inhibited insulin's ability to promote GLUT4 dispersal, suggesting that EFR3a is required for the transition of GLUT4 from clustered to dispersed monomers in the PM (Koester et al., 2022b). In addition, genetic analyses have linked EFR3 to T2D and body mass index. This indicates that this newly identified signalling nexus may also play an essential role in human disease (Bradfield et al., 2011; Pulit et al., 2019). Such findings, along with evidence of insulin resistance negatively impacting GLUT4 dispersal (see section [1.4.3.1](#)), hint that a better understanding of the mechanisms described above, in both health and disease, could help further develop treatment options for diabetes.

Based on these data, we hypothesised that, localised at the PM, EFR3a recruits and activates PI4K-III α under insulin stimulation, leading to the phosphorylation of PI, which in turn loses the ability to 'coral' GLUT4 clusters (**Figure 3.1**). This chapter describes experiments which aim to test this hypothesis.

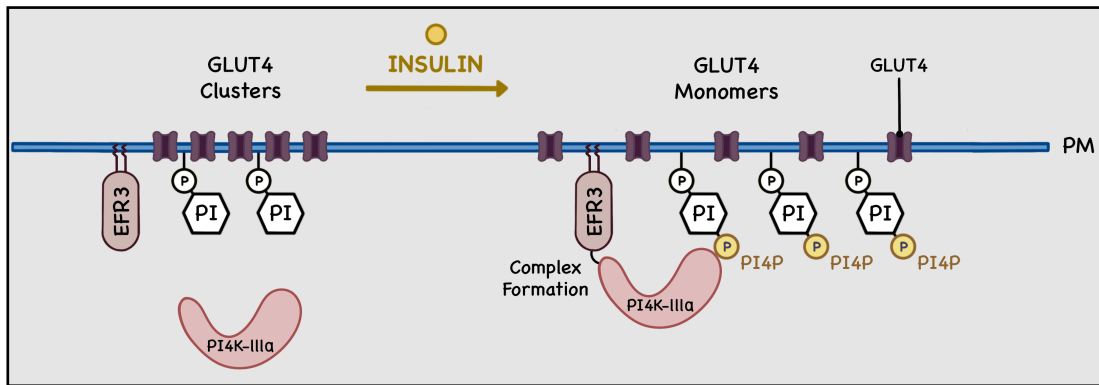


Figure 3.1. Hypothetical Model of EFR3a/PI4K-IIIa-Regulated GLUT4 Dispersal within the Plasma Membrane of Adipocytes.

Insulin stimulates GLUT4 dispersal within the plasma membrane (PM) in an EFR3a/PI4K-IIIa-dependent manner. In the basal state, both the membrane protein, EFR3a, and phosphatidylinositol 4-kinase type IIIa (PI4K-IIIa) are inactive, and PM-fused GLUT4 molecules (shown as purple structures) are immobilised in clusters. Under insulin stimulation, EFR3a recruits and forms a complex with PI4K-IIIa at the PM, leading to the phosphorylation of phosphoinositides (PI) into phosphatidylinositol 4-phosphate (PI4P). PI lose the ability to 'corral' GLUT4 clusters, releasing GLUT4 transporters into the PM as monomers and allowing their dispersal.

3.1.3 Chapter 3 - Aims

This chapter aims to further characterise how EFR3a and PI4K-IIIa relate to GLUT4 insulin-stimulated trafficking to and dispersal within the PM of adipocytes.

Using 3T3-L1 adipocytes, our specific aims are:

- (i) to KD the expression of either EFR3a, PI4K-IIIa, or both proteins using siRNA and test the hypothesis that these proteins are coordinately regulated.

- (ii) to ascertain whether the depletion of either or both of these proteins impacted adipogenesis or insulin signalling in KD cells.

- (iii) to use pharmacological inhibition as a second route to test the role of PI4K-III α in insulin-stimulated glucose uptake.

- (iv) to use sub-cellular and lipid raft fractionation methods to identify the major sites of expression of both EFR3a and PI4K-III α and understand how KD of either or both proteins relates to the distribution of GLUT4 upon insulin stimulation.

- (v) to examine whether insulin regulates levels of PI4P at the PM.

- (vi) to use CRISPR-Cas9 technology to generate EFR3a KO 3T3-L1 cell lines as a more permanent alternative to siRNA-mediated gene KD.

3.2 Chapter 3 - List of Methods

The methods below have been used in this chapter and are further detailed in section 2.2.

2.2.1 Cell Culture

2.2.1.1 3T3-L1 Fibroblasts Growth and Maintenance

2.2.1.2 3T3-L1 Adipocyte Differentiation

2.2.1.3 Insulin Stimulation of 3T3-L1 Adipocytes

2.2.1.4 Insulin Stimulation, PI4K-III α Pharmacological Inhibition, and Glucose Uptake Assay in 3T3-L1 Adipocytes

2.2.1.5 siRNA-Mediated Gene Knockdown in 3T3-L1 Adipocytes

2.2.1.6 CRISPR/Cas9-Mediated Gene Knockout in 3T3-L1 Fibroblasts

2.2.1.6.1 CRISPR/Cas9 System Delivery using Ribonucleoprotein

2.2.1.6.2 CRISPR/Cas9 System Delivery using Plasmid DNA

2.2.1.6.3 Puromycin Selection

2.2.1.6.4 Single-Cell Expansion by Dilution Plating

2.2.3 Cell Lysates and Tissue Homogenates

2.2.3.3 3T3-L1 and HEK295 Whole Cells Lysate

2.2.4 Cellular Methods

2.2.4.1 Sub-Cellular Fractionation of 3T3-L1 Adipocytes and HEK295 Cells

2.2.4.2 Lipid Raft Fractionation of 3T3-L1 Adipocytes

2.2.5 Protein-Specific Assays

2.2.5.1 Bicinchoninic Acid Assay and Sample Preparation for Immunoblotting

2.2.5.2 SDS-PAGE

2.2.5.3 Wet Transfer

2.2.5.4 Dot Blot Sample Preparation

2.2.5.5 Immunoblotting

2.2.6 Molecular Methods

2.2.6.1 Polymerase Chain Reaction (PCR)

2.2.6.2 Agarose Gel Electrophoresis

2.2.6.3 Surveyor® Nuclease Assay for Gene Modification

2.2.7 Microscopy

2.2.7.1 Sample Preparation

2.2.7.1.1 Cellular Fixation, Immunofluorescent,
and Permanent DNA-PAINT Staining

2.2.7.2 Imaging Setups and Data Acquisition

2.2.7.2.1 STEDYCON (STED and Confocal) Microscope

2.2.7.2.4 Confocal Microscope

2.2.8 Data and Statistical Analyses

2.2.8.1 Densitometry

2.2.8.2 Quantitative Analysis of PI4P Distribution
within 3T3-L1 Adipocytes expressing HA-GLUT4-GFP

2.2.8.5 Statistical Analysis

3.3 Chapter 3 - Results

3.3.1 Targeting the EFR3a/PI4K-III α Machinery in 3T3-L1 Adipocytes

3.3.1.1 siRNA-Mediated Gene Knockdown of Efr3a or Pi4ka in 3T3-L1 Adipocytes

Previous studies using siRNA to KD the expression of either EFR3a or PI4K-III α showed that both proteins are required for insulin-stimulated glucose transport into 3T3-L1 adipocytes and that KD of *Efr3a* impairs insulin-stimulated GLUT4 dispersal at the PM (Koester et al., 2022b). Our first goal was, therefore, to better characterise the impact of siRNA-mediated *Efr3a*, *Pi4ka* (i.e., the gene encoding for PI4K-III α), or *Efr3a* and *Pi4ka* (double) KD in these cells. We aimed to confirm the effectiveness of this technique by showing that knocking down *Efr3a* and/or *Pi4ka* does not affect 3T3-L1 adipogenesis and capacity to respond to insulin, as well as to ascertain whether these proteins are coordinately regulated.

Efr3a and/or *Pi4ka* were knocked down in 3T3-L1 adipocytes six days post-differentiation using siRNA (see section [2.2.1.5](#)). Western blot analysis confirmed the depletion of EFR3a and PI4K-III α by 73.4% ($p < 0.0001$; **Figure 3.2A,B**) and 63.0% ($p = 0.0004$; **Figure 3.3A,B**), respectively, in cells transfected with either *Efr3a*- or *Pi4ka*-targeting siRNA compared to cells treated with negative control non-targeting siRNA. In these cells, KD of *Efr3a* and *Pi4ka* did not affect the protein content of either studied counterparts (i.e., PI4K-III α and EFR3a, respectively; **Figure 3.2-3A,C**). Conversely, data obtained from double KD cells revealed reduced EFR3a

and PI4K-III α levels (EFR3a: 76.1% - $p < 0.0001$, PI4K-III α : 81.0% - $p < 0.0001$; **Figure 3.4A,B**).

Subsequently, to determine whether adipogenesis was affected by siRNA-mediated KD of *Efr3a* and/or *Pi4ka*, the protein content of the lipogenic proteins ACC and fatty acid synthase (FAS) was assessed and found to be at comparable levels in both KD and control cells (**Figure 3.2-4A,D,E**).

Similarly, to rule out any effects on the ability of insulin to stimulate signalling processes, we assayed the phosphorylation of Akt, a known downstream effector of insulin stimulation. Akt S473 phosphorylation upon insulin stimulation confirmed the cells' ability to retain insulin sensitivity in all three KD conditions (**Figure 3.2-4A**). Finally, no significant changes in GLUT4 levels were observed upon KD of *Efr3a* and/or *Pi4ka* (**Figure 3.2-4A,F**), indicating that the differentiation process was unaffected.

Overall, these data suggest that EFR3a and PI4K-III α are not required for adipogenesis in this model and suggest that any effects that might be observed in the future regarding GLUT4 trafficking and dispersal within the PM in *Efr3a* and/or *Pi4ka* KD 3T3-L1 adipocytes are unlikely to be a consequence of either de-differentiation of the cells or a loss of insulin signalling.

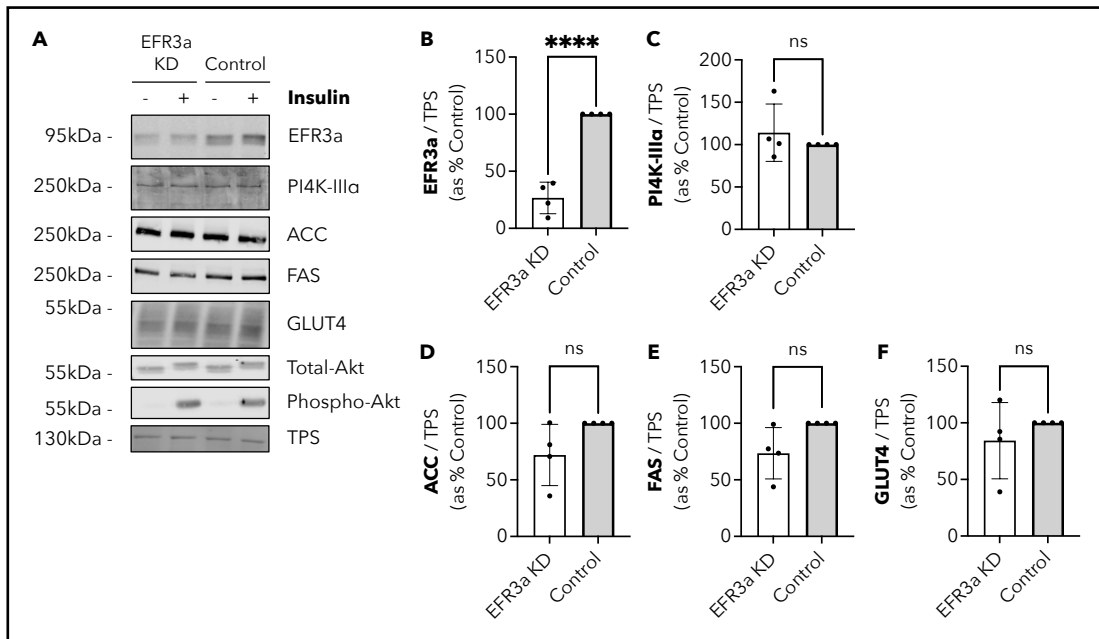


Figure 3.2. *Efr3a* Knockdown and its Effect on Adipogenesis and Insulin Action in Differentiated 3T3-L1 Adipocytes.

(A) Immunoblot showing levels of EFR3a, phosphatidylinositol 4-kinase type III α (PI4K-III α), acetyl-CoA carboxylase (ACC), fatty acid synthase (FAS), GLUT4, total-Akt, and phosphorylated (S473) Akt in 3T3-L1 adipocytes transfected with siRNA designed to knockdown the expression of EFR3a (EFR3a KD) or negative control non-targeting siRNA (Control), six days post-differentiation, and treated with or without 100 nM insulin for 20 min. Total protein stain (TPS) was used as a loading control. All cell lysates were produced and loaded as described in [2.2.3.3](#) and [2.2.5.2](#). Blots were visualised with a LI-COR Odyssey-SA system; data from a representative experiment are shown (n = 4). (B) Mean \pm s.d. of the protein content of EFR3a under basal conditions in EFR3a KD and Control 3T3-L1 adipocytes (expressed relative to TPS and compared to % Control; n = 4). Data indicate a decrease in EFR3a levels of 73.4% upon *Efr3a* siRNA-mediated KD. Similar results were obtained in insulin-stimulated cells (panel A; quantification not shown). (C-F) Mean \pm s.d. of the protein content of PI4K-III α (C), ACC (D), FAS (E), and GLUT4 (F) under basal condition (expressed relative to TPS and compared to % Control; n = 4). Data indicate no statistically significant decrease in protein levels upon *Efr3a* siRNA-mediated KD. Similar data were obtained in insulin-stimulated cells (panel A; quantification not shown). For normalisation, TPS bands were obtained from the same membrane. **** represent $p \leq 0.0001$, and ns signify non-significant. Two-tailed unpaired t-tests were performed on all raw data.

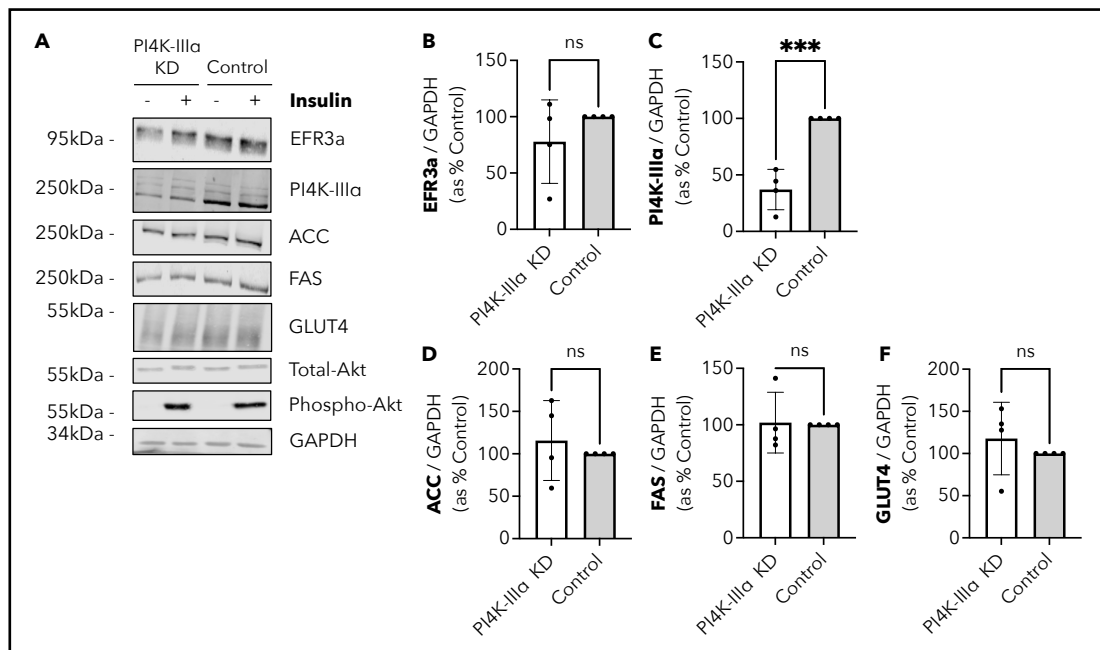


Figure 3.3. *Pi4ka* Knockdown and its Effect on Adipogenesis and Insulin Action in Differentiated 3T3-L1 Adipocytes.

(A) Immunoblot showing levels of EFR3a, PI4K-IIIa, ACC, FAS, GLUT4, total-Akt, and phosphorylated (S473) Akt in 3T3-L1 adipocytes transfected with siRNA designed to knockdown the expression of PI4K-IIIa (PI4K-IIIa KD) or negative control non-targeting siRNA (Control), performed as described in **figure 3.2**. GAPDH was used as a loading control. All cell lysates were produced and loaded as described in 2.2.3.3 and 2.2.5.2. Blots were visualised with a LI-COR Odyssey-SA system; data from a representative experiment is shown ($n = 4$). (B,D-F) Mean \pm s.d. of the protein content of EFR3a (B), ACC (D), FAS (E), and GLUT4 (F) under basal conditions in PI4K-IIIa KD and Control 3T3-L1 adipocytes (expressed relative to GAPDH and compared to % Control; $n = 4$). Data indicate no statistically significant decrease in protein levels upon *Pi4ka* siRNA-mediated KD. Similar data were obtained in insulin-stimulated cells (panel A; quantification not shown). (C) Mean \pm s.d. of the protein content of PI4K-IIIa under basal condition (expressed relative to GAPDH and compared to % Control; $n = 4$). Data indicate a decrease in PI4K-IIIa levels of 63.0% upon *Pi4ka* siRNA-mediated KD. Similar results were obtained in insulin-stimulated cells (panel A; quantification not shown). For normalisation, GAPDH signals were obtained from the same membrane. *** represent $p \leq 0.001$, and ns signify non-significant. Two-tailed unpaired t-tests were performed on all raw data.

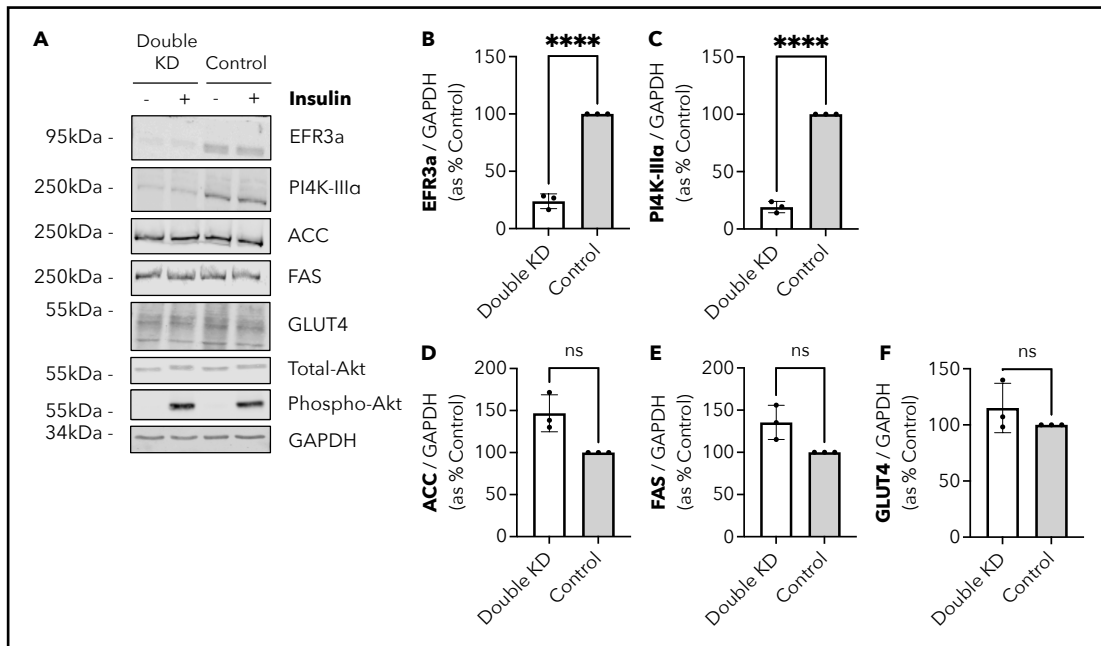


Figure 3.4. *Efr3a* and *Pi4ka* Double Knockdown and its Effect on Adipogenesis and Insulin Action in Differentiated 3T3-L1 Adipocytes.

(A) Immunoblot showing levels of EFR3a, PI4K-III α , ACC, FAS, GLUT4, total-Akt, and phosphorylated (S473) Akt in 3T3-L1 adipocytes transfected with siRNAs designed to knockdown the expression of EFR3a and PI4K-III α (Double KD) or negative control non-targeting siRNA (Control), performed as described in **figure 3.2**. GAPDH was used as a loading control. All cell lysates were produced and loaded as described in 2.2.3.3 and 2.2.5.2. Blots were visualised with a LI-COR Odyssey-SA system; data from a representative experiment is shown (n = 3). (B,C) Mean \pm s.d. of the protein content of EFR3a (B) and PI4K-III α (C) under basal conditions in Double KD and Control 3T3-L1 adipocytes (expressed relative to GAPDH and compared to % Control; n = 3). Data indicate a decrease in EFR3a and PI4K-III α levels of 76.1% and 81.0%, respectively, upon siRNA-mediated KD of both *Efr3a* and *Pi4ka*. Similar results were obtained in insulin-stimulated cells (panel A; quantification not shown). (D-F) Mean \pm s.d. of the protein content of ACC (D), FAS (E), and GLUT4 (F) under basal condition (expressed relative to GAPDH and compared to % Control; n = 3). Data indicate no statistically significant decrease in protein levels upon siRNA-mediated KD of both *Efr3a* and *Pi4ka*. Similar data were obtained in insulin-stimulated cells (panel A; quantification not shown). For normalisation, GAPDH signals were obtained from the same membrane. **** represent $p \leq 0.0001$, and ns signify non-significant. Two-tailed unpaired t-tests were performed on all raw data.

3.3.1.2 Pharmacological Inhibition of PI4K-III α in 3T3-L1 Adipocytes

Previous studies showed that KD of *Pi4ka* in 3T3-L1 adipocytes reduced insulin-stimulated glucose uptake (Koester et al., 2022b). Here, we used a pharmacological approach to target PI4K-III α as a further means to validate this conclusion.

Treatment with the selective PI4K-III α inhibitor C7 (Waring et al., 2014) impairs insulin-stimulated glucose uptake in 3T3-L1 adipocytes (see section [2.2.1.4](#)). In untreated cells, glucose uptake analysis found that insulin increases 2DG transport into 3T3-L1 adipocytes by 4.5-fold when compared to non-insulin-stimulated (basal) cells ($p = 0.0043$; **Figure 3.5A**). Treatment of 3T3-L1 adipocytes with 200 nM C7 reduced insulin-stimulated 2DG uptake by 41.8%, leading to a reduced, non-significant, increase in 2DG uptake under insulin stimulation of 2.6-fold compared to basal cells ($p = 0.0613$; **Figure 3.5B**).

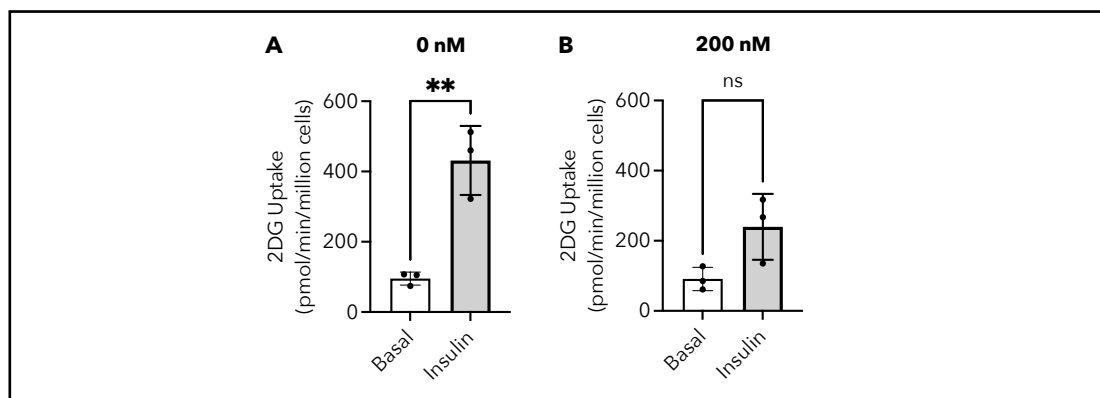


Figure 3.5. Inhibition of PI4K-III α impairs insulin-stimulated 2-deoxy-D-glucose uptake in 3T3-L1 adipocytes.

Mean \pm s.d. of 2-deoxy-D-glucose (2DG) uptake (pmol/min/million cells) in 3T3-L1 adipocytes treated with or without 100 nM insulin for 15 min and subjected to 0 nM (vehicle control; A) or 200 nM (B) of PI4K-III α inhibitor C7 (Waring et al., 2014) (n = 3, per each condition, each biological replicate is the average of 3 technical replicates). While untreated cells showed a significant increase in 2DG uptake under insulin stimulation of 4.5-fold (relative to Basal), inhibition of PI4K-III α impaired insulin-stimulated 2DG uptake by 41.8% (relative to Basal). All glucose uptake assays in this section were kindly performed by Prof. Gwyn W. Gould as described in [2.2.1.4](#). ** represent $p \leq 0.01$, and ns signify non-significant. Two-tailed unpaired t-tests were performed on all raw data.

3.3.2 Characterisation of the EFR3a/PI4K-III α Machinery in 3T3-L1 Adipocytes

3.3.2.1 EFR3a and PI4K-III α Localisation at the Plasma Membrane is Increased in Insulin-Stimulated 3T3-L1 Adipocytes

Using sub-cellular fractionation techniques (see section [2.2.4.1](#)), the PM, LDM, HDM, and SP were isolated from WT 3T3-L1 adipocytes, as well as from siRNA-mediated *Efr3a*, *Pi4ka*, and Double (*Efr3a* and *Pi4ka*) KD cells. HDM contains the endoplasmic reticulum and other dense membrane fractions, and the LDM is enriched in GSC, early endosomal, and TGN markers. Finally, isolated PM fractions are enriched in PM proteins, including Syntaxin4, which is used in this section as a PM marker (Bryant et al., 2002).

EFR3a and PI4K-III α are found in all membrane-enriched fractions and, therefore, not specific to the PM (**Figures 3.6A and 3.7A**). Consistent with

previous findings (Koester et al., 2022b), quantification of immunoblot signals in WT cells showed that EFR3a (0.6-fold, $p = 0.0100$; **Figure 3.6A,B**) and PI4K-III α (1.7-fold, $p = 0.0087$; **Figure 3.7A,C**) levels significantly increase at the PM under insulin stimulation along with GLUT4 (0.6-fold, $p = 0.0009$; **Figure 3.8A,B**). It is worth noting that this crude fractionation method consistently underestimates the extent of translocation (Bryant et al., 2002). It is tempting to argue that, as for GLUT4, these increases in EFR3a and PI4K-III α at the PM might be explained by a relocation of the latter proteins from intracellular compartments to the PM upon insulin stimulation. However, while GLUT4 levels decreased by 36.7% in LDM ($p < 0.0001$; **Figure 3.8B**), no significant changes were observed in neither EFR3a (**Figure 3.6B**) nor PI4K-III α (**Figure 3.7C**) levels in LDM of WT 3T3-L1 adipocytes, suggesting that the latter proteins do not traffic to the PM along with GLUT4-containing intracellular vesicles.

Therefore, we examined whether these proteins' levels within SP fractions were impacted. While as membrane-associated proteins, both EFR3a and GLUT4 were not detected in SP fractions (data not shown), PI4K-III α levels increased by 182.3% ($p = 0.0013$; **Figure 3.7B,D**) in EFR3a KD adipocytes, consistent with the role of EFR3a in anchoring PI4K-III α at the PM (see section [3.1.1](#)). EFR3a KD cells would be expected to possess reduced recruitment of PI4K-III α to the PM under insulin stimulation, as observed in **Figure 3.7D**, subsequently leading to an increased accumulation of unbound PI4K-III α in SP fractions. These data suggest that PI4K-III α traffics to the PM from SP fractions in response to insulin. This is further supported by the 24.6% decrease in PI4K-III α levels in SP fractions of insulin-stimulated PI4K-III α KD cells ($p = 0.0120$; **Figure 3.7B,E**), as well as by the negation of both EFR3a- and PI4K-III α KD-induced effect in Double KD

adipocytes (**Figure 3.7B,F**). Interestingly, the reduction of PI4K-III α expression in PI4K-III α KD cells also inhibited the increased presence of its studied counterparts (i.e., EFR3a) at the PM under insulin stimulation (**Figures 3.6D**), suggesting the potential existence of a feedback loop between both proteins.

The quantification of PM-fused GLUT4 in WT and EFR3a KD cells from dSTORM datasets (Koester et al., 2022b) has previously suggested that EFR3a is not involved in the translocation of GLUT4 to the PM and only has an impact on GLUT4 dispersal within the PM. However, the methodology used in that study was an indirect approach. Hence, we also chose to analyse GLUT4 levels in the fractions obtained from the present KD studies to test the hypothesis that EFR3 and/or PI4K-III α modulates GLUT4 presence at the PM in response to insulin. The data show a significant reduction in insulin-stimulated GLUT4 levels at the PM of EFR3a KD cells compared to WT adipocytes ($p = 0.0342$; **Figure 3.8F**). While this change in signal does not appear to be seen between WT and either PI4K-III α KD or Double KD cells, it highlights the need for additional studies about the role of the EFR3a/PI4K-III α machinery in GLUT4 translocation to the PM.

Nevertheless, this sub-cellular analysis further confirmed the PM localisation of EFR3a and PI4K-III α in 3T3-L1 adipocytes under insulin-stimulated conditions and strengthened the hypothesis that the latter proteins are involved in regulating GLUT4 at the PM.

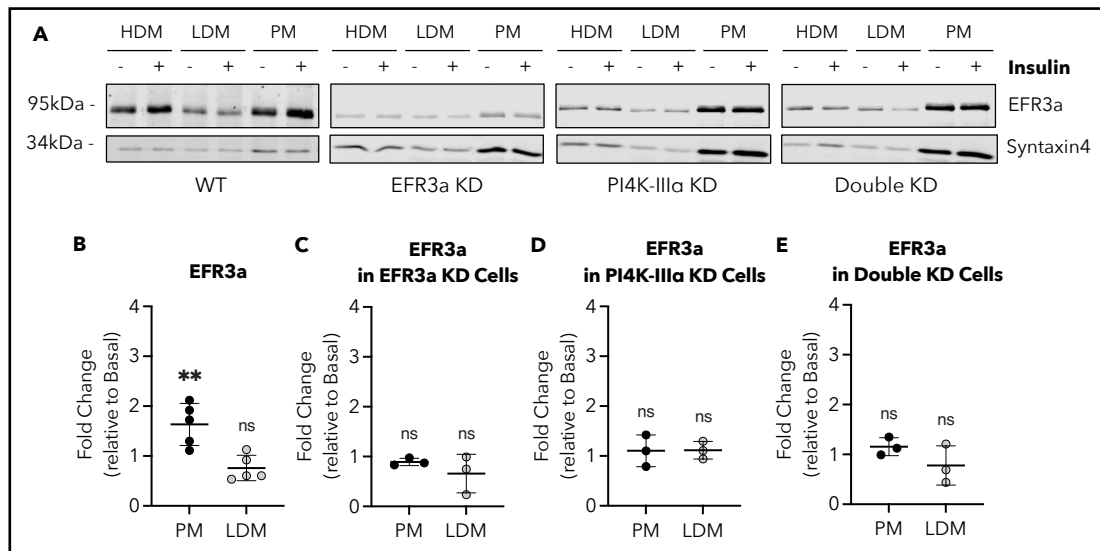


Figure 3.6. EFR3a Localisation in Insulin-Stimulated WT, EFR3a KD, PI4K-III α KD, and EFR3a KD and PI4K-III α KD 3T3-L1 Adipocytes.

(A) Immunoblot showing levels of EFR3a in PM-enriched, low-density microsomes (LDM), and high-density microsomes (HDM) fractions of wild-type (WT) 3T3-L1 adipocytes, as well as adipocytes transfected with siRNAs designed to knockdown the expression of EFR3a (EFR3a KD), PI4K-III α (PI4K-III α KD), and EFR3a and PI4K-III α (Double KD), six days post-differentiation, and treated with or without 100 nM insulin for 20 min. Syntaxin4 was used as a PM protein marker (Bryant et al., 2002). Sub-cellular fractions were produced and loaded as described in 2.2.4.1 and 2.2.5.2. Blots were visualised with a LI-COR Odyssey-SA system; data from a representative experiment are shown (WT, n = 5; KDs, n = 3). (B-E) Mean \pm s.d. fold-changes of EFR3a protein content in PM and LDM fractions of WT (B; n = 5), EFR3a KD (C; n = 3), PI4K-III α KD (D; n = 3), and Double KD (E; n = 3) 3T3-L1 adipocytes under insulin stimulation (values expressed relative to Basal). Data indicate an increase in PM EFR3a levels in WT cells under insulin stimulation, consistent with previous findings (Koester et al., 2022b). This was abrogated in EFR3a KD, PI4K-III α KD, and Double KD 3T3-L1 adipocytes. ** represent $p \leq 0.01$, and ns signify non-significant. Two-tailed unpaired t-tests were performed on all raw data.

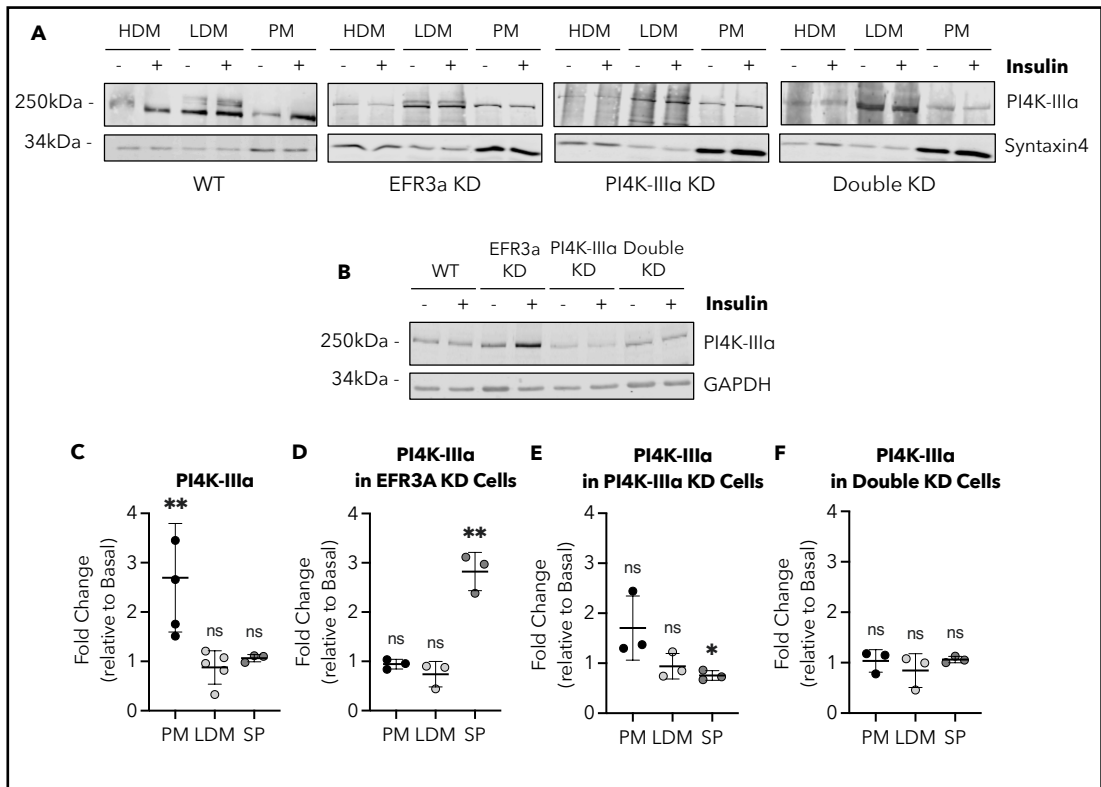


Figure 3.7. PI4K-III α Localisation in Insulin-Stimulated WT, EFR3a KD, PI4K-III α KD, and EFR3a KD and PI4K-III α KD 3T3-L1 Adipocytes.

(A) Immunoblot showing levels of PI4K-III α in PM-enriched, LDM, and HDM fractions of WT and KD 3T3-L1 adipocytes, as outlined in **figure 3.6**. (B) Immunoblot showing protein contents of PI4K-III α in soluble protein (SP)-enriched fractions of WT, EFR3a KD, PI4K-III α KD, and Double KD 3T3-L1 adipocytes treated with or without 100 nM insulin for 20 min. GAPDH was used as a loading control. All sub-cellular fractions were produced and loaded as described in [2.2.4.1](#) and [2.2.5.2](#). Blots were visualised with a LI-COR Odyssey-SA system; data from a representative experiment are shown (WT, n = 5; KDs, n = 3). (C-F) Mean \pm s.d. fold-changes of PI4K-III α protein content in PM, LDM, and SP fractions of WT (B; n = 5), EFR3a KD (C; n = 3), PI4K-III α KD (D; n = 3), and Double KD (E; n = 3) 3T3-L1 adipocytes under insulin stimulation (values expressed relative to Basal). In WT cells, data indicate increased PM PI4K-III α levels under insulin stimulation and non-significant changes in LDM and SP fractions. In EFR3a KD cells, data indicate non-significant changes in LDM and SP fractions and an increase in SP PI4K-III α levels under insulin stimulation. In PI4K-III α KD cells, data indicate non-significant changes in LDM and SP fractions and an increase in SP PI4K-III α levels under insulin stimulation. Finally, in Double KD cells, data indicate non-significant changes in PI4K-III α levels under insulin stimulation in all three studied fractions. *, ** represent $p \leq 0.05$, $p \leq 0.01$ and ns signify non-significant. Two-tailed unpaired t-tests were performed on all raw data.

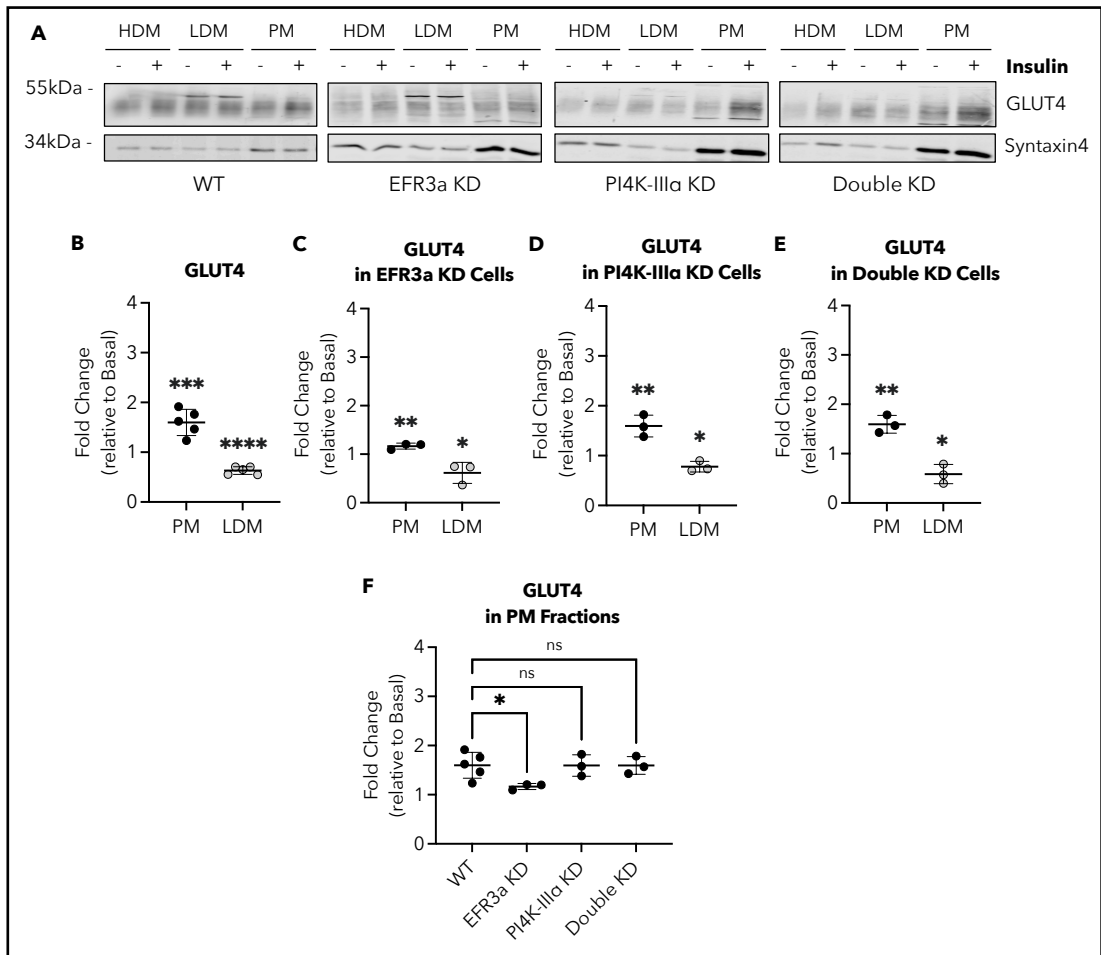


Figure 3.8. GLUT4 Localisation in Insulin-Stimulated WT, EFR3a KD, PI4K-III α KD, and EFR3a KD and PI4K-III α KD 3T3-L1 Adipocytes.

(A) Immunoblot showing levels of GLUT4 in PM-enriched, LDM, and HDM fractions of WT and KD 3T3-L1 adipocytes, as outlined in **figure 3.6**. Sub-cellular fractions were produced and loaded as described in [2.2.4.1](#) and [2.2.5.2](#). Blots were visualised with a LI-COR Odyssey-SA system; data from a representative experiment are shown (WT, n = 5; KDs, n = 3). (B-E) Mean \pm s.d. fold-changes of GLUT4 protein content in PM and LDM fractions of WT (B; n = 5), EFR3a KD (C; n = 3), PI4K-III α KD (D; n = 3), and Double KD (E; n = 3) 3T3-L1 adipocytes under insulin stimulation (values expressed relative to Basal). (F) Mean \pm s.d. fold-changes of GLUT4 protein content in PM fractions of WT (B; n = 5), EFR3a KD (C; n = 3), PI4K-III α KD (D; n = 3), and Double KD (E; n = 3) 3T3-L1 adipocytes under insulin stimulation (values expressed relative to Basal). Data indicate a significant decrease in insulin-stimulated GLUT4 protein content at the PM of EFR3a KD cells compared to WT adipocytes. In contrast, no significant change in signal is observed between WT and either PI4K-III α KD or Double KD cells. *, **, ***, **** represent $p \leq 0.05$, $p \leq 0.01$, $p \leq 0.001$, $p \leq 0.0001$, and ns signify non-significant. Two-tailed unpaired t-tests were performed on all raw data.

3.3.2.2 EFR3a Localisation in Lipid Raft in 3T3-L1 Adipocytes

Recent studies have suggested that EFR3a is localised in lipid rafts (Trybus et al., 2023). Additionally, Yan et al. have suggested that GLUT1 cluster formation at the cell surface of HeLa cells might partially be regulated by lipid rafts (Yan et al., 2018). To investigate the presence and distribution of GLUT4, EFR3a, and PI4K-III α within lipid rafts of 3T3-L1 adipocytes, lipid raft fractions were isolated as described in section [2.2.4.2](#). Rafts were identified by the presence of caveolin-1, which accumulates at the 5% and 30% sucrose interface (Chamberlain and Gould, 2002); solubilised proteins remained in the 80% sucrose layer.

Figure 3.9A,B show that GLUT4 molecules are primarily detected as solubilised proteins in the 80% sucrose layer under basal conditions with $27.6 \pm 12.5\%$ ($n = 3$) of total isolated GLUT4 in the raft fractions. In contrast, a significantly higher ($p = 0.0151$) caveolin-1 protein content was observed in lipid rafts ($83.1 \pm 5.6\%$; $n = 3$), consistent with previous studies (Chamberlain and Gould, 2002). No change in GLUT4 lipid raft content was observed under insulin stimulation (**Figure 3.9C**). Similar data were observed for PI4K-III α (**Figure 3.9**), with a significantly lower ($p = 0.0224$) protein content under basal conditions in raft fractions compared to caveolin-1 and no change in the presence of insulin. Differently to GLUT4 and PI4K-III α ($p = 0.0247$ and $p = 0.0173$, respectively), immunoblotting results indicate that EFR3a is significantly enriched in lipid raft fractions under basal conditions ($81.3 \pm 11.8\%$; $n = 3$) (**Figure 3.9A,B**) However, EFR3a's association with rafts was observed to decrease in response to insulin, indicating its movement out of lipid rafts ($p = 0.0105$; **Figure 3.9C**).

These results, therefore, suggest that while GLUT4 and PI4K-III α do not appear to significantly localise in lipid raft fractions, the localisation of EFR3a within these PM microdomains and its exclusion from these rafts under insulin stimulation imply that lipid rafts may indirectly play a role in the spatial organisation of GLUT4 at the PM of adipocytes. Under basal conditions, lipid rafts appear to act as storage compartments for EFR3a at the PM. Insulin stimulation then triggers its dispersal and the recruitment of PI4K-III α across the PM, leading to the phosphorylation of PI into PI4P and the subsequent release of GLUT4 into the PM (see sections [3.1.2](#) and [3.3.2.1](#)).

It is also worth noting that while the present data (**Figure 3.9**) did not show a significant presence of GLUT4 in PM raft fractions, Chamberlain and Gouls have reported its presence in lipid rafts and exclusion under insulin stimulation (Chamberlain and Gould, 2002). Whether these results are the consequence of the total increase of GLUT4 at the PM under insulin stimulation or a specific increase in raft GLUT4 is yet to be determined. Finally, the large variation in PI4K-III α results between PM fractions (**Figure 3.9C**) may account for the absence of significant findings. These observations underscore the complexity of the molecular interactions involved here and the need for further studies to clarify these mechanisms.

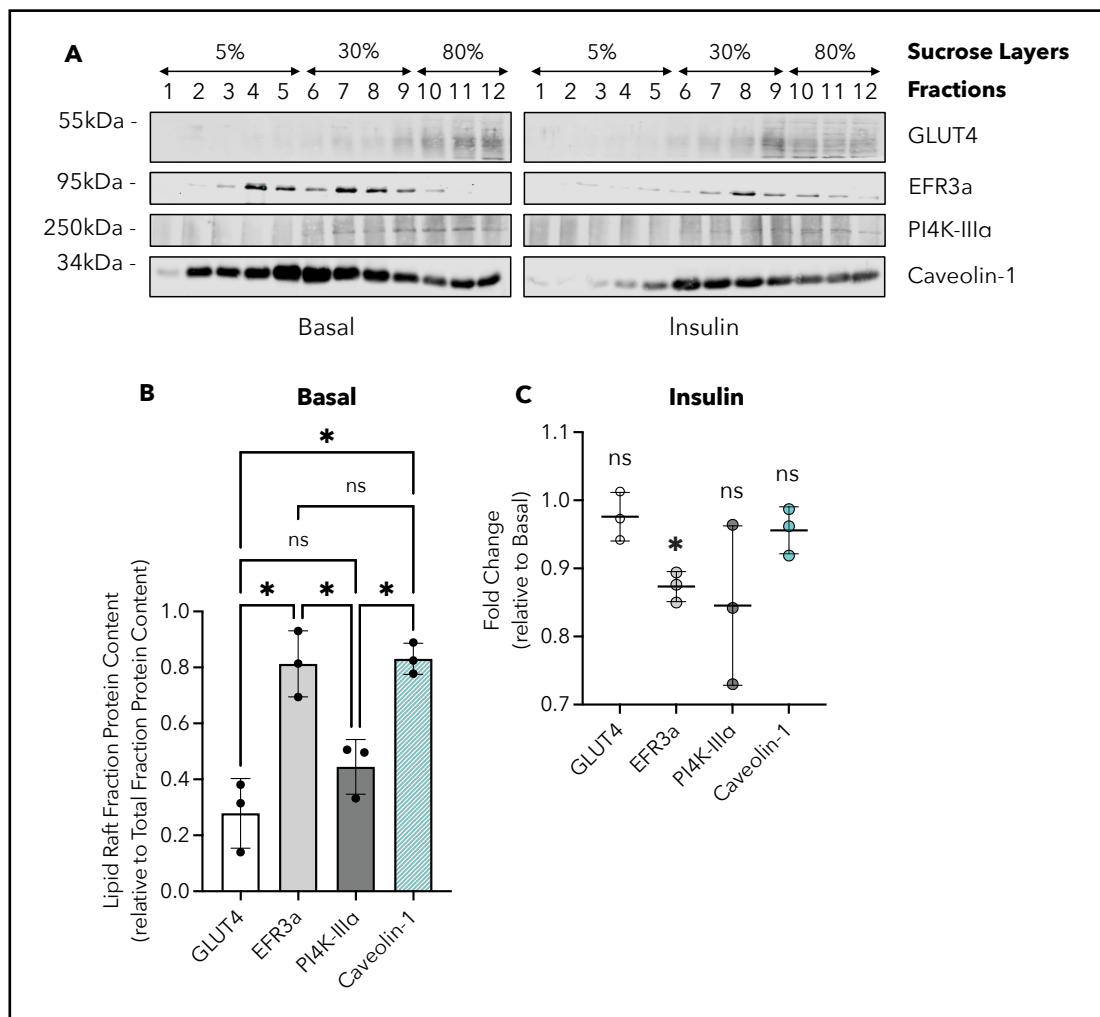


Figure 3.9. GLUT4, EFR3a, and PI4K-III α Lipid Raft Association in Insulin-Stimulated WT 3T3-L1 Adipocytes.

(A) Immunoblot showing GLUT4, EFR3a, and PI4K-III α levels in lipid raft fractions of wild-type (WT) 3T3-L1 adipocytes, treated with or without 100 nM insulin for 20 min. Caveolin-1 was used as a lipid raft protein marker (Chamberlain and Gould, 2002). Lipid raft fractions were produced and loaded as described in [2.2.4.2](#) and [2.2.5.2](#). Fractions were retrieved from the top (fraction number 1) to the bottom (fraction number 12) of the sucrose gradient (Fractions 1-5 = 5% Sucrose Layer, Fractions 6-9 = 30% Sucrose, and Fractions 10-12 = 80% Sucrose). Solubilised proteins remained in the 80% sucrose layer, whereas insoluble rafts accumulated between the 5% and 30% sucrose layers at the interface. Blots were visualised with a LI-COR Odyssey-SA system; data from a representative experiment are shown (n = 3). (B) Mean \pm s.d. of GLUT4, EFR3a, PI4K-III α , and Caveolin-1 protein content in lipid raft fractions of WT 3T3-L1 adipocytes under basal condition (n = 3; values expressed relative to total fractions proteins content). (C) Mean \pm s.d. fold-changes of GLUT4, EFR3a, PI4K-III α , and Caveolin-1 protein content in lipid raft fractions of WT 3T3-L1 adipocytes under insulin stimulation (n = 3; values expressed relative to Basal). Data solely indicate a significant decrease in insulin-stimulated EFR3a protein content in lipid rafts of WT adipocytes. * represents $p \leq 0.05$ and ns signify non-significant. Two-tailed unpaired t-tests and a one-way ANOVA with Turkey's multiple comparisons test were performed on all raw data of (B) and (C), respectively.

3.3.2.3 PI4P Localisation at the Plasma Membrane is Increased in Insulin-Stimulated 3T3-L1 Adipocytes

As previously mentioned, PI4P is one of the most abundant members of the PI family and the primary product of PI4K-III α at the PM of mammalian cells (see section [3.1.1](#)). We hypothesised that in basal conditions, PI possesses the ability to 'coral' GLUT4 into clusters. Upon insulin stimulation, EFR3a localises at PM and subsequently recruits PI4K-III α , leading to the phosphorylation of PI into PI4P and causing GLUT4 to disperse within the

PM as individual molecules (see section [3.1.2](#)). To ascertain the role of PI4P in controlling GLUT4 dispersal, we aimed to further identify and confirm the cellular localisation of PI4P in 3T3-L1 adipocytes under the influence of insulin and in cells where the expression of EFR3a, PI4K-III α , and both EFR3a and PI4K-III α have been KD using siRNA (see section [3.3.1.1](#)). Here, we took advantage of the anti-PI4P antibody described by Bojjireddy et al. (Bojjireddy et al., 2014) (see section [2.1.2.1](#)).

Dolt blot experiments were first performed on sub-cellular fractions isolated from, and whole cell lysates (WCL) of, WT and siRNA-treated 3T3-L1 adipocytes (see sections [2.2.3.3](#), [2.2.4.1](#), and [2.2.5.4](#)). No changes in PI4P levels were observed in the LDM, HDM, and WCL samples. However, in WT cells, PI4P content significantly increased at the PM after insulin stimulation ($p = 0.0041$; **Figure 3.10A,B**). This increase was abrogated in EFR3a, PI4K-III α , and Double KD cells (**Figure 3.10A,C-E**).

Of note, KD of EFR3a alone inhibited the insulin-stimulated increase of PI4P levels at the PM, suggesting that both EFR3a and PI4K-III α as a complex are required to phosphorylate PI4P under insulin stimulation. In addition, as this phenomenon appears to only affect PM fractions, this further strengthens the hypothesis that the EFR3a/PI4K-III α machinery's main site of action is at the PM.

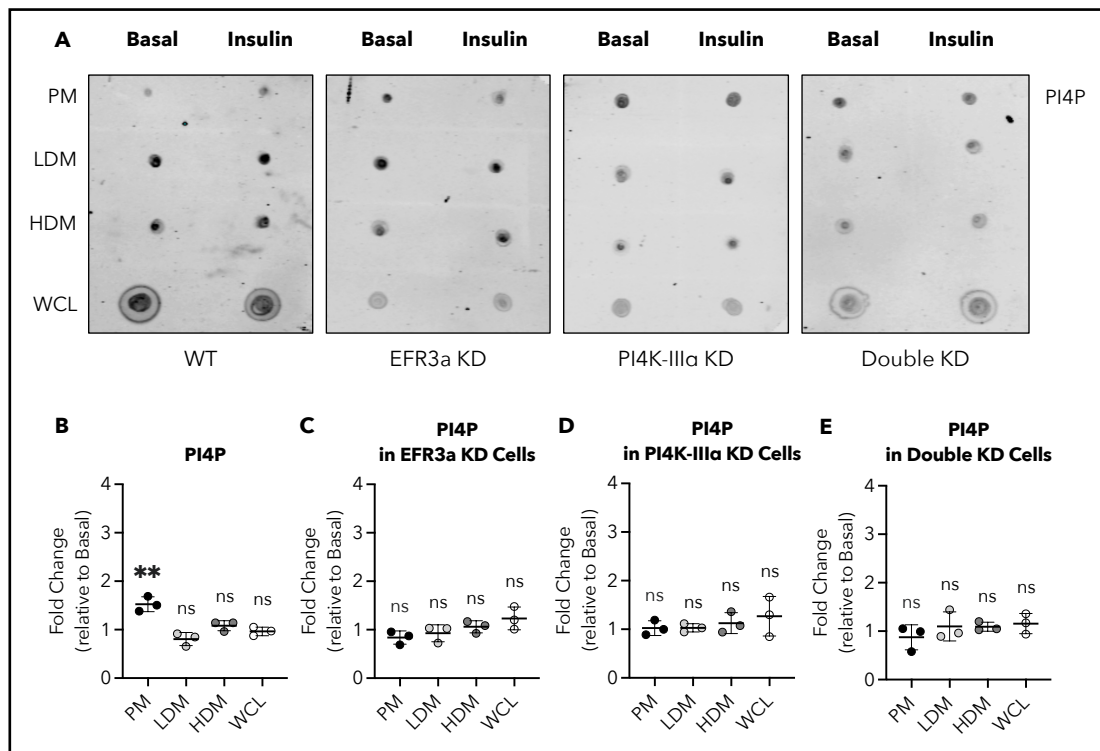


Figure 3.10. PI4P Localisation in Insulin-Stimulated WT, EFR3a KD, PI4K-III α KD, and EFR3a KD and PI4K-III α KD 3T3-L1 Adipocytes.

(A) Dot blot showing PI4P contents in PM-enriched, low-density microsomes (LDM), high-density microsomes (HDM) fractions, and whole cell lysate (WCL) samples of wild-type (WT) 3T3-L1 adipocytes, as well as adipocytes transfected with siRNAs designed to knockdown the expression of EFR3a (EFR3a KD), PI4K-III α (PI4K-III α KD), and EFR3a and PI4K-III α (Double KD), six days post-differentiation, and treated with or without 100 nM insulin for 20 min. Sub-cellular fractions and WCL were produced and processed as described in [2.2.4.1](#), [2.2.3.3](#), and [2.2.5.4](#). Blots were visualised with a LI-COR Odyssey-SA system; data from a representative experiment are shown ($n = 3$). (B-E) Mean \pm s.d. fold-changes of PI4P levels in PM fractions, LDM, HDM and WCL of WT (B; $n = 3$), EFR3a KD (C; $n = 3$), PI4K-III α KD (D; $n = 3$), and Double KD (E; $n = 3$) 3T3-L1 adipocytes under insulin stimulation (values expressed relative to Basal). Data indicate an increase in PI4P levels under insulin stimulation in the PM of WT cells. No further significant signals were observed in these datasets. ** represents $p \leq 0.01$ and ns signify non-significant. Two-tailed unpaired t-tests were performed on all raw data.

To gain further insight, we evaluated the distribution of PI4P and GLUT4 in WT and EFR3a KD 3T3-L1 adipocytes expressing HA-GLUT4-GFP under basal and insulin-stimulated conditions. We measured and compared the fluorescence intensity profiles of immunostained PI4P and GLUT4-GFP across the width (x-axis) of the cells (i.e., from one side to the other, PM to PM, passing through the nucleus when possible) using STED and confocal-acquired images, respectively (**Figure 3.11**) (see sections [2.2.7.2.1](#) and [2.2.8.2](#)). Information on the position of where PI4P and GLUT4 signals peak along the breadth of fluorescence intensity profiles (**Figure 3.11; Right Panel**) was extracted from the Kurtosis value of each profile within each condition, as described in section [2.2.8.2](#). Briefly, a significant increase in Kurtosis in response to insulin indicates the detection of immunostained PI4P and GLUT4-GFP with a higher content toward the PM and at the centre of insulin-stimulated cells.

As expected, our data highlight a significant increase in GLUT4-GFP fluorescence signals toward the PM under insulin stimulation in WT adipocytes ($p = 0.0158$). This distribution does not appear to be affected in EFR3a KD cells ($p = 0.0125$; **Figures 3.11B,D and 3.12A**). On the other hand, while an increase of PI4P fluorescence signals toward the PM is also observed in WT insulin-stimulated cells ($p = 0.0376$), siRNA-mediated *Efr3a* KD was observed to prohibit this effect ($p = 0.6657$; **Figures 3.11B,D and 3.12B**), further strengthening the results obtained from the above dot blot experiments.

Overall, these observations, together with the localisation of EFR3a and PI4K-III α at the PM under insulin stimulation (see section [3.3.2.1](#)), suggest that we are getting one step closer to testing the hypothesis that the

EFR3a/PI4K-III α machinery regulates insulin-stimulated GLUT4 dispersal within the PM of adipocytes through the phosphorylation of PI into PI4P.

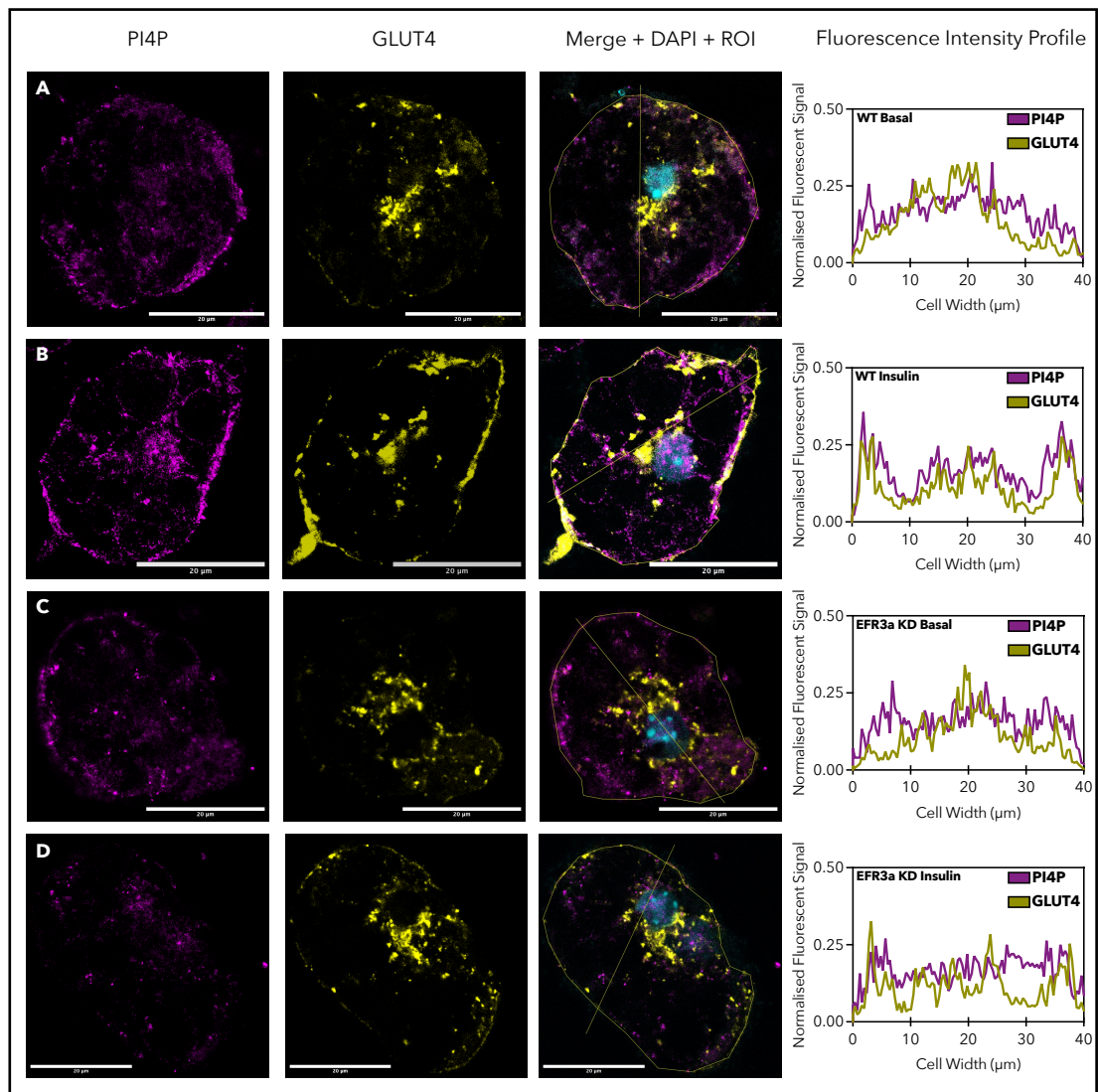


Figure 3.11. Representative Immunofluorescence Staining of PI4P and Quantification of PI4P and GLUT4 Distribution in WT and EFR3a KD 3T3-L1 HA-GLUT4-GFP Adipocytes.

Representative STED and confocal images of wild-type (WT) 3T3-L1 HA-GLUT4-GFP adipocytes treated without (A) or with (B) 100 nM insulin for 20 min, and 3T3-L1 HA-GLUT4-GFP adipocytes transfected with siRNA designed to knockdown the expression of EFR3a (EFR3a KD) treated without (C) or with (D) 100 nM insulin for 20 min. Left Panel: STED images of immunostained PI4P fluorescence (magenta). Middle Left Panel: Confocal images of GLUT4-GFP fluorescence (yellow). Middle Right Panel: Merge and confocal-acquired DAPI fluorescence (cyan). As described in section [2.2.8.2](#), using the line selection tool in Fiji (Schindelin et al., 2012), intensity plots regions of interest (ROI) were manually segmented in each cell by drawing a line (yellow line) from one side of the cell to the other, PM to PM passing through the nucleus when possible so that the final line width equalled 40 μm . For clarity, cell edges are also highlighted (yellow circle). Right Panel: Mean fluorescence intensity line profiles of PI4P (magenta) and GLUT4-GFP (yellow) fluorescence across the cell width (x-axis) for visualisation purposes. Fluorescent signal values are expressed relative to the highest intensity values within each extracted profile. For each condition, final mean fluorescence intensity line profiles were generated from three biological replicates ($n = 3$). Each biological replicate includes three cells (i.e., nine cells per condition). Cells were fixed and immunostained as described in [2.2.7.1.1](#). Secondary VHH antibodies labelled with Alexa Fluor® 647 were used (see section [2.1.2](#)). All images were acquired using a STEDYCON system (see section [2.2.7.2.1](#)). Scale Bars = 20 μm .

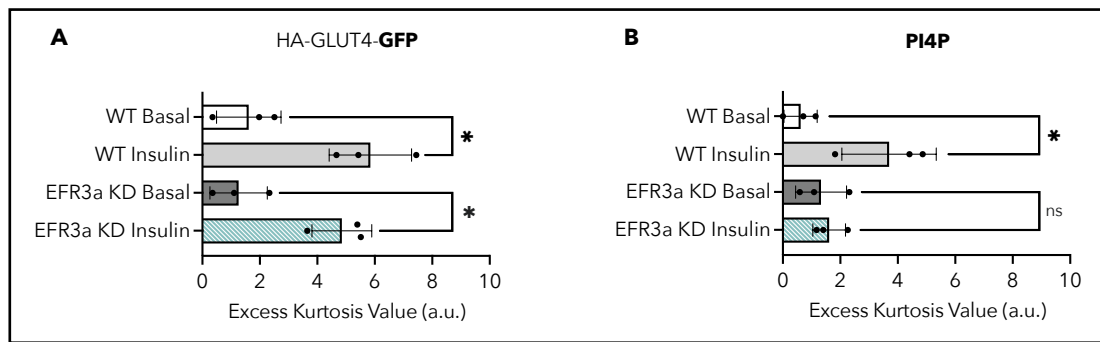


Figure 3.12. Excess Kurtosis Values of GLUT4-GFP and PI4P Fluorescence Intensity Profiles in Insulin-Stimulated WT and EFR3a KD 3T3-L1 Adipocytes.

(A,B) Mean \pm s.d. excess Kurtosis value of GLUT4-GFP (A) and immunostained PI4P (B) fluorescence intensity profiles across the width (x-axis) of WT and EFR3a KD 3T3-L1 adipocytes expressing HA-GLUT4-GFP under both basal and insulin-stimulated conditions (**Figure 3.11**; $n = 3$, per each condition, each biological replicate is the average of 3 cells). In both WT and EFR3a KD cells, higher excess Kurtosis values when compared to basal conditions indicate a significant increase in GLUT4-GFP fluorescence signals toward the PM under insulin stimulation. Similar results were obtained for PI4P fluorescence signals in WT cells. However, no significant differences in excess Kurtosis values between basal and insulin-stimulated EFR3a KD cells were observed. Cells were immunostained and imaged, and Kurtosis values were extracted as described in [2.2.7.1.1](#), [2.2.7.2.1](#), and [2.2.8.2](#). * represents $p \leq 0.05$, and ns signify non-significant. Two-tailed unpaired t-tests were performed on all raw data.

3.3.3 CRISPR-Cas9-Mediated *Efr3a* Gene Knockout as a Permanent Alternative to siRNA-Mediated Knockdown

While effective, siRNA-mediated KD approaches are costly and exhibit batch-to-batch variations. Hence, we attempted to KO the *Efr3a* gene using two different non-viral delivery strategies (i.e., RNP and plasmid DNA) to introduce CRISPR/Cas9 systems into 3T3-L1 fibroblasts.

3.3.3.1 Ribonucleoprotein-Mediated CRISPR-Cas9 Genome Editing

RNP is one of the most common non-viral carriers for the delivery into cells of Cas9 proteins and gRNA sequences for the latter endonuclease to the targeted locus. By incubating single-stranded gRNA with Cas9 proteins in vitro, RNP complexes can be formed and subsequently transfected into the cell (see section [2.2.1.6.1](#)).

In *Mus musculus*, the *Efr3a* gene is located on chromosome 15 and consists of 23 coding exons. Based on their low off-target scores, two different gRNA sequences were selected in this experiment to target exons 1 (gRNA #1) and 6 (gRNA #2). All guides are designed to be found immediately 3' to a Cas9 binding PAM sequence, allowing a Cas9-induced double-strand break (DSB) to occur specifically three nucleotides 3' to such PAM site (see Appendix [7.2.1](#)). A Cas9-induced DSB is either repaired by non-homologous end joining (NHEJ) or homology-directed repair. While the latter mechanism is more accurate, the NHEJ repair mechanism is more prone to error, frequently causing small nucleotide insertions or deletions, which can result in frameshift mutations leading to premature stop codons within the open reading frame of the targeted gene (Her and Bunting, 2018). In our case, we hope that errors generated by NHEJ will result in loss-of-function mutations.

In addition to genotype cells for a successful CRISPR/Cas9-mediated KO, different sets of PCR primers were designed using Primer-BLAST to amplify each selected gRNA sequence, that is, primer pair #1.1, #1.2, and #1.3 for gRNA #1 and primer pair #2.1 and #2.2 for gRNA #2 (see Appendix [7.2.1](#)). While computational tools such as Primer-BLAST help to select primers with low off-target specificity, further testing of the designed primer pairs

was performed to validate their amplification efficiency and robustness (Delghandi et al., 2022). Primer pairs were tested via PCR using DNA extracted from WT 3T3-L1 fibroblasts (**Figure 3.13**).

A first PCR was run using primer pair #1.1 at an annealing temperature (T_a) of 65°C. However, as shown in **Figure 3.13A, Lane 1**, no PCR product was observed. Because a known pair of primers was used in parallel as a positive control and successfully visualised (**Figure 3.13A; Lane 6**), the subsequent optimisation step was to reduce the T_a to a temperature further away from the primers' melting temperature (T_m). If set too high or too close to the T_m , improper T_a can prevent the binding of the primers to the DNA template. As a rule of thumb, setting the T_a 5°C lower than the T_m of the primers is standard practice. While the T_m of Fw #1.1 is 70.0°C, Rv #1.1 has a T_m of 67.7°C (see Appendix [7.2.1.1](#)), only 2.7°C above the previously set T_a of 65°C. As such, the T_a was subsequently set at 55°C. As a result, a band at the expected PCR product size for primer pair #1.1 (184 bp) was successfully detected. However, multiple other bands were also visualised above and below 184 bp (**Figure 3.13A; Lane 2**), suggesting non-specific binding of the primers. Unfortunately, similarly to primer pair #1.1, primer pair #1.2 was also found to generate multiple non-specific bands (**Figure 3.13A; Lane 3**). As such, a final PCR was run using primer pairs #1.3a and #1.3b at a T_a of 55°C. A singular band was obtained for both sets of primers. However, primer pair #1.3a showed a band at 498 bp, slightly higher than the expected product size (**Figure 3.13A; Lane 4**). Fortunately, primer pair #1.3b produced a predicted PCR product of 259 bp (**Figure 3.13A; Lane 5**). While it is possible that the slightly larger PCR product obtained for primer pair #1.3a was simply due to the

contamination of the reaction mix, primers Fw #1.3b and Rv #1.3 were selected as an optimal primer pair to amplify the gRNA #1 sequence.

Similarly, the specificity of the primers designed for gRNA #2 (see Appendix [7.2.1.3](#)) was also tested (data not shown). As shown in **Figure 3.13B**, the optimal primer combination was Fw #2.1 and Rv #2.2, with a predicted band visualised at 1009 bp.

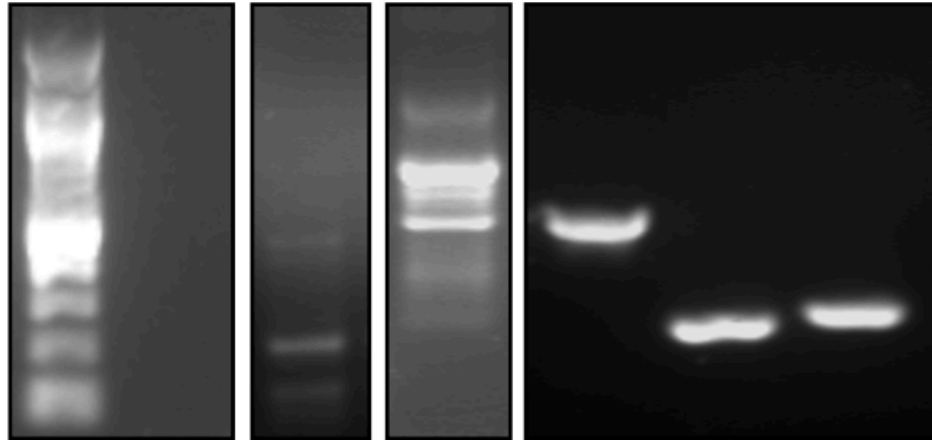
Primer pairs #1.3b and Fw #2.1/Rv #2.2 were consequently confidently used to target gRNA #1 and #2, respectively, during subsequent mutation detection analysis and DNA sequencing (see sections [2.2.6.3](#) and [2.2.1.6.4](#)).

A Primer Pair

	#1.1	#1.1	#1.2	Fw #1.3a Rv #1.3	Fw #1.3b Rv #1.3	Known Control
Ta	65°C	55°C	55°C	55°C	55°C	55°C
Product Size	184 bp	184 bp	344 bp	498 bp	259 bp	270 bp

Base Pair

1,517 -
1,200 -
1,000 -
900 -
800 -
700 -
600 -
500 -
400 -
300 -
200 -
100 -



B Primer Pair

	Fw #2.1 Rv #2.2	Known Control
Ta	55°C	55°C
Product Size	1009 bp	270 bp

Base Pair

1,517 -
1,200 -
1,000 -
900 -
800 -
700 -
600 -
500 -
400 -
300 -
200 -
100 -

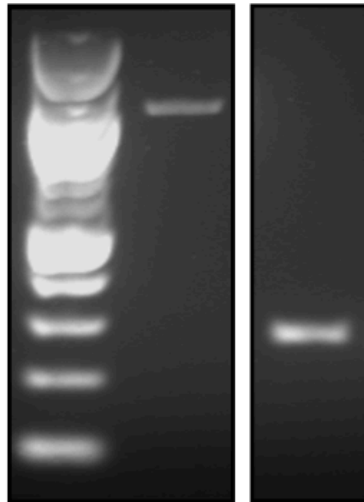


Figure 3.13. Optimisation and Validation of Primer Design for CRISPR/Cas9-Mediated Gene Knockout of *Efr3a* using Ribonucleoprotein.

Agarose gel electrophoresis showing PCR products of DNA extracted from WT 3T3-L1 fibroblasts treated with designed (A) primer pair #1.1, #1.2, and #1.3 for gRNA #1 and (B) primer Fw#2.1 and Rv#2.2 for gRNA #2 (annealing temperature, T_a ; see Appendix [7.2.1](#)). A known pair of primers with a product of 270 bp was used as a positive control and successfully visualised in every experiment. Primer pairs selected for final mutation detection experiments and DNA sequencing are shown in red. DNA was extracted and PCR run as described in sections [2.2.1.6.4](#) and [2.2.6.1](#), respectively. A 100 bp DNA ladder and 1.5% agarose gels were used and visualised under UV light with a Syngene Gel Documentation System.

gRNA #1 or #2, along with Cas9 proteins, were then transfected as RNP complexes into 3T3-L1 fibroblasts using Xfect™ Transfection Reagent (see section [2.2.1.6.1](#)).

To estimate the targeting efficiency of each guide, genomic DNA was isolated 48h post-transfection (see section [2.2.1.6.4](#)) and used as DNA templates for Surveyor® nuclease assays (see section [2.2.6.3](#)). Briefly, in the absence of mutations, no heteroduplexes can be formed, and therefore, the Surveyor® nuclease will not produce any cleaved products; only a single parental band will be observed. Product sizes post-Surveyor® nuclease assay for the selected primer pairs #1.3b and #Fw2.1/Rv2.2 can be found in Appendix [7.2.1](#).

Unfortunately, neither guide resulted in detectable modifications of the target loci by Surveyor® nuclease assay. Similarly to negative control DNA samples, only singular bands at 259 bp and 1009 bp were observed in the genomic DNA extracted from cells transfected with gRNA #1 and gRNA #2,

respectively (**Figure 3.14**). DNA sequencing results (data not shown) confirmed that neither gRNA targeted exon 1 or 6 of the *Efr3a* gene.

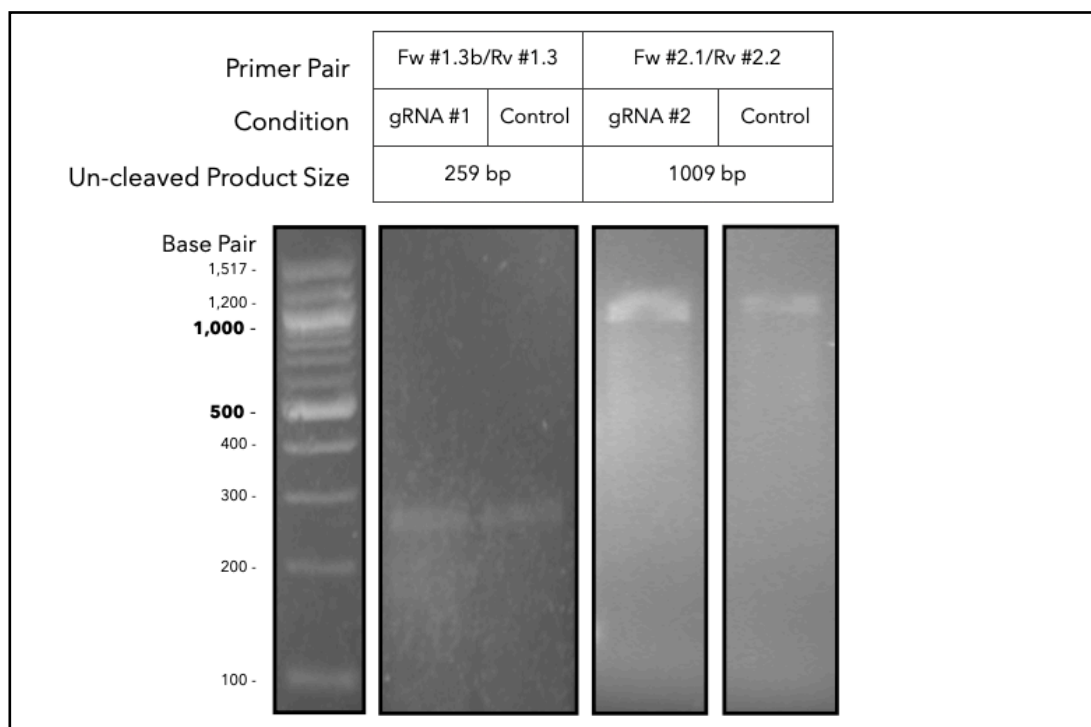


Figure 3.14. Validation of CRISPR/Cas9-Mediated *Efr3a* Knockout in 3T3-L1 Fibroblasts using Ribonucleoprotein.

Agarose gel electrophoresis showing Surveyor® nuclease assay in 3T3-L1 fibroblasts transfected with gRNA #1 or #2 and negative control cells (Control). Selected primer pairs (**Figure 3.13**) were used for appropriate gRNA targeting. For primer pair Fw#1.3b/Rv1.3 and #Fw2.1/Rv2.2 combinations, the band size of the product un-cleaved by Surveyor® nuclease are respectively 259 bp and 1009 bp (see Appendix 7.2.1). Surveyor® nuclease assay was performed as described in section 2.2.6.3. A 100 bp DNA ladder and 1.0% agarose gels were used and visualised under UV light with a Syngene Gel Documentation System.

3.3.3.2 Plasmid DNA-Mediated CRISPR-Cas9 Genome Editing

Our second attempt involved using a plasmid DNA instead of RNP to deliver the CRISPR/Cas9 system in 3T3-L1 fibroblasts. The plasmid DNA used encloses Cas9, an *Efr3a*-targeting gRNA at exon 17, and a puromycin resistance gene (pRP[CRISPR]-Puro-hCas9-U6>mEfr3a[gRNA#5786]; see Appendix [7.2.2.1](#)). The advantage of this approach is the presence of an antibiotic-resistance gene, allowing for an additional clonal selection step.

As previously mentioned (see section [3.3.3.1](#)), to ensure the effective subsequent genotyping of clones, the primer pair associated with the inserted gRNA within the purchased plasmid was first tested via PCR, using DNA extracted from WT 3T3-L1 fibroblasts (**Figure 3.15**). Primer pair #3 was successfully shown to produce a predicted PCR product of 1147 bp (**Figure 3.15; Lane 1**) and was, therefore, confidently used for subsequent mutation detection analysis and DNA sequencing (see sections [2.2.6.3](#) and [2.2.1.6.4](#)).

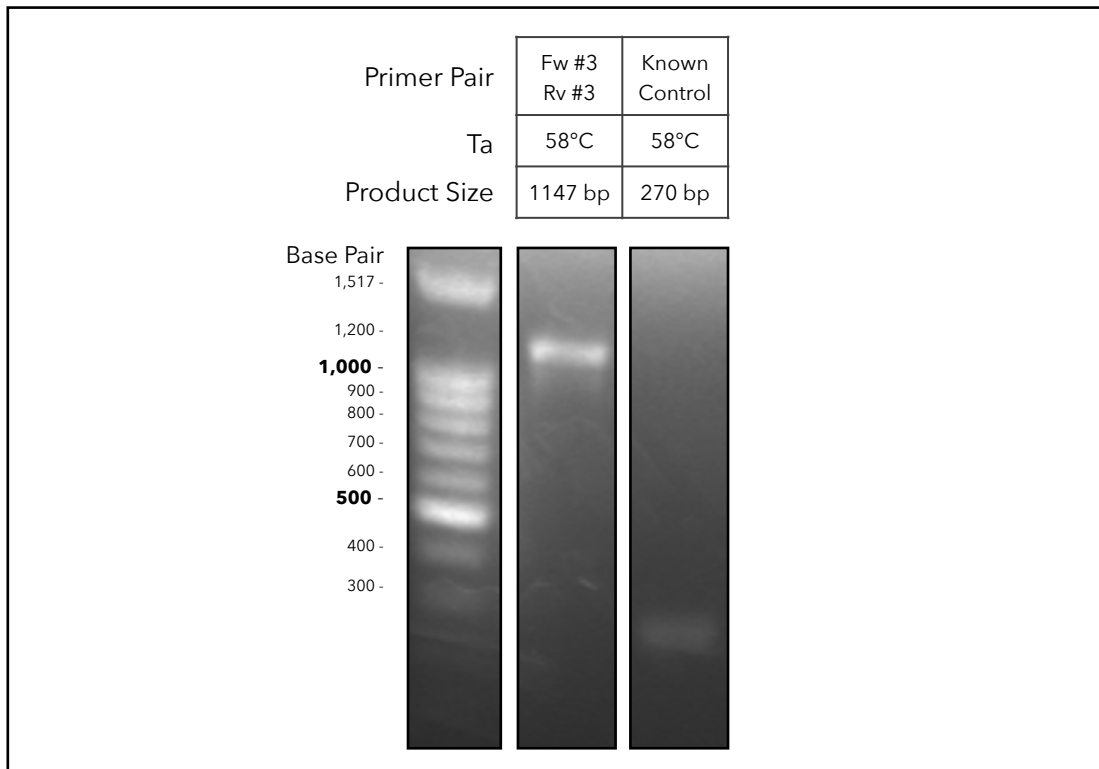


Figure 3.15. Optimisation and Validation of Primer Design for CRISPR/Cas9-Mediated Gene Knockout of *Efr3a* using Plasmid DNA.

Agarose gel electrophoresis showing PCR products of DNA extracted from WT 3T3-L1 fibroblasts treated with plasmid DNA-associated primer pair #3 (annealing temperature, Ta; see Appendix [7.2.2.1.2](#)). A known pair of primers with a product of 270 bp was used as a positive control and successfully visualised in every experiment. DNA was extracted and PCR run as described in sections [2.2.1.6](#) and [2.2.6.1](#), respectively. A 100 bp DNA ladder and 0.8% agarose gel were used and visualised under UV light with a Syngene Gel Documentation System.

The plasmid DNA was then transfected into 3T3-L1 fibroblasts using Xfect™ Transfection Reagent and subjected to puromycin selection before undergoing single-cell expansion (see section [2.2.1.6.2](#), [2.2.1.6.3](#), and [2.2.1.6.4](#)).

To confirm genome modification, a Surveyor® nuclease assay was performed on heterogeneous DNA populations extracted from pools of

CRISPR/Cas9-treated and negative control cells collected before single-cell colony expansion (see section [2.2.6.3](#)). The plasmid DNA-associated gRNA and Cas9 protein were shown to induce mutations within the target locus. While a singular parental band is observed in the negative control DNA sample at 1147 bp, the genomic DNA extracted from CRISPR/Cas9-treated cells presents with two additional cleaved products at the expected size of 656 and 491 bp (see Appendix [7.2.2.1.2](#)) (**Figure 3.16**). Gene modification efficiency was estimated at 42.14%.

Five clones were established from CRISPR/Cas9-treated cells, and modifications within the targeted locus in exon 17 of the *Efr3a* gene were confirmed by DNA sequencing (**Figure 3.17**). We also isolated clones from negative control cells. Sequence analysis revealed that genome editing caused the insertion of T and C nucleotides, 2 and 4 bases 3' to the PAM sequence, respectively, resulting in a frameshift mutation and the appearance of a premature stop codon in exon 18 within all generated clones (**Figure 3.17B**). Interestingly, however, immunoblotting of CRISPR/Cas9-generated clone adipocyte lysate revealed no visible changes in EFR3a protein content (**Figure 3.17C**).

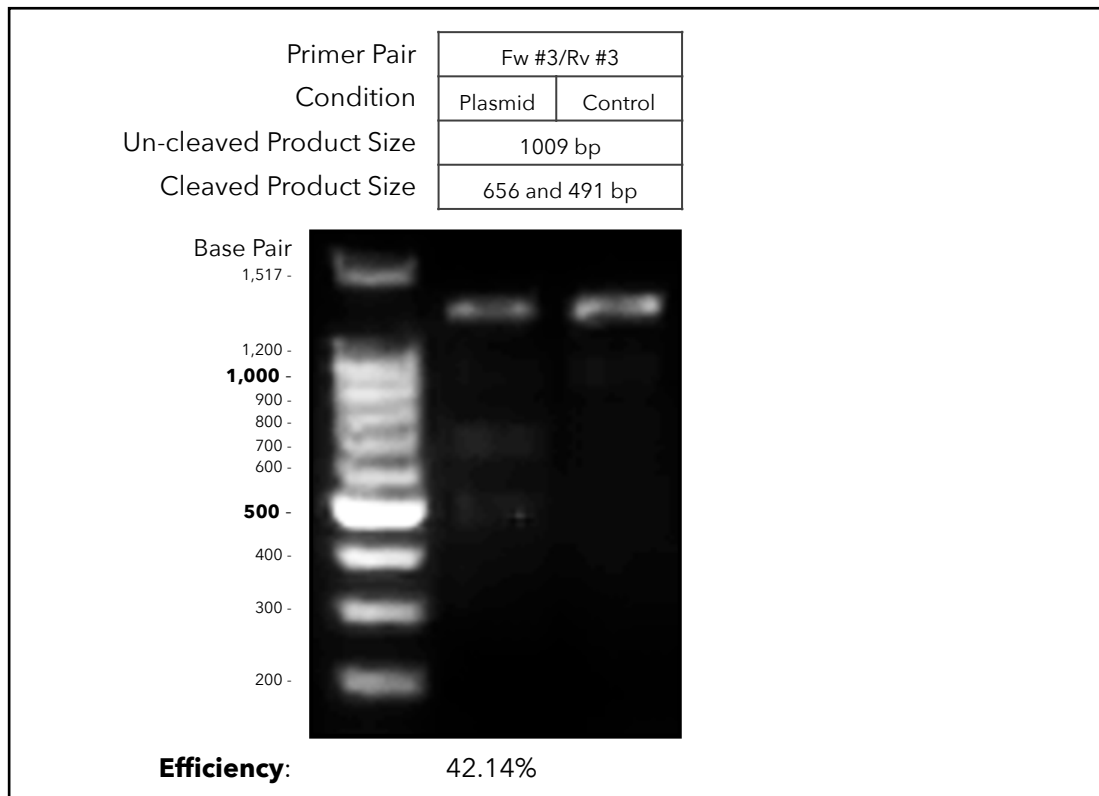


Figure 3.16. Validation of CRISPR/Cas9-Mediated *Efr3a* Knockout in 3T3-L1 Fibroblasts using Plasmid DNA.

Agarose gel electrophoresis showing Surveyor® nuclease assay in 3T3-L1 fibroblasts transfected with pRP[CRISPR]-Puro-hCas9-U6>mEfr3a[gRNA#5786] (Plasmid) and negative control cells (Control). Using primer pair #3 (**Figure 3.15**), DNA duplexes' un-cleaved and cleaved product sizes are 1147 bp and 656 and 491 bp (see Appendix [7.2.2.1](#)). Extracted gene modification efficiency from band intensity was 42.14%. Surveyor® nuclease assay was performed as described in section [2.2.6.3](#). A 100 bp DNA ladder and 1.0% agarose gel were used and visualised under UV light with a Syngene Gel Documentation System.

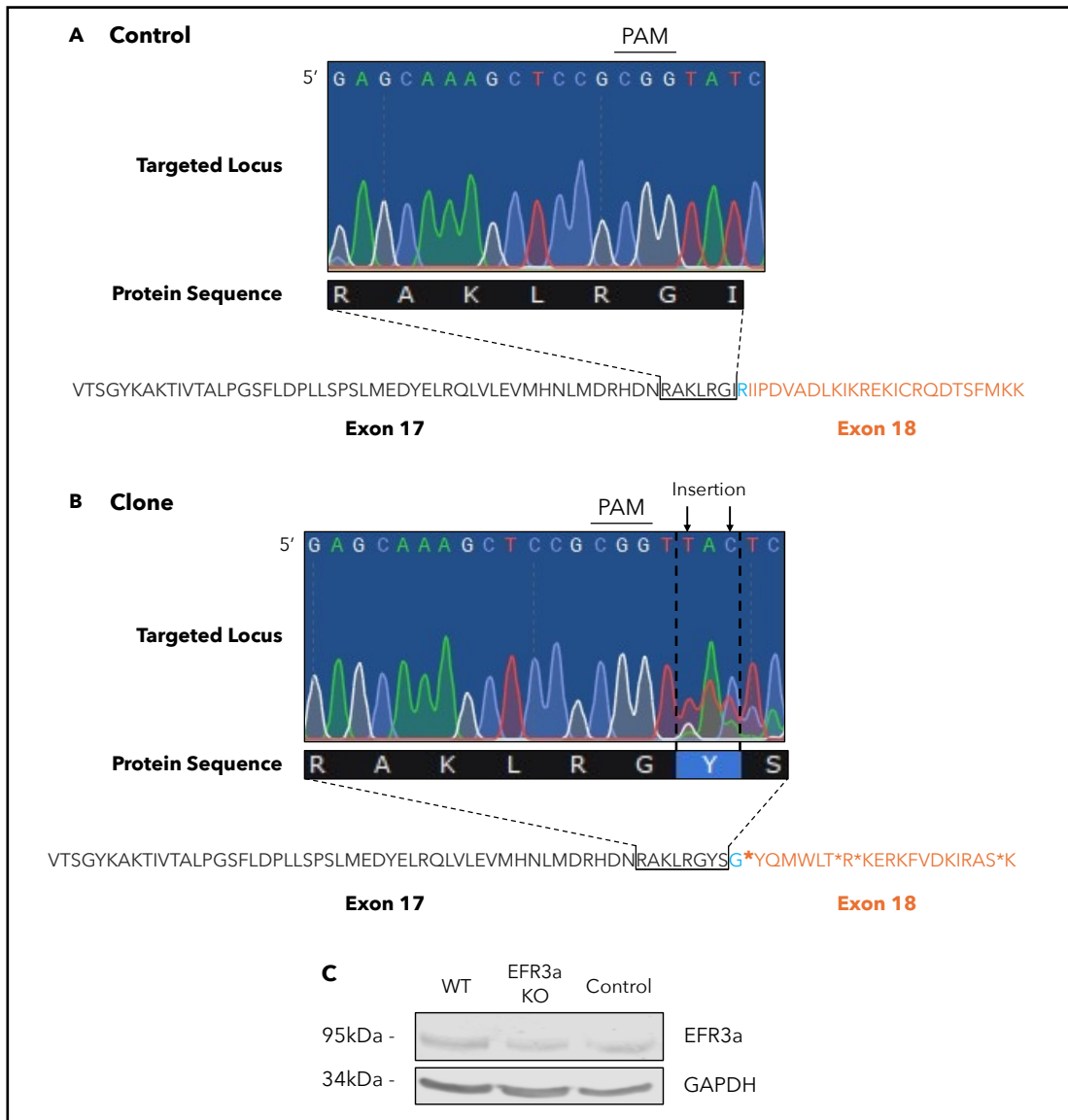


Figure 3.17. Characterisation of Plasmid DNA-Mediated CRISPR/Cas9 *Efr3a* Knockout 3T3-L1 Clones.

DNA sequencing of the targeted locus (see Appendix [7.2.2.1](#)) in (A) negative control cells (Control) and (B) *Efr3a* KO 3T3-L1 fibroblast clones generated using plasmid DNA (pRP[CRISPR]-Puro-hCas9-U6>mEfr3a[gRNA#5786])-mediated CRISPR/Cas9 genome editing. Data reveal the insertion of T and C nucleotides, 2 and 4 bases 3' to the PAM sequence, resulting in a frameshift mutation and a premature stop codon (bold orange *) in exon 18 (orange) within generated clones. Blue residue represents an overlap splice site between exon 17 (black) and exon 18. DNA sequencing was performed as described in section [2.2.1.6.4](#) using forward primer #3 (see Appendix [7.2.2.1.2](#)); data from a representative generated clone are shown. (C) Immunoblot showing protein contents of EFR3a in untreated/wild-type (WT), CRISPR/Cas9-treated (EFR3a KO), and negative control 3T3-L1 adipocytes, ten days post-differentiation. GAPDH was used as a loading control. GAPDH bands were obtained from the same membrane. All cell lysates were produced and loaded as described in [2.2.3.3](#) and [2.2.5.2](#). Blots were visualised with a LI-COR Odyssey-SA system.

3.4 Chapter 3 - Discussion and Future Work

3.4.1 *EFR3a* and *PI4K-III α* :

The Premise of a Newly Identified GLUT4 Dispersal Machinery

Over the years, details regarding the intracellular trafficking of GLUT4 have become clearer. While it is now indisputable that the main site for GLUT4 function and regulation is at the PM (Bai et al., 2007), little is known about the behaviour of GLUT4 once fused to the PM. Several lines of investigation suggest that controlling GLUT4 at the PM could be a key facet of insulin action. In 2005, Koumanov et al. first provided compelling evidence for an insulin-regulated event at the PM upon GLUT4 fusion (Koumanov et al., 2005). With the emergence of SRM techniques, further studies confirmed that insulin has a fundamental impact on the spatial distribution of PM-fused GLUT4 (see section [1.4](#)). More specifically, these studies described the fusion of GLUT4 clusters in the PM and the ability of insulin to promote GLUT4 dispersal from these clusters (Gao et al., 2017; Lizunov et al., 2013; Stenkula et al., 2010). It is only recently that new mechanistic details on how GLUT4 clustering might be modulated at the PM have come to light.

The findings in this section highlight the localisation of, and functional interaction between, GLUT4, *EFR3a*, *PI4K-III α* , and *PI4P* at the PM of 3T3-L1 adipocytes, shedding light on the complexity of this regulatory system's spatial organisation. Overall, these results reinforce our hypothesis that the *EFR3a/PI4K-III α* complex regulates insulin-stimulated GLUT4 dispersal in the PM of adipocytes through the phosphorylation of PI into *PI4P* (**Figure**

3.1), hinting toward an added regulatory component that is lipid rafts, and therefore opening new lines of investigation to explore.

Consequently, further studies are warranted to dissect the detailed molecular interactions and to explore the potential therapeutic implications of targeting the EFR3a/PI4K-III α machinery in metabolic disorders such as insulin resistance and T2D. Detailed mechanistic studies should be conducted to investigate the precise molecular interactions between EFR3a, PI4K-III α , and other potential regulatory components at the PM. For instance, caveolae, a specialised subset of lipid rafts, are small, flask-shaped invaginations of the PM enriched in cholesterol, sphingolipids and specifically marked by the presence of caveolin proteins (Sowa et al., 2001). While the proposed functions of lipid rafts and caveolae remain somewhat controversial, previous studies have identified caveolae, and more specifically caveolin-1, as significant sites for IR localisation and signalling in adipocytes (Gustavsson et al., 1999; Nystrom et al., 1999). This, with present findings suggesting the presence of EFR3a in lipid rafts (see section [3.3.2.2](#)), which may well encompass caveolae, therefore raises questions about the potential interaction between the IR and the EFR3a/PI4K-III α dispersal machinery. The spatial proximity of EFR3a and the IR within these microdomains could facilitate efficient insulin signal transduction and rapid regulation of the PM lipid composition, previously hypothesised to be essential for proper GLUT4 dispersal (see section [2.3.2.3](#)).

Techniques such as co-immunoprecipitation, Förster resonance energy transfer, and proximity ligation assays could help us better understand the dynamics and physical interactions within the EFR3a/PI4K-III α machinery,

further highlighting, for example, the involvement of TTC7, FAM126A, and TMEM150A (see section [3.1.1](#)). These techniques can also provide insights into the interactions of EFR3a/PI4K-III α complexes with its surroundings. In addition to repeating Kurtosis analyses presented in section [3.3.2.3](#) on *Pi4ka* and double (*Efr3a* and *Pi4ka*) KD cells, comprehensive lipidomic analyses should also be performed to further characterise the lipid composition of the PM and microdomains (Neuhaus et al., 2023), where EFR3a and GLUT4 are enriched under both basal and insulin-stimulated conditions. This could reveal specific lipid species that may facilitate or modulate the recruitment and activity of EFR3a and PI4K-III α . Imaging techniques, such as SRM, should also be utilised to visualise the dynamics of EFR3a, PI4K-III α , and GLUT4 at the PM (see [Chapter 4](#)).

3.4.2 *A Need for Standardisation of CRISPR/Cas9 Genome Editing Protocols*

While the above results argue in favour of using siRNA KD and pharmacological inhibition to address the role of endogenous EFR3a and PI4K-III α in the dispersal mechanism of GLUT4 at the PM of adipocytes, another and more permanent alternative is CRISPR/Cas9-mediated gene KO. Unfortunately, this thesis failed to validate a CRISPR/Cas9 strategy to KO the *Efr3a* gene in 3T3-L1 cells. As a gene editing tool, the CRISPR/Cas9 system has revolutionised many areas of biomedical research. Its flexibility to target nearly any locus within the genome explains its popularity and widespread use. However, several factors must be addressed for a CRISPR/Cas9 system to be effective. As established in this study, these factors are

target site selection, gRNA and primers design, and how to deliver the required components.

Different approaches have been reported to identify proper target site selection pre-transfection over the years. Most commonly, computational tools (see Appendix [7.2.1](#)) are used to design gRNA and predict the likelihood of off- and on-target Cas9 cleavage. Another potential *in silico* prediction method includes assessing potential editing activity by enzymatic assays based on mismatch-sensitive endonucleases (e.g., Surveyor[®] nuclease assay) pre-transfection and DNA sequencing (Tycko et al., 2016). Both methods require the designed guide sequence to be inserted into plasmids if not already present. However, due to time constraints and lack of expertise, most scientists, including ourselves, tend to rely solely on computational tools and trust commercial suppliers, thereby limiting their chances of success. The work described in this study reminds us that, along with the selection of appropriate gRNA, the design of primers needs to be considered in CRISPR/Cas9 experiments. As seen in **Figure 3.13**, while the use of bioinformatics tools such as Primer-BLAST facilitates the first steps of primer design, a time for potential subsequent optimisation and validation experiments needs to be taken into account, as well as the characteristics of the sequence surrounding the targeted site, such as repetitive DNA sequences and G-C nucleotide concentrations.

Subsequently, while several methods are available, the delivery (viral or non-viral) of the CRISPR components (RNA, DNA, or protein) remain the most significant obstacle. CRISPR components can take three forms. Firstly, as separate Cas9 protein and gRNA (RNA). Secondly, as an RNP complex consisting of the Cas9 protein and gRNA assembled together (protein; see

section [3.3.3.1](#)). Finally, as a DNA plasmid containing the sequence for Cas9 and the gRNA (DNA; see section [3.3.3.2](#)). The most widely used is the DNA plasmid option. The advantage of this method is that antibiotic-resistance genes can easily be included in the plasmid, allowing rapid clonal selection (see section [2.2.1.6.3](#)). It remains that numerous problems can arise from using DNA plasmids. For instance, off-target cleavage levels increase with sustained exposure to Cas9. Controlling or limiting the time of Cas9 expression in the cell is often required to improve the system's efficacy. While not performed in this study, this is easily achievable when using the burst-like kinetics of RNP delivery and associated Cas9 exposure, as opposed to a more stable plasmid-driven expression. Once the CRISPR components have been chosen, several specific vehicles are available for delivery into the cells. Over the years, the use of viral vectors such as adenovirus or lentivirus has shown to be the most effective option. However, while effective, this option remains more expensive and technically more challenging. As a result, non-viral delivery options, as used in this study, are often favoured (Tycko et al., 2016).

Overall, more than one method is applicable to CRISPR/Cas9 genome editing. While each option has benefits and limitations, our journey with CRISPR/Cas9 highlights a need for standardisation, allowing scientists from different fields and expertise to take advantage of the CRISPR/Cas9 system. Due to time constraints, we used non-viral transfection methods to deliver our CRISPR/Cas9 systems into 3T3-L1 cells. However, considering the above options and our lack of success so far, using a viral delivery system for this study may need to be considered for future work.

Finally, in our plasmid DNA-mediated CRISPR-Cas9 genome editing experiment (see section [3.3.3.2](#)), we targeted exon 16 out of 23 of the *Efr3a* gene. While this approach was successful in terms of gene modification (**Figures 3.16-17**), selecting an earlier exon for KO experiments is generally more advantageous. Targeting an earlier exon increases the likelihood of producing a complete KO as the disruption occurs closer to the gene's start codon. This early interruption prevents the production of functional protein, ensuring a more definitive loss of gene function. Conversely, targeting a later exon, such as exon 16, may have resulted in a partial KO of EFR3a where truncated or partially functional proteins are still produced. As the EFR3a band for CRISPR/Cas9-treated cells in **Figure 3.17C** does not appear at a lower molecular weight compared to control adipocytes, the former option seems unlikely. However, the function of EFR3a proteins in both control and CRISPR/Cas9-treated cells was not assessed in this study. Therefore, future research could involve subjecting the obtained CRISPR/Cas9-treated clones to a glucose uptake assay, similar to the method used in section [3.3.1.2](#), to evaluate the functionality of EFR3a in these cells.

Chapter 4 - Optimising Single-Molecule Localisation Microscopy for Advanced Analysis of GLUT4 Dispersal at the Plasma Membrane

4.1 Chapter 4 - Introduction

4.1.1 GLUT4 Dispersal and Clustering: Size of Clusters and Effects on Activity

With the advance of SRM, the macro-organisation of membrane proteins within the PM specifically, has received much attention, enhancing our understanding of the regulation of oligomerisation (Kasai and Kusumi, 2014; Levental and Lyman, 2023; Sych et al., 2022), the assembly of mobile and non-mobile structures (Jaqaman et al., 2011; Levental and Lyman, 2023; Sych et al., 2022; Trimble and Grinstein, 2015), the role of lipid rafts (Kusumi et al., 2020), and the concept of transient confinement zones (Godó et al., 2021; Kusumi et al., 2020). Hence, there is an increasing understanding that the regulation of proteins within the PM can have significant implications on their function, as has been suggested by studies on GLUT4 dispersal described above (see Chapter 3).

Increased understanding inevitably leads to more focused questions about, for instance, the size of clusters and their effects on glucose transporter activity. Using dSTORM, Yan et al. studied the behaviour of GLUT1 at the cell surface of HeLa cells (Yan et al., 2018). Their results showed that GLUT1 molecules form clusters, which are suggested to be regulated by lipid rafts, the actin cytoskeleton, and glycosylation of GLUT1. Clusters were observed to possess an average diameter of 250 nm on the

apical membrane (i.e., medium-exposed membrane) and 137 nm on the basal surface of cells (i.e., facing the coverslip) (Yan et al., 2018). Estimations of the number of GLUT1 in these structures revealed that the majority contained between two and four molecules and that approximately 35% of these clusters were associated with lipid rafts. While these data provide clear evidence in favour of GLUT1 adopting a clustered state, it should be noted that these estimates are subject to the linkage error of labelling antibodies, as previously described (see section [1.4.1.2.2](#)). Hence, the precise stoichiometry of these clusters remains uncertain. It is important to clarify that previous studies performed in our laboratory using dSTORM, mentioned in the above chapter (see section [3.1.2](#)), are subject to similar limitations; thus, our reluctance to quantify the numbers of GLUT4 molecules per cluster under control and EFR3a KD conditions at the time (Koester et al., 2022a; Koester et al., 2022b). This is a challenge we will address in this chapter.

Nevertheless, Yan et al. considered how GLUT1 clustering may be related to its activity. Both methyl-cyclodextrin (a cholesterol-depletion agent) and sodium azide (a metabolic poison) are known to mediate a small increase in glucose transport in HeLa cells. dSTORM analysis suggested that upon treatment with these agents, the number of GLUT1 monomers increased while the apparent diameter of clusters decreased. These results further indicate that the activation of GLUT1 might correlate with changes in the molecular organisation of its clusters (Yan et al., 2018). However, it remains important to remember the concerns about cluster size quantification mentioned above when interpreting these results. While correlative, these observations provide a further potential link between GLUT dispersal and increased activity. Using classical kinetic approaches, GLUT1

oligomerisation has been implicated in the control of transport activity, but how this oligomerisation relates to clusters reported by dSTORM remains uncertain (Cloherty et al., 2001; Coderre et al., 1995; Diamond and Carruthers, 1993). A driver for further consideration of this point has been provided by recent data indicating that some mutations of GLUT1-deficiency syndrome, involving reduced expression or loss of function of GLUT1 in the brain, may impact GLUT1 oligomerisation (Raja and Kinne, 2020). This is an exciting area of research worthy of further investigation.

Using dSTORM datasets from control and EFR3a KD adipocytes, Koester et al. used a recently described ImageJ plug-in (van de Linde, 2019) to quantify the amount of GLUT4 molecules present at the PM (\neq within clusters). While the KD of EFR3a significantly decreased GLUT4 dispersal at the PM, total levels of GLUT4 in both control and EFR3a KD cells appeared to be similar, suggesting that EFR3a is not engaged in the translocation of GLUT4 to the PM (Koester et al., 2022b). Under the same conditions, however, insulin-stimulated glucose transport is impaired upon EFR3a KD. Hence, similarly to GLUT1, these (correlative) findings further suggest that regulation of dispersal may represent a physiological control mechanism for this group of transport proteins. Further studies are needed to evaluate this hypothesis. However, to further our understanding of GLUT4 at the PM using SRM, it has become evident and essential to enhance the localisation precision of SMLM techniques. Such an improvement will allow for the accurate quantification of GLUT4 in clusters and provide deeper insights into the mechanisms regulating GLUT4 activity at the PM.

4.1.2 *Exchange-PAINT: The True Power of DNA-PAINT*

As previously explained, DNA-PAINT uses pairs of imaging-docking oligonucleotides to bypass the diffraction barrier of light. Fluorophore-labelled imaging strands transiently hybridise to their complementary docking DNA strands, previously labelled onto the molecular target of interest, creating the observed blinking behaviour in SMLM. Imaged over several thousand frames, these blinking events allow for the temporal separation of detected fluorescent signals, which can then be regrouped into one final super-resolved image (see section [1.4.1.2.2](#)).

The programmable nature of DNA, decoupling both the blinking properties of SMLM and the molecular identity of the studied targets from the imaged fluorophore, has led to several improvements over more traditional super-resolution approaches. One of the most promising is using DNA-based imaging probes to enable high 'multiplexing' of target detection by Exchange-PAINT (Jungmann et al., 2014; Schnitzbauer et al., 2017). While the use of photo-switchable fluorophores in dSTORM limits options for multi-target/colour imaging as different dyes with good blinking properties often have different buffer requirements and are therefore difficult to combine (Valli et al., 2021), sequential fluid exchange or multiplexing of distinct imaging strands can be achieved more easily in DNA-PAINT. Exchange-PAINT allows imaging strands of a selected target to be washed off and exchanged to introduce a different imager strand species. Multiple rounds can be performed one after the other to image numerous biological targets without spatial overlapping issues (Jungmann et al., 2014). As only one imager species is present in the solution in each imaging round, using different fluorophores for each new DNA sequence is not required. In theory, Exchange-PAINT can facilitate spatially unlimited multiplexing, one of the only limitations being the orthogonality of DNA

sequences and the availability of immunolabelling probes for the selected biological targets. Additionally, the preparation of samples for Exchange-PAINT is similar to that for singleplex experiments, the only difference being the requirement of a perfusion chamber allowing for fluid exchange (Schnitzbauer et al., 2017). A point we will return to below (see sections [4.1.3](#) and [4.3.1](#)).

In recent years, several adaptations to the DNA-PAINT system have been introduced and further applied to Exchange-PAINT. While some allow for brighter and faster Exchange-PAINT imaging through the design of novel transient probes (Lycas and Manley, 2024), others have improved the spatial resolution of DNA-PAINT into the Ångström scale using resolution enhancement by sequential imaging. By sequentially imaging sparse target subsets at moderate spatial resolutions of approximately 15 nm, Reinhardt et al. demonstrate that single-protein resolution can be achieved in biological contexts, bypassing the labelling linkage issue (see section [4.1.4](#)) and closing the gap between SRM and structural biology (Reinhardt et al., 2023).

In our quest to understand insulin-stimulated GLUT4 dispersal at the PM of adipocytes, sequential multicolour imaging methods, such as Exchange-PAINT, would, therefore, allow us not only to further clarify how EFR3a and PI4K-IIIa relate to GLUT4 dynamics and how the insulin signalling pathway interacts with this machinery but also provide deeper insights into the stoichiometry of GLUT4 clustering, all from a single, super-resolved multiplexed image.

4.1.3 Super-Resolution Microscopy:

An Open-Source Hardware Initiative

While SRM allows for better detection methods to achieve improved spatial resolution, opening the range of structures and biological processes that can be studied, it remains a relatively new technology, perceived by many as complex, expensive, and time-consuming. In particular, the specific hardware requirements for SRM have been of particular concern for biologists. For instance, syringe pumps are basic and excellent tools used in many different areas of research, from physics (Zeng et al., 2015), flow chemistry (Zhao et al., 2018) to microfluidics (Convery and Gadegaard, 2019), that have now reached SRM. Sequential multicolour imaging methods, such as Exchange-PAINT (see section [4.1.2](#)), are powerful techniques for biological research. However, they typically require expensive fluidic setups to allow multiple rounds of buffer exchange, adding to the complexity of a super-resolution imaging system (Jungmann et al., 2014; Schnitzbauer et al., 2017).

To help researchers access and use advanced microscopy in a simpler way so that everyone can benefit from this powerful technology, the past decade has seen the emergence of a range of open-source hardware initiatives in microscopy (Hohlbein et al., 2022), simultaneously seeking to improve reproducibility, transparency, and sharing of resources (UNESCO, 2021). As a result, the availability of imaging setup descriptions and blueprints has helped make SRM more accessible, leading many groups to switch to a low-cost do-it-yourself (DIY) approach. An example of this movement's outcomes is the MesoSPIM initiative, which allows researchers to build their own light sheet system, enabling imaging of specimens up to 1 cm³ with 6.5 μm isotropic resolution (Voigt et al., 2019).

The rapid evolution of 3D printing technologies has also provided new opportunities to make microscopy more accessible, particularly in low-resource settings (Baden et al., 2015). On the one hand, fused deposition modelling (FDM) printing represents a well-established method for manufacturing large models with high mechanical stability from the heated plastic filament. Using FDM, the OpenFlexure project successfully produced a high-performing, customisable, open-source optical microscope (Collins et al., 2020). On the other hand, high-precision 3D-printed elements, such as optical lenses, can be obtained using resin-based methods such as stereolithography (Christopher et al., 2024; Rooney et al., 2024).

Similarly, numerous DIY fluidic systems have been published over the years. While one group used Lego blocks to build a set of syringe pumps, allowing for super-resolved multiplexed STORM and DNA-PAINT experiments (Almada et al., 2019), others took advantage of the ever-growing field of 3D printing mentioned above (Booeshaghi et al., 2019). While these DIY approaches represent excellent opportunities to enter the open-source hardware DIY field, some have highlighted the limits of these systems, i.e., the knowledge of electronics and programming that is usually required to build these pumps. To bypass these issues, Bass and Saggiomo shared how to repurpose the electronics and mechanics of a Creality Ender-3 3D printer, one of the cheapest FDM printers on the market, for building and controlling via G-code (3D printer programming language) a set of perfusion syringes (Baas and Saggiomo, 2021).

Such open-source approaches have allowed for the simple and cheap acquisition of microscopy hardware, independent of funding and previous expert knowledge.

4.1.4 The Labelling Linkage Issue in Single-Molecule Localisation Microscopy

SMLM methods enable the visualisation of structures smaller than the diffraction limit by capturing images of sparse populations of fluorophores that are iteratively made visible, ensuring that only a few single molecules are detected at any given time. These isolated signals, recorded over several thousand frames, are then reconstructed into super-resolved images (see section [1.4.1.2.2](#)). However, as discussed above, the use of labelling probes to attach a fluorescent marker to a target molecule inherently creates a spatial offset between the target's true location and the fluorophore's observed position. This phenomenon, known as the labelling linkage error, becomes particularly critical in SMLM, where the precision of detecting individual molecules depends heavily on how accurately their localisation can be predicted. Thus, the linkage error directly impacts the LP achievable in these imaging techniques. When positioned further away from each other than the LP of a system, it is possible to distinguish two single molecular targets. However, suppose the labelling linkage error causes the LP radius of two targets to overlap. In that case, it may lead to a misinterpretation of the spatial arrangement and positions of the imaged molecular targets. It is, therefore, crucial to carefully consider the labelling strategies of a molecular target in SMLM to maximise the precision and reliability of obtained datasets.

A common labelling method for SMLM is the immunolabeling of the molecular target of interest with either a single primary antibody (direct labelling) or a combination of primary and secondary antibodies (indirect labelling). While dSTORM has been shown to generate consistent imaging datasets over the years, its requirement for fluorescently labelled antibodies introduces a localisation offset of approximately 10 nm per antibody (Ries et al., 2012) and up to 25 nm when using indirect immunolabelling in biological contexts (Banerjee et al., 2023; Koester et al., 2022b; Maidorn et al., 2016; Ries et al., 2012), ultimately limiting localisation measurement accuracy of the studied molecular targets. DNA-PAINT uses fluorescently labelled imaging-docking strand pairings of typically ten nucleotides in length, which were shown to enable ultra-sub-5-nm spatial resolution and reach close to 1 nm LP on DNA nanostructures (Jungmann et al., 2010; Schnitzbauer et al., 2017). However, as for dSTORM, the requirement of docking strands labelling onto the molecular target of interest and how this is achieved also significantly impacts the localisation accuracy of DNA-PAINT systems in biological contexts.

The conjugation of docking strands to antibodies can be achieved through various chemical methods. Biotin-avidin and covalent coupling are the most widely used strategies (Banerjee et al., 2023). Initial implementations of DNA-PAINT for cellular target imaging used commercially available biotin-modified antibodies and streptavidin to link biotinylated docking strands to the target of interest (Jungmann et al., 2010). Due to its low cost, this biotin-avidin coupling strategy has prevailed as a DNA-PAINT labelling strategy. However, streptavidin is a tetramer with a 5 nm diameter (Kuzuya et al., 2008), contributing to the linkage error issue. As a result, biotin-avidin

strategies are commonly favoured during the optimisation phase of DNA-PAINT projects. In contrast, the preferred coupling strategy in a DNA-PAINT final imaging system has been defined as the covalent conjugation of docking strands to antibodies using chemical crosslinking strategies such as amine-NHS conjugation. Yet, ultimately, the linkage error of antibodies remains the primary linkage issue in SMLM systems. In addition to the systematic localisation offset that it introduces between fluorophores and molecular targets, the intramolecular flexibility and the random attachment sites of antibodies increase localisation imprecision.

This antibody linkage error can be somewhat minimised through post-processing analysis (Koester et al., 2022b) or by using smaller labelling probes. The use of single-domain antibodies, for instance, also known as nanobodies (Hamers-Casterman et al., 1993), has gained popularity in recent years in the field of SRM (Fabricius et al., 2018; Mikhaylova et al., 2015). Nanobodies are obtained from unconventional camelid heavy chain antibodies, resulting in a functional probe of only 2-3 nm in size (Kirchhofer et al., 2010). Nanobody-based DNA-PAINT, therefore, has emerged as an efficient solution to the labelling linkage issue, allowing the exploitation of the full power of DNA-PAINT for cellular imaging. Unfortunately, as for the covalent coupling of DNA strands, nanobodies remain an expensive technology that is not yet widely commercialised, limiting availabilities to many targets (see section [4.1.5](#)).

4.1.5 The HA-Tag: Success, Limitations, and Alternative

As previously explained (see section [1.4](#)), from 1996 (Dobson et al., 1996), the use of GLUT4-GFP transgenic constructs has laid the foundations for

many studies using fluorescence microscopy to investigate GLUT4 trafficking at the PM. The addition of an HA-tag to the first exofacial loop of the latter construct has then allowed the distinction between intracellular and PM-fused GLUT4 populations. More specifically, the combination of the HA-GLUT4-GFP construct and SRM techniques has been instrumental in advancing our understanding of GLUT4 dynamics at the PM of adipocytes. This includes its clustering behaviour, subsequent insulin-stimulated dispersal (see section [1.4.3](#)), and the influence of various regulatory proteins within this machinery (Koester et al., 2022b). This comprehensive insight is crucial for understanding the cellular basis of insulin resistance (Koester et al., 2022a) and other metabolic disorders, offering potential avenues for therapeutic intervention.

However, many questions remain unanswered about the clustering nature of GLUT4 and how these uncertainties relate to the limitations of certain SRM techniques have been highlighted above (see sections [4.1.1](#) and [4.1.4](#)). The labelling linkage issue in SMLM has previously hindered the accurate quantification of GLUT4 molecules within clusters at the PM of 3T3-L1 adipocytes expressing the HA-GLUT4-GFP construct (see section [4.1.1](#)). Using indirect labelling of the HA-tag, Koester et al. achieved a LP of 25 nm using dSTORM. Although these data indicate that GLUT4 abides in a clustered state under insulin stimulation in EFR3a KD adipocytes, the precise stoichiometry of these clusters remained uncertain due to the antibody linkage error obscuring the true density and organisation of GLUT4 clusters (Koester et al., 2022a; Koester et al., 2022b).

As previously mentioned (see section [4.1.4](#)), different labelling strategies have been developed to minimise this antibody linkage error. The most

prominent one is the use of single-domain antibodies, also known as nanobodies, of only a few nm in size (Kirchhofer et al., 2010). The HA-tag (Field et al., 1988), with its 9-amino acid sequence, YPYDVPDYA, derived from the human influenza hemagglutinin protein (Field et al., 1988), is well-established and widely used in molecular biology. However, while the availability of high-quality anti-HA antibodies and related reagents from multiple suppliers boosted its popularity, the small number of commercially available nanobodies for HA-tag detection makes it suboptimal for SRM.

In contrast, the ALFA-tag, developed by NanoTag Biotechnologies, is a 13-amino acid sequence (SRLEEELRRRLTE) which forms a stable α -helix. It was designed for improved performance in detection and purification applications, featuring high affinity and specificity for its corresponding developed nanobody (Götzke et al., 2019).

4.1.6 Chapter 4 - Aims

Building on our laboratory's previous work showing the impact of EFR3a on PM-fused GLUT4 using dSTORM (Koester et al., 2022b), this chapter aims to develop a DNA-PAINT, and more specifically, an Exchange-PAINT imaging system, allowing for enhanced single-molecule localisation accuracy. This first involved the development of a perfusion system based on the work of Baas and Saggiomo on adapting an FDM 3D printer for this purpose (Baas and Saggiomo, 2021). The long-term goal of this system is to use Exchange-PAINT to further test and characterise at a single-molecular level the hypothesised EFR3a/PI4K-III α -regulated GLUT4 dispersal model described in Chapter 3 (see section [3.1.2](#)).

Therefore, as HA-GLUT4-GFP currently remains the most accessible and established construct for the study of GLUT4 at the PM, we next aimed to address the labelling linkage error associated with the HA-tag by evaluating the immunofluorescence staining capabilities of a biotin-conjugated anti-HA nanobody developed by ABclonal (see section [2.1.2](#)). By doing so, we aimed to determine the potential for this nanobody to enhance the LP of future DNA-PAINT experiments.

As an alternative to the HA-GLUT4-GFP construct, we aimed to characterise a newly developed recombinant GLUT4 construct with an inserted ALFA-tag on its first exofacial loop designed by our group (see Appendix [7.2.2.2](#)). The ability of ALFA-GLUT4 to translocate to the PM in response to insulin was initially investigated and compared with that of the HA-GLUT4-GFP construct through immunofluorescence analysis in transiently transfected HEK293 cells. Following the confirmation of these results, we sought to generate a stable cell line. Finally, immunofluorescence and sub-cellular fractionation of insulin-stimulated HEK293 cells expressing stably transfected ALFA-GLUT4 were used to assess whether this new construct mimics the trafficking journey of endogenous GLUT4.

4.2 Chapter 4 - List of Methods

The methods below have been used in this chapter and are further detailed in section 2.2.

2.2.1 Cell Culture

2.2.1.1 3T3-L1 Fibroblasts Growth and Maintenance

2.2.1.2 3T3-L1 Adipocyte Differentiation

2.2.1.3 Insulin Stimulation of 3T3-L1 Adipocytes

2.2.1.7 HEK295 Cells Growth, Maintenance, and Insulin Stimulation

2.2.1.8 Plasmid DNA Transfection in HEK295 Cells

2.2.1.9 Generation of ALFA-GLUT4 Stable HEK293 Cell Lines:
G418 Selection and Clone Isolation

2.2.3 Cell Lysates and Tissue Homogenates

2.2.3.3 3T3-L1 and HEK295 Whole Cells Lysate

2.2.4 Cellular Methods

2.2.4.1 Sub-Cellular Fractionation of 3T3-L1 Adipocytes
and HEK295 Cells

2.2.5 Protein-Specific Assays

2.2.5.1 Bicinchoninic Acid Assay and Sample Preparation
for Immunoblotting

2.2.5.2 SDS-PAGE

2.2.5.3 Wet Transfer

2.2.5.5 Immunoblotting

2.2.7 Microscopy

2.2.7.1 Sample Preparation

2.2.7.1.1 Cellular Fixation, Immunofluorescent,
and Permanent DNA-PAINT Staining

2.2.7.1.3 Single-Molecule Surfaces for DNA-PAINT Imaging

2.2.7.2 Imaging Setups and Data Acquisition

2.2.7.2.2 Perfusion Syringe System and
pH Measurement Experiment

2.2.7.2.3 Single-Molecule Localisation Microscope

2.2.7.2.4 Confocal Microscope

2.2.8 Data and Statistical Analyses

2.2.8.1 Densitometry

2.2.8.3 DNA-PAINT Data Analysis

4.3 Chapter 4 - Results

4.3.1 *A Journey Toward Exchange-PAINT*

4.3.1.1 Fluid Transfer Accuracy of a Homemade Perfusion System

As previously highlighted, both dSTORM and DNA-PAINT are powerful SRM techniques with unique strengths. While both currently offer similar spatial resolution capabilities in biological contexts, generally around 20 nm (see section [4.1.4](#)), DNA-PAINT has the potential to reach greater resolution due to the precision of DNA hybridisation and increased imaging speed (Lycas and Manley, 2024; Reinhardt et al., 2023) (see section [4.1.2](#)).

Adapting DNA-PAINT technologies, Exchange-PAINT can further allow for the multiplexing of distinct imaging strands to their complementary docking strands on multiple molecular targets within the same sample without spatial overlap issues (Jungmann et al., 2014). This is primarily possible by using fluidic systems to deliver specific imager strands to the sample in a controlled manner, ensuring that only one type of imager strand is present during each imaging cycle. Fluidic systems facilitate thorough washing between imaging cycles, reducing background fluorescence and photobleaching, which help maintain high imaging quality. Additionally, accurate fluid transfer on and off the sample plays an important role in Exchange-PAINT, allowing for precise control and adjustment of the concentration and flow of imaging strands during the imaging process. During the optimisation phase, this feature provides real-

time feedback and allows for immediate changes to the imaging strand concentration to be applied, enhancing the overall imaging process. In contrast, dSTORM does not allow for real-time adjustments once the imaging has begun. Any changes would need to be planned and executed prior to an imaging session, limiting the utility of this approach.

In this section, as the initial step towards creating a fully functional Exchange-PAINT imaging system, we utilised an open-source approach (see section [4.1.3](#)) to build a perfusion system based on the work of Baas and Saggiomo and Schnitzbauer et al. (Baas and Saggiomo, 2021; Schnitzbauer et al., 2017). This involved modifying a Creality Ender-3 V2 3D printer to create a set of perfusion syringes, as described in [2.2.7.2.2](#), at a total cost of £180. To demonstrate the system's precision in fluid delivery (i.e., how close the delivered fluid volume is to the intended volume), we first measured the pH of delivered fluid volumes and compared them to pH values obtained from manual pipetting. Overall, 21 measurements were performed, with expected pH ranging from 6.3 to 8.4. While the experiment was only performed once, results showed that the perfusion syringe system processed relatively high accuracy in delivering fluid volumes, with the largest difference between the perfusion system and manual pipetting pH values obtained being 0.07 (measurement 10) (**Figure 4.1**).

Overall, this homemade perfusion system appears to be reliable for precise fluid delivery in applications such as Exchange-PAINT.

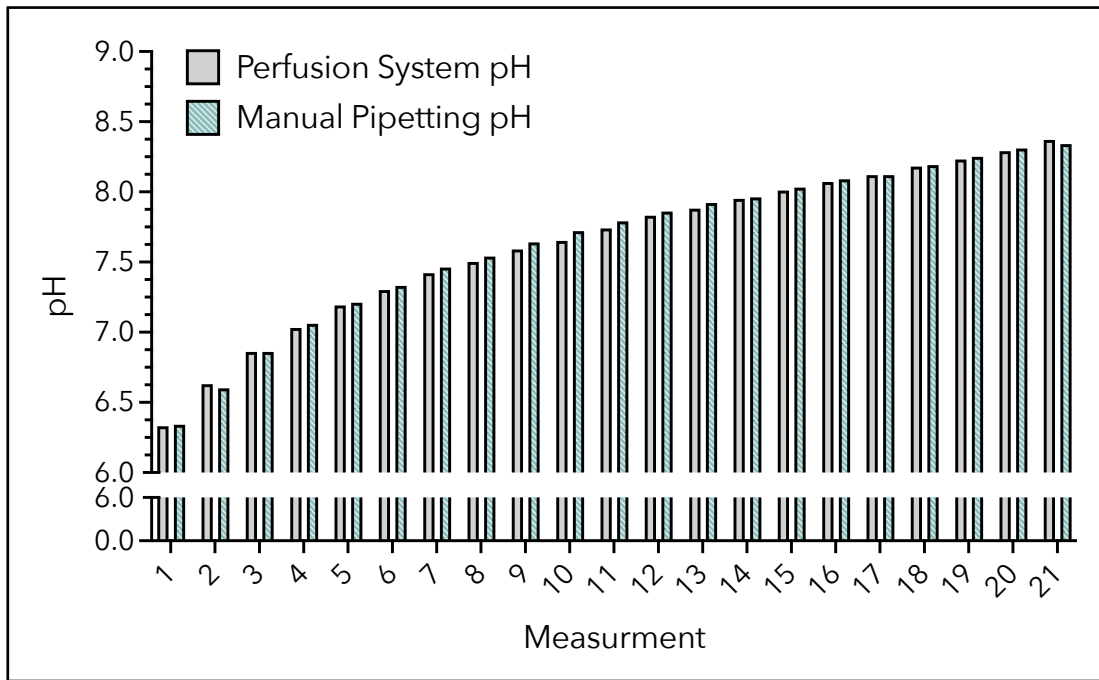


Figure 4.1. pH Measurements Accuracy between Homemade Perfusion Syringe System and Manual Pipetting.

Comparison of pH values obtained from delivered fluid volumes (grey) and manual pipetting (blue). 21 measurements were performed, with the expected pH ranging from 6.3 to 8.4. Perfusion system and manual dilutions were performed simultaneously as described in [2.2.7.2.2](#) (n = 1). pH values were measured with an Oakton 700 pH Meter. Measured pH values showed low deviation, indicating relatively high accuracy in the delivered volume by the homemade perfusion syringe system.

4.3.1.2 Automatised DNA-PAINT Imaging using a Homemade Perfusion System

In addition to accurate fluid delivery, automation is paramount in a perfusion system for Exchange-PAINT. Automated systems ensure consistent and reproducible results, streamline complex sequential delivery of different imager strands, and allow dynamic adjustments. Consequently, to evaluate our perfusion system's effectiveness and automation capabilities in a DNA-PAINT experiment, we tested the system's

ability to adjust the concentration of imaging strands over time (15,000 frames; see section [2.2.7.2.3](#)). We first prepared single-molecule surfaces for DNA-PAINT imaging and programmed the perfusion system using G-code to automatically vary the concentration of imaging strands during the imaging sessions (see sections [2.2.7.1.3](#), [2.2.7.2.3](#), and Appendix [7.4](#)). We tested two different imaging strand concentration profiles: a 0 to 100% pulse profile (**Figure 4.2A**) and a stepwise increase and decrease profile (**Figure 4.2B**).

The 0 to 100% pulse profile (**Figure 4.2A**), where 0% corresponded to 0 nM of the imaging strand and 100% corresponded to 0.3 nM, first demonstrated the system's ability to handle abrupt changes in imaging strand concentration without disrupting the imaging process. Over three pulses, the average number of blinking events reached 13800, with a coefficient of variation of 2.115%. Between pulses, however, the number of blinking events did not return to 0, indicating that the time between each pulse was insufficient for all imaging strands to be fully washed out. This hysteresis can be easily corrected by increasing the time between pulses, a modification that can be implemented with minimal effort by simply reprogramming the system.

For testing of a stepwise concentration profile, the imaging strand concentration was incrementally increased from 0 to 0.1, to 0.2, and finally to 0.3 nM. This was followed by a reverse stepwise decrease of these same concentrations. As depicted in **figure 4.2B**, each concentration adjustment resulted in clear increases and decreases in blinking events. This demonstrates the system's high accuracy and transition capability between different imaging strand concentrations.

Overall, the adaptability of this perfusion syringe system is crucial for optimising imaging conditions on the fly and demonstrates the potential for significant time and resource savings in DNA-PAINT experiments.

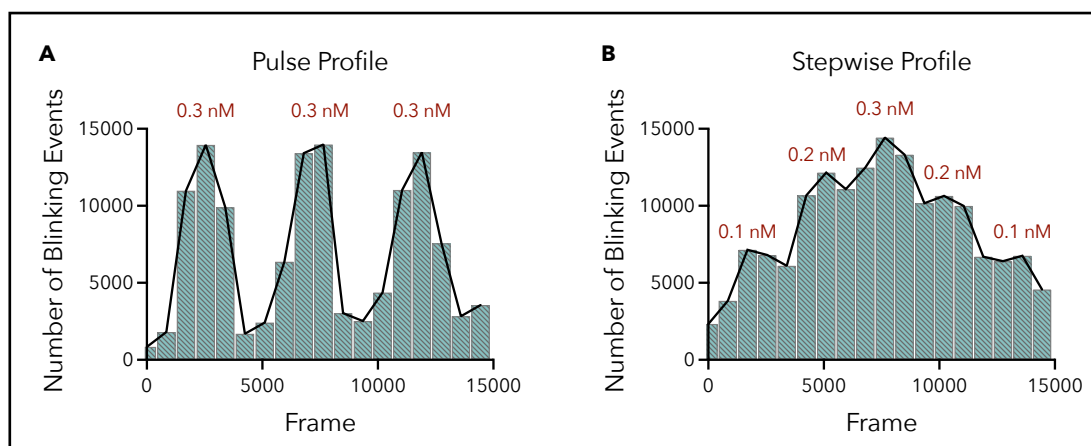


Figure 4.2. Blinking Event Profiles Under Automated DNA-PAINT Imaging Strand Perfusion Using a Homemade Perfusion Syringe System.

These histograms illustrate the number of blinking events observed during DNA-PAINT experiments, as described in sections [2.2.7.1.3](#), [2.2.7.2.3](#), and [Appendix 7.4](#), over 15,000 recorded frames. The x-axis is divided into bins (blue) of 850 frames each, starting from frame one and ending at the last frame of the experiment. Each bin represents the number of blinking events recorded within its 850-frame interval. The y-axis shows the count of blinking events per bin. The concentrations of imaging strands at different frames are indicated in red above the respective peaks or steps. (A) 0 to 100% pulse profile plots three successive pulses of 0.3 nM (100%) concentration, each causing a peak in blinking events. (B) Stepwise increase and decrease profiles show blinking events for imaging strand concentrations increasing from 0.1 nM to 0.2 nM and 0.3 nM, then decreasing back to 0.1 nM. The gradual increase and decrease in blinking events match the changes in concentration.

4.3.2 *A New Probe for GLUT4 Imaging at the Plasma Membrane: Reducing the Labelling Linkage Error*

4.3.2.1 Identification and Characterisation of an HA-Tag Nanobody: Redemption of the HA-GLUT4-GFP Construct?

As mentioned above, extending the use of the HA-GLUT4-GFP construct to SRM is hindered by the lack of accessible nanobodies specific to the HA-tag, which contributes to the antibody linkage error and compromises LP in super-resolution imaging. In a promising development, we identified an anti-HA-tag nanobody developed by ABclonal (see section [2.1.2](#)), which is biotin-conjugated, potentially allowing for the improvement of the antibody linkage error issue in SMLM experiments. This biotinylated nanobody was considered particularly suitable for DNA-PAINT, whose main labelling strategy involves using biotin-modified antibodies and avidin proteins to connect biotinylated docking strands to the target of interest (see section [4.1.4](#)). This HA-tag-directed nanobody could, therefore, be applied in DNA-PAINT and further in Exchange-PAINT experiments, enabling the accurate quantification of GLUT4 molecule numbers in clusters at the PM, a measurement that was previously challenging to achieve using dSTORM (Koester et al., 2022a; Koester et al., 2022b).

To test whether the identified anti-HA-tag nanobody effectively binds to its target, we examined its performance in 3T3-L1 adipocytes stably expressing the HA-GLUT4-GFP construct, with the expectation that it would allow for the distinction between intracellular GLUT4-GFP and PM-fused and immunostained HA-tagged GLUT4 under insulin stimulation. We

compared multiple HA-tag labelling strategies, including indirect immunolabelling and DNA-PAINT labelling, using a known biotin-HA-tag antibody or the new biotin-conjugated nanobody. While DNA-PAINT typically relies on the transient binding of fluorescently labelled DNA imaging strands to complementary docking strands attached to the molecular target, in this section, we employed imaging strands that form a permanent bond with the docking strands (see section [2.2.7.1.1](#)). This modification enabled the subsequent visualisation of labelled structures using confocal microscopy (see section [2.2.7.2.4](#)), allowing for a detailed comparison of the different labelling techniques' effectiveness in identifying PM-bound GLUT4.

The results demonstrated no fluorescent staining when using the biotin-anti-HA-tag nanobody (**Figure 4.3D**), in contrast to the distinct staining observed around the PM with indirect immunostaining and DNA-PAINT labelling using biotin-anti-HA antibodies (positive controls; **Figure 4.3A, B**). Various concentrations of the nanobody, from 1:200 to 1:50, were tested; only the results from the 1:50 dilution are shown here. At all tested concentrations, the nanobody produced similar outcomes to that of DNA-PAINT antibody labelling without the addition of imaging strands (negative control; **Figure 4.3C**). These findings, therefore, suggest ineffective binding of the identified nanobody to the HA-tag at the PM of insulin-stimulated 3T3-L1 adipocytes, rendering it unsuitable for further DNA-PAINT experiments. Meanwhile, the GLUT4-GFP signal remained consistent across all conditions (**Figure 4.3**), further supporting the assertion that the nanobody staining is not functioning as expected. The anti-HA nanobody assessed here was initially developed to be conjugated to agarose beads

for immunoprecipitation assays. This might explain its lack of functionality in this context.

Therefore, we decided to focus our efforts on characterising a new probe for imaging GLUT4 at the PM, namely the ALFA-GLUT4 construct (see section [4.3.2.2](#)).

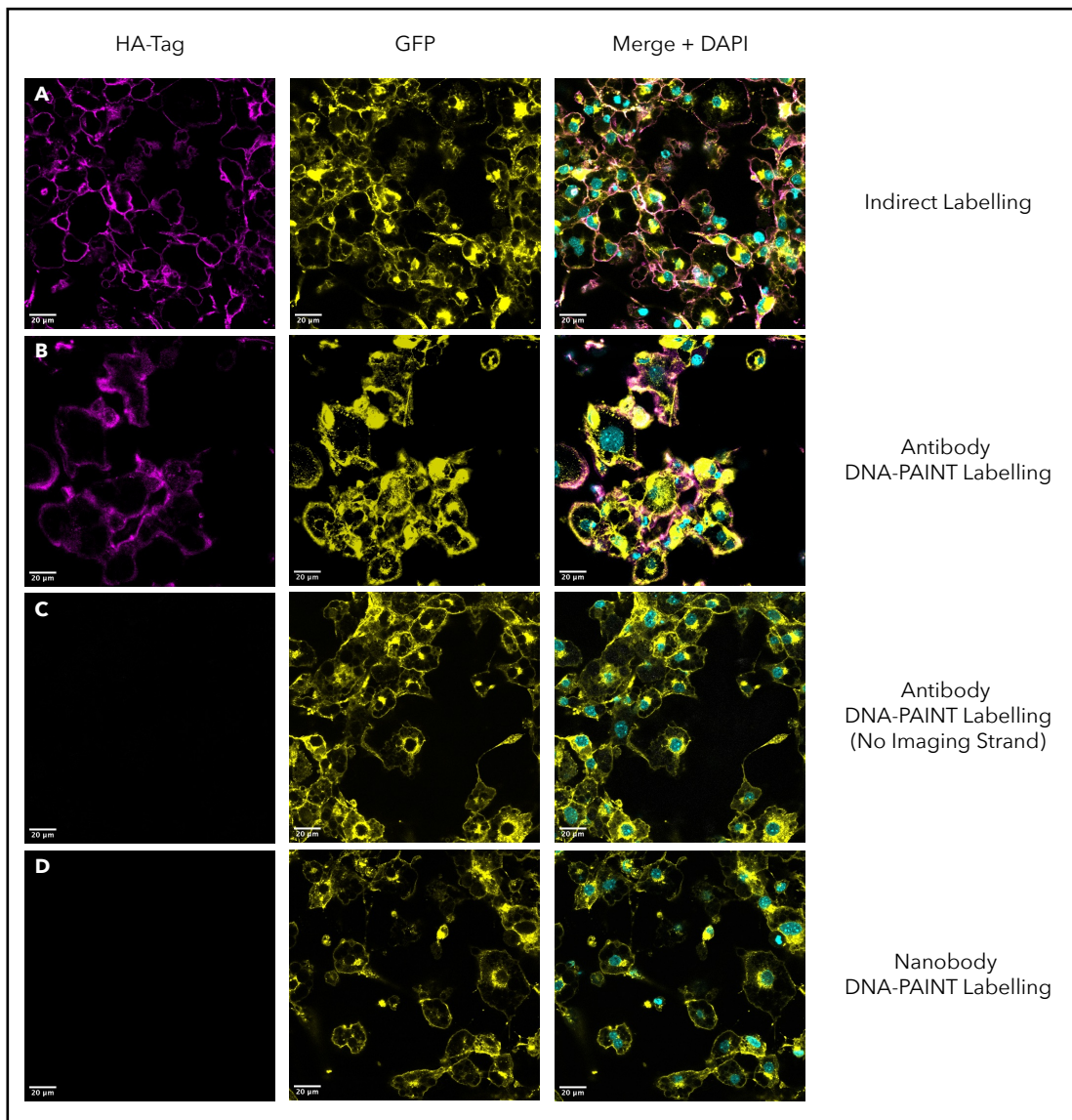


Figure 4.3. Representative Immunofluorescence and DNA-PAINT Staining of the HA-Tag using Different Labelling Strategies in 3T3-L1 HA-GLUT4-GFP Adipocytes.

Representative confocal images of 3T3-L1 HA-GLUT4-GFP adipocytes treated with 100 nM insulin for 20 min (n = 2). Left Panel: Confocal images of immunostained HA-tag fluorescence (magenta) using indirect immunostaining (A), permanent DNA-PAINT labelling using biotin-anti-HA antibody (B), DNA-PAINT labelling using biotin-anti-HA antibody in the absence of imaging strands (C), and permanent DNA-PAINT labelling using biotin-anti-HA nanobody (D). Middle Panel: Confocal images of GFP fluorescence (yellow). Right Panel: Merge and DAPI fluorescence (cyan). Cells were fixed and immunostained as described in [2.2.7.1.1](#). For indirect labelling (A), secondary antibodies labelled with Alexa Fluor® 647 were used (see section [2.1.2](#)) and imaging DNA strands labelled with ATTO655 were used for DNA-PAINT labelling (B, D). All images were acquired using a 40× water immersion objective on a Leica TCS SP8 confocal microscope (see section [2.2.7.2.4](#)). Scale Bars = 20 µm.

4.3.2.2 Characterisation of the ALFA-GLUT4 Construct as a New Probe for GLUT4 Imaging at the Plasma Membrane

This section presents results obtained in part by Roisin Kelly, a master's student I supervised during this thesis. Additionally, for cost-efficient reasons, an anti-ALFA-tag antibody (see section [2.1.2](#)) from the same company that developed the ALFA-tag-nanobody pair was used for the initial characterisation of the new ALFA-GUT4 construct.

4.3.2.2.1 Insulin-Stimulated Translocation of ALFA-GLUT4 in Transiently Transfected HEK293 Cells

A plasmid was custom-synthesised to express GLUT4 with an ALFA-

tag inserted into its first exofacial loop (see Appendix [7.2.2.2](#)). This modification was made in place of the commonly used HA-tag (see Appendix [7.2.2.3](#)). The substitution of the HA-tag with the ALFA-tag was intended to leverage the specific interaction between the ALFA-tag and its associated nanobody (Götzke et al., 2019) as a more efficient probe for SRM techniques, such as DNA-PAINT, allowing for improved spatial localisation of GLUT4 at the PM.

HEK293 cells have been shown to express functional IR and show responsiveness to insulin (Borisov et al., 2009; Kellerer et al., 2001; Rossiter et al., 2022). As a result, expressing GLUT4 constructs in HEK293 cells, a human embryonic kidney cell line which does not endogenously express GLUT4, has become a valuable first step in understanding the basic mechanisms of the regulation and trafficking of exogenous epitope-tagged GLUT4. The present study, therefore, provides a simplified and controlled system to characterise the ALFA-GLUT4 construct and lays the groundwork for more detailed investigations in physiologically relevant cell types, such as adipocytes and muscle cells. The capability of ALFA-GLUT4 to translocate to the PM in response to insulin was, therefore, first investigated and compared with that of the HA-GLUT4-GFP construct through immunofluorescent analysis in transiently transfected HEK293 cells.

Figure 4.4A,B depicts HEK293 cells under basal and insulin-stimulated conditions transiently transfected with ALFA-GLUT4, as described in section [2.2.1.8](#). In the absence of insulin (basal state), no cell surface expression of ALFA-GLUT4 was observed. Upon insulin stimulation (see section [2.2.1.7](#)), a marked translocation of ALFA-tagged GLUT4 to the PM occurred after 15 min. This pattern aligns with established data indicating that GLUT4

translocation reaches a steady-state level by 15 to 20 min post-insulin stimulation (Bogan et al., 2001). These findings are consistent with data from **figure 4.4C,D**, which shows HEK293 cells transiently transfected with the well-established HA-GLUT4-GFP construct, where a similar translocation pattern was observed. These results are further corroborated by the previously described immunofluorescence analysis on 3T3-L1 adipocytes stably expressing HA-GLUT4-GFP (**Figure 4.3**).

Overall, these data suggest a conserved mechanism of ALFA-GLUT4 translocation in response to insulin in HEK293 cells, providing confidence to proceed with the next step in this study, which involves generating HEK293 cell lines stably expressing the latter exogenous GLUT4 construct.

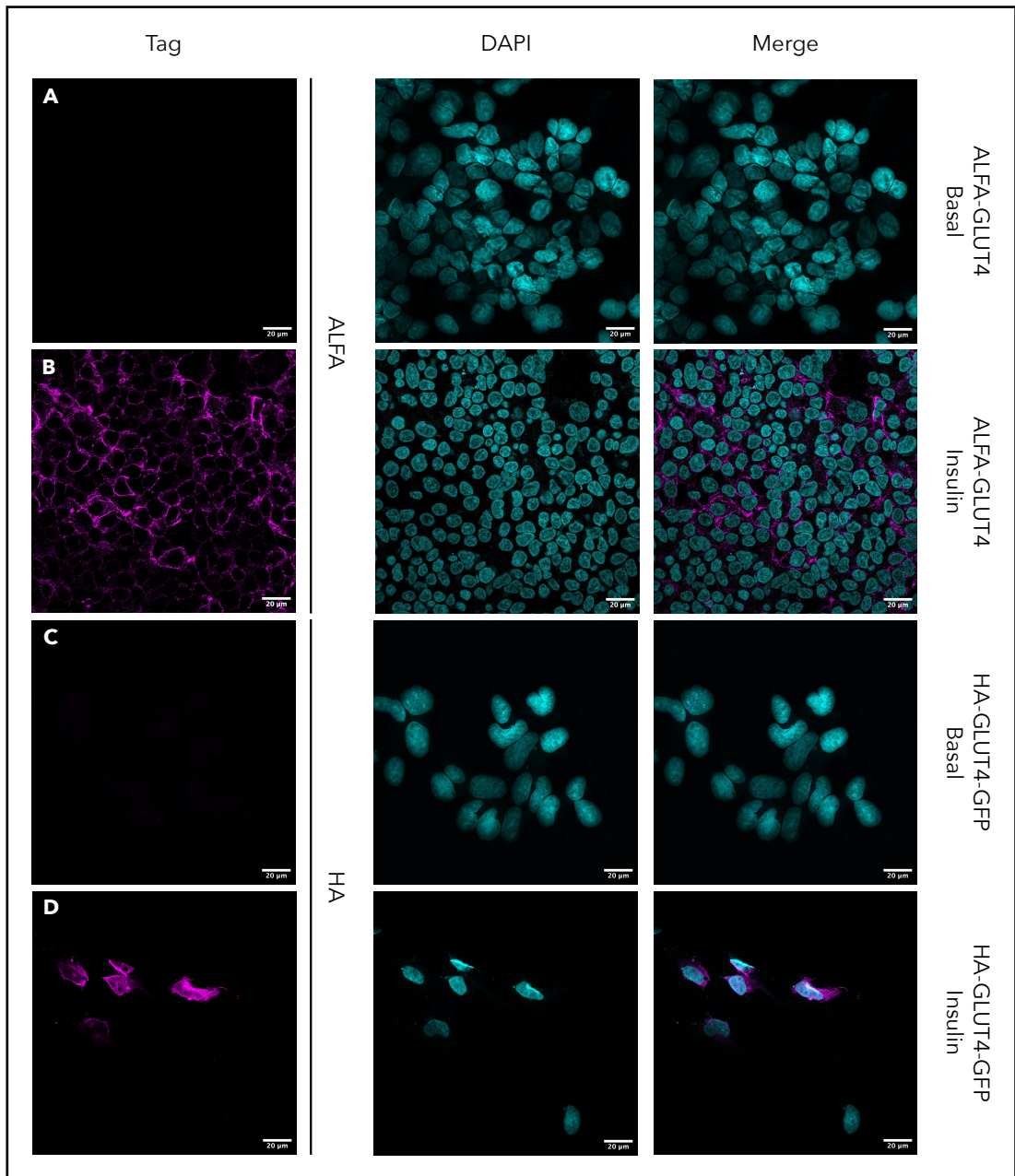


Figure 4.4. Characterisation of ALFA-GLUT4 Insulin-Stimulated Trafficking to the Plasma Membrane in Transiently Transfected HEK293 Cells.

(A,B) Confocal images of HEK293 cells transiently transfected (see section [2.2.1.8](#)) with ALFA-GLUT4 (see Appendix [7.2.2.2](#)), treated without (Basal; A) and with 100 nM insulin for 15 min (B). (C,D) Confocal images of HEK293 cells transiently transfected with HA-GLUT4-GFP (see Appendix [7.2.2.3](#)), treated without (Basal; C) and with 100 nM insulin for 15 min (D). Left Panel: Confocal images of immunostained ALFA- (A,B) or HA-tag (C,D) fluorescence (magenta). Middle Panel: Confocal images of DAPI fluorescence (cyan). Right Panel: Merge epitope tags and DAPI fluorescence (magenta and cyan, respectively). Cells were fixed and immunostained as described in [2.2.7.1.1](#). Secondary antibodies labelled with Alexa Fluor™ 488 and Alexa Fluor® 647 were used from immunostaining of the ALFA- (A,B) and HA-tag (C,D), respectively (see section [2.1.2](#)). All images were acquired using a 40× water immersion objective on a Leica TCS SP8 confocal microscope (see section [2.2.7.2.4](#)). Scale Bars = 20 µm.

4.3.2.2.2 Generation and Characterisation of an ALFA-GLUT4 Stable HEK293 Cell Line

Building on promising data obtained from transient transfection studies (see section [4.3.2.2.1](#)), we aimed to develop HEK293 cell lines stably expressing the ALFA-GLUT4 construct. Creating a stable cell line relied on the transfected plasmid DNA conferring resistance to G418 to isolate clonal cell lines (Durmaz et al., 2022).

We used a G418 concentration of 0.5 mg/mL for the initial selection of stably transfected cells. Subsequently, cells were maintained in 0.1 mg/mL G418, as described in section [2.2.1.9](#). This approach ensured that only cells expressing the resistant ALFA-GLUT4 construct survived, facilitating the

establishment of a stable cell line suitable for further experimental investigations.

To confirm the presence of the ALFA-GLUT4 construct in stably transfected HEK293 cells, both monoclonal (M) and polyclonal (P) cell populations were analysed by immunoblotting. As shown in **figure 4.5**, both cell populations exhibited clear signals for both GLUT4 and the ALFA-tag, indicating successful expression of the transfected construct. In contrast, untransfected HEK293 cells showed no detectable signals for either GLUT4 or the ALFA-tag.

In conclusion, these results verify the successful integration and expression of the ALFA-GLUT4 construct in the isolated HEK293 cell lines.

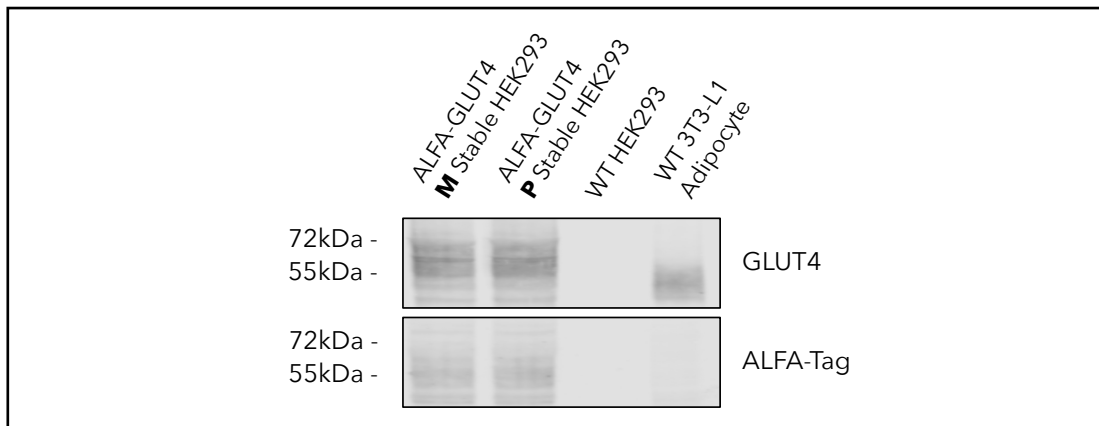


Figure 4.5. Confirmation of ALFA-GLUT4 Expression in Stably Transfected HEK293 Clones.

Immunoblot showing protein contents of GLUT4 and the ALFA-tag in monoclonal (M) and polyclonal (P) HEK293 cell populations stably transfected with the ALFA-GLUT4 DNA plasmid (see Appendix [7.2.2.2](#)), untreated/wild-type (WT) HEK293 cells, and WT 3T3-L1 adipocytes. Results show successful detections of both GLUT4 and the ALFA-tag signals stably transfected HEK293 clones, in contrast to WT HEK293 cells. 3T3-L1 adipocytes, which naturally express GLUT4, served as a positive control for GLUT4 detection but show no ALFA-tag signal. All cell lysates were produced and loaded as described in [2.2.3.3](#) and [2.2.5.2](#). Blots were visualised with a LI-COR Odyssey-SA system.

Following confirmation of the stable ALFA-GLUT4 expression in HEK293 cells, we next assessed whether the ALFA-GLUT4 construct mimics the trafficking pattern of endogenous GLUT4 to the PM upon insulin stimulation in these cells using immunofluorescent staining. As illustrated in **figure 4.6A,B**, detection of the ALFA-tag revealed the translocation of ALFA-GLUT4 proteins to the PM under insulin stimulation. To further substantiate these observations, **figure 4.6C,D** demonstrates the movement of ALFA-tagged GLUT4 from intracellular compartments towards the PM between basal and insulin-stimulated states. As for transiently transfected cells (see section [4.3.2.2.1](#)), this translocation pattern is consistent with the expected behaviour of GLUT4 in response to insulin, indicating that the ALFA-GLUT4 construct accurately mimics endogenous GLUT4 trafficking.

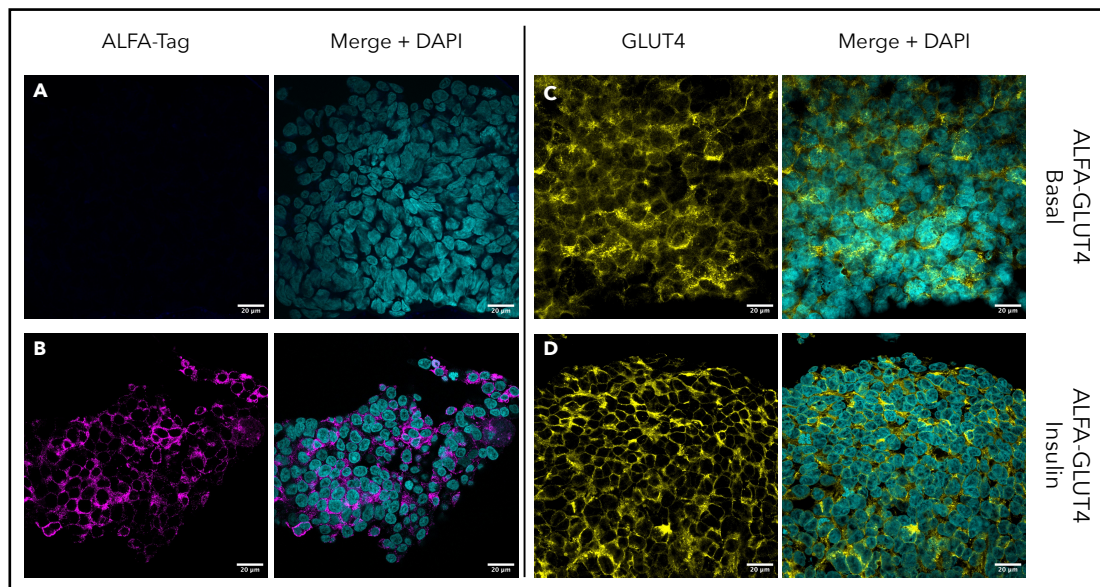


Figure 4.6. Characterisation of ALFA-GLUT4 Insulin-Stimulated Trafficking to the Plasma Membrane in Stably Transfected HEK293 Cells.

Representative confocal images of HEK293 cells stably transfected (see sections [2.2.1.8](#) and [2.2.1.9](#)) with ALFA-GLUT4 (see Appendix [7.2.2.2](#)), treated without (Basal; A,C) and with 100 nM insulin for 15 min (B,D). (A,B) Confocal images of immunostained ALFA-tag fluorescence (magenta; left panel) merged with DAPI fluorescence (cyan) in the middle left panel. (C,D) Confocal images of immunostained GLUT4 fluorescence (yellow; middle right panel) merged with DAPI fluorescence (cyan) in the right panel. Data from a representative experiment are shown (n = 3). Cells were fixed and immunostained as described in [2.2.7.1.1](#). Secondary antibodies labelled with Alexa Fluor™ 488 were used from immunostaining (see section [2.1.2](#)). All images were acquired using a 40× water immersion objective on a Leica TCS SP8 confocal microscope (see section [2.2.7.2.4](#)). Scale Bars = 20 μm.

Having established that the ALFA epitope tag does not interfere with insulin-stimulated GLUT4 translocation via microscopy, we further investigated the translocation capacity of ALFA-GLUT4 in response to insulin using subcellular fractionation. This method allowed us to assess the distribution of the ALFA-GLUT4 construct within cellular compartments. In this section, we used the IR as a PM protein marker to confirm the

successful separation of cellular fractions (PM, plasma membrane; LDM, low-density microsomes; HDM, high-density microsomes).

Densitometry analysis of immunoblots showed that both ALFA-tag and GLUT4 signals increased at the PM under insulin stimulation while corresponding decreases were observed in LDM fractions (**Figure 4.7**). Although this experiment was conducted only once, precluding statistical analysis, the data are consistent with the well-established GLUT4 translocation from GSC to the PM upon insulin stimulation (see section [1.3.2.2](#)). These findings also align with previous subcellular fractionation analyses observed in WT 3T3-L1 adipocytes, as detailed in section [3.3.2.1](#), further supporting the integrity of the ALFA-GLUT4 construct in mimicking endogenous GLUT4 behaviour.

Overall, both microscopy and subcellular fractionation analyses provided deeper insights into the intracellular dynamics integration of the ALFA-GLUT4 construct in HEK293 cells, confirming that it behaves similarly to endogenous GLUT4 in response to insulin. This gives us confidence in using the ALFA-GLUT4 construct moving forward, as results indicate its viability as a model for studying GLUT4 behaviour at the PM.

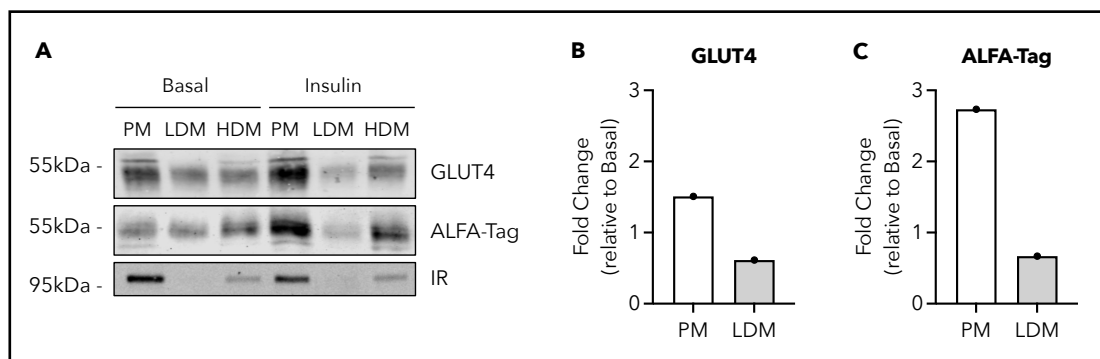


Figure 4.7. ALFA-GLUT4 Localisation in Insulin-Stimulated Stably Transfected HEK293 Cells.

(A) Immunoblot showing GLUT4 and ALFA-tag signals in PM-enriched, low-density microsomes (LDM), and high-density microsomes (HDM) fractions of a polyclonal population of HEK293 cells stably transfected with the ALFA-GLUT4 DNA plasmid (see Appendix [7.2.2.2](#)) and treated with or without 100 nM insulin for 15 min. The insulin receptor (IR) was used as a PM protein marker. Sub-cellular fractions were produced and loaded as described in [2.2.4.1](#) and [2.2.5.2](#). Blots were visualised with a LI-COR Odyssey-SA system. (B,C) Fold-changes of GLUT4 (B) and ALFA-tag (C) immunoblot signals in PM and LDM fractions of a polyclonal population of HEK293 cells stably transfected with the ALFA-GLUT4 under insulin stimulation (values expressed relative to Basal; n = 1). In PM fractions, data indicate both GLUT4 and ALFA-tag signals increase at the PM under insulin stimulation, while corresponding decreases are observed in LDM fractions.

4.4 Chapter 4 - Discussion and Future Work

4.4.1 Exchange-PAINT: Project Focus Adjustment and Future Work

Present data have demonstrated the ability of a homemade, low-cost perfusion system to automate and dynamically adjust the concentration of imaging strands during DNA-PAINT experiments, highlighting the system's potential for advanced applications in future Exchange-PAINT imaging modality (see section [4.3.1](#)).

This project was intended to be performed in collaboration with Dr Peter W. Tinning, a post-doctoral fellow at the time, under the supervision of Prof. Gwyn W. Gould, Prof. Gail McConnell, and Dr Sebastian van de Linde for the development of an Exchange-PAINT system. Our role was to contribute the biological expertise necessary for the successful implementation of the system, whose immediate goal was to further study insulin-stimulated GLUT4 dispersal at the PM of adipocytes. However, due to the conclusion of Dr Peter W. Tinning's post-doctoral contract and subsequent technical issues with the SMLM system, we lacked the necessary expertise to proceed further in this project during my time as a student. As this PhD reached its end, we therefore decided to refocus our efforts on other aspects of this thesis.

The hope is that the successful implementation of a fully functioning Exchange-PAINT system will provide deeper insights into how EFR3a and PI4K-III α relate to GLUT4 dynamics at the PM and how the insulin signalling pathway interacts with this machinery. Building on the work of Koester et al., one of the primary objectives will be to repeat their studies using first

DNA-PAINT instead of dSTORM to examine GLUT4 dispersal at the PM of 3T3-L1 adipocytes expressing HA-GLUT4-GFP (Koester et al., 2022b), specifically investigating the effects of knocking down *Efr3a* and *Pi4ka* (see section [3.3.2](#)). The long-term goal is then to extend this research to sequential multitarget imaging using Exchange-PAINT, allowing for the super-resolved visualisation of the GLUT4 machinery at the PM. For example, PM-bound proteins such as IR could be studied simultaneously with GLUT4 and EFR3a to provide a more comprehensive understanding of their interactions and functions within this signalling cascade (see section [3.4.1](#)). Adding a live-cell imaging aspect could also provide temporal resolution to complement the spatial data obtained using SRM techniques.

4.4.2 *The ALFA-GLUT4 Construct: Potential for Success*

Another crucial aspect of the development of an Exchange-PAINT system, as described above, involved the development and characterisation of DNA-PAINT molecular labelling strategies that ensure accurate and detailed imaging of molecular interactions and dynamics in biological contexts. As previously mentioned (see section [4.1.1](#)), subjected to the linkage error of labelling antibodies, the work of Koester et al. performed using dSTORM did not allow for the accurate quantification of the numbers of GLUT4 molecules per cluster at the PM (Koester et al., 2022b).

The present findings demonstrate the successful generation and characterisation of HEK293 cell lines stably expressing the ALFA-GLUT4 construct (see section [4.3.2](#)). ALFA-GLUT4 expression and insulin-stimulated translocation were confirmed using immunoblotting and immunofluorescence staining. Although only performed once, subcellular

fractionation analysis also suggests that the ALFA-GLUT4 construct can translocate in response to insulin to the PM, consistent with the established mechanisms of GLUT4 trafficking in adipocytes. This consistency supports the use of the ALFA-GLUT4 construct as a model for studying GLUT4 behaviour and regulation within cells.

Therefore, future work includes repeating some of these experiments to allow for statistical analysis and validation of our findings. Our long-term goal is to extend the protocols used in this section to 3T3-L1 cells to determine the suitability of ALFA-GLUT4 for characterising GLUT4 dispersal dynamics at the PM of adipocytes and further its potential applications to muscle cells. As previously mentioned, this construct and its nanobody labelling ability may enable SMLM techniques, such as DNA-PAINT, to achieve improved localisation of individual GLUT4 molecules at the PM. The use of nanobodies in these experiments is particularly advantageous as they reduce the linkage error typically associated with conventional antibodies, thereby increasing localisation precision. This approach will improve our understanding of the kinetic changes involved in the transition of GLUT4 from clusters to monomers, as well as the regulatory mechanisms responsible for insulin-stimulated dispersal.

Had time permitted, we would have utilised the nanobody developed against the ALFA-tag (Götzke et al., 2019) present in our recombinant GLUT4 in DNA-PAINT, and more specifically, Exchange-PAINT experiments to perform novel GLUT4 localisation studies.

Finally, there is evidence showing that HA-tagged GLUT4 constructs are not functional as glucose transporters (Lizunov et al., 2012). The ALFA-tag,

however, was specifically developed to be compatible with protein function, regardless of its position on the protein of interest (Götzke et al., 2019). If the ALFA-GLUT4 construct proves to be fully functional, it would revolutionise the field of GLUT4 biology by providing a model that closely mirrors physiological conditions. To confirm this, a simple glucose uptake assay in future work could determine the functional capacity of the ALFA-GLUT4 construct, thereby further validating its use in studying GLUT4 dynamics and insulin sensitivity in a more accurate biological context.

5.1 Chapter 5 - Introduction

5.1.1 *Cardiac Metabolic Disturbance in Diabetes*

Chronic exposure to elevated blood glucose levels is known to decrease insulin signalling and glucose uptake in cardiomyocytes (Joseph et al., 2014). As a result, shifting away from glucose as an energy source (see section [1.2.2](#)), the diabetic heart becomes “metabolically inflexible”. It enters a state of prolonged reliance on FA oxidation, limiting its ability to oxidise glucose during periods of stress and enhanced energetic demands such as hypoxia and ischemia, where glucose usually represents a significant energy source. The balance between glucose and FA being broken, a dilemma, therefore, arises with the Randle cycle now not only functioning in a glucose-sparing direction but also acting as a feed-forward system, increasing cardiac metabolic inflexibility (see section [1.2.2](#); **Figure 1.2**) (Battault et al., 2020; Lopaschuk and Stanley, 1997).

Almost entirely dependent on FA as a source of energy, diabetic hearts, therefore, exhibit an increase in expression and trafficking of the FA transporter CD36 (Jia et al., 2016), as well as activation of the peroxisome proliferator-activated receptor (PPAR)- α signalling pathway (Lee et al., 2017). While not all studies agree about all aspects of this metabolic shift, it is evident that disproportional reliance on FA oxidation for ATP production increases oxidative stress and disrupts significant aspects of cardiac physiology (Bayeva et al., 2013). Not only does the requirements for

oxygen increase, leading to a reduction in oxidative phosphorylation efficiency, but other cardiac key energetics are also affected, including cellular ATP shuttling, mitochondrial coupling, and energy transfer within cardiomyocytes (Anderson et al., 2009; Bayeva et al., 2013). Importantly, lipid deposits in the cytosol of cardiomyocytes have been reported in animal models with DM, and cardiac steatosis has been documented in human hearts, with a trend toward significantly higher triglyceride content in individuals with diabetes (Harmancey and Taegtmeyer, 2008; Sharma et al., 2004). As a result, excessive accumulation of lipids was shown to promote further myocardial insulin resistance and reduced NO bioavailability (Avogaro et al., 2006).

As previously mentioned (see section [1.1.2.2](#)), the prognosis of individuals with HF, including HF with reduced ejection fraction (HFrEF) and even more so HF with preserved ejection fraction (HFpEF), is worsened with DM (Adams et al., 2005; Kannel et al., 1974; Sarma et al., 2013). However, the mechanism(s) behind this relationship remains unclear. In 2019, Ljubkovic et al. showed that even in the absence of contractile failure, diabetic hearts exhibit mitochondrial dysfunction, intracellular lipid accumulation, and cellular apoptosis (Ljubkovic et al., 2019). This begs the question: is cardiac metabolic disturbance in diabetes the cause or a consequence of HF? Marafella et al. highlighted the importance of the toxic metabolic milieu of diabetes in the early progression of DCM, starting with cardiomyocyte lipid accumulation (Marfella et al., 2020). In addition, Hu et al. showed that while decreased myocardial glucose metabolism is a major hallmark of DM, often allowing early diagnosis of the disease, it is not specifically associated with DM. They reported that multiple metabolic factors can cause disturbance in

cardiac metabolism and that each case is specific to the individual (Hu et al., 2018).

5.1.2 *Cardiac Regional Heterogeneity*

Over the years, the identification of metabolic abnormalities in HF has driven numerous studies to better define metabolic differences between healthy and diseased hearts. The use of in vivo imaging approaches has provided a wealth of insight into cardiac metabolic activity, for example, by quantifying absolute values of ATP and phosphocreatine using ³¹P magnetic resonance spectroscopy (³¹P-MRS). Studies have reported reduced phosphocreatine:ATP ratios in patients with HF, confirming metabolic dysfunction (Conway et al., 1991; Hardy et al., 1991; Neubauer et al., 1997; Neubauer et al., 1992; Tsampasian et al., 2023). Similarly, positron emission tomography (PET) has been developed as a unique non-invasive approach to evaluate myocardial glucose, FA turnover, and tissue perfusion (Kudo et al., 2002; Taylor et al., 2001). More specifically, PET can quantify regional myocardial blood flow, providing functional and structural insights into the effects of different diseases across distinct anatomical regions of the heart and revealing changes in both global and regional cardiac metabolism.

Differences between atrial and ventricular metabolism have been established in numerous mammalian species (Bass et al., 1993). Considering, for instance, the major risk factors of HF, which include diabetes and obesity (Kannel et al., 1974; Kenchaiah et al., 2002; Kenny and Abel, 2019), studies have used technologies such as ³¹P-MRS and PET to describe distinct heterogeneous features associated with such diseases

(Edvardsen and Klaeboe, 2019). The hemodynamic changes observed in obesity have been shown to induce left atrial enlargement and left ventricular wall stress (Alpert et al., 2014). Similarly, the altered metabolic milieu seen in diabetes has been shown to contribute to cardiac chamber remodelling. For instance, Gulsin et al. showed that individuals with HFpEF and T2D have increased concentric left ventricular remodelling, decreased left atrial volumes, and increased systemic inflammation compared to individuals without T2D (Gulsin et al., 2019). Linssen et al. also associate (pre)diabetes with structural changes in the RA and RV, as well as impaired right ventricular systolic and diastolic function (Linssen et al., 2020).

Cardiac remodelling is a multifactorial process that not only includes a structural response of myocardial tissue to different pathophysiological processes (Cohn, 1995; Planinc et al., 2021) but also involves biochemical remodelling (van Bilsen et al., 2004). Focusing on GLUT4, Ware et al. observed a 2.5-fold increase in protein content in the LV in chronic HF (Ware et al., 2011). This up-regulation was suggested to provide an adaptive metabolic profile to support increased energetic demands in response to ventricular wall stress and hypertrophy. They also detected a paradoxical decrease in GLUT4 content in the RA (Ware et al., 2011). Similarly, Maria et al. observed a down-regulation of GLUT4 levels by 70% at the surface of atrial cardiomyocytes from individuals with T1D, which they postulated might limit the ability of the heart to properly use glucose as a source of energy in diabetes, therefore impairing recovery (Maria et al., 2015). In addition, distinct patterns of GLUT4 and GLUT8 expression in different heart chambers in the latter study highlight a further aspect of cardiac regional heterogeneity, whereby different GLUT isoforms might play a greater role in regulating glucose uptake in the myocardium under

pathological circumstances (Maria et al., 2015). However, it is unclear whether these reported variations in protein expression represent a global change or whether distinct architectural features within different heart regions adapt differently to pathological stimuli.

5.1.3 *The Challenges of Cardiovascular Research*

The study of CVD presents numerous challenges. One significant hurdle is illustrated in our current ability to link structural and biochemical cardiac processes, specifically linking them to distinct metabolic changes. This complexity is evident from the information and data presented above (see section [5.1.2](#)), highlighting an unmet need to quantify protein levels and changes within distinct 3D structures of intact hearts. This is further emphasised by in vitro studies such as those performed by Doll et al. and Linscheid et al., who produced quantitative proteomic maps of human hearts (Doll et al., 2017; Linscheid et al., 2020). These studies provide cardiac metabolic information at a molecular level, highlighting regional variations in protein expression within different heart regions. However, these variations, which might be reorganised in diseased hearts, often remain indistinguishable in clinical settings. To date, most approaches for the study of regional protein heterogeneity rely on some degree of manual tissue dissection, thus introducing a level of error, inconsistency and destruction of specific regional information that could be evident in intact tissues. On the other hand, the spatial resolution of in vivo imaging technologies, such as ³¹P-MRS and PET previously mentioned, is poor, and the mechanisms behind the structural and metabolic changes obtained in intact hearts remain elusive and challenging to quantify at the single-cell level.

Isolating viable cardiomyocytes also poses significant challenges in cardiovascular research. While high-quality isolated cardiomyocytes are crucial for studying cardiac molecular and cellular mechanisms and morphology, these cells exhibit rapid calcium transients and electrical signals and are highly sensitive to shear stress. These characteristics make it difficult to develop viable in vitro models that accurately replicate the heart's physiological or pathological conditions. Despite these challenges, several studies have made strides in developing functional in vitro cardiac tissue models (Mathur et al., 2016; Zuppinger, 2019). A critical step in this process is the identification of optimal sources of cardiomyocytes.

Neonatal cardiomyocytes, commonly isolated from mice and rats, are frequently used in research due to their higher post-isolation survival rate. They are less sensitive to calcium reintroduction and easier to transfect. Yet, despite usually yielding lower cell counts and being harder to genetically manipulate, isolated adult cardiomyocytes still represent the most accurate models for most cardiac studies (Parameswaran et al., 2013).

Primary adult cardiomyocytes are notoriously difficult to isolate due to their susceptibility to damage during isolation. This fragility often compromises cell viability, limiting their utility in downstream applications. Over the years, various species, including rats (Powell and Twist, 1976), rabbits (Dani et al., 1977), and canines (Vahouny et al., 1979), have been used to develop cardiomyocyte isolation techniques. However, no consensus remains on the optimal protocol for isolating these cells. Despite this, the core of most protocols still relies on enzymatic digestion of the heart, a method that remains prevalent and has even been adapted for isolating cardiomyocytes from small tissue samples, such as human biopsies (Coppini et al., 2014).

Isolating myocytes from rodent hearts also presents independent challenges due to the distinct physiology of rodent cardiomyocytes compared to larger mammals. For instance, rodent cardiomyocytes exhibit higher intracellular sodium levels, making them prone to calcium overload during cardiac arrest and under hypoxic conditions (Bers, 2002). Consequently, most current isolation protocols predominantly rely on retrograde heart perfusion with an enzymatic solution using a Langendorff perfusion system (Liao and Jain, 2007; Louch et al., 2011; O'Connell et al., 2007). This method allows for the controlled delivery of perfused solutions to the heart (Bell et al., 2011), ensuring uniform enzyme exposure and supporting cellular viability during isolation. However, these systems are also accompanied by several logistical and technical barriers. Setups are costly, require precise calibration, and require extensive operator training, making them less accessible and more challenging to replicate previously developed isolation protocols.

Overall, cardiovascular research underscores the need for improved methodologies to accurately study and understand the heart's interlaced structural and biomolecular dynamics in health and disease.

5.1.4 *Optical Mesoscopy: Introduction to the Mesolens*

Optical mesoscopy is an emerging field that focuses on imaging and studying structures that lie between the microscopic and macroscopic scales through the integration of advanced optical designs that balance a wide FOV with high resolution. In conventional microscopes, the common

trade-off is that increasing the FOV leads to decreased pixel density and, therefore, reduced image resolution.

One established approach in mesoscopic imaging to overcome this limitation is the use of objective lenses with a high NA combined with lower magnification. This allows mesoscopes to capture large sample volumes while resolving fine details at cellular or sub-cellular levels (see section [1.4.1.1](#)). However, this is not the only method available. Some systems, such as those from Thorlabs, rely on computational techniques, using a large low-resolution FOV to randomly access and identify ROI, which can then be zoomed in for detailed, high-resolution imaging (Sofroniew et al., 2016). An improved option includes the real-time, ultra-large-scale, high-resolution mesoscope named RUSH, developed by Fan et al., effectively combining optical and computational strategies (Fan et al., 2019). Using an objective lens with 8x magnification and an NA of 0.35, it first broadly scans a large FOV with an initial optical resolution of approximately 1.2 μm to then zoom in on specific ROI for higher-resolution imaging (Fan et al., 2019; McConnell, 2019).

Located at the University of Strathclyde, the Mesolens is an advanced optical instrument specifically made for mesoscopic imaging by using an objective lens with an NA of 0.47 and a 4x magnification (McConnell et al., 2016). It is similar to the RUSH system in that they both use giant lens approaches. The primary difference, however, is that the Mesolens can also perform sub-cellular-resolution imaging of thick specimens at depth using confocal laser scanning mesoscopy. It was initially designed to image full mouse embryos (McConnell et al., 2016) and has subsequently allowed the visualisation of whole adult *Drosophila melanogaster* (McConnell and

Amos, 2018), retaining details throughout a large imaging volume (6 mm x 6 mm x 3 mm), with a measured resolution down to 0.7 μm laterally and 7 μm axially. The physical size and thorough selection of each Mesolens component ensure that even as the imaging area expands, the pixel density remains sufficient to provide detailed and precise images, giving rise to an optical throughput 25-fold higher than that of conventional 4x objective lenses (McConnell et al., 2016).

More details about the Mesolens specifications are described in the methods (see section [2.2.7.2.5](#)).

5.1.5 *Chapter 5 - Aims*

In this chapter, we first present a novel optical mesoscopy approach that allows the study of protein expression levels and structural distribution within ultrathick sections of intact mouse hearts. As the primary glucose transporter expressed in the heart, we use GFP-tagged GLUT4 as a proof-of-concept protein in this study.

Using the Mesolens' imaging capability, this chapter's first aims are:

- (i) to show how regional variations in GLUT4 expression can be observed and quantified systematically in whole mounts of heart tissue up to 5 mm x 5 mm x 3 mm in size while allowing a clear view of intact protein levels within this large tissue volume (see section [5.1.4](#)).
- (ii) to compare GLUT4 distribution in intact hearts from mice fed standard chow or HFD, the latter being a well-established method to induce

obesity and insulin resistance (Inui, 2003; Sato et al., 2010; Speakman et al., 2007).

(iii) to ascertain how GLUT4 levels and distribution might be affected under pathological circumstances caused by HFD.

To complement this, given the challenges associated with isolating primary adult cardiomyocytes, we then focused on optimising a Langendorff-free isolation method for viable cardiomyocytes from the hearts of HA-GLUT4-GFP transgenic mice. This method tackles the challenges associated with isolating adult cardiomyocytes for studying GLUT4 dynamics at the cellular level, including:

(iv) ensuring their survival after isolation.

(v) effectively performing immunostaining.

(vi) assessing insulin stimulation.

With these advancements, we hope to enhance our understanding of GLUT4's role in cardiac glucose metabolism, more specifically aiming to extend the study performed on adipocytes to muscle cells (see Chapters [3](#) and [4](#)) and offer valuable tools for studying the effects of pathological conditions on GLUT4 in both organ-scale and single-cell contexts.

5.2 Chapter 5 - List of Methods

The methods below have been used in this chapter and are further detailed in section 2.2.

2.2.2 Animal Work

2.2.2.1 Mice

2.2.2.2 High-Fat Diet-Feeding, Weighing, and Blood Glucose Measurement in Mice

2.2.2.3 Heart Collection and Dissection

2.2.2.3.1 Mouse Heart Collection for Mesolens Imaging

2.2.2.3.2 Mouse and Rat Heart Collection and Sectioned for Quantitative Immunoblotting

2.2.2.4 Cardiomyocyte Isolation

2.2.2.4.1 Buffer and Surgical Area Preparation

2.2.2.4.2 Primary Adult Mouse Cardiomyocyte Langendorff-Free and Enzymatic Dissociation-Based Isolation

2.2.2.4.3 Cardiomyocyte Collection and Calcium Reintroduction

2.2.2.4.4 Insulin Stimulation of

Primary Adult Isolated Cardiomyocytes

2.2.3 Cell Lysates and Tissue Homogenates

2.2.3.1 Sectioned Cardiac Tissue Homogenisation

2.2.3.2 Primary Adult Isolated Cardiomyocytes Lysate

2.2.5 Protein-Specific Assays

2.2.5.1 Bicinchoninic Acid Assay and Sample Preparation for Immunoblotting

2.2.5.2 SDS-PAGE

2.2.5.3 Wet Transfer

2.2.5.5 Immunoblotting

2.2.5.6 PNGase F-Mediated Protein De-Glycosylation

2.2.7 Microscopy

2.2.7.1 Sample Preparation

2.2.7.1.2 Primary Isolated Mouse Cardiomyocytes Fixation and Immunofluorescent Staining

2.2.7.1.4 Mouse Heart Optical Clearing

2.2.7.2 Imaging Setups and Data Acquisition

2.2.7.2.4 Confocal Microscopy

2.2.7.2.5 The Mesolens

2.2.8 Data and Statistical Analyses

2.2.8.1 Densitometry

2.2.8.4 Mesolens-Acquired Data Processing and Analysis

2.2.8.4.1 Analysis of Global Regional Fluorescence

2.2.8.4.2 Analysis of Transmural Fluorescence

2.2.8.4.3 Analysis of Lumen Size

2.2.8.4.4 Visualisation and Presentation

2.2.8.5 Statistical Analysis

5.3 Chapter 5 - Results

5.3.1 *A Novel 3D Imaging Approach for Quantification of GLUT4 Levels across the Intact Myocardium*

Here, we used transgenic mice expressing HA- and GFP-tagged GLUT4 (Fazakerley et al., 2009; Lizunov et al., 2012) (see section [2.2.2.1](#)). This construct is widely used in studies of GLUT4 dynamics (see section [1.4](#) and [Chapter 4](#)) and exhibits insulin-dependent movement to the PM in isolated cells, including cardiomyocytes (Blot and McGraw, 2008; Fazakerley et al., 2009; Habtemichael et al., 2011; Klip et al., 2019; Muretta et al., 2008). Hence, we reasoned that this would provide a useful proof of concept for our analysis pipeline. This approach avoids the need for immunostaining in the development of a novel optical mesoscopy approach (see section [5.1.4](#)), allowing the study of GLUT4 levels and structural distribution within ultrathick sections of intact mouse hearts.

In this section, we use the term 'intact' to reflect the use of isolated heart sections, typically 5 mm × 5 mm × 3 mm in size, where the core structure remains untouched and individual cardiac chambers undissected (see section [2.2.2.3.1](#)).

5.3.1.1 Axial Imaging Depth with and without Organ Perfusion

Using optical mesoscopy, we were able to visualise GFP-tagged GLUT4 within optically cleared ultrathick sections of intact mouse hearts (**Figure 5.1A**). Samples were cleared using the iDISCO method (Renier et al., 2014)

(see section [2.2.7.1.4](#)). **Figure 5.1B** displays an average intensity axial projection of GLUT4-GFP fluorescence within a whole mount (5 mm × 5 mm × 3 mm) of a typical ventricular cardiac tissue section. Visible intact 3D anatomical structures are clearly observed, including the LV, the two papillary muscles of the LV, the interventricular septum, and the RV (**Figure 5.1B**).

Optimisation of the tissue clearing protocol has highlighted the importance of blood removal for organ optical clearing, especially in haem-rich tissues, such as the heart. Simple buffer perfusion of the tissue has been shown to remove unwanted red blood cells effectively. As described in section [2.2.2.3.1](#), a Langendorff-free perfusion method was used to remove as much blood as possible from isolated hearts. Without this perfusion step, the total imaging depth of heart sections was restricted to less than 1 mm (0.76 ± 0.18 mm; **Figure 5.1C**). With the inclusion of a perfusion step in our method, specimens (n = 14 included in this study) were imaged using a 5 µm z-step size and yielded a significantly higher average imaging depth of 2.06 ± 0.33 mm ($p < 0001$; **Figure 5.1C,D**; see Appendix [7.5.1](#)).

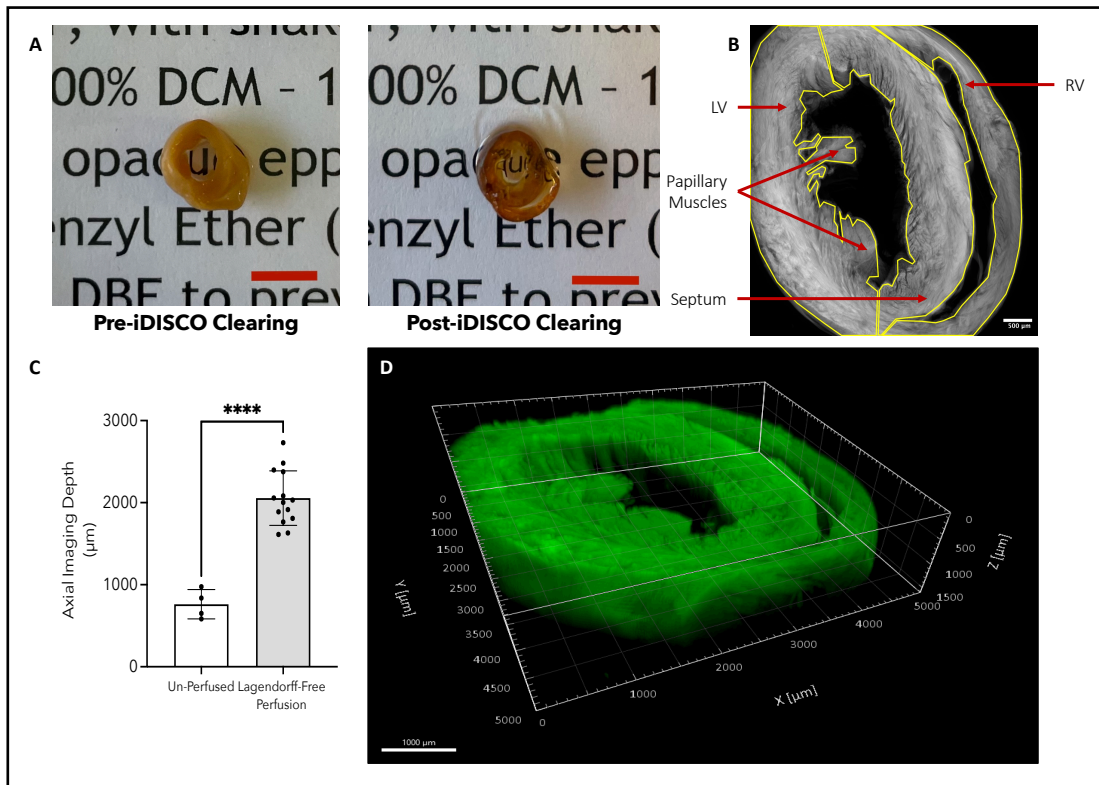


Figure 5.1. Visualisation of GLUT4-GFP in Ultrathick Sections of Cleared Mouse Hearts and Characterisation of Axial Imaging Depth with and without Organ Perfusion.

(A) Representative images of pre- and post-iDISCO optical clearing of a perfused 3-mm thick mouse ventricular heart section. Scale bars = 5 mm. (B) Representative average intensity axial-projected image of GLUT4-GFP fluorescence within perfused and iDISCO optically cleared 3-mm thick mouse ventricular heart section showing distinct structural features: the left ventricle (LV), the two papillary muscles of the LV, the interventricular septum and the right ventricle (RV). Scale bar = 500 μm . (C) Mean \pm s.d. of axial imaging depth (μm) in un-perfused (white bar; n = 4) iDISCO optically cleared 3-mm thick mouse ventricular heart sections compared to perfused (grey bar; Langendorff-free perfusion, n = 14) hearts. Using a Langendorff-free perfusion system, the axial imaging depth increases to 2.06 ± 0.33 mm compared to 0.76 ± 0.18 mm in un-perfused hearts. (D) 3D render of GLUT4-GFP fluorescence (green) within a whole mount of optically cleared 3-mm thick mouse ventricular heart section. Scale bar = 1000 μm . Images representative of 14 repeats. Specimens were collected, cleared and imaged using the Mesolens system over a 5 mm \times 5 mm \times 3 mm volume using a z-step size of 5 μm as described in sections [2.2.2.3.2](#), [2.2.7.1.4](#), and [2.2.7.2.5](#). **** represents $p \leq 0.0001$. A two-tailed unpaired t-test with Welch's correction was performed on raw data of (C). Published in Geiser et al. (2024).

5.3.1.2 Quantitative Analysis of GLUT4 Levels and Distribution within Intact Ventricular Cardiac Sections

Molecular and structural regional heterogeneity in both healthy and diseased hearts has become well-characterised (see section [5.1.2](#)). However, linking specific metabolic changes and protein expression patterns to the 3D architecture of intact heart regions remains an unmet challenge. Considering that the fluorescence of GLUT4-GFP within ultrathick cardiac tissue section can be effectively detected using optical mesoscopy (**Figure 5.1**), we, therefore, reasoned that regional variations in

GLUT4 expression could be observed and systematically quantified within acquired 3D reconstructed volumes of intact ventricular heart sections. We chose to test this hypothesis using hearts from mice fed standard chow (control) or an HFD to examine how pathophysiological changes might be identified using our method. As expected, mice fed an HFD presented with elevated body weight and blood glucose (see Appendix 7.5.2) (Inui, 2003; Sato et al., 2010; Speakman et al., 2007).

The developed analysis pipeline for image processing, visualisation, and quantification of GLUT4-GFP fluorescence signals is outlined in detail in section 2.2.8.4 and summarised in **figure 5.2**.

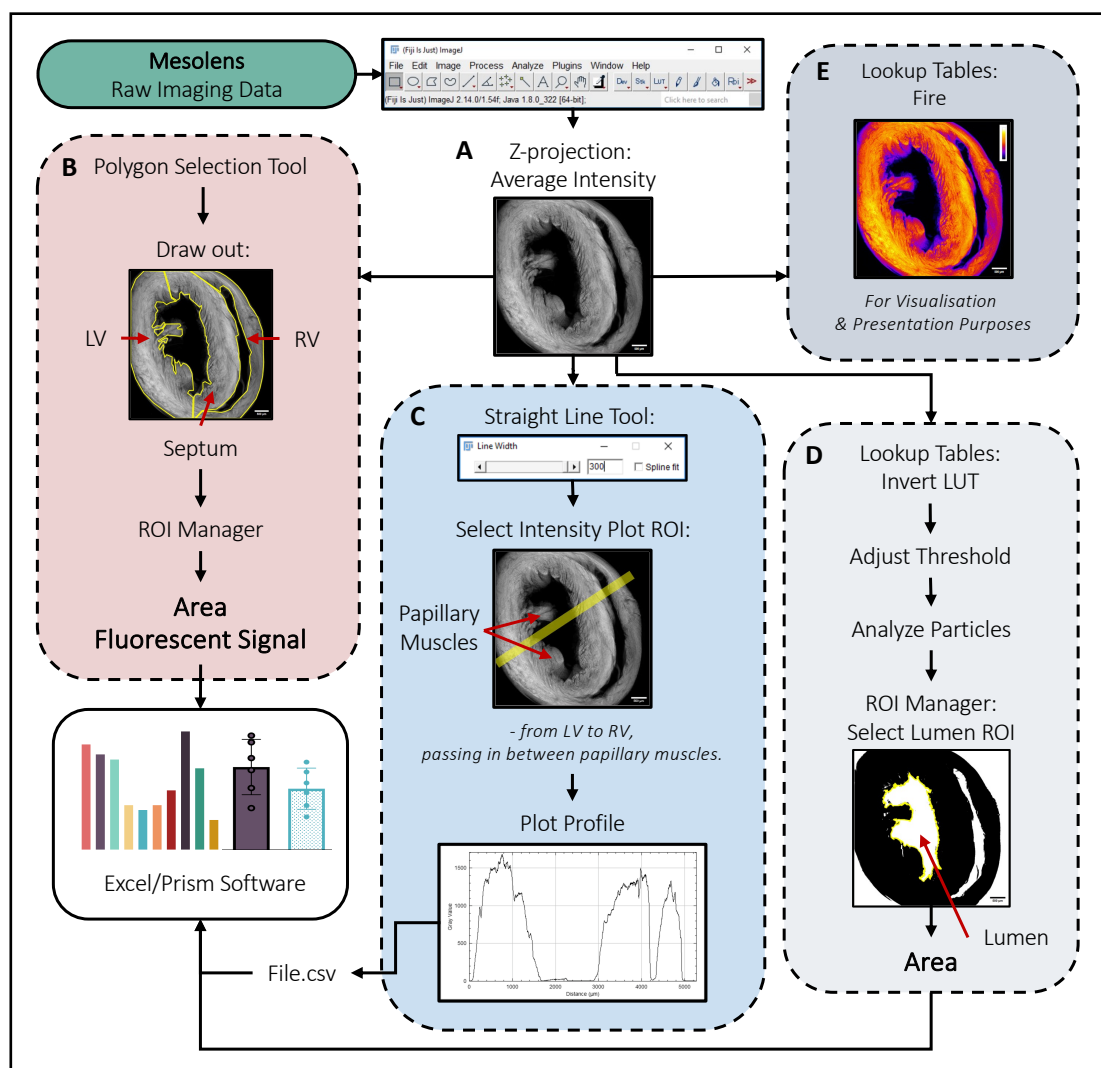


Figure 5.2. Summarised Flowchart of the Analysis Pipeline for Quantification of GLUT4-GFP Levels in Ultrathick Sections of Cleared Mouse Hearts.

Following acquisition, raw Mesolens imaging data were processed using Fiji image processing software. (A) Acquired 3D volumes were transformed into 2D images by performing an average-intensity axial projection. (B) Using the polygon selection tool, regions of interest (ROI) within heart sections, including the LV, septum and RV, were manually segmented and saved in the ROI Manager to then allow measurement of the 2D surface area and GLUT4-GFP fluorescent signals. (C) Using the line selection tool, the intensity plot ROI was manually segmented by drawing a line from the LV to the RV, crossing the septum and passing between LV papillary muscles. The Plot Profile tool was then used to generate fluorescence intensity profiles. (D) To isolate and quantify the 2D area of the lumen, axial-projected datasets were subjected to thresholding. The Analyze Particles tool was then used to select the lumen as ROI. The 2D area of the lumen was then measured. (E) Colour-coding of fluorescence intensity within axial-project images was performed using the “fire” lookup table for presentation and visualisation purposes. Extracted values and parameters from Fiji were further processed as described in section [2.2.8.4](#). Published in Geiser et al. (2024).

5.3.1.2.1 Global Regional GLUT4 Expression Levels

To quantify and compare regional GLUT4-GFP protein content in both control and HFD intact ventricular heart sections, we first displayed the Mesolens-acquired reconstructed volumes as 2D images by performing an average intensity axial projection of the 3D datasets. All subsequent analyses were then performed from each specimen's axial-projected images (**Figure 5.2A**).

Figure 5.3A displays representative axial GLUT4-GFP fluorescence projections within control and HFD hearts. In both groups, no statistically significant differences in GLUT4-GFP fluorescence, expressed relative to

left ventricular signals, were observed between the LV, septum and RV (**Figure 5.3B**). This result is in good agreement with immunoblotting data shown in **figure 5.3C,D**, where no significant regional heterogeneity in GLUT4 levels is observed in tissue homogenates dissected from the hearts of mice fed a standard chow diet. Nevertheless, this approach allows an appreciation of intrinsic ventricular and atrial regional heterogeneity (**Figure 5.3C**) in protein expression evident within a healthy heart (Bass et al., 1993; Doll et al., 2017), facilitating a comparison of intact tissue in two distinct physiological states.

Indeed, **figure 5.3C** interestingly also illustrates differences in the electrophoretic mobility of GLUT4 between isolated cardiac regions, including the LV, RV, left atrium (LA), RA, and septum. GLUT4 is a glycoprotein exhibiting a complex heterogeneous glycosylation pattern (Lau et al., 2007), which gives rise to the migration of GLUT4 as a smear on SDS gels at around 50 kDa. To further investigate whether these observed differences in molecular weight represent specific post-translational glycosylation patterns of GLUT4 in each cardiac region, heart homogenates were treated with Peptide:*N*-Glycosidase F (PNGase F; [2.2.5.6](#)). PNGase catalyses the removal of most amino-linked oligosaccharides from glycoproteins. As a result, PNGase F treatment changed the apparent mass of GLUT4 to a sharp band of approximately 43 kDa in all mice heart sections (**Figure 5.4A**), consistent with the predicted molecular weight of GLUT4 from its amino acid sequence. Similar observations were made in rats fed a standard chow diet (**Figure 5.4B**). These findings, therefore, suggest an intrinsic regional heterogeneity in GLUT4 amino-glycosylation patterns in the hearts of 'healthy' mice and rats, with GLUT4 appearing heavier in the atria compared to the ventricles and the septum (**Figures**

5.3.C and 5.4). Interestingly, these differences in GLUT4 mobility differed slightly in rabbit hearts compared to mice and rats (**Figure 5.4C**), highlighting potential differences in GLUT4 amino-glycosylation between species and across different cardiac chambers.

Briefly, we would also like to highlight that both GLUT4 and GAPDH immunoblotting bands exhibit slight widening following PNGase F treatment (**Figure 5.4A, B**). Although the molecular weight of GAPDH remains at approximately 34 kDa, this widening suggests that deglycosylation may subtly influence its migration. The removal of oligosaccharide chains (see section [2.2.5.6](#)) likely prompts GAPDH to adopt a more expanded or less compact conformation, resulting in a broader band appearance. This finding indicates that, while GAPDH is less glycosylated than GLUT4, treatment with PNGase F still impacts its conformation and interaction with the gel matrix, further emphasizing the role of glycosylation in protein electrophoretic mobility.

Finally, in **figure 5.3E**, we compare GLUT4-GFP signals within the LV, septum, and RV between control and HFD intact hearts. Although the data suggest a trend towards lowered GLUT4-GFP levels in HFD tissues; these differences did not reach statistical significance (**Figure 5.3E**). We note that decreased GLUT4 in HFD-fed mice has been reported by others, highlighting the repressive effect of an HFD on total GLUT4 content in the heart (Jackson et al., 2015; Wright et al., 2009). To this end, it is also important to note that the GLUT4-GFP transgene in these animals is under the control of the muscle creatinine kinase promoter rather than the endogenous GLUT4 promoter; hence, transcriptional control pathways might not be completely mimicked in this model. Nevertheless, these

results illustrate a simple quantitative analysis procedure that enables the study of both global and regional protein content within anatomically complex tissue volumes.

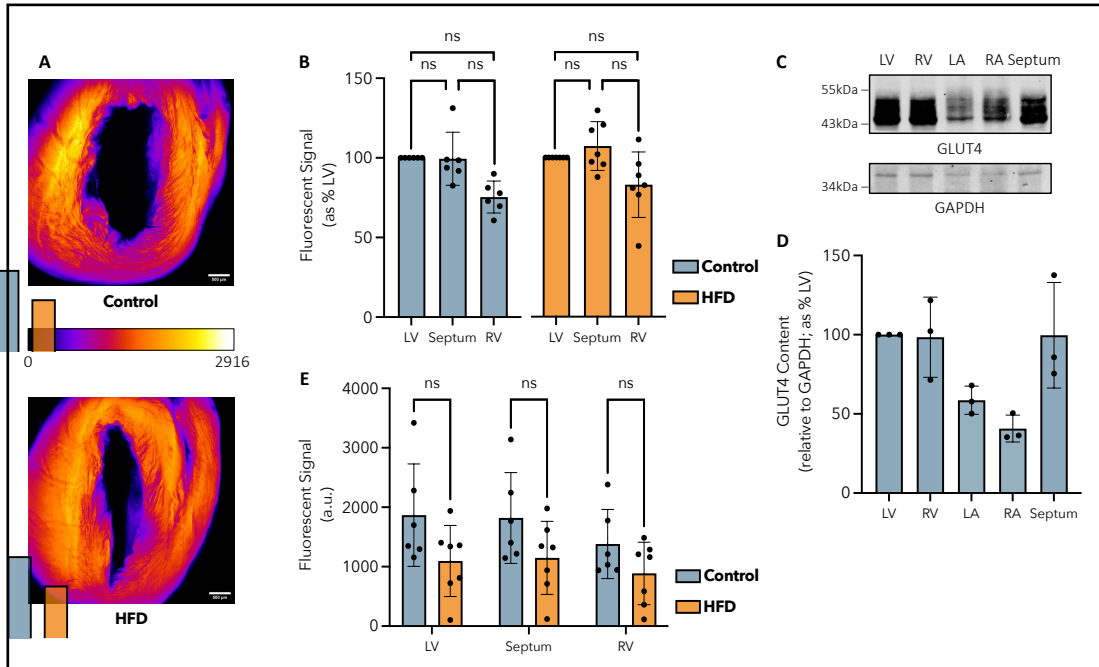


Figure 5.3. Representative Axial Projections of GLUT4-GFP Fluorescence and Quantification of Global Regional GLUT4 Expression Levels in Control and HFD Hearts.

(A) Representative average intensity axial projections of GLUT4-GFP fluorescence within control and HFD hearts (hearts no. 5 and 11, respectively; see Appendix [7.5.2](#)). Specimens were imaged over a 5 mm × 5 mm × 3 mm volume using a z-step size of 5 μm as described in section [2.2.7.2.5](#). Axial-projected images were colour-coded by fluorescence intensity using the “fire” lookup table. Intensity values are expressed relative to the highest intensity values between the two images (maximum intensity = 2916.00 in arbitrary units; heart no. 5, control). Scale bars = 500 μm. (B) Mean ± s.d. of GLUT4- GFP fluorescent signal in the LV, septum and RV of control (blue; n = 6) and HFD (orange; n = 7) hearts, expressed as a percentage relative to the value for LV (set at 100%). Data indicate no statistically significant differences between cardiac regions within each group. (C) Representative immunoblot of GLUT4 levels in isolated heart sections from mice fed a standard chow diet, including the LV, RV, left atrium (LA), right atrium (RA) and the septum. GAPDH was used as a loading control; bands were obtained from the same membrane. Tissue homogenates were produced and loaded as described in sections [2.2.3.1](#) and [2.2.5.2](#); data from a representative experiment are shown (n = 3). Blots were visualised with a LI-COR Odyssey-SA system. (D) Mean ± s.d. of total GLUT4 content in isolated LV, RV, LA, RA, and septum tissue homogenates from mice fed a standard chow diet. Values were quantified from immunoblots of the type shown in C, expressed relative to GAPDH, and expressed as a percentage relative to the value for LV (set at 100%) (n = 3). Data indicate no statistically significant differences between cardiac regions. (E) Mean ± s.d. of GLUT4-GFP fluorescent signal (a.u.) in the LV, septum, and RV of control (blue; n = 6) hearts compared to HFD (orange; n = 7) hearts. Data indicate no statistically significant differences between control and HFD hearts within each cardiac region. a.u., arbitrary units. ns signify non-significant. Brown-Forsythe and Welch ANOVA tests and multiple two-tailed unpaired t-tests with Welch’s correction were performed on all raw data of (B,D) and (E), respectively. Adapted from Geiser et al. (2024).

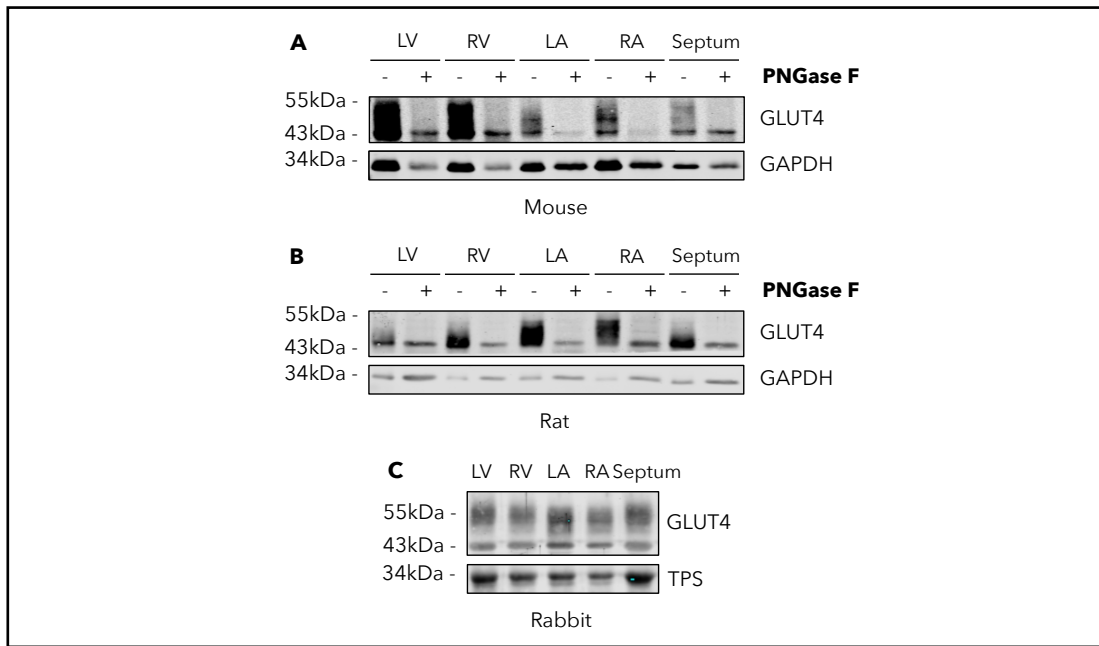


Figure 5.4. GLUT4 N-Glycosylation Cardiac Regional Heterogeneity in Mouse, Rat, and Rabbit.

(A,B) Representative immunoblot of GLUT4 levels in isolated heart sections from mice (A) and rats (B) fed a standard chow diet, including the LV, RV, LA, RA and the septum, denatured without and with PNGase F (see section 2.2.5.6). GAPDH was used as a loading control; bands were obtained from the same membrane. Data from a representative experiment are shown (Mouse, n = 4; Rat, n = 2). (C) Representative immunoblot of GLUT4 levels in isolated rabbit heart sections, including the LV, RV, LA, RA and the septum, denatured without PNGase F. Total protein stain (TPS) was used as a loading control; bands were obtained from the same membrane (n = 1). Tissue homogenates were produced and loaded as described in sections 2.2.3.1 and 2.2.5.2. Blots were visualised with a LI-COR Odyssey-SA system. Rabbit tissues were kindly gifted by Prof. Godfrey Smith from the Institute of Cardiovascular and Medical Sciences, University of Glasgow, UK.

5.3.1.2.2 Transmural Fluorescence:

GLUT4 Distribution Across Cardiac Walls

To assess protein distribution across the myocardium walls, we next quantified and compared transmural fluorescence profiles of GLUT4- GFP

across the width (x-axis) of left ventricular, septal and right ventricular walls within Mesolens-acquired 3D reconstructed cardiac volumes (**Figure 5.5**). For clarity, in the following results, all transmural datasets are displayed and were analysed, from left to right, in the following order: LV, septum and RV.

Cardiac regions were easily identified within extracted profiles (**Figure 5.5A**). **Figure 5.5A** compares the mean transmural fluorescence profiles of control and HFD hearts. At first glance, the fluorescence intensity from GLUT4-GFP appears to be reduced in HFD hearts compared to that in control specimens. However, similar to what was seen in previous results obtained from total regional measurements (**Figure 5.3E**), quantification of fluorescence signals from the area under the curve of each transmural profile revealed no statistically significant differences in any of the regions of study between control and HFD mice (**Figure 5.5B**).

In addition to total fluorescence signals, information on where GLUT4-GFP fluorescence peaks along the breadth of each cardiac region (lateral position of maximum fluorescence) was also extracted and normalised relative to total ventricular or septal wall width (**Figure 5.5A,C,D**). Final values, therefore, illustrate whether detected GLUT4-GFP is expressed with a higher content toward the left or right-hand side of the studied ventricular or septal structures within (**Figure 5.5C**) and between (**Figure 5.5D**) each studied experimental group (control and HFD). Our data highlight a significant regional heterogeneity in GLUT4-GFP transmural distribution amongst cardiac regions (**Figure 5.5C**). In both control and HFD hearts, **figure 5.5C** shows GLUT4-GFP fluorescence significantly peaking toward the right-hand side of the septal wall when compared to the LV (Control: $p = 0.0005$; HFD: $p = 0.0002$) and RV (Control: $p = 0.0014$;

HFD: $p < 0.0001$), where a left-skewed accumulation of GLUT4-GFP proteins is observed along the width of both ventricular walls (**Figure 5.5C**). These results, therefore, suggest an asymmetry within GLUT4-GFP distribution profiles for different cardiac regions. Strikingly, although no differences were observed in the distribution of GLUT4-GFP within the septal and right ventricular walls, our data reveal a significant change in the lateral position of GLUT4-GFP maximum fluorescence toward the centre of the LV in HFD hearts when compared to that in control specimens ($p = 0.0076$; **Figure 5.5D**). Our data indicates that although total levels of GLUT4-GFP remain consistent in the LV, protein distribution across the left ventricular wall is changed upon HFD feeding. This might well underscore changes in contractile activities in this region.

Finally, **figure 5.5A** also highlights the presence of GLUT4-GFP in more complex structural cardiac features - the LV papillary muscles (red arrow). Although not quantified in this analysis, this reveals the potential additional insight our approach can provide and exemplifies the potential of assessing protein content distribution profiles across the width of the 3D structure under study.

Figure 5.5. Quantification of Transmural GLUT4-GFP Fluorescence in Control and HFD Hearts.

(A) Mean transmural line profiles of GLUT4-GFP fluorescence across the width (x-axis) of left ventricular, septal, and right ventricular walls in control (blue; n = 6) and HFD (orange; n = 7) hearts. Fluorescence signal values are expressed relative to the highest intensity values between each group (maximum intensity = 2584.46 a.u.; control, LV). The position of LV papillary muscles along line ROI profiles in both groups is indicated by red arrows.

(B) Mean \pm s.d. of GLUT4-GFP fluorescent signal (a.u.) in the LV, septum and RV of control (blue; n = 6) hearts compared to HFD (orange; n = 7) hearts. (C) Mean \pm s.d. of GLUT4-GFP maximum fluorescence lateral position along the LV, septum and RV breadth in control (blue; n = 6) and HFD hearts (orange; n=7), expressed relative to total wall width. Dotted lines represent the horizontal centre of each cardiac wall. In both control and HFD hearts, data indicate GLUT4 fluorescence significantly peaking toward the right-hand side of the septal wall when compared to the LV and RV, where a left-skewed accumulation of GLUT4 proteins is observed along the width of both ventricular walls. (D) This panel presents the same data as in C but as side-by-side comparisons between both studied experimental groups within each cardiac region. Mean \pm s.d. of GLUT4- GFP maximum fluorescence lateral position along the breadth of the LV, septum, and RV of control (blue; n=6) hearts compared to HFD (orange; n=7) hearts, expressed relative to total wall width. Data indicate a significant change in the lateral position of GLUT4-GFP maximum fluorescence toward the centre of the LV in HFD hearts when compared to control specimens. All lateral position values in C and D were measured from individual transmural fluorescence profiles. Profiles and fluorescent signal values were measured as described in section 2.2.8.4.2. a.u., arbitrary units. **, ***, **** represent $p \leq 0.01$, $p \leq 0.001$, $p \leq 0.0001$, and ns signify non-significant. Two-tailed unpaired t-tests with Welch's correction and Brown-Forsythe and Welch ANOVA tests were performed on all raw data of (B,D) and (C), respectively. Published in Geiser et al. (2024).

5.3.1.2.3 Sex-Specific Impact of a High-Fat Diet

No statistically significant differences were observed in GLUT4-GFP fluorescence signals and protein distribution patterns between male and female hearts examined as a single cohort within any of the examined cardiac sections (**Figure 5.6A,B**). However, a significant decrease was observed in left ventricular GLUT4-GFP levels in the heart of HFD females compared to control littermates ($p = 0.0404$; **Figure 5.6C**). Although the same statistical evaluation could not be applied to male specimens due to a low sample size for control males ($n = 2$), these data suggest that an HFD over 20 weeks might impact left ventricular GLUT4-GFP levels in females more significantly than in males. No significant differences in GLUT4-GFP fluorescence signals between control and HFD were found in the septum and RV of either males or females (see Appendix [7.5.3](#)).

In addition, a more variable and higher intra-specimen range in the GLUT4 fluorescence signal is evident in **figure 5.6C** for control females compared to HFD littermates. Interestingly, the opposite can be observed in males, suggesting an inverted effect of HFD feeding on left ventricular GLUT4 distribution between sexes. Further studies are needed to unravel the potential mechanisms at play.

Information on the lateral position of GLUT4-GFP maximum fluorescence along the breadth of each cardiac region was also extracted and studied within and between male and female hearts (see Appendix [7.5.3](#)).

Although the data highlight a significant regional heterogeneity in GLUT4-GFP transmural distribution among cardiac regions in both males and females, sex does not appear to significantly affect the distribution of GLUT4-GFP within either the septal or ventricular wall.

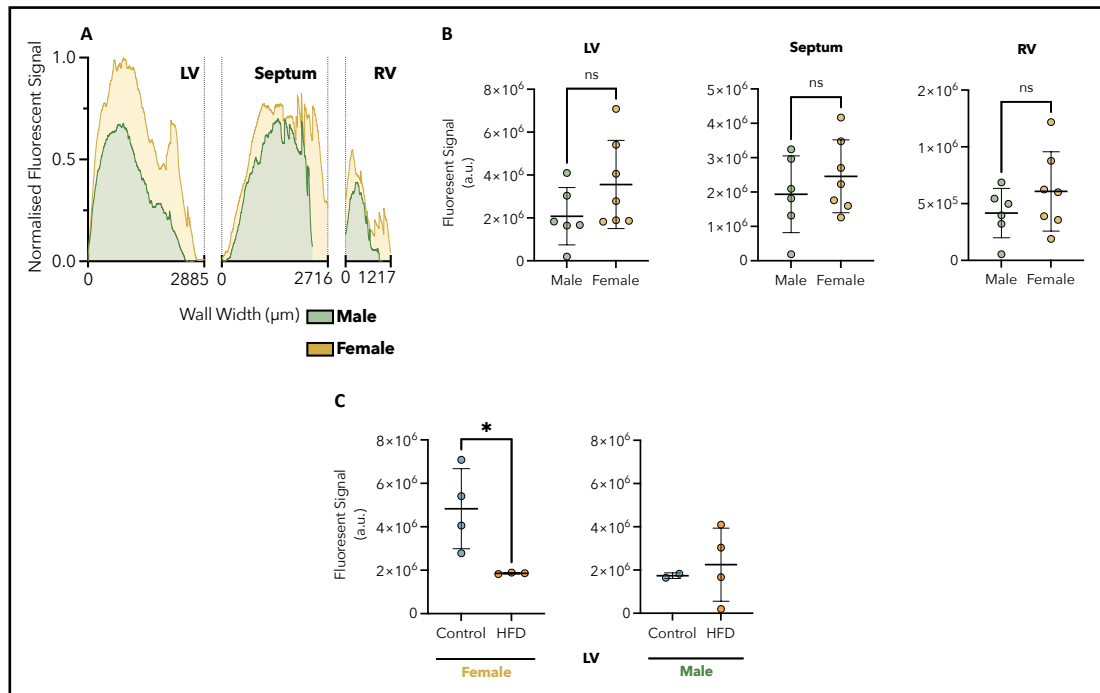


Figure 5.6. Quantification of Transmural GLUT4-GFP Fluorescence in Male and Female Hearts and the Impact of HFD in Females.

(A) Mean transmural line profiles of GLUT4-GFP fluorescence across the width (x-axis) of left ventricular, septal and right ventricular walls in male (green; $n = 6$, control = 2, HFD = 4) and female (yellow; $n = 7$, control = 4, HFD = 3) hearts. Fluorescence signal values are expressed relative to the highest intensity values between each group (maximum intensity = 2236.20 a.u.; Female, LV). (B) Mean \pm s.d. of GLUT4-GFP fluorescent signal (a.u.) in the LV, septum, and RV of male (green; $n = 6$, control = 2, HFD = 4) hearts compared to female (yellow; $n = 7$, control = 4, HFD = 3) hearts. (C) Mean \pm s.d. of GLUT4-GFP fluorescence signal (a.u.) in the LV of control (blue) compared to HFD (orange) hearts, in female (yellow; $n = 7$, control = 4, HFD = 3) and male (green; $n = 6$, control = 2, HFD = 4). Data indicate a significant decrease in left ventricular GLUT4-GFP fluorescent signal in HFD female hearts compared to control littermates. No statistical evaluation was applied to male specimens due to a low sample size for control males ($n=2$). Profiles and fluorescent signal values were measured as described in section 2.2.8.4.2. a.u., arbitrary units. * represents $p \leq 0.05$ and ns signify non-significant. Two-tailed unpaired t-tests with Welch's correction were performed on all raw data. Published in Geiser et al. (2024).

5.3.1.3 Anatomical Parameters of Cardiac Structure

The obtained 3D datasets can also be easily used to assess the gross anatomical features of the imaged myocardium. In addition to visualisation and measurement of fluorescence signals from GLUT4-GFP, we also extracted further anatomical parameters of cardiac structure from the Mesolens-acquired 3D reconstructed ventricular volumes, including the 2D surface area and width of cardiac walls of each studied region, as well as the size of the lumen (see Appendix [7.5.4](#) and see section [2.2.8.4](#)). Although the comparison of fluorescence between control and HFD tissues showed no statistical significance, these results exemplify the ability of optical mesoscopy to assess protein levels in concert with quantifiable parameters of cardiac structures.

Overall, the work presented in this section provides a set of quantitative analysis options that allow for a better understanding of GLUT4 distribution within 3D specimens of intact hearts using the open-source image processing Fiji software. This analysis pipeline is widely adaptable to diverse molecular and structural targets of interest.

5.3.2 *Optimisation of a Langendorff-Free Isolation Method for Viable Primary Adult Cardiomyocytes*

Aiming to extend the studies performed on adipocytes (see Chapters [3](#) and [4](#)) to muscle cells, this chapter develops a Langendorff-free cardiomyocyte isolation method. While Langendorff systems have been a staple in cardiac research, the challenges associated with these systems (see section [5.1.3](#)) have led to a growing interest in developing more accessible methods for isolating primary adult cardiomyocytes. A promising advancement in this field is the development of a Langendorff-free isolation technique (Ackers-Johnson et al., 2016), whereby enzymatic perfusion and cell dissociation are achieved through intraventricular injection. This alternative method aims to simplify the isolation process by eliminating the need for complex equipment and reducing the reliance on highly specialised skills.

5.3.2.1 Ensuring Cell Survival

Based on the work of Ackers-Johnson et al. (2016), we first optimised a Langendorff-free and enzymatic dissociation-based method for the isolation of adult cardiomyocytes from transgenic mice expressing HA-GLUT4-GFP (see section [2.2.2.1](#)), ensuring optimal cell yield and survival.

Initial experiments first involved cells reintroduction to supraphysiological calcium levels using a series of five calcium concentrations ranging from 100 μ M to 1.8 mM (Initial Concentrations; see section [2.1.1](#)), as recommended by Ackers-Johnson et al. (2016). This protocol, however,

resulted in a total cell number per mL of $12,500 \pm 1,838$ ($n = 2$), with $79.8 \pm 2.9\%$ of the isolated cells being non-viable hypercontracted cells (**Figure 5.7**). To try to improve these results, the number of calcium solutions used in reintroduction was reduced to two (Final Concentrations; see section [2.1.1](#)), only allowing for a modest increase in the total number of collected cells per mL ($20,400 \pm 7,637$, $n = 2$; **Figure 5.7B**), and, despite this adjustment, levels of hypercontractive cells remained relatively similar ($81.2 \pm 8.8\%$).

However, the introduction of BDM, a known myosin ATPase inhibitor, in the Perfusion and EDTA Buffers (see section [2.1.1](#)) appeared to prevent cardiomyocytes hypercontraction, thereby preserving their rod-shaped morphology (**Figure 5.7A**). By incorporating BDM, the balance between rod-shaped and hypercontracted cells shifted favourably towards an increased yield of rod-shaped cardiomyocytes (**Figure 5.7B**). Further optimisation was achieved by reducing the total heart digestion time from 10-12 min to 8-10 min (see section [2.2.2.4.2](#)). This suggests that digestion times exceeding 10 min may lead to over-digestion and reduced cell survival. Under these optimised conditions (2x Calcium Reintroduction Solutions, Addition of BDM, and Reduction of Digestion Time), the isolation protocol reproducibly yielded a total cell count per mL of $72,933 \pm 13,155$ ($n = 3$; **Figure 5.7B**), with a significantly higher number of viable rod-shaped cardiomyocytes ($71.0 \pm 3.8\%$; $p = 0.0369$).

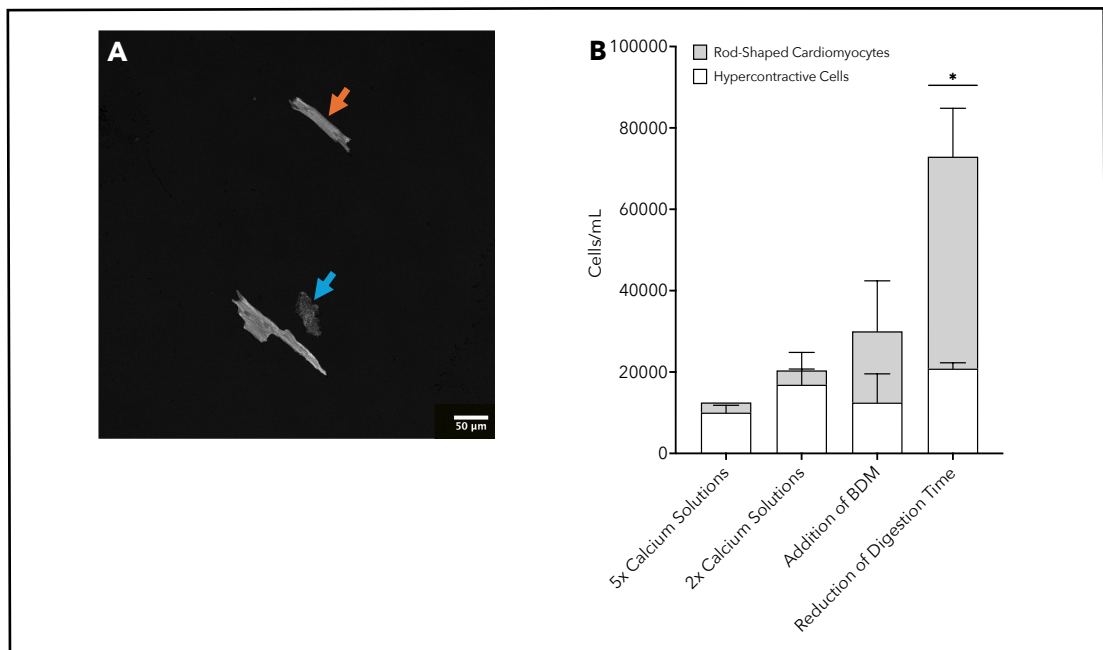


Figure 5.7. Protocol Optimisation for High Yields of Langendorff-Free Isolated Rod-Shaped Adult Mouse Cardiomyocytes.

(A) Representative confocal images of GFP fluorescence (grey) of untreated fixed adult mouse cardiomyocytes expressing HA-GLUT4-GFP isolated using BDM-free buffers as described in section 2.2.2.4.2 and reintroduced to supraphysiological calcium levels using 5 calcium concentrations ranging from 100 μ M to 1.8 mM (Initial Concentrations, see section 2.1.1; n = 2). Orange and blue arrows, respectively, point to viable rod-shaped cardiomyocytes and non-viable hypercontractive cells. Image was acquired using a 20 \times water immersion objective on a Leica TCS SP8 confocal microscope (see section 2.2.7.2.4). Scale Bars = 50 μ m. (B) Bar chart representation of total cell number per mL, including mean \pm s.d. number of viable rod-shaped cardiomyocytes (grey) and non-viable hypercontractive cells (white), measured using a hemocytometer after calcium reintroduction (see section 2.2.2.4.3). Protocol adjustments included calcium reintroduction using 5x calcium solutions or 2x calcium solutions (see section 2.1.1), the addition of BDM in Perfusion and EDTA Buffers (see section 2.1.1), and a decrease in heart digestion time from around 10-12 min to 8-10 min (see section 2.2.2.4.2). All data are representative of n = 2 independent experiments for each condition (1x male and 1x female), excluding when a reduction in digestion time was applied (n = 3 independent experiments, 2x male and 1x female). * represents $p \leq 0.05$. A two-tailed paired t-test was performed on raw data.

5.3.2.2 Immunostaining of Langendorff-Free Isolated Cardiomyocytes

Next, we assessed the effectiveness of immunofluorescent staining for detecting HA-tagged GLUT4 in primary adult mouse-isolated cardiomyocytes. Cardiomyocytes were incubated with anti-HA antibodies (non-biotinylated; see section [2.1.2](#)) under different conditions, and confocal microscopy was used to assess the resulting fluorescent signals. Anti-HA antibodies were added to non-permeabilised cells to allow the specific identification of GLUT4 correctly inserted into the PM (**Figure 4.6B,D**). As shown in **figure 5.8A,B**, when incubated with anti-HA antibodies for 1 h at room temperature, both non-permeabilised and permeabilised cells displayed near identical fluorescence intensity and co-localisation between the HA-tag and GFP signals, raising concerns about autofluorescence. The lack of difference between GFP fluorescence and the HA-tag signal reinforced the idea that antibody binding might not have been optimised under these conditions and that 1 h incubation time might have been insufficient to achieve HA-specific staining.

To address this, we increased the incubation time to overnight (O/N) at 4°C. The extended incubation yielded markedly improved results, as demonstrated in **figure 5.8C,D**. In non-permeabilised cells (**Figure 5.8C**), there was a clear distinction between the HA-tag and GFP signals, indicative of more specific HA-tag binding. More notably, in permeabilised cells (**Figure 5.8D**), the anti-HA staining highlighted the presence of internal GLUT4 vesicles in close proximity to the PM. Therefore, these findings (**Figure 5.8C,D**) confirmed the presence of stained HA-tagged

GLUT4. This demonstrates that the modified protocol can successfully label and differentiate between internal and PM-fused GLUT4 in isolated cardiomyocytes. Our long-term goal is to use this protocol in SRM studies to investigate GLUT4 dispersal across the PM (see [Chapter 4](#)).

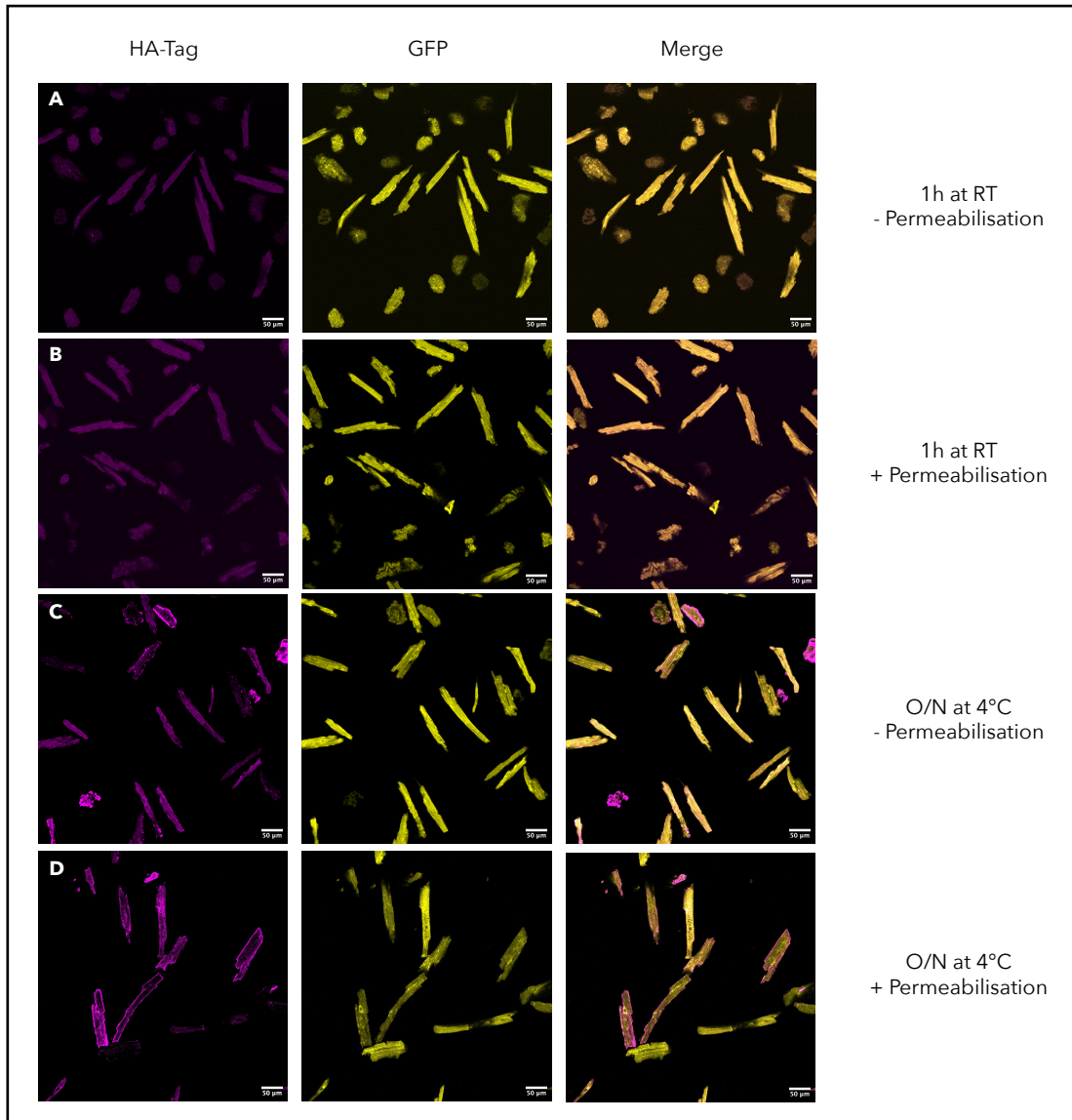


Figure 5.8. Optimisation of HA-Tagged GLUT4 Immunofluorescent Staining in Adult Mouse Isolated Cardiomyocytes.

Confocal images of untreated adult mouse cardiomyocytes expressing HA-GLUT4-GFP isolated as described in section [2.2.2.4](#). Left Panel: Confocal images of immunostained HA-tag fluorescence (magenta) in cells incubated with primary antibodies for 1 h at room temperature without (A) and with (B) permeabilisation or overnight at 4°C without (C) and with (D) permeabilisation (see section [2.2.7.1.2](#)). Middle Panel: Confocal images of GFP fluorescence (yellow). Right Panel: Merged immunostained HA-tag and GFP fluorescences. The staining protocols in (A,B) and (C,D) were performed on cells isolated from independent male mouse hearts. Each staining protocol was performed once. Secondary antibodies labelled with Alexa Fluor™ 647 were used from immunostaining (see section [2.1.2](#)). All images were acquired using a 20× water immersion objective on a Leica TCS SP8 confocal microscope (see section [2.2.7.2.4](#)). Scale Bars = 50 μm.

5.3.2.3 Insulin Stimulation of Langendorff-Free Isolated Cardiomyocytes

To validate whether isolated cardiomyocytes could respond to insulin stimulation, we first adapted our standard protocol for insulin stimulation used in 3T3-L1 adipocytes (see section [2.2.1.3](#)). Given the sensitivity of primary adult cardiomyocytes, cells were first only serum-starved for 1 h and then insulin-stimulated for 20 min (see section [2.2.2.4.4](#)). Confocal images were captured to assess the localisation of HA-tagged GLUT4. As shown in **figure 5.9A,B**, no major differences were observed between basal and insulin-stimulated cells in terms of GLUT4 translocation, as evidenced by the similar distribution of immunostained HA-tag signals.

To further verify the efficiency of insulin stimulation, we assessed the phosphorylation of Akt, a key downstream target of insulin signalling (see

section [1.3.2.1](#)), using western blot analysis (**Figure 5.9C**). Cardiomyocytes were serum-starved for either 1 h or 1 h 30, then insulin-stimulated for 20 min, and lysed for protein analysis (see section [2.2.3.2](#)). Surprisingly, phospho-Akt (S473) was detected under both basal and insulin-stimulated conditions, regardless of the serum starvation time. This finding suggests that the isolated cardiomyocytes may have lost their ability to properly reset to a basal state and, therefore, their capacity to exhibit a clear insulin response.

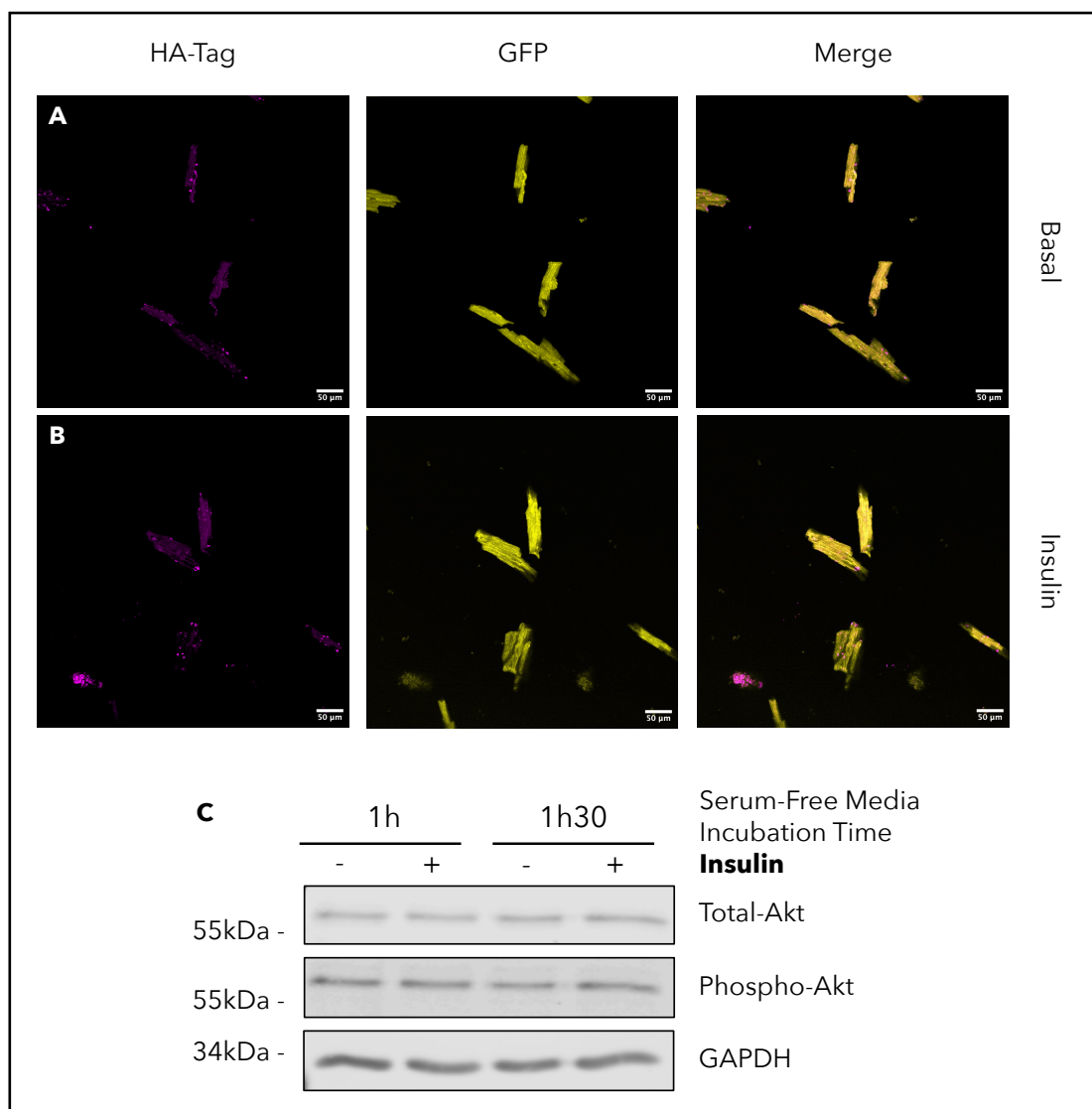


Figure 5.9. Insulin Stimulation of Adult Mouse Langendorff-Free Isolated Cardiomyocytes.

(A,B) Confocal images of adult mouse cardiomyocytes expressing HA-GLUT4-GFP isolated using a Langendorff-free and enzymatic dissociation-based isolation method as described in section [2.2.2.4](#), and treated without (Basal; A) and with 100 nM insulin for 20 min (B). Left Panel: Confocal images of immunostained HA-tag fluorescence (magenta). Middle Panel: Confocal images of GFP fluorescence (yellow). Right Panel: Merged immunostained HA-tag and GFP fluorescences. Data from a representative experiment are shown (n = 2; 1x male and 1x female). Cells were fixed and immunostained as described in [2.2.7.1.2](#). Secondary antibodies labelled with Alexa Fluor™ 647 were used from immunostaining (see section [2.1.2](#)). All images were acquired using a 20× water immersion objective on a Leica TCS SP8 confocal microscope (see section [2.2.7.2.4](#)). Scale Bars = 50 μm. (C) Immunoblot showing levels of total-Akt and phosphorylated (S473) Akt in adult mouse cardiomyocytes isolated using a Langendorff-free and enzymatic dissociation-based isolation method, serum-starved for either 1 h or 1 h 30 and treated without and with 100 nM insulin for 20 min (n = 1; female). GAPDH was used as a loading control. All cell lysates were produced and loaded as described in [2.2.3.2](#) and [2.2.5.2](#). Blots were visualised with a LI-COR Odyssey-SA system.

The observed lack of insulin responsiveness in isolated mouse cardiomyocytes (**Figure 5.9**) raised concerns about the relative quality and functional integrity of the cells isolated in this study. To determine whether this issue was specific to the isolation technique or inherent to the cells, we repeated the above insulin stimulation experiments using adult rat cardiomyocytes isolated using a Langendorff perfusion system. Although more complex, this approach is well-established for providing higher cell viability and integrity (Bell et al., 2011).

As shown in **figure 5.10A,B**, contrary to mouse cardiomyocytes, the HA-tag is detected at the PM in rat cardiomyocytes under both basal and

insulin-stimulated conditions. However, the intensity of the HA-tag signal appears stronger in the insulin-stimulated state, suggesting an increased translocation of GLUT4 to the membrane upon insulin stimulation.

Western blot analysis provided further insights into the insulin responsiveness of Langendorff-isolated cardiomyocytes from rats (**Figure 5.10C**). While phosphorylated Akt was detectable in the basal state, the intensity of phospho-Akt bands increased after insulin stimulation.

These results suggest that the observed lack of a responsive insulin signalling pathway in mouse cardiomyocytes may be linked to the isolation method, which could impair the cells' ability to reset to a proper basal state. Although a Langendorff-based isolation technique appears to offer better conditions for cardiomyocyte viability and insulin signalling, further optimisation of the isolation process may be required to achieve clear, insulin-induced GLUT4 translocation in isolated cardiomyocytes.

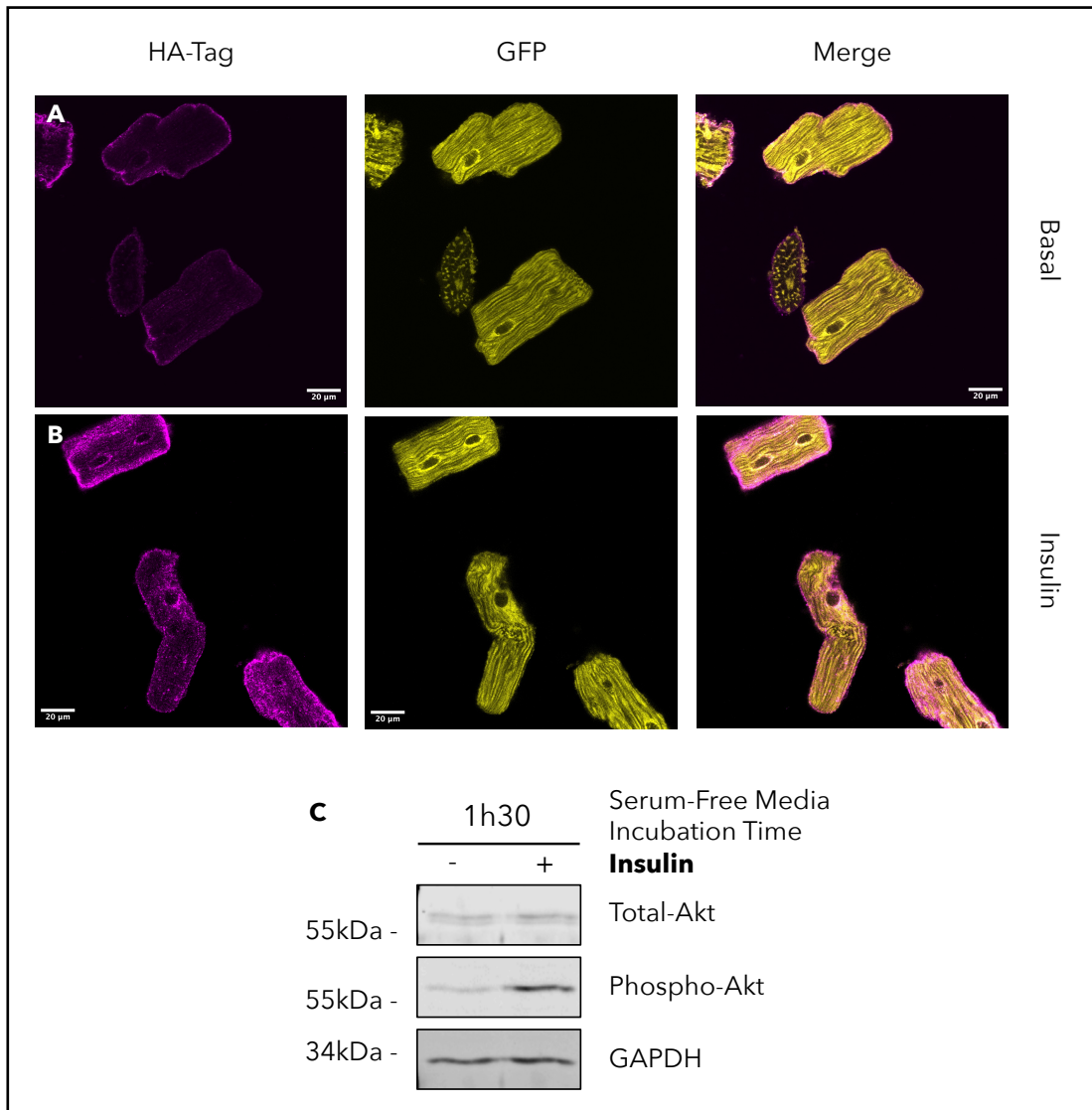


Figure 5.10. Insulin Stimulation of Adult Rat Cardiomyocytes Isolated using a Langendorff Perfusion System.

(A,B) Confocal images of adult rat cardiomyocytes transfected with HA-GLUT4-GFP and isolated using a Langendorff-based isolation method, and treated without (Basal; A) and with 100 nM insulin for 20 min (B) (n = 1; male). Cells were kindly gifted by Prof. Luc Bertrand and Dr. Laurent Bultot from the Institut de Recherche Expérimentale et Clinique, Université Catholique de Louvain, Belgium. Left Panel: Confocal images of immunostained HA-tag fluorescence (magenta). Middle Panel: Confocal images of GFP fluorescence (yellow). Right Panel: Merged immunostained HA-tag and GFP fluorescences. Cells were immunostained as described in [2.2.7.1.2](#). Secondary antibodies labelled with Alexa Fluor™ 647 were used from immunostaining (see section [2.1.2](#)). All images were acquired using a 20× water immersion objective on a Leica TCS SP8 confocal microscope (see section [2.2.7.2.4](#)). Scale Bars = 50 μm. (C) Immunoblot showing levels of total-Akt and phosphorylated (S473) Akt in adult rat cardiomyocytes isolated using a Langendorff-based isolation method, serum-starved for 1 h 30 and treated without and with 100 nM insulin for 20 min (n = 1; male). Cells were kindly provided by Prof. Susan Currie and Zainab Olatunji from the Strathclyde Institute of Pharmacy & Biomedical Sciences, University of Strathclyde, UK. GAPDH was used as a loading control. All cell lysates were produced and loaded as described in [2.2.3.2](#) and [2.2.5.2](#). Blots were visualised with a LI-COR Odyssey-SA system.

5.4 Chapter 5 - Discussion and Future Work

5.4.1 Expanding Mesoscopy Applications

In section [5.3.1](#), we used, for the first time, the imaging capability of the Mesolens to visualise and analyse intact cardiac tissues. We show that optical mesoscopy allows for a non-destructive visualisation of whole mounts of anatomical intact heart sections up to 5 mm×5 mm×3 mm in size with high spatial resolution in 3D. Using GFP-tagged GLUT4 as proof of concept, we demonstrate that the visualisation of GLUT4-GFP fluorescence within distinct anatomical structures across the myocardium is feasible in tissues up to 3 mm thick (**Figure 5.1**). While we focused on ventricular structures, as isolation of the atria would have required further dissection technique optimisation due to their small size in mice, we note that our approach could equally be applied to smaller tissue sections, such as atria or any tissue samples where dimensions do not exceed those used here. The use of a Langendorff-based perfusion method for the isolation of haem-rich organs such as the heart (Bell et al., 2011), as well as the addition of N,N,N',N'-Tetrakis(2-hydroxypropyl)ethylenediamine (Quadrol) as a decolorising agent (Jing et al., 2018), have been suggested to improve axial imaging depth; the current limitation of imaging depth is the 3 mm working distance of the Mesolens (McConnell et al., 2016) but these present opportunities for further bioimaging technology development.

Here, we recognise the limitation of using a GFP-tagged GLUT4 transgene to interpret the biological significance of any observed changes, as the transgenic GLUT4 construct is not likely to be transcriptionally regulated in

the same fashion as endogenous proteins. However, we want to emphasise that the presented mesoscopy approach is applicable to any target protein that can be labelled for light microscopy (i.e., via transgenic fluorescent labelling or immunostaining). For instance, in conditions such as HFpEF, literature has shown that enlargement of the heart, defined as concentric hypertrophy, arises from lipid infiltration and adipocyte dysfunction within the myocardium (Katz and Rolett, 2016; Murdolo et al., 2015). Whether concentric hypertrophy affects the distribution of cardiomyocyte-expressed proteins across different cardiac structures is an important question that requires further analysis. Therefore, visualisation of the FA transporter, CD36, using the present mesoscopy approach could provide further insight into this question. In addition, the potential to marry this approach to additional markers within the same dataset in future studies, such as nuclear content for cell number quantification or cell type-specific markers, could considerably enrich this approach. We note that these (and other) studies are possible using the Mesolens, for instance, by focusing on more extremely obese animal models and by including both adipocytes and cardiomyocyte cellular markers within a single dataset. However, it is important to note that these additions come with significant data volume size constraints.

Ware et al. and Maria et al. have previously revealed cardiac regional heterogeneity in GLUT4 content under pathological conditions (Maria et al., 2015; Ware et al., 2011) (see section [5.1.2](#)). However, from the use of crude cellular samples, the question remained whether variations in protein content represented a global change or whether distinct architectural features within different heart regions might adapt differently. Here, we show a skewed distribution of GLUT4-GFP levels along ventricular

and septal wall width within 3D myocardial volumes (**Figure 5.5D**), which could well underscore changes in contractile activities. Such changes cannot be detected using other currently available approaches. In addition, within the context of the heart, some further notable points revealed by this study include a capacity to visualise and quantify structures that have been classically difficult to study, such as the septum and papillary muscles, and an ability to systematically quantify protein distribution across myocardial walls on the micron- scale in intact tissues.

Examining defined cardiac regions also revealed a significant decrease in GLUT4-GFP levels in the LV of female mice fed an HFD compared to control littermates (**Figure 5.6C**). These data are intriguing, considering that human females with diabetes have a 50% higher risk of developing fatal CHD compared to males with diabetes (Huxley et al., 2006). Similarly, studies have shown that individuals with HFpEF are predominantly female and that females are more likely to have multiple comorbidities, including diabetes and obesity (Cheng et al., 2014; McHugh et al., 2019). However, although animal models are widely used to study the pathophysiology of human diseases, the distinctions of diet style-induced cardiovascular disease between males and females remain largely unexplored. Our data highlight the importance of sex equality in research and, later, the development of adapted treatments.

Finally, we introduced a set of quantitative analysis options that allow for a better understanding of protein distribution within 3D specimens of intact hearts using the Fiji image processing software. This analysis pipeline remains widely adaptable to diverse molecular targets of interest and the understanding of distinct dynamic patterns within complex tissues. It

should be noted that the 3D datasets captured using the Mesolens provide considerably more information than analysed in this thesis. For example, the possibility of defining changes in protein expression levels following specific cardiac events, such as myocardial ischemia, in relation to the distinct location of the infarct, as well as in tissue adjacent and distal to the injured area, could provide real value in understanding whether the damage might be reversible or not (Zimmermann et al., 2017). Similarly, quantification of protein expression patterns across endo-, mid- and epicardial layers of each chamber of the heart is a possibility that could provide detailed information associated with contractile parameters, such as global longitudinal strain (Currie et al., 2005).

Overall, we believe that this novel 3D imaging approach could offer new insight into metabolic changes across the intact heart in models of cardiovascular disease, reconciling research of cardiac remodelling both at a structural and biomolecular level.

5.4.2 *Deciphering the Role of GLUT4 N-Glycosylation*

In section [5.3.1](#), we also highlighted the regional heterogeneity in GLUT4 amino-glycosylation patterns across different cardiac chambers in mice fed a standard chow diet, suggesting potential interspecies variation in these glycosylation profiles (**Figures 5.3.C and 5.4**).

In 1996, Ing et al. first proposed that amino-glycosylation of GLUT4 could play a crucial role in regulating its trafficking and sorting into GSC (Ing et al., 1996). Glycans on glycoproteins are well-established for modulating various physicochemical properties of proteins, such as solubility, folding

capacity, and thermal stability. Beyond these effects, glycosylation can influence the bioactivity of proteins and their intracellular and intercellular transport. Given these wide-ranging impacts, it is unsurprising that subsequent studies confirmed GLUT4 amino-glycosylation as a facilitator of interactions between GLUT4 and other GSC cargo proteins such as sortilin (Haga et al., 2011; Shi and Kandror, 2007).

Sortilin is a 110 kDa protein encoded by the *SORT1* gene, which belongs to the vacuolar protein sorting 10 protein (Vps10p) family of type I transmembrane receptors, which are highly expressed in the atrium (Linscheid et al., 2020; Mazella et al., 1998; Morris et al., 1998). In adipocytes and myocyte cell lines, sortilin has been shown to have a high degree of colocalisation with GLUT4 and to be involved in the biogenesis of IRV, highlighting sortilin as a scaffolding protein between GLUT4, IRV, and other GSC (Lin et al., 1997; Morris et al., 1998; Shi and Kandror, 2005). In adipocytes, sortilin scaffolding abilities were found to be dependent on its palmitoylation (McCormick et al., 2008; Ren et al., 2013). Sortilin was shown to enable GLUT4 retrieval from the endosomal system back to the TGN (Ariga et al., 2008; Shi and Kandror, 2005). More specifically, sortilin was found to bind with GLUT4 proteins via its Vps10p domain in endosomal membranes and to recruit retromer to the cytoplasmic side of the donor membrane via its carboxy-terminus to facilitate GLUT4 retrieval from the endosomal system to the TGN (Pan et al., 2017). Pan et al. also established that palmitoylation was requested for interactions with retromers to happen (Pan et al., 2017).

In line with this model and the data presented in **figures 5.3.C and 5.4**, it is therefore tempting to speculate on the degree to which the GLUT4

trafficking pathway in cardiac tissue is dependent on these post-translational modifications across different regions of the heart and species. To gain deeper insights into this phenomenon, future research should aim to replicate these findings in additional accessible species while expanding the focus to investigate proteins involved in the GLUT4 glycosylation process in different heart regions. Furthermore, comparative studies between healthy and diseased hearts will be essential to understand how these modifications may change in pathological conditions, potentially offering new therapeutic targets for cardiovascular diseases.

5.4.3 Isolation of Adult Rodent Cardiomyocytes:

To Langendorff, or Not to Langendorff?

As illustrated in section [5.3.2](#), the development of a Langendorff-free cardiomyocyte isolation method, although simplifying the process and increasing accessibility, required significant optimisation to enhance cell viability and minimise hypercontraction. Adjustments, including the incorporation of BDM and the modification of calcium reintroduction protocols, led to improved yields of viable rod-shaped cardiomyocytes. However, challenges remained in maintaining functional insulin responsiveness in these isolated cardiomyocytes.

Contrary to the suggestions of Ackers-Johnson et al. (Ackers-Johnson et al., 2016), we therefore propose that cells isolated using the traditional Langendorff-based method exhibit higher quality. One inherent drawback of a Langendorff-free approach is the manual control of perfusion, making it challenging to regulate the flow rate. In contrast, a Langendorff system

can maintain constant pressure and flow (Bell et al., 2011). To obtain similar results to that of a Langendorff-based method, the addition of a syringe pump, similar to the one described in Chapter 4 (see section [4.3.1](#)), to the isolation protocol used in this study may offer assistance. In addition, perfusing mice hearts by repeatedly inserting a needle into the LV requires caution to prevent ruptures or leaks in the ventricular walls due to the heart's small size and thinness of the walls. This process could also be improved by using a multi-syringe pump, allowing solutions to be perfused through a single insertion point.

Overall, the data presented in this section suggest that additional studies are warranted to definitively demonstrate the ability of a Langendorff-free isolation method to preserve the physiological integrity of cardiomyocytes, especially for studies investigating insulin-mediated pathways.

Final Conclusion and Future Perspectives

In conclusion, this thesis has furthered our understanding of the regulation of the GLUT4 machinery in adipose and muscle tissues by integrating molecular and cellular methods and innovative state-of-the-art imaging techniques.

As a result, we first propose here a refined model for the regulation of GLUT4 dispersal by the EFR3a/PI4K-III α complex (**Figure 6.1**), wherein EFR3a is sequestered within lipid rafts under basal conditions, which restrict its interaction with PI4K-III α . This spatial segregation is hypothesised to play a key role in maintaining GLUT4 in a clustered state within the PM, preventing premature dispersal. Upon insulin stimulation, EFR3a is released from lipid rafts, and its localisation within the PM is increased, facilitating the recruitment of soluble PI4K-III α to the PM. This leads to increased production of PI4P, which disrupts the corral formation around GLUT4 clusters, promoting the dispersal of GLUT4 monomers and facilitating increased glucose uptake. This model thereby emphasises the importance of the spatial organisation of GLUT4 at the PM for an effective insulin response.

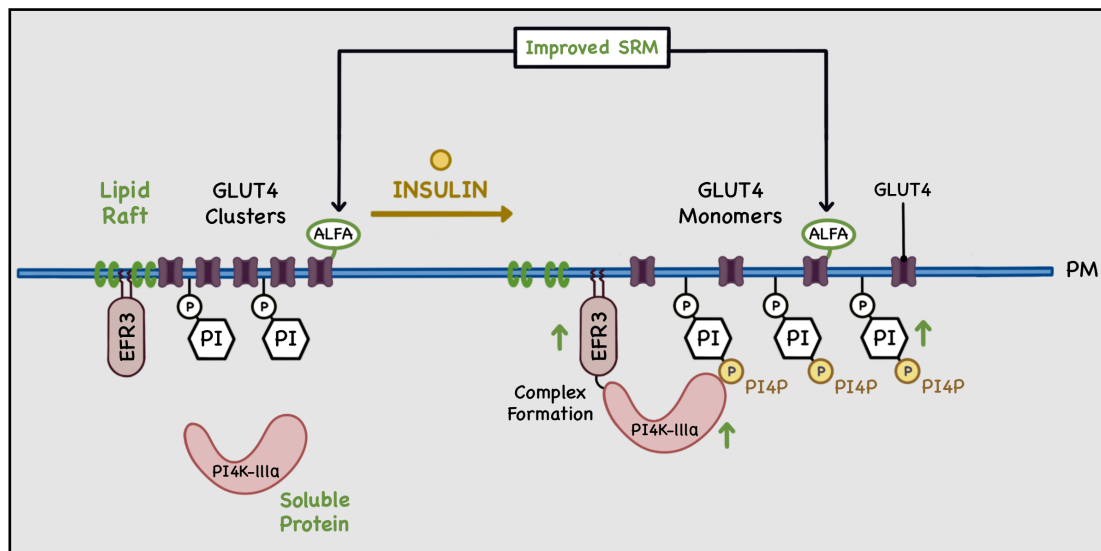


Figure 6.1. Updated Model of EFR3a/PI4K-IIIa-Regulated GLUT4 Dispersal in Adipocytes and Methodological Advancement for the Study of GLUT4 Spatial Organisation within the Plasma Membrane.

A refined model (updates are shown in green) for the regulation of insulin-stimulated GLUT4 dispersal within the plasma membrane (PM) by the EFR3a/PI4K-IIIa complex. In the basal state, EFR3a is sequestered within lipid rafts, which restrict its interaction with PI4K-IIIa, and PM-fused GLUT4 molecules (shown as purple structures) are maintained in clusters. EFR3a is released from lipid rafts, and its localisation within the PM is increased, facilitating the recruitment of soluble PI4K-IIIa to the PM. This leads to the phosphorylation of phosphoinositides (PI) into phosphatidylinositol 4-phosphate (PI4P), which disrupts the corral formation around GLUT4 clusters, promoting the dispersal of GLUT4 monomers. The ALFA-GLUT4 construct represents a notable methodological advancement, allowing for improving the spatial localisation and tracking of GLUT4 at the PM using SRM techniques.

While this proposed model of EFR3a/PI4K-III α -mediated regulation of GLUT4 dispersal offers a compelling framework, further experimental validation is necessary. The development of the ALFA-GLUT4 construct marks a notable methodological advancement for future research. By replacing the traditional HA-tag with an ALFA-tag, the construct has the potential to allow improved spatial localisation and tracking of GLUT4 using SRM techniques (**Figure 6.1**). This innovation also sets the stage for similar approaches to study other membrane proteins and expands the potential for multiplexing target detection using Exchange-PAINT. Additionally, incorporating live-cell imaging could provide the temporal resolution needed to complement the spatial data obtained through SRM, enabling researchers to capture dynamic changes in GLUT4 localisation and dispersal in response to real-time insulin stimulation. This combined approach could be further broadened to include the study of other key regulatory proteins in the EFR3a/PI4K-III α complex, such as TTC7, FAM126A, and TMEM150A. Such expansion would offer a more comprehensive understanding of the molecular machinery that controls glucose metabolism.

Extending the above methodology to other tissues, such as cardiac muscles, could provide even broader insights into the regulation of the GLUT4 machinery. This thesis, therefore, also addressed methodological challenges in cardiovascular research. At the single-cell level, the aim was to develop a Langendorff-free cardiomyocyte isolation method. While this approach is promising in its accessibility and simplified process, further optimisation is needed to match the physiological integrity of cells obtained via a traditional Langendorff-based method.

On the other hand, advanced imaging using the Mesolens has provided unprecedented clarity in visualising GLUT4 distribution across cardiac walls. This method not only uncovered changes in GLUT4 expression in response to HFD feeding but also revealed sex-dependent differences. The novel 3D imaging approach presents valuable insights into metabolic alterations within the heart in models of cardiovascular disease, bridging the gap between structural and molecular research on cardiac remodelling. We emphasise that the analysis pipeline presented here remains widely adaptable to diverse molecular targets of interest, allowing for the enhancement of our understanding of distinct protein dynamic patterns within complex tissues in both health and disease (see section [5.4.1](#)).

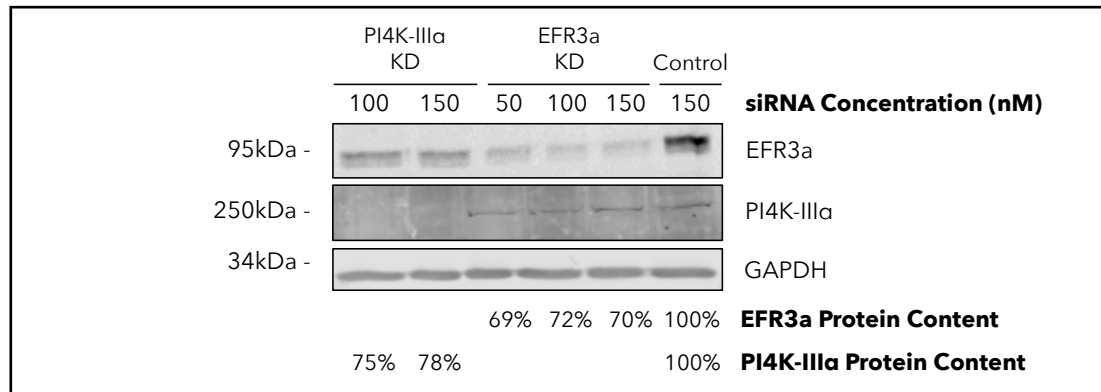
Finally, integrating multi-omics approaches, such as proteomics, lipidomics, and transcriptomics, with the spatial imaging techniques used in this thesis could reveal new regulatory networks underlying GLUT4 dynamics and suggest novel therapeutic interventions. Specifically, targeting EFR3a/PI4K-III α interactions may enhance GLUT4 dispersal and glucose uptake in insulin-resistant tissues, presenting new avenues for treating metabolic and cardiovascular diseases.

Overall, the present findings and novel tools and methods introduced in this thesis hold the potential to contribute to the development of new therapeutic strategies for managing metabolic diseases and enhancing the precision and scope of cellular biological research.

Appendices

7.1. Effectiveness of siRNA-Mediated *Efr3a* and *Pi4ka*

Knockdown in 3T3-L1 Adipocytes



Appendix Figure 7.1. Effectiveness of siRNA-Mediated *Efr3a* and *Pi4ka* Knockdown in 3T3-L1 Adipocytes.

Immunoblot showing protein contents of EFR3a and phosphatidylinositol 4-kinase type IIIα (PI4K-IIIα) in untreated WT 3T3-L1 adipocytes transfected with different final concentrations of siRNA designed to KD the expression of either PI4K-IIIα (PI4K-IIIα KD; Lane 1: 100 nM, Lane 1: 150 nM), EFR3a (EFR3a KD; Lane 3: 50 nM, Lane 4: 100 nM, Lane 5: 150 nM) or negative control non-targeting siRNA (Control; Lane 6: 150 nM, matching the maximal targeting-siRNA concentration used), six days post-differentiation. Starting concentrations were selected based on previous work in our laboratory (Koester et al., 2022b). GAPDH was used as a loading control. All cell lysates were produced and loaded as described in [2.2.3.3](#) and [2.2.5.2](#). Blots were visualised with a LI-COR Odyssey-SA system. EFR3a and PI4K-IIIα protein contents (expressed relative to GAPDH and compared to % Control; n = 1) within their respective KD cells are shown at the bottom. Optimal *Efr3a* and *Pi4ka* siRNA concentrations were selected as the lowest concentration yielding the relatively most efficient KD effect.

7.2 gRNA, Plasmid DNA, and Primers

7.2.1 CRISPR/Cas9 gRNA and Associated Primers

The *Mus musculus Efr3a* gene (Ensembl (Gene): ENSMUSG00000015002; forward strand), located on chromosome 15, was targeted for CRISPR/Cas9-mediated gene KO in WT 3T3-L1 fibroblasts (see section [2.2.1.6](#)). 23 coding exons were identified (Ensembl (Transcript): ENSMUST00000211878.2).

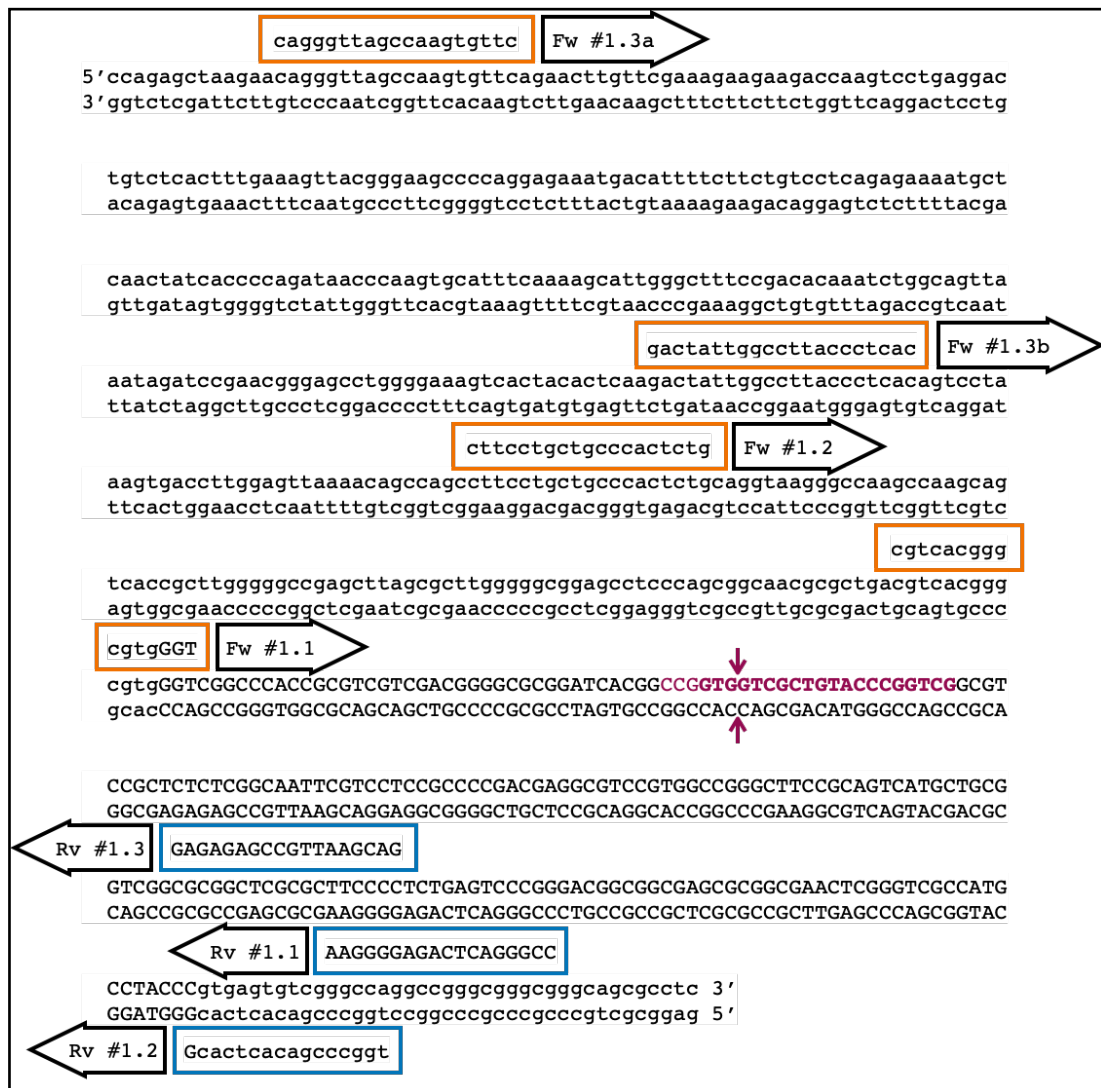
All gRNA and primers were designed using Custom Alt-R® CRISPR-Cas9 gRNA (https://eu.idtdna.com/site/order/designtool/index/CRISPR_CUSTOM; Integrated DNA Technologies) and Primer-BLAST (<https://www.ncbi.nlm.nih.gov/tools/primer-blast/>; NCBI), respectively.

7.2.1.1 CRISPR/Cas9 gRNA/Primers Set #1

Target Site	PAM		gRNA		
Primers	Tm	PCR Ta	PCR Product	Product Post-Surveyor® Nuclease Assay	
Exon 1	CCG GTGGTCGCTGTACCCGGTCCG				
Fw #1.1: CGTCACGGGCGTGGGT	70.0°C				
Rv #1.1: CCGGGACTCAGAGGGGAA Reverse complement: TTCCCCTCTGAGTCCCGG	67.7°C	65 & 55°C	184 bp	129 bp & 55 bp	
Fw #1.2: CTTCTGCTGCCCACTCTG	66.3°C				
Rv #1.2: TGGCCCGACACTCACG Reverse complement: CGTGAGTGTCGGGCCA	66.4°C	55°C	344 bp	186 bp & 158 bp	
Fw #1.3a: CAGGGTTAGCCAAGTGTT	59.8°C				
Fw #1.3b: GACTATTGGCCTTACCCTCAC	61.3°C	55°C	a) 498 bp b) 259 bp	a) 453 bp & 45 bp b) 214 bp & 45 bp	
Rv #1.3: GACGAATTGCCGAGAGAG Reverse complement: CTCTCTCGGCAATTCGTC	61.2°C				

Appendix Table 7.1. CRISPR/Cas9 gRNA/Primers Set #1 Specificities.

7.2.1.2 CRISPR/Cas9 gRNA/Primers Set #1 Targeting the *Efr3a* gene (Exon 1)



Appendix Figure 7.2. Schematic of CRISPR/Cas9 gRNA/Primers Set #1 Targeting Exon 1 of the *Efr3a* Gene.

Exon (uppercase) 1 is surrounded by sections of introns (lowercase) 1 and 2, and gRNA #1 is shown in bold purple, immediately adjacent to the Cas9-binding PAM sequence 5' CCG 3' (shown in purple). Purple arrows show Cas9-induced DSB location, 3 nucleotides 3' to the PAM site. Primer pairs #1.1, #1.2, and #1.3, designed for genotyping, are framed by orange (forward; Fw) and blue (reverse; Rv) boxes.

7.2.1.3 CRISPR/Cas9 gRNA/Primers Set #2

Target Site	PAM	gRNA		
Exon 6		CCT CGCTACAAACGTCTGGTGA		
Primers	Tm	PCR Ta	PCR Product	Product Post-Surveyor® Nuclease Assay
Fw #2.1: GCATCTCTCCTCACGTCCA	58.8°C			
Rv #2.1: GAGAAAGGTAAGCAAGCAAGGG	59.5°C			
Reverse complement: CCCTTGCTTGCTTACCTTTCTC				
Fw #2.2: GCAAAGCACAGAAAGCACGA	60.0°C			
Rv #2.2: CTGGCCATCATTGCATCT	58.0°C			
Reverse complement: AGATGCGAATGATGGCCAG				

Appendix Table 7.2. CRISPR/Cas9 gRNA/Primers Set #2 Specificities.

7.2.1.4 CRISPR/Cas9 gRNA/Primers Set #2 Targeting the *Efr3a* gene (Exon 6)



Appendix Figure 7.3. Schematic of CRISPR/Cas9 gRNA/Primers Set #2 Targeting Exon 6 of the *Efr3a* Gene.

Exon (uppercase) 6 is surrounded by sections of introns (lowercase) 6 and 7, and gRNA #2 is shown in bold purple, immediately adjacent to the Cas9-binding PAM sequence 5' CCT 3' (shown in purple). Purple arrows show Cas9-induced DSB location, 3 nucleotides 3' to the PAM site. Primer pairs #2.1 and #2.2, designed for genotyping, are framed by orange (forward; Fw) and blue (reverse; Rv) boxes.

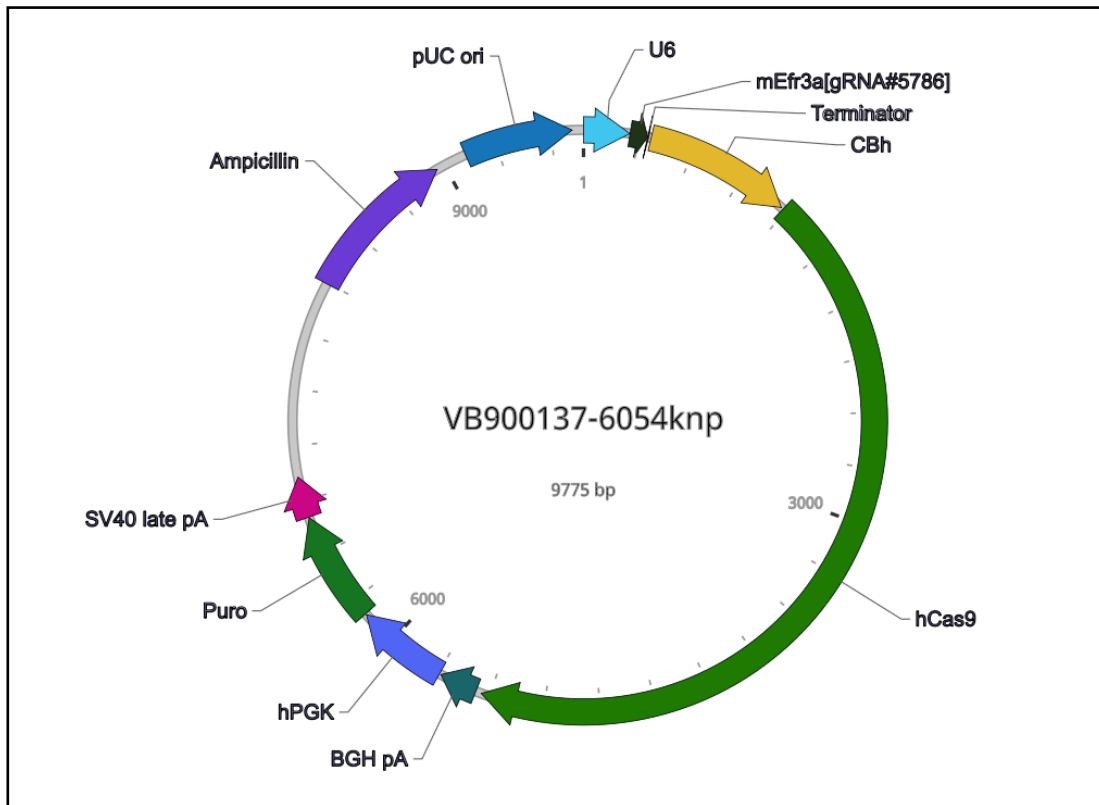
7.2.2 Plasmid DNA and Associated Primers

7.2.2.1 CRISPR/Cas9 Plasmid DNA and Associated Primers

7.2.2.1.1 CRISPR/Cas9 Plasmid DNA Map:

pRP[CRISPR]-Puro-hCas9-U6>mEfr3a[gRNA#5786]

The plasmid DNA pRP[CRISPR]-Puro-hCas9-U6>mEfr3a[gRNA#5786] was used to mediate CRISPR/Cas9 KO of *Efr3a*. It contains the sequences for Cas9, Efr3a-targeting gRNA at exon 17, and a puromycin resistance gene. The vector was ordered from VectorBuilder (Vector ID: VB900137-6054knp). Forward and reverse primer sequences associated with the inserted gRNA were provided along with the purchased plasmid.



Appendix Figure 7.4. CRISPR/Cas9 DNA Plasmid Vector Map of pRP[CRISPR]-Puro-hCas9-U6>mEfr3a[gRNA#5786].

7.2.2.1.2 CRISPR/Cas9 Plasmid DNA-Associated gRNA/Primers

Target Site	gRNA		PAM	
Primers	Tm	PCR Ta	PCR Product	Product Post-Surveyor® Nuclease Assay
Exon 17			GAGCAAAGCTCCG CGG TATC	
Fw #3: GGCTTCCTCTGTGTAAGGGTGTATC	66.7°C			
Rv #3: CTAAATTAGCACACGCACTTTCGAC	66.4°C	58°C	1147 bp	491 bp & 656 bp
Reverse complement: GTCGAAAGTGCGTGTGCTAATTTAG				

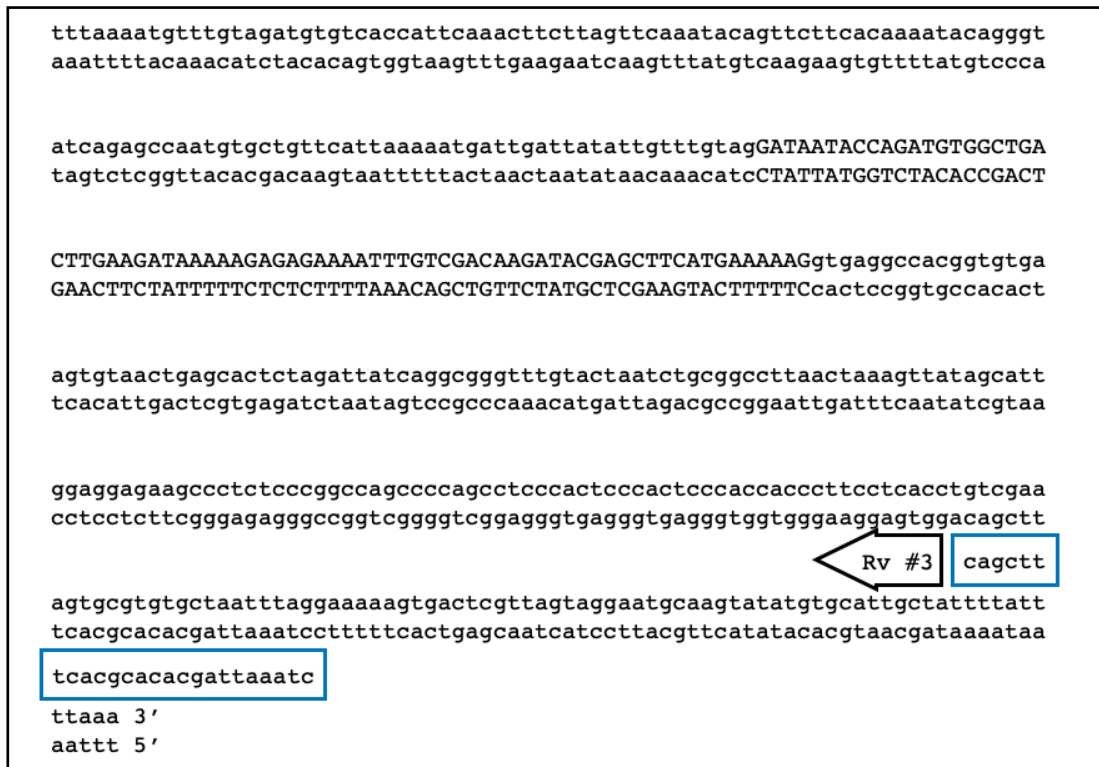
Appendix Table 7.3. CRISPR/Cas9 Plasmid DNA gRNA/Primers

Specificities.

7.2.2.1.3 CRISPR/Cas9 Plasmid DNA-Associated gRNA/Primers

Targeting the *Efr3a* gene (Exon 17)

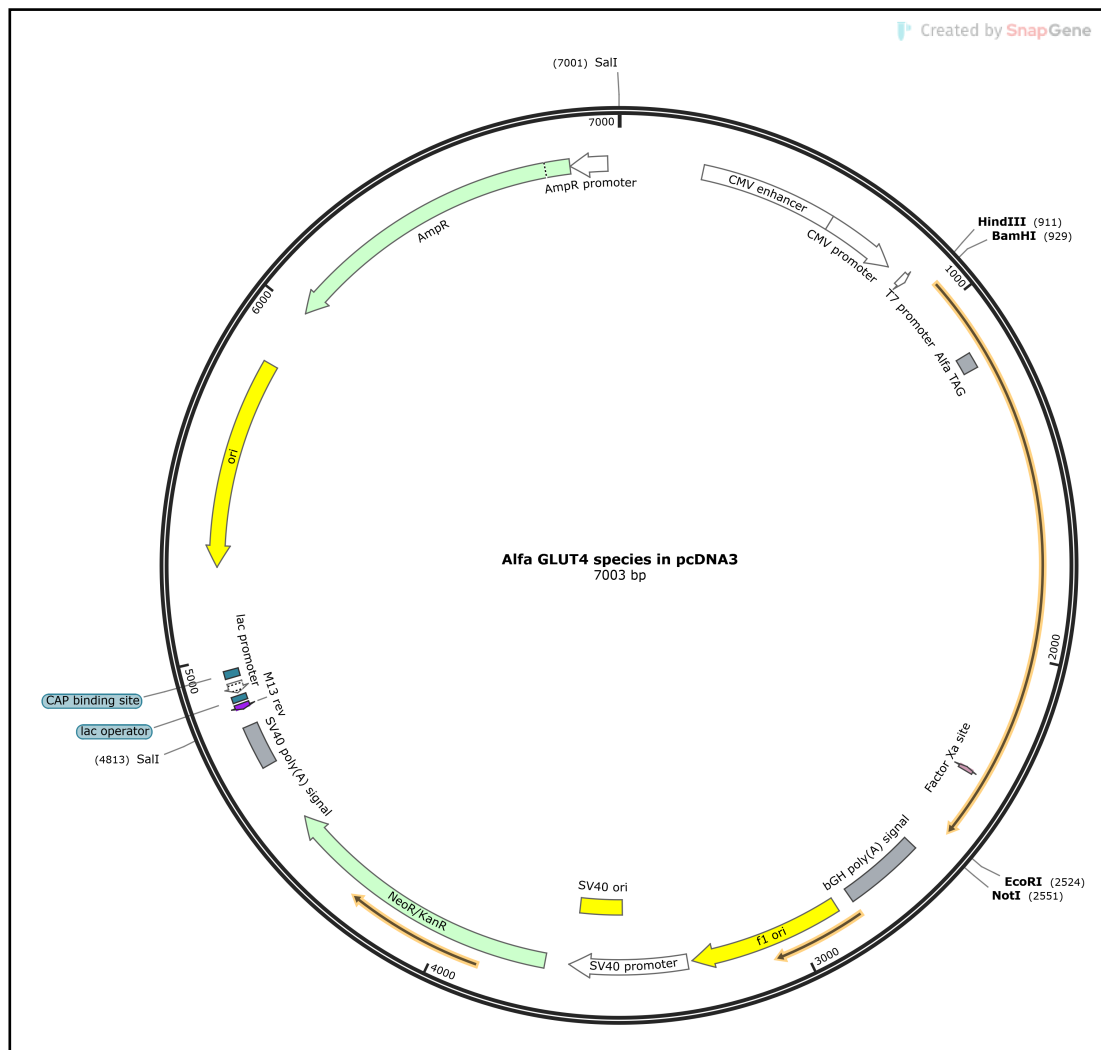
```
5' taagttgagtaacaaacacaatTTTCCAAACTGAAATATGTTCTATTCTTCCACTGCCTCTCTGAAA
3' attcaactcattgTTTGTGTTAAAAGTTTGACTTTTATACAAGGATAAGAAGGTGGACGTGAGAGACATTT
      ggcttcctctgtgtaaggggtatc Fw #3
tgtgTTGCCCTACTGTCTCCCTGGCTTCTCTGTGTAAGGGTGTATCAGCCTGCCTGACAGACAGCAGCC
acacaacggggatggacagagggaccgaaggagacacattcccacatagtcggacggactgtctgtcgtcgg
aagacagagttgacagggcatgtaatgtcgTACTTGcagttgagcctgcacatggtaccacatatgtgatgtg
ttctgtctcaactgtccgtacattacagcatgaacgtcaactcggacgtgtaccatggtgtatacactacac
catcttaaacttgTTTCAAaactgatcctgacataactaacatcttgactgcccgacagggttccttcatat
gtagaatttgaacaaagTTTatgactaggactgtatgattgtagaactgacgggtgtcccaaggaagtata
atTTCTtaggcttgtgcctatagTTTctgtttcccaacagaatTTTgttattaaaagagaatgtgataa
taaagaaatccgaacacggatatcaaagcaaagggTTTgtcttaaacaataatTTTctcttacactatt
tttTgcctaaagactcaagagaacatcgTTgtttgTTaatTTcccccttgtaatcagGTGACTTCTGGATAC
aaaacggatttctgagttctcttTgtagcaacaaacaattaagggggaacattagtcCACTGAAGACCTATG
AAAGCCAAGACAATTGTTACTGCACTGCCTGGGTCATTTCTGGATCCTCTATTGTCGCCATCCCTCATGGAA
TTTCGGTCTGTAAACAATGACGTGACGGACCCAGTAAAGACCTAGGAGATAACAGCGGTAGGGAGTACCTT
GACTATGAGCTGAGGCAGTTAGTCTTGAAGTAATGCACAACCTAATGGATCGCCATGACAACAGAGCAAAG
CTGATACTCGACTCCGTCAATCAGAACCTTCATTACGTGTGGATTACCTAGCGGTACTGTTGTCTCGTTTC
CTCCGCGGTATCAGgtgactcaccagactgggagggcttcaggagagcttttagtttctagtttctctca
GAGGCCCATAGTCcactgagtggtctgacctcccgaagtcctctcgaaaatcaaagatcaaagagagt
      ↓
      ↑
gtcagtggttgaatctgtgtgttgagcagggcgggggtgggggggtgtatatttagttggtgtcaaaa
cagtcacacaactttagacacacaacctcgtccgccccccaccccccaacataataatcaaccacagtttt
tgatttattaatttgatgactacgcatggattaaaaactggTTTTattttacttttgctttaagccaacaaa
actaaataaataaactactgatgcgtacctaatttttgacaaaataaaaatgaaaacgaaattcggttgttt
tgccactatgaaggaagatgatgtaactcctggTTaaacatgatcatccagtaatatcatttcatataaaca
acggtgatacttctctactacattgaggaccaatTTgtactagtaggtcattatagtaaagtatatTTgt
```



Appendix Figure 7.5. Schematic of CRISPR/Cas9 Plasmid DNA-Associated gRNA/Primers Targeting Exon 17 of the *Efr3a* Gene.

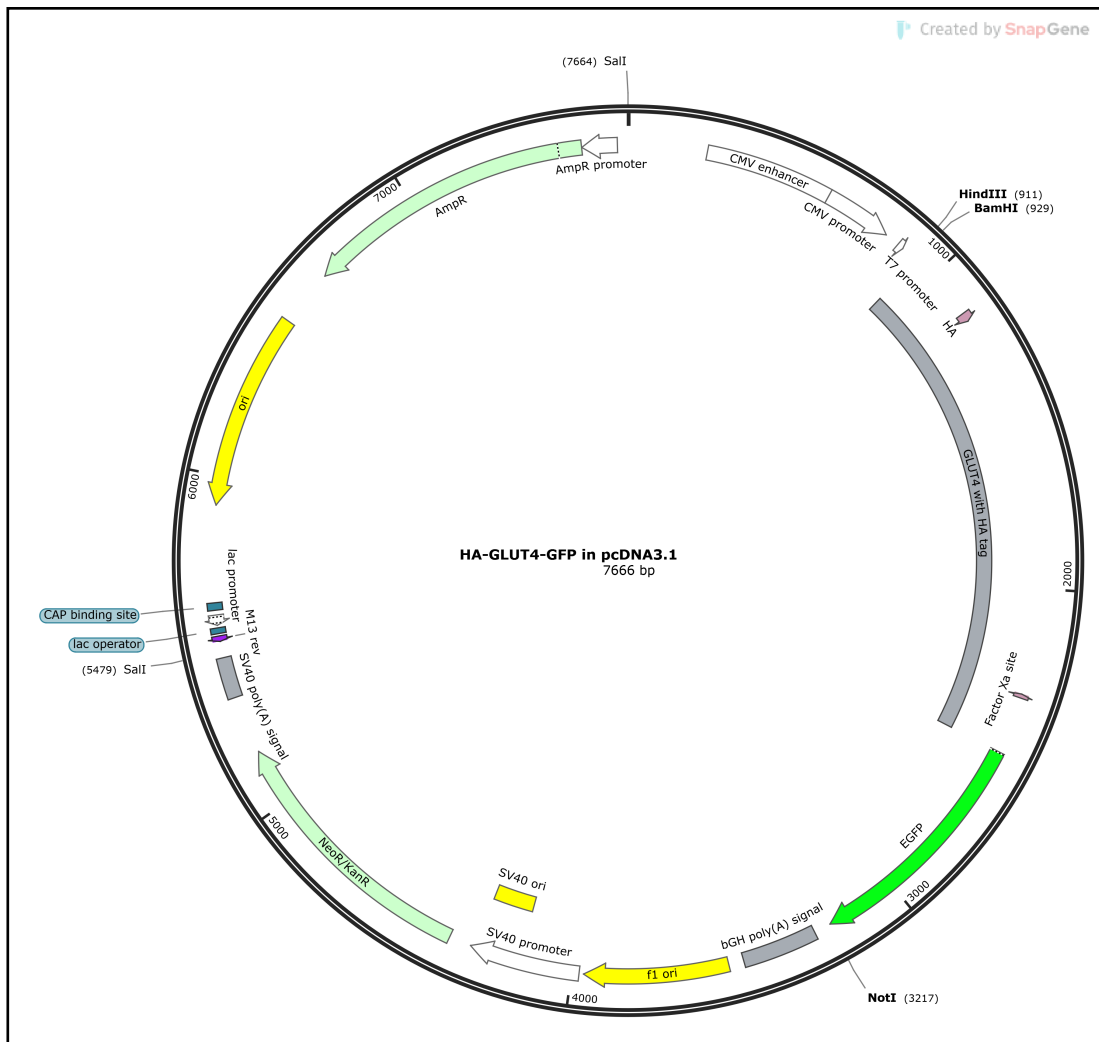
Exon (uppercase) 17 is surrounded by a section of intron (lowercase) 17 and intron 18, followed by exon 18 and a section of intron 19. Plasmid DNA-associated gRNA is shown in bold purple. The Cas9-binding PAM sequence 5' CGG 3' is shown in purple. Purple arrows show Cas9-induced DSB location, 3 nucleotides 3' to the PAM site. Primer pairs #3, designed for genotyping, are framed by orange (forward; Fw) and blue (reverse; Rv) boxes.

7.2.2.2 ALFA-GLUT4 Plasmid DNA Map



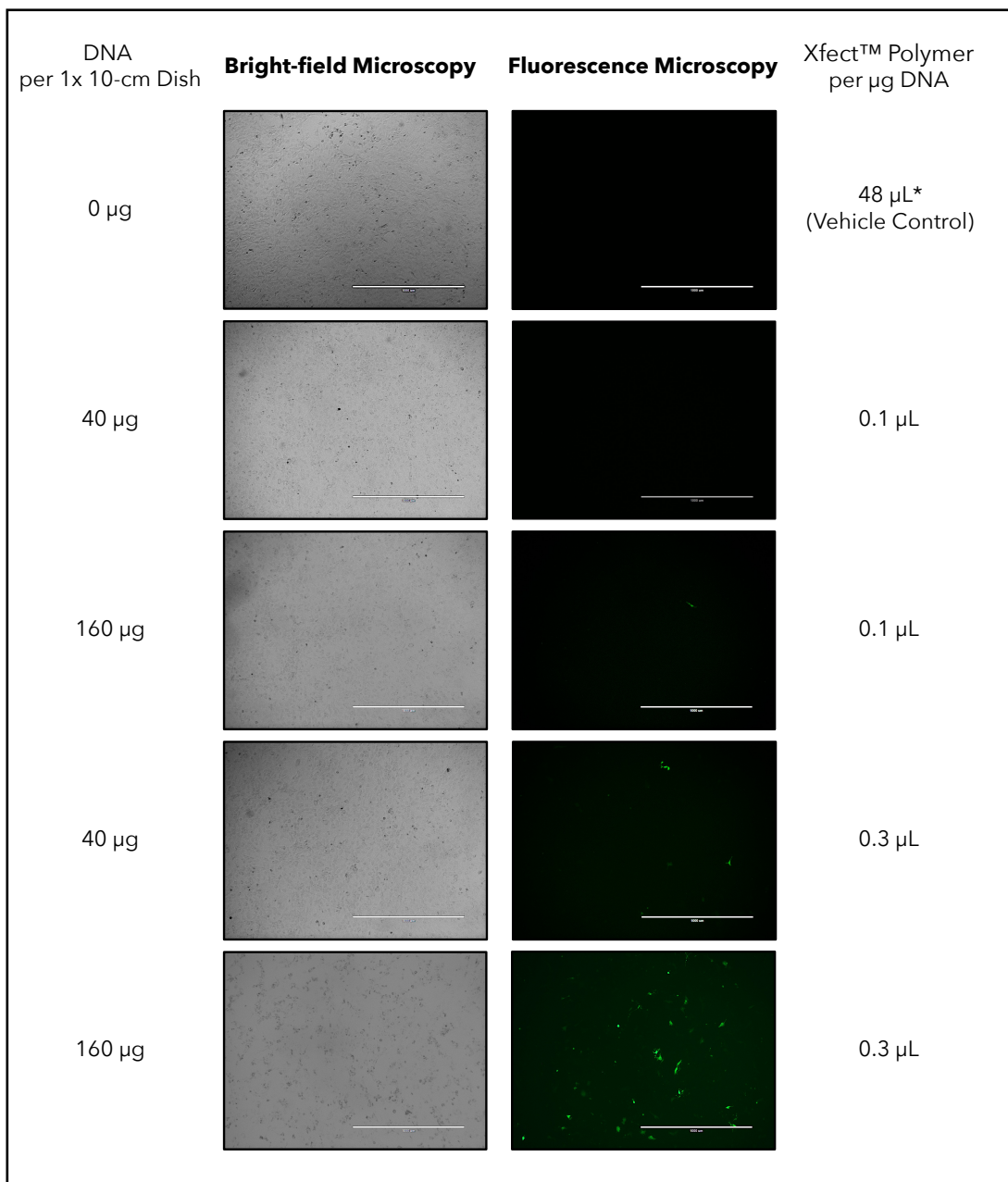
Appendix Figure 7.6. DNA Plasmid Vector Map of pcDNA3.1 (+) ALFA-GLUT4.

7.2.2.3 HA-GLUT4-GFP Plasmid DNA Map



Appendix Figure 7.7. DNA Plasmid Vector Map of pcDNA3.1 (+) HA-GLUT4-GFP.

7.3. Plasmid DNA Transfection Optimisation in 3T3-L1 Fibroblasts using Xfect™ Transfection Reagent



Appendix Figure 7.8. Optimisation of the Transient Transfection Protocol of pEGFP-C1-P4M-SidMx1 Plasmid DNA in 3T3-L1 Fibroblasts using Xfect™ Transfection

Reagent.

Volumes were calculated for transfection in a 1x 10-cm dish. Bright-field and fluorescence microscopy images of 3T3-L1 fibroblasts (WT) transfected with pEGFP-C1-P4M-SidMx1 plasmid DNA (Addgene, P/N 51469) using Xfect™ Transfection Reagent with two different concentrations of DNA (40 or 160 µg) and Xfect™ Polymer (0.1 or 0.3 µL per µg DNA). Expression of EGFP-P4M-SidM allowed visualisation of transfection efficiency. Optimal plasmid DNA and Xfect™ Polymer concentrations were selected as 160 µg DNA and 0.3 µL per µg DNA. * Top Line: Cells were transfected with the maximum volume of Xfect™ Polymer used (i.e., 48 µL = 0.3 µL Xfect™ Polymer * 160 µg DNA) as a vehicle control. Images were acquired with an EVOS® FL Auto Imaging System. Scale bars = 1000 µm.

7.4. Automated DNA-PAINT Imaging Strand Perfusion: Homemade Perfusion Syringe System G-code

(A)

M302 S0

M211 S0

G91

G0 Y-4 X0 F1

G0 Y0 X-4 F1

G0 Y-4 X0 F1

G0 Y0 X4 F1

G0 Y-4 X0 F1

G0 Y0 X-4 F1

M84

(B)

M302 S0

M211 S0

G91

G0 Y-1.33 X-2.66 F0.655

G0 Y-2.66 X-1.33 F0.655

G0 Y-4 X0 F1

G0 Y-2.66 X-1.33 F0.655

G0 Y-1.33 X-2.66 F0.655

G0 Y0 X-4 F1

M84

**Appendix Figure 7.9. Automated DNA-PAINT Imaging Strand Perfusion:
Homemade Perfusion Syringe System G-code.**

(A) 0 to 100% Pulse Profile. (B) Stepwise Increase and Decrease Profile.

Commands: M302 S0; set the printer to move the motors without checking the temperature of the hot end. M211 S0; disable the end stops. G91; use relative positioning so the motors do not start from a 0.0.0 position and use that as a reference point. G0; start movement after all previous moves are completed. Y is Imaging Strand Channel (mL). X is DNA-PAINT Solution (mL). F is Perfusion Rate (mL/min). M84; stop command. For more details, see (Baas and Saggiomo, 2021).

7.5. A Novel 3D Imaging Approach for Quantification of GLUT4 Levels across the Intact Myocardium: Supplementary Information

7.5.1 *Illustrative Movies*

7.5.1.1 Illustrative Movies of 3D Render of GLUT4-GFP in Ultrathick Sections of Cleared Mouse Heart.

<https://movie.biologists.com/video/10.1242/jcs.262146/video-1>

Appendix Figure 7.10. Illustrative Movies of 3D Render of GLUT4-GFP in Ultrathick Sections of Cleared Mouse Heart.

Movie of 3D render of GLUT4-GFP fluorescence (green) within a whole mount of optically cleared 3-mm thick mouse ventricular heart section. The specimen was imaged using the Mesolens system over a 5 mm × 5mm x 3mm volume using a z-step size of 5 μm as described in section [2.3.8.4](#). Published in Geiser et al. (2024).

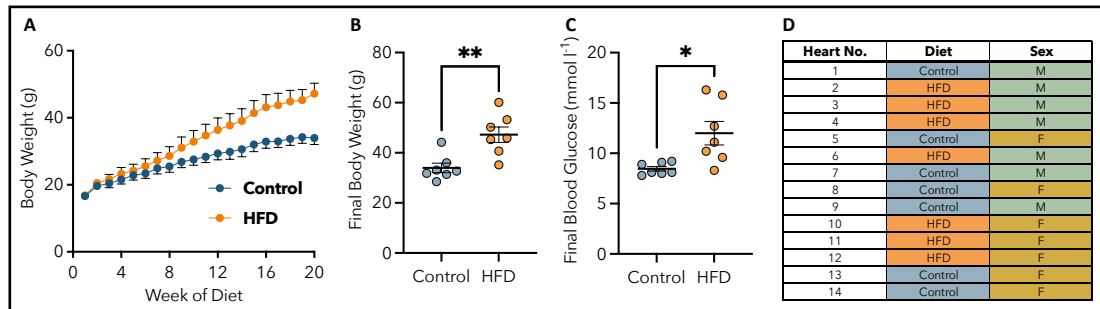
7.5.1.2 Illustrative Movies of Sequential Render of GLUT4-GFP in Ultrathick Sections of Cleared Mouse Heart.

<https://movie.biologists.com/video/10.1242/jcs.262146/video-2>

Appendix Figure 7.11. Illustrative Movies of Sequential Render of GLUT4-GFP in Ultrathick Sections of Cleared Mouse Heart.

Movie of 3D render of GLUT4-GFP fluorescence (green) within a whole mount of optically cleared 3-mm thick mouse ventricular heart section. The specimen was imaged using the Mesolens system over a 5 mm × 5mm x 3mm volume using a z-step size of 5 μm as described in section [2.3.8.4](#). Published in Geiser et al. (2024).

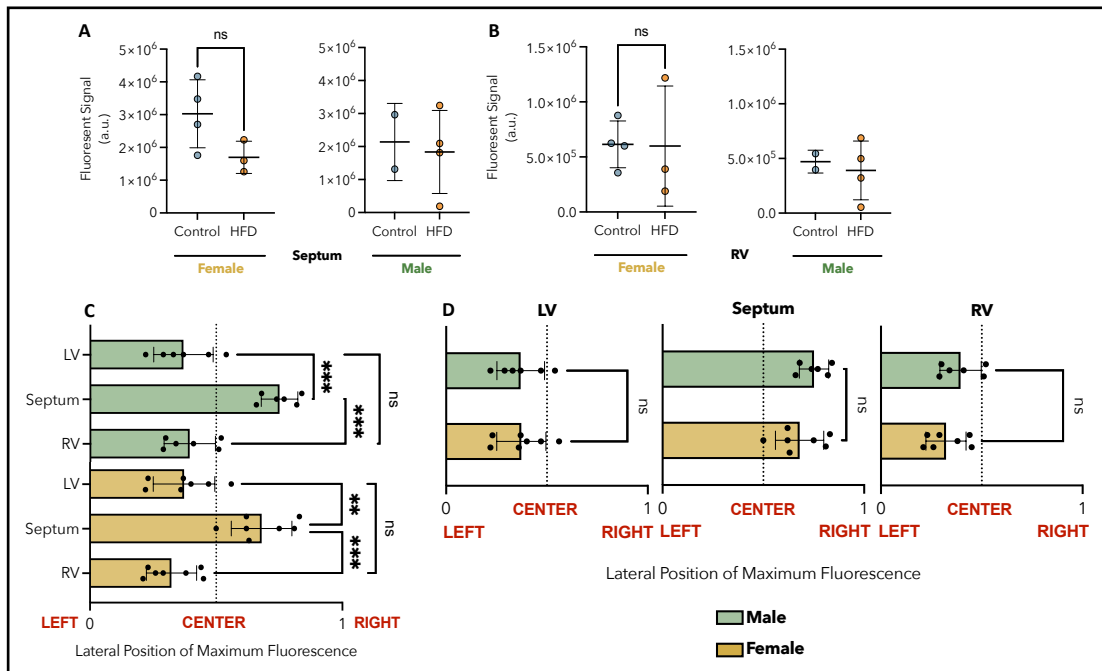
7.5.2 Impact of High-Fat Diet-Feeding on Body Weights and Blood Glucose Levels, and Summary of Isolated Hearts.



Appendix Figure 7.12. Impact of High-Fat Diet-Feeding on Body Weight and Final Blood Glucose Levels in Mice, and Summary of Isolated Hearts Specifications.

HA-GLUT4-GFP transgenic mice were fed standard chow (blue; Control, n = 7) or high-fat (orange; HFD, n = 7) diets over 20 weeks. (A) Body weight (g) curves over 20 weeks. Values are expressed as Mean \pm s.d. and measured weekly as described in section [2.2.2.2](#). (B) Mean \pm s.d. of final body weight (g) measurement on week 20 comparing Control and HFD mice. Data indicate a significant increase in body weight in HFD mice compared to control littermates. (C) Mean \pm s.d. of final blood glucose (mmol l⁻¹) measurement comparing Control and HFD mice. Measurements were performed in mice fasted overnight for 12 hours on week 18, as described in section [2.2.2.2](#). Data indicate a significant increase in blood glucose levels in HFD mice compared to Control littermates. (D) Table of isolated hearts specifications including diet and sex (Male; M, green and Female; F, yellow) of mice. *, ** represent $p \leq 0.05$, $p \leq 0.01$. Two-tailed unpaired t-tests with Welch's correction were performed on all raw data. Published in Geiser et al. (2024).

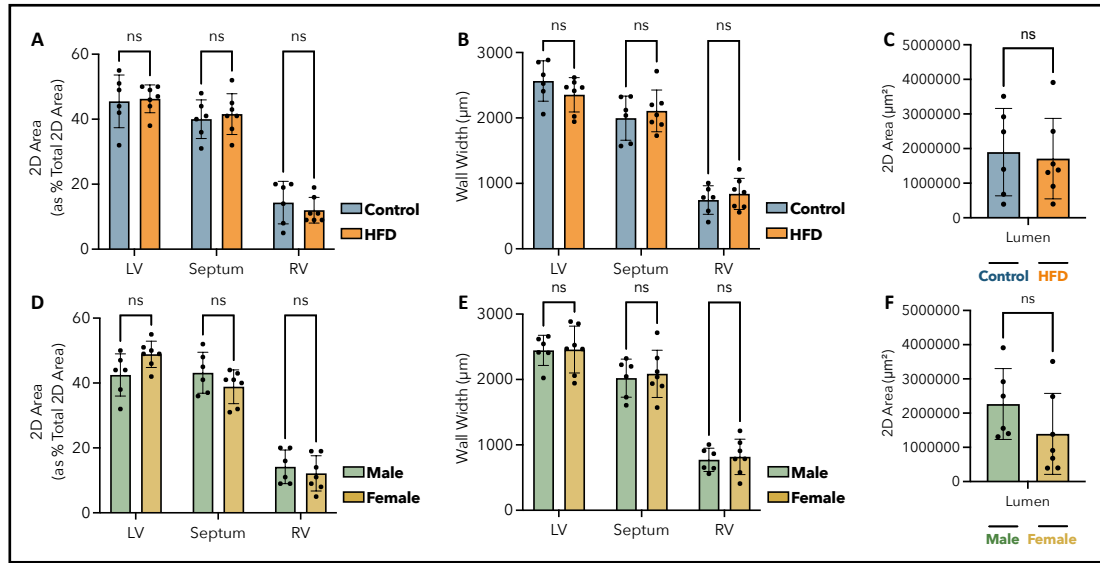
7.5.3 Impact of High-Fat Diet-Feeding on GLUT4-GFP Fluorescence in the Septum and RV of Male and Female Mouse Hearts



Appendix Figure 7.13. Impact of HFD on GLUT4-GFP Fluorescent Signal in the Septum and RV of Male and Female Hearts and Quantification of Lateral Position of Maximum GLUT4-GFP Fluorescence Along the Breadth of Male and Female Cardiac Walls.

(A,B) Mean \pm s.d. of GLUT4-GFP fluorescent signal (a.u.) in the septum (A) and RV (B) of Control (blue) compared to HFD (orange) hearts, in female (yellow; n = 7, Control = 4, HFD = 3) and male (green; n = 6, Control = 2, HFD = 4). No statistical evaluation was applied to male specimens due to a low sample size for Control males (n = 2). (C) Mean \pm s.d. of GLUT4-GFP maximum fluorescence lateral position along the breadth of the LV, septum, and RV in male (green; n = 6, Control = 2, HFD = 4) and female hearts (yellow; n = 7, Control = 4, HFD = 3), expressed relative to total wall width. Dotted lines represent the horizontal centre of each cardiac wall. In both male and female hearts, data indicate GLUT4 fluorescence significantly peaking toward the right-hand side of the septal wall when compared to the LV and RV, where a left-skewed accumulation of GLUT4 proteins is observed along the width of both ventricular walls. (D) This panel presents the same data as (C), displayed as side-by-side comparisons between both studied experimental groups within each cardiac region. Mean \pm s.d. of GLUT4-GFP maximum fluorescence lateral position along the breadth of the LV, septum, and RV of in male (green; n = 6, Control = 2, HFD = 4) hearts compared to female (yellow; n = 7, Control = 4, HFD = 3) hearts, expressed relative to total wall width. All lateral position values in C and D were measured from individual transmural fluorescence. Profiles and fluorescent signal values were measured as described in section [2.2.8.4.2](#). **, *** represent $p \leq 0.01$, $p \leq 0.001$, and ns signify non-significant. Two-tailed unpaired t-tests with Welch's correction and Brown-Forsythe and Welch ANOVA tests were performed on all raw data of (A,B,D) and (C), respectively. Published in Geiser et al. (2024).

7.5.4 Quantification of Gross Anatomical Features



Appendix Figure 7.14. Quantification of Gross Anatomical Features in Imaged Myocardium.

(A,D) Mean \pm s.d of the 2D surface area of the LV, septum, and RV in Control (blue; $n = 6$) hearts compared to HFD (orange; $n = 7$) hearts (A), and in male (green; $n = 6$) compared to female (yellow; $n = 7$) hearts (D). Values are expressed relative to % the total 2D area of hearts and measured from 2D axial-projected images as described in the Methods. (B,E) Mean \pm s.d. of LV, septum, and RV wall width (μm) in Control (blue; $n = 6$) hearts compared to HFD (orange; $n = 7$) hearts (B), and in male (green; $n = 6$) compared to female (yellow; $n = 7$) hearts (E). Values were measured from individual transmural fluorescence profiles as described in section 2.2.8.4.2. (C,F) Mean \pm s.d. of lumen 2D area (μm^2) in Control (blue; $n = 6$) hearts compared to HFD (orange; $n = 7$) hearts (C), and in male (green; $n = 6$) compared to female (yellow; $n = 7$) hearts (F). Values were measured from 2D axial-projected images as described in section 2.2.8.4.3. ns signify non-significant. Multiple two-tailed unpaired t-tests with Welch's correction and two-tailed unpaired t-tests with Welch's correction were performed on all raw data of (A,B,D,E) and (C,F), respectively. Published in Geiser et al. (2024).

Bibliography

- Abbe, E. 1873. Beiträge zur Theorie des Mikroskops und der mikroskopischen Wahrnehmung. *Archiv für Mikroskopische Anatomie*. 9:413-468.
- Abel, E., Dale. 2004. Glucose transport in the heart. *Frontiers in Bioscience*. 9:201.
- Abel, E.D., O. Peroni, J.K. Kim, Y.B. Kim, O. Boss, E. Hadro, T. Minnemann, G.I. Shulman, and B.B. Kahn. 2001. Adipose-selective targeting of the GLUT4 gene impairs insulin action in muscle and liver. *Nature*. 409:729-733.
- Ackers-Johnson, M., P.Y. Li, A.P. Holmes, S.M. O'Brien, D. Pavlovic, and R.S. Foo. 2016. A Simplified, Langendorff-Free Method for Concomitant Isolation of Viable Cardiac Myocytes and Nonmyocytes From the Adult Mouse Heart. *Circ Res*. 119:909-920.
- Adams, K.F., Jr., G.C. Fonarow, C.L. Emerman, T.H. LeJemtel, M.R. Costanzo, W.T. Abraham, R.L. Berkowitz, M. Galvao, and D.P. Horton. 2005. Characteristics and outcomes of patients hospitalized for heart failure in the United States: rationale, design, and preliminary observations from the first 100,000 cases in the Acute Decompensated Heart Failure National Registry (ADHERE). *Am Heart J*. 149:209-216.
- Almada, P., P.M. Pereira, S. Culley, G. Caillol, F. Boroni-Rueda, C.L. Dix, G. Charras, B. Baum, R.F. Laine, C. Leterrier, and R. Henriques. 2019. Automating multimodal microscopy with NanoJ-Fluidics. *Nat Commun*. 10:1223.
- Alpert, M.A., C.J. Lavie, H. Agrawal, K.B. Aggarwal, and S.A. Kumar. 2014. Obesity and heart failure: epidemiology, pathophysiology, clinical manifestations, and management. *Transl. Res*. 164:345-356.

Ambrose, E.J. 1956. A surface contact microscope for the study of cell movements. *Nature*. 178:1194.

Ampofo, A.G., and E.B. Boateng. 2020. Beyond 2020: Modelling obesity and diabetes prevalence. *Diabetes Research and Clinical Practice*. 167:108362.

Anderson, E.J., A.P. Kypson, E. Rodriguez, C.A. Anderson, E.J. Lehr, and P.D. Neuffer. 2009. Substrate-Specific Derangements in Mitochondrial Metabolism and Redox Balance in the Atrium of the Type 2 Diabetic Human Heart. *Journal of the American College of Cardiology*. 54:1891-1898.

Antar, S.A., N.A. Ashour, M. Sharaky, M. Khattab, N.A. Ashour, R.T. Zaid, E.J. Roh, A. Elkamhawy, and A.A. Al-Karmalawy. 2023. Diabetes mellitus: Classification, mediators, and complications; A gate to identify potential targets for the development of new effective treatments. *Biomedicine & Pharmacotherapy*. 168:115734.

Ariga, M., T. Nedachi, H. Katagiri, and M. Kanzaki. 2008. Functional role of sortilin in myogenesis and development of insulin-responsive glucose transport system in C2C12 myocytes. *J Biol Chem*. 283:10208-10220.

Artasensi, A., A. Pedretti, G. Vistoli, and L. Fumagalli. 2020. Type 2 Diabetes Mellitus: A Review of Multi-Target Drugs. *Molecules*. 25:1987.

Atkinson, M.A., G.S. Eisenbarth, and A.W. Michels. 2014. Type 1 diabetes. *The Lancet*. 383:69-82.

Avogaro, A., G.P. Fadini, A. Gallo, E. Pagnin, and S. de Kreutzenberg. 2006. Endothelial dysfunction in type 2 diabetes mellitus. *Nutr Metab Cardiovasc Dis*. 16 Suppl 1:S39-45.

Axelrod, D. 1981. Cell-substrate contacts illuminated by total internal reflection fluorescence. *J. Cell. Biol.* 89:141-145.

Axelrod, D., T.P. Burghardt, and N.L. Thompson. 1984. Total internal reflection fluorescence. *Annu Rev Biophys Bioeng*. 13:247-268.

Baas, S., and V. Saggiomo. 2021. Ender3 3D printer kit transformed into open, programmable syringe pump set. *HardwareX*. 10:e00219.

Baden, T., A.M. Chagas, G.J. Gage, T.C. Marzullo, L.L. Prieto-Godino, and T. Euler. 2015. Open Labware: 3-D printing your own lab equipment. *PLoS Biol*. 13:e1002086.

Bae, S.S., H. Cho, J. Mu, and M.J. Birnbaum. 2003. Isoform-specific regulation of insulin-dependent glucose uptake by Akt/protein kinase B. *J Biol Chem*. 278:49530-49536.

Bai, L., Y. Wang, J. Fan, Y. Chen, W. Ji, A. Qu, P. Xu, D.E. James, and T. Xu. 2007. Dissecting Multiple Steps of GLUT4 Trafficking and Identifying the Sites of Insulin Action. *Cell Metab*. 5:47-57.

Baird, D., C. Stefan, A. Audhya, S. Weys, and S.D. Emr. 2008. Assembly of the PtdIns 4-kinase Stt4 complex at the plasma membrane requires Ypp1 and Efr3. *J. Cell Biol*. 183:1061-1074.

Bairstow, S.F., M.W. Bunce, and R.A. Anderson. 2004. Phosphoinositide 4- and 5-Kinases and Phosphatases. In *Encyclopedia of Biological Chemistry*. W.J. Lennarz and M.D. Lane, editors. Elsevier, New York. 287-291.

Balla, A., and T. Balla. 2006. Phosphatidylinositol 4-kinases: old enzymes with emerging functions. *Trends in Cell Biology*. 16:351-361.

Banerjee, A., M. Anand, and M. Ganji. 2023. Labeling approaches for DNA-PAINT super-resolution imaging. *Nanoscale*. 15:6563-6580.

Baskin, J.M., X. Wu, R. Christiano, M.S. Oh, C.M. Schauder, E. Gazzero, M. Messa, S. Baldassari, S. Assereto, R. Biancheri, F. Zara, C. Minetti, A. Raimondi, M. Simons, T.C. Walther, K.M. Reinisch, and P. De Camilli. 2016. The leukodystrophy protein FAM126A (hyccin) regulates PtdIns(4)P synthesis at the plasma membrane. *Nat Cell Biol*. 18:132-138.

- Bass, A., M. Stejskalova, B. Ostadal, and M. Samanek. 1993. Differences between atrial and ventricular energy-supplying enzymes in five mammalian species. *Physiol Res.* 42:1-6.
- Battault, S., E. Renguet, A. Van Steenberg, S. Horman, C. Beauloye, and L. Bertrand. 2020. Myocardial glucotoxicity: Mechanisms and potential therapeutic targets. *Archives of Cardiovascular Diseases.* 113:736-748.
- Bayeva, M., K.T. Sawicki, and H. Ardehali. 2013. Taking Diabetes to Heart—Deregulation of Myocardial Lipid Metabolism in Diabetic Cardiomyopathy. *Journal of the American Heart Association.* 2:e000433.
- Beauloye, C., A.S. Marsin, L. Bertrand, J.L. Vanoverschelde, M.H. Rider, and L. Hue. 2002. The stimulation of heart glycolysis by increased workload does not require AMP-activated protein kinase but a wortmannin-sensitive mechanism. *FEBS Lett.* 531:324-328.
- Becker, C., L. Sevilla, E. Tomàs, M. Palacin, A. Zorzano, and Y. Fischer. 2001. The Endosomal Compartment Is an Insulin-Sensitive Recruitment Site for GLUT4 and GLUT1 Glucose Transporters in Cardiac Myocytes. *Endocrinology.* 142:5267-5276.
- Bell, G.I., T. Kayano, J.B. Buse, C.F. Burant, J. Takeda, D. Lin, H. Fukumoto, and S. Seino. 1990. Molecular biology of mammalian glucose transporters. *Diabetes Care.* 13:198-208.
- Bell, R.M., M.M. Mocanu, and D.M. Yellon. 2011. Retrograde heart perfusion: The Langendorff technique of isolated heart perfusion. *J. Mol. Cell. Cardiol.* 50:940-950.
- Benavides-Vallve, C., D. Corbacho, O. Iglesias-Garcia, B. Pelacho, E. Albiasu, S. Castaño, A. Muñoz-Barrutia, F. Prosper, and C. Ortiz-de-Solorzano. 2012. New strategies for echocardiographic evaluation of left ventricular function in a mouse model of long-term myocardial infarction. *PLoS One.* 7:e41691.

Bernardo, B.C., K.L. Weeks, L. Pretorius, and J.R. McMullen. 2010. Molecular distinction between physiological and pathological cardiac hypertrophy: Experimental findings and therapeutic strategies. *Pharmacology & Therapeutics*. 128:191-227.

Bernhardt, U., F. Carlotti, R.C. Hoeben, H.-G. Joost, and H. Al-Hasani. 2009. A dual role of the N-terminal FQQI motif in GLUT4 trafficking. *Biol. Chem*. 390:883-892.

Bers, D.M. 2002. Cardiac Na/Ca exchange function in rabbit, mouse and man: what's the difference? *J Mol Cell Cardiol*. 34:369-373.

Bertero, E., and C. Maack. 2018. Metabolic remodelling in heart failure. *Nat Rev Cardiol*. 15:457-470.

Betzig, E., G.H. Patterson, R. Sougrat, O.W. Lindwasser, S. Olenych, J.S. Bonifacino, M.W. Davidson, J. Lippincott-Schwartz, and H.F. Hess. 2006. Imaging intracellular fluorescent proteins at nanometer resolution. *Science*. 313:1642-1645.

Blot, V., and T.E. McGraw. 2008. Molecular mechanisms controlling GLUT4 intracellular retention. *Mol Biol Cell*. 19:3477-3487.

Bogan, J.S. 2012. Regulation of Glucose Transporter Translocation in Health and Diabetes. *Annu. Rev. Biochem*. 81:507-532.

Bogan, J.S., A.E. McKee, and H.F. Lodish. 2001. Insulin-responsive compartments containing GLUT4 in 3T3-L1 and CHO cells: regulation by amino acid concentrations. *Mol Cell Biol*. 21:4785-4806.

Bojjireddy, N., J. Botyanszki, G. Hammond, D. Creech, R. Peterson, D.C. Kemp, M. Snead, R. Brown, A. Morrison, S. Wilson, S. Harrison, C. Moore, and T. Balla. 2014. Pharmacological and genetic targeting of the PI4KA enzyme reveals its important role in maintaining plasma membrane phosphatidylinositol 4-phosphate and phosphatidylinositol 4,5-bisphosphate levels. *J Biol Chem*. 289:6120-6132.

Bojjireddy, N., M.L. Guzman-Hernandez, N.R. Reinhard, M. Jovic, and T. Balla. 2015. EFR3s are palmitoylated plasma membrane proteins that control responsiveness to G-protein-coupled receptors. *J. Cell Sci.* 128:118-128.

Booeshaghi, A.S., E.D.V. Beltrame, D. Bannon, J. Gehring, and L. Pachter. 2019. Principles of open source bioinstrumentation applied to the poseidon syringe pump system. *Sci Rep.* 9:12385.

Borisov, N., E. Aksamitiene, A. Kiyatkin, S. Legewie, J. Berkhout, T. Maiwald, N.P. Kaimachnikov, J. Timmer, J.B. Hoek, and B.N. Kholodenko. 2009. Systems-level interactions between insulin-EGF networks amplify mitogenic signaling. *Mol Syst Biol.* 5:256.

Boyle, P.J. 2007. Diabetes mellitus and macrovascular disease: mechanisms and mediators. *Am J Med.* 120:S12-17.

Bradfield, J.P., H.Q. Qu, K. Wang, H. Zhang, P.M. Sleiman, C.E. Kim, F.D. Mentch, H. Qiu, J.T. Glessner, K.A. Thomas, E.C. Frackelton, R.M. Chiavacci, M. Imielinski, D.S. Monos, R. Pandey, M. Bakay, S.F. Grant, C. Polychronakos, and H. Hakonarson. 2011. A genome-wide meta-analysis of six type 1 diabetes cohorts identifies multiple associated loci. *PLoS Genet.* 7:e1002293.

Bremner, S.K., W.S. Al Shammari, R.S. Milligan, B.D. Hudson, C. Sutherland, N.J. Bryant, and G.W. Gould. 2022. Pleiotropic effects of Syntaxin16 identified by gene editing in cultured adipocytes. *Front Cell Dev Biol.* 10:1033501.

Bryant, N.J., R. Govers, and D.E. James. 2002. Regulated transport of the glucose transporter GLUT4. *Nat. Rev. Mol. Cell Biol.* 3:267-277.

Bugger, H., and E.D. Abel. 2014. Molecular mechanisms of diabetic cardiomyopathy. *Diabetologia.* 57:660-671.

Campbell, N.A., L.A. Urry, M.L. Cain, S.A. Wasserman, P.V. Minorsky, and J.B. Reece. 2017. *Biology: A Global Approach*. Pearson Education Limited : distributor Pearson Education Ltd : distributor United Book Distributors : distributor Edify Limited : distributor Pearson Holdings South Africa (PHSA), Harlow. 1512 p. pp.

Carayannopoulos, M.O., M.M.Y. Chi, Y. Cui, J.M. Pingsterhaus, R.A. McKnight, M. Mueckler, S.U. Devaskar, and K.H. Moley. 2000. GLUT8 is a glucose transporter responsible for insulin-stimulated glucose uptake in the blastocyst. *Proceedings of the National Academy of Sciences*. 97:7313-7318.

Carpenter, C.L., and L.C. Cantley. 1996. Phosphoinositide kinases. *Curr Opin Cell Biol*. 8:153-158.

Chamberlain, L.H., and G.W. Gould. 2002. The vesicle- and target-SNARE proteins that mediate Glut4 vesicle fusion are localized in detergent-insoluble lipid rafts present on distinct intracellular membranes. *J Biol Chem*. 277:49750-49754.

Chang, L., S.H. Chiang, and A.R. Saltiel. 2007. TC10alpha is required for insulin-stimulated glucose uptake in adipocytes. *Endocrinology*. 148:27-33.

Charron, M.J., F.C. Brosius, S.L. Alper, and H.F. Lodish. 1989. A glucose transport protein expressed predominately in insulin-responsive tissues. *PNAS*. 86:2535-2539.

Chatterjee, S., K. Khunti, and M.J. Davies. 2017. Type 2 diabetes. *The Lancet*. 389:2239-2251.

Cheng, R.K., M. Cox, M.L. Neely, P.A. Heidenreich, D.L. Bhatt, Z.J. Eapen, A.F. Hernandez, J. Butler, C.W. Yancy, and G.C. Fonarow. 2014. Outcomes in patients with heart failure with preserved, borderline, and reduced ejection fraction in the Medicare population. *Am. Heart J*. 168:721-730.e723.

Christopher, J., L.M. Rooney, M. Donnachie, D. Uttamchandani, G. McConnell, and R. Bauer. 2024. Low-cost 3D printed lenses for brightfield and fluorescence microscopy. *Biomed Opt Express*. 15:2224-2237.

Chung, J., F. Nakatsu, J.M. Baskin, and P.D. Camilli. 2015. Plasticity of PI4KIIIa interactions at the plasma membrane. *EMBO Rep*. 16:312-320.

Clapperton, M., T. Kunanandam, C.D. Florea, C.M. Douglas, and G. McConnell. 2024. Multimodal optical mesoscopy reveals the quantity and spatial distribution of Gram-positive biofilms in ex vivo tonsils. *J Microsc*. 295:121-130.

Cloherty, E.K., K.B. Levine, and A. Carruthers. 2001. The red blood cell glucose transporter presents multiple, nucleotide-sensitive sugar exit sites. *Biochem*. 40:15549-15561.

Coderre, P.E., E.K. Cloherty, R.J. Zottola, and A. Carruthers. 1995. Rapid substrate translocation by the multisubunit, erythroid glucose transporter requires subunit associations but not cooperative ligand binding. *Biochem*. 34:9762-9773.

Cohn, J.N. 1995. Structural Basis for Heart Failure. *Circ*. 91:2504-2507.

Collins, J.T., J. Knapper, J. Stirling, J. Mduda, C. Mkindi, V. Mayagaya, G.A. Mwakajinga, P.T. Nyakyi, V.L. Sanga, D. Carbery, L. White, S. Dale, Z. Jieh Lim, J.J. Baumberg, P. Cicutta, S. McDermott, B. Vodenicharski, and R. Bowman. 2020. Robotic microscopy for everyone: the OpenFlexure microscope. *Biomed Opt Express*. 11:2447-2460.

Convery, N., and N. Gadegaard. 2019. 30 years of microfluidics. *Micro and Nano Engineering*. 2:76-91.

Conway, M.A., J. Allis, R. Ouwerkerk, T. Niioka, B. Rajagopalan, and G.K. Radda. 1991. Detection of low phosphocreatine to ATP ratio in failing hypertrophied human myocardium by ³¹P magnetic resonance spectroscopy. *Lancet*. 338:973-976.

Cook, S.A., A. Varela-Carver, M. Mongillo, C. Kleinert, M.T. Khan, L. Leccisotti, N. Strickland, T. Matsui, S. Das, A. Rosenzweig, P. Punjabi, and P.G. Camici. 2010. Abnormal myocardial insulin signalling in type 2 diabetes and left-ventricular dysfunction. *Eur Heart J.* 31:100-111.

Coppini, R., C. Ferrantini, A. Aiazzi, L. Mazzone, L. Sartiani, A. Mugelli, C. Poggesi, and E. Cerbai. 2014. Isolation and functional characterization of human ventricular cardiomyocytes from fresh surgical samples. *J Vis Exp.*

Corvera, S., A. Chawla, R. Chakrabarti, M. Joly, J. Buxton, and M.P. Czech. 1994. A double leucine within the GLUT4 glucose transporter COOH-terminal domain functions as an endocytosis signal. *The Journal of cell biology.* 126:979-989.

Coven, D.L., X. Hu, L. Cong, R. Bergeron, G.I. Shulman, D.G. Hardie, and L.H. Young. 2003. Physiological role of AMP-activated protein kinase in the heart: graded activation during exercise. *Am J Physiol Endocrinol Metab.* 285:E629-E636.

Cross, D.A., D.R. Alessi, P. Cohen, M. Andjelkovich, and B.A. Hemmings. 1995. Inhibition of glycogen synthase kinase-3 by insulin mediated by protein kinase B. *Nature.* 378:785-789.

Currie, S., F.R. Quinn, R.A. Sayeed, A.M. Duncan, S. Kettlewell, and G.L. Smith. 2005. Selective down-regulation of sub-endocardial ryanodine receptor expression in a rabbit model of left ventricular dysfunction. *J Mol Cell Cardiol.* 39:309-317.

Cushman, S.W., and L.J. Wardzala. 1980. Potential mechanism of insulin action on glucose transport in the isolated rat adipose cell. Apparent translocation of intracellular transport systems to the plasma membrane. *J. Biol. Chem.* 255:4758-4762.

Dani, A.M., A. Cittadini, G. Flamini, G. Festuccia, and T. Terranova. 1977. Preparation and some properties of isolated beating myocytes from adult rabbit heart. *J Mol Cell Cardiol.* 9:777-784.

Dawson, K., A. Aviles-Hernandez, S.W. Cushman, and D. Malide. 2001a. Insulin-Regulated Trafficking of Dual-Labeled Glucose Transporter 4 in Primary Rat Adipose Cells. *Biochem. Biophys. Rep.* 287:445-454.

Dawson, P.A., J.C. Mychaleckyj, S.C. Fossey, S.J. Mihic, A.L. Craddock, and D.W. Bowden. 2001b. Sequence and Functional Analysis of GLUT10: A Glucose Transporter in the Type 2 Diabetes-Linked Region of Chromosome 20q12-13.1. *Molecular Genetics and Metabolism.* 74:186-199.

DeBosch, B., N. Sambandam, C. Weinheimer, M. Courtois, and A.J. Muslin. 2006. Akt2 Regulates Cardiac Metabolism and Cardiomyocyte Survival. *JBC.* 281:32841-32851.

Delghandi, M., M.P. Delghandi, and S. Goddard. 2022. The Significance of PCR Primer Design in Genetic Diversity Studies: Exemplified by Recent Research into the Genetic Structure of Marine Species. *Methods Mol Biol.* 2392:3-15.

Delibegović, M., S. Dall'Angelo, and R. Dekeryte. 2024. Protein tyrosine phosphatase 1B in metabolic diseases and drug development. *Nat Rev Endocrinol.* 20:366-378.

Dendup, T., X. Feng, S. Clingan, and T. Astell-Burt. 2018. Environmental Risk Factors for Developing Type 2 Diabetes Mellitus: A Systematic Review. *Int J Environ Res Public Health.* 15.

Di Paolo, G., and P. De Camilli. 2006. Phosphoinositides in cell regulation and membrane dynamics. *Nature.* 443:651-657.

Diamond, D.L., and A. Carruthers. 1993. Metabolic control of sugar transport by derepression of cell surface glucose transporters. An insulin-

independent recruitment-independent mechanism of regulation. *J. Biol. Chem.* 268:6437-6444.

Dobson, S.P., C. Livingstone, G.W. Gould, and J.M. Tavaré. 1996. Dynamics of insulin-stimulated translocation of GLUT4 in single living cells visualised using green fluorescent protein. *FEBS Lett.* 393:179-184.

Doerge, H., A. Schürmann, G. Bahrenberg, A. Brauers, and H.-G. Joost. 2000. GLUT8, a Novel Member of the Sugar Transport Facilitator Family with Glucose Transport Activity. *Journal of Biological Chemistry.* 275:16275-16280.

Doll, S., M. Dressen, P.E. Geyer, D.N. Itzhak, C. Braun, S.A. Doppler, F. Meier, M.A. Deutsch, H. Lahm, R. Lange, M. Krane, and M. Mann. 2017. Region and cell-type resolved quantitative proteomic map of the human heart. *Nat. Commun.* 8:1469.

Douen, A.G., T. Ramlal, S. Rastogi, P.J. Bilan, G.D. Cartee, M. Vranic, J.O. Holloszy, and A. Klip. 1990. Exercise induces recruitment of the "insulin-responsive glucose transporter". Evidence for distinct intracellular insulin- and exercise-recruitable transporter pools in skeletal muscle. *J Biol Chem.* 265:13427-13430.

Duh, E.J., J.K. Sun, and A.W. Stitt. 2017. Diabetic retinopathy: current understanding, mechanisms, and treatment strategies. *JCI Insight.* 2.

Durmaz, Y.T., A. Shatadal, and K. Friend. 2022. Geneticin reduces mRNA stability. *PLoS One.* 17:e0272058.

Ebina, Y., L. Ellis, K. Jarnagin, M. Edery, L. Graf, E. Clauser, J.H. Ou, F. Masiarz, Y.W. Kan, I.D. Goldfine, and et al. 1985. The human insulin receptor cDNA: the structural basis for hormone-activated transmembrane signalling. *Cell.* 40:747-758.

Edvardsen, T., and L.G. Klæboe. 2019. Imaging and heart failure: myocardial strain. *Curr. Opin. Cardiol.* 34:490-494.

- Fabricius, V., J. Lefèbre, H. Geertsema, S.F. Marino, and H. Ewers. 2018. Rapid and efficient C-terminal labeling of nanobodies for DNA-PAINT. *Journal of Physics D: Applied Physics*. 51:474005.
- Fagerberg, L., K. Jonasson, G. von Heijne, M. Uhlén, and L. Berglund. 2010. Prediction of the human membrane proteome. *Proteomics*. 10:1141-1149.
- Fan, J., J. Suo, J. Wu, H. Xie, Y. Shen, F. Chen, G. Wang, L. Cao, G. Jin, Q. He, T. Li, G. Luan, L. Kong, Z. Zheng, and Q. Dai. 2019. Video-rate imaging of biological dynamics at centimetre scale and micrometre resolution. *Nat Photonics*. 13:809-816.
- Fazakerley, D.J., G.D. Holman, A. Marley, D.E. James, J. Stöckli, and A.C.F. Coster. 2010. Kinetic Evidence for Unique Regulation of GLUT4 Trafficking by Insulin and AMP-activated Protein Kinase Activators in L6 Myotubes. *Journal of Biological Chemistry*. 285:1653-1660.
- Fazakerley, D.J., S.P. Lawrence, V.A. Lizunov, S.W. Cushman, and G.D. Holman. 2009. A common trafficking route for GLUT4 in cardiomyocytes in response to insulin, contraction and energy-status signalling. *J. Cell Sci*. 122:727-734.
- Field, J., J. Nikawa, D. Broek, B. MacDonald, L. Rodgers, I.A. Wilson, R.A. Lerner, and M. Wigler. 1988. Purification of a RAS-responsive adenylyl cyclase complex from *Saccharomyces cerevisiae* by use of an epitope addition method. *Mol Cell Biol*. 8:2159-2165.
- Fischer, Y., J. Thomas, G.D. Holman, H. Rose, and H. Kammermeier. 1996. Contraction-independent effects of catecholamines on glucose transport in isolated rat cardiomyocytes. *Am J Physiol*. 270:C1204-C1210.
- Fischer, Y., J. Thomas, L. Sevilla, P. Munoz, C. Becker, G. Holman, I.J. Kozka, M. Palacin, X. Testar, H. Kammermeier, and A. Zorzano. 1997. Insulin-induced recruitment of glucose transporter 4 (GLUT4) and GLUT1 in

isolated rat cardiac myocytes. Evidence of the existence of different intracellular GLUT4 vesicle populations. *J Biol Chem.* 272:7085-7092.

Fish, K.N. 2009. Total internal reflection fluorescence (TIRF) microscopy. *Curr Protoc Cytom.* Chapter 12:Unit12.18.

Foley, K., S. Boguslavsky, and A. Klip. 2011. Endocytosis, Recycling, and Regulated Exocytosis of Glucose Transporter 4. *Biochem.* 50:3048-3061.

Foster, D.W., and J.D. McGarry. 1983. The metabolic derangements and treatment of diabetic ketoacidosis. *N Engl J Med.* 309:159-169.

Fowler, M.J. 2008. Microvascular and Macrovascular Complications of Diabetes. *Clinical Diabetes.* Vol.26(2):77-82.

Franchi, F., B.E. Knudsen, E. Oehler, S.C. Textor, L.O. Lerman, J.P. Grande, and M. Rodriguez-Porcel. 2013. Non-invasive assessment of cardiac function in a mouse model of renovascular hypertension. *Hypertens Res.* 36:770-775.

Freychet, P., J. Roth, and D.M. Neville. 1971. Insulin Receptors in the Liver: Specific Binding of ¹²⁵I Insulin to the Plasma Membrane and Its Relation to Insulin Bioactivity. *Proceedings of the National Academy of Sciences.* 68:1833-1837.

Fukumoto, H., T. Kayano, J.B. Buse, Y. Edwards, P.F. Pilch, G.I. Bell, and S. Seino. 1989. Cloning and characterization of the major insulin-responsive glucose transporter expressed in human skeletal muscle and other insulin-responsive tissues. *J. Biol. Chem.* 264:7776-7779.

Funk, S.D., A. Yurdagul, Jr., and A.W. Orr. 2012. Hyperglycemia and endothelial dysfunction in atherosclerosis: lessons from type 1 diabetes. *Int J Vasc Med.* 2012:569654.

Galbraith, C.G., and J.A. Galbraith. 2011. Super-resolution microscopy at a glance. *J. Cell Sci.* 124:1607-1611.

Gao, L., J. Chen, J. Gao, H. Wang, and W. Xiong. 2017. Super-resolution microscopy reveals the insulin-resistance-regulated reorganization of GLUT4 on plasma membranes. *J. Cell Sci.* 130:396-405.

Garcia de Herreros, A., and M.J. Birnbaum. 1989. The acquisition of increased insulin-responsive hexose transport in 3T3-L1 adipocytes correlates with expression of a novel transporter gene. *J. Biol. Chem.* 264:19994-19999.

Godó, S., K. Barabás, F. Lengyel, D. Ernszt, T. Kovács, M. Kecskés, C. Varga, T.Z. Jánosi, G. Makkai, G. Kovács, B. Orsolits, T. Fujiwara, A. Kusumi, and I.M. Ábrahám. 2021. Single-Molecule Imaging Reveals Rapid Estradiol Action on the Surface Movement of AMPA Receptors in Live Neurons. *Front. Cell Dev. Biol.* 9:708715.

Gosmanov, A.R., E.O. Gosmanova, and A.E. Kitabchi. 2000. Hyperglycemic Crises: Diabetic Ketoacidosis and Hyperglycemic Hyperosmolar State. In *Endotext*. K.R. Feingold, B. Anawalt, A. Boyce, G. Chrousos, W.W. de Herder, K. Dhatariya, K. Dungan, J.M. Hershman, J. Hofland, S. Kalra, G. Kaltsas, C. Koch, P. Kopp, M. Korbonits, C.S. Kovacs, W. Kuohung, B. LaFerrere, M. Levy, E.A. McGee, R. McLachlan, J.E. Morley, M. New, J. Purnell, R. Sahay, F. Singer, M.A. Sperling, C.A. Stratakis, D.L. Trence, and D.P. Wilson, editors, South Dartmouth (MA).

Götzke, H., M. Kilisch, M. Martínez-Carranza, S. Sograte-Idrissi, A. Rajavel, T. Schlichthaerle, N. Engels, R. Jungmann, P. Stenmark, F. Opazo, and S. Frey. 2019. The ALFA-tag is a highly versatile tool for nanobody-based bioscience applications. *Nat Commun.* 10:4403.

Gould, G.W., F.M. Brodsky, and N.J. Bryant. 2020. Building GLUT4 Vesicles: CHC22 Clathrin's Human Touch. *Trends Cell Biol.* 30:705-719.

Green, H., and M. Meuth. 1974. An established pre-adipose cell line and its differentiation in culture. *Cell.* 3:127-133.

Grover-McKay, M., S.A. Walsh, and S.A. Thompson. 1999. Glucose transporter 3 (GLUT3) protein is present in human myocardium. *Biochimica et Biophysica Acta (BBA) - Biomembranes*. 1416:145-154.

Gulsin, G.S., P. Kanagala, D.C.S. Chan, A.S.H. Cheng, L. Athithan, M.P.M. Graham-Brown, A. Singh, J. Yang, Z. Li, K. Khunti, M.J. Davies, J.R. Arnold, I.B. Squire, L.L. Ng, and G.P. McCann. 2019. Differential left ventricular and left atrial remodelling in heart failure with preserved ejection fraction patients with and without diabetes. *Ther. Adv. Endocrinol. Metab.* 10:2042018819861593.

Guma, A., J.R. Zierath, H. Wallberg-Henriksson, and A. Klip. 1995. Insulin induces translocation of GLUT-4 glucose transporters in human skeletal muscle. *American Journal of Physiology-Endocrinology and Metabolism*. 268:E613-E622.

Gustavsson, J., S. Parpal, M. Karlsson, C. Ramsing, H. Thorn, M. Borg, M. Lindroth, K.H. Peterson, K.E. Magnusson, and P. Strålfors. 1999. Localization of the insulin receptor in caveolae of adipocyte plasma membrane. *Faseb j.* 13:1961-1971.

Habtemichael, E.N., P.D. Brewer, I. Romenskaia, and C.C. Mastick. 2011. Kinetic evidence that Glut4 follows different endocytic pathways than the receptors for transferrin and alpha2-macroglobulin. *J Biol Chem*. 286:10115-10125.

Haffner, S.M., S. Lehto, T. Ronnema, K. Pyorala, and M. Laakso. 1998. Mortality from coronary heart disease in subjects with type 2 diabetes and in nondiabetic subjects with and without prior myocardial infarction. *N Engl J Med*. 339:229-234.

Haga, Y., K. Ishii, and T. Suzuki. 2011. N-Glycosylation Is Critical for the Stability and Intracellular Trafficking of Glucose Transporter GLUT4. *THE JOURNAL OF BIOLOGICAL CHEMISTRY*. 286:31320 -31327.

Haller, H., L. Ji, K. Stahl, A. Bertram, and J. Menne. 2017. Molecular Mechanisms and Treatment Strategies in Diabetic Nephropathy: New Avenues for Calcium Dobesilate-Free Radical Scavenger and Growth Factor Inhibition. *Biomed Res Int.* 2017:1909258.

Hamers-Casterman, C., T. Atarhouch, S. Muyldermans, G. Robinson, C. Hamers, E.B. Songa, N. Bendahman, and R. Hamers. 1993. Naturally occurring antibodies devoid of light chains. *Nature.* 363:446-448.

Hardy, C.J., R.G. Weiss, P.A. Bottomley, and G. Gerstenblith. 1991. Altered myocardial high-energy phosphate metabolites in patients with dilated cardiomyopathy. *Am Heart J.* 122:795-801.

Harmancey, R., and H. Taegtmeyer. 2008. The complexities of diabetic cardiomyopathy: lessons from patients and animal models. *Curr Diab Rep.* 8:243-248.

Heilemann, M., S. van de Linde, M. Schüttpelz, R. Kasper, B. Seefeldt, A. Mukherjee, P. Tinnefeld, and M. Sauer. 2008. Subdiffraction-resolution fluorescence imaging with conventional fluorescent probes. *Angew. Chem. Int. Ed.* 47:6172-6176.

Hell, S.W., and J. Wichmann. 1994. Breaking the diffraction resolution limit by stimulated emission: stimulated-emission-depletion fluorescence microscopy. *Opt. Lett.* 19:780-782.

Her, J., and S.F. Bunting. 2018. How cells ensure correct repair of DNA double-strand breaks. *J Biol Chem.* 293:10502-10511.

Herdly, L., P. Janin, R. Bauer, and S. van de Linde. 2021. Tunable Wide-Field Illumination and Single-Molecule Photoswitching with a Single MEMS Mirror. *ACS Photonics.* 8:2728-2736.

Herdly, L., P.W. Tinning, A. Geiser, H. Taylor, G.W. Gould, and S. van de Linde. 2023. Benchmarking Thiolate-Driven Photoswitching of Cyanine Dyes. *J. Phys. Chem. B.* 127:732-741.

Hohlbein, J., B. Diederich, B. Marsikova, E.G. Reynaud, S. Holden, W. Jahr, R. Haase, and K. Prakash. 2022. Open microscopy in the life sciences: quo vadis? *Nat Methods*. 19:1020-1025.

Holman, G.D., L. Lo Leggio, and S.W. Cushman. 1994. Insulin-stimulated GLUT4 glucose transporter recycling. A problem in membrane protein subcellular trafficking through multiple pools. *J. Biol. Chem.* 269:17516-17524.

Hu, L., C. Qiu, X. Wang, M. Xu, X. Shao, and Y. Wang. 2018. The association between diabetes mellitus and reduction in myocardial glucose uptake: a population-based (18)F-FDG PET/CT study. *BMC Cardiovasc Disord.* 18:203.

Huang, B., M. Bates, and X. Zhuang. 2009. Super-resolution fluorescence microscopy. *Annu. Rev. Biochem.* 78:993-1016.

Hue, L., and H. Taegtmeyer. 2009. The Randle cycle revisited: a new head for an old hat. *Am J Physiol Endocrinol Metab.* 297:E578-591.

Huxley, R., F. Barzi, and M. Woodward. 2006. Excess risk of fatal coronary heart disease associated with diabetes in men and women: meta-analysis of 37 prospective cohort studies. *BMJ.* 332:73-78.

Ijuin, T., N. Hatano, T. Hosooka, and T. Takenawa. 2015. Regulation of insulin signaling in skeletal muscle by PIP3 phosphatase, SKIP, and endoplasmic reticulum molecular chaperone glucose-regulated protein 78. *Biochim Biophys Acta.* 1853:3192-3201.

Ing, B.L., H. Chen, K.A. Robinson, M.G. Buse, and M.J. Quon. 1996. Characterization of a mutant GLUT4 lacking the N-glycosylation site: studies in transfected rat adipose cells. *Biochem Biophys Res Commun.* 218:76-82.

- Inoué, S. 2006. Foundations of Confocal Scanned Imaging in Light Microscopy. *In Handbook Of Biological Confocal Microscopy*. Springer US. 1-19.
- Inui, A. 2003. Obesity – a chronic health problem in cloned mice? *TIPS*. 24:77-80.
- Isakoff, S.J., C. Taha, E. Rose, J. Marcusohn, A. Klip, and E.Y. Skolnik. 1995. The inability of phosphatidylinositol 3-kinase activation to stimulate GLUT4 translocation indicates additional signaling pathways are required for insulin-stimulated glucose uptake. *Proc Natl Acad Sci U S A*. 92:10247-10251.
- Jackson, E.E., E. Rendina-Ruedy, B.J. Smith, and V.A. Lacombe. 2015. Loss of Toll-Like Receptor 4 Function Partially Protects against Peripheral and Cardiac Glucose Metabolic Derangements During a Long-Term High-Fat Diet. *PLOS ONE*. 10:e0142077.
- Jacquemet, G., A.F. Carisey, H. Hamidi, R. Henriques, and C. Leterrier. 2020. The cell biologist's guide to super-resolution microscopy. *J. Cell Sci*. 133:jcs240713.
- James, D.E., R. Brown, J. Navarro, and P.F. Pilch. 1988. Insulin-regulatable tissues express a unique insulin-sensitive glucose transport protein. *Nature*. 333:183-185.
- Jaqaman, K., H. Kuwata, N. Touret, R. Collins, W.S. Trimble, G. Danuser, and S. Grinstein. 2011. Cytoskeletal control of CD36 diffusion promotes its receptor and signaling function. *Cell*. 146:593-606.
- Jia, G., V.G. DeMarco, and J.R. Sowers. 2016. Insulin resistance and hyperinsulinaemia in diabetic cardiomyopathy. *Nat Rev Endocrinol*. 12:144-153.
- Jiang, L., J. Fan, L. Bai, Y. Wang, Y. Chen, L. Yang, L. Chen, and T. Xu. 2008. Direct Quantification of Fusion Rate Reveals a Distal Role for AS160 in

Insulin-stimulated Fusion of GLUT4 Storage Vesicles. *J. Biol. Chem.* 283:8508-8516.

Jing, D., S. Zhang, W. Luo, X. Gao, Y. Men, C. Ma, X. Liu, Y. Yi, A. Bugde, B.O. Zhou, Z. Zhao, Q. Yuan, J.Q. Feng, L. Gao, W.-P. Ge, and H. Zhao. 2018. Tissue clearing of both hard and soft tissue organs with the PEGASOS method. *Cell Res.* 28:803-818.

Joost, H.-G., and B. Thorens. 2001. The extended GLUT-family of sugar/polyol transport facilitators: nomenclature, sequence characteristics, and potential function of its novel members. *Mol. Membr. Biol.* 18:247-256.

Joseph, D., C. Kimar, B. Symington, R. Milne, and M. Faadiel Essop. 2014. The detrimental effects of acute hyperglycemia on myocardial glucose uptake. *Life Sciences.* 105:31-42.

Jungmann, R., M.S. Avendano, J.B. Woehrstein, M. Dai, W.M. Shih, and P. Yin. 2014. Multiplexed 3D cellular super-resolution imaging with DNA-PAINT and Exchange-PAINT. *Nat Methods.* 11:313-318.

Jungmann, R., C. Steinhauer, M. Scheible, A. Kuzyk, P. Tinnefeld, and F.C. Simmel. 2010. Single-molecule kinetics and super-resolution microscopy by fluorescence imaging of transient binding on DNA origami. *Nano Lett.* 10:4756-4761.

Kaestner, K.H., R.J. Christy, J.C. McLenithan, L.T. Braiterman, P. Cornelius, P.H. Pekala, and M.D. Lane. 1989. Sequence, tissue distribution, and differential expression of mRNA for a putative insulin-responsive glucose transporter in mouse 3T3-L1 adipocytes. *PNAS.* 86:3150-3154.

Kannel, W.B., M. Hjortland, and W.P. Castelli. 1974. Role of diabetes in congestive heart failure: the Framingham study. *Am J Cardiol.* 34:29-34.

Kannel, W.B., and D.L. McGee. 1979. Diabetes and cardiovascular disease. The Framingham study. *JAMA.* 241:2035-2038.

Karlsson, H.K.R., A.V. Chibalin, H.A. Koistinen, J. Yang, F. Koumanov, H. Wallberg-Henriksson, J.R. Zierath, and G.D. Holman. 2009. Kinetics of GLUT4 Trafficking in Rat and Human Skeletal Muscle. *Diabetes*. 58:847-854.

Kasahara, T., and M. Kasahara. 1997. Characterization of rat Glut4 glucose transporter expressed in the yeast *Saccharomyces cerevisiae*: comparison with Glut1 glucose transporter. *Biochim. Biophys. Acta Biomembr.* 1324:111-119.

Kasai, R.S., and A. Kusumi. 2014. Single-molecule imaging revealed dynamic GPCR dimerization. *Curr. Opin. Cell Biol.* 27:78-86.

Kasuga, M., Y. Zick, D.L. Blithe, M. Crettaz, and C.R. Kahn. 1982. Insulin stimulates tyrosine phosphorylation of the insulin receptor in a cell-free system. *Nature*. 298:667-669.

Katz, A.M., and E.L. Rolett. 2016. Heart failure: when form fails to follow function. *Eur Heart J.* 37:449-454.

Kayano, T., C.F. Burant, H. Fukumoto, G.W. Gould, Y.S. Fan, R.L. Eddy, M.G. Byers, T.B. Shows, S. Seino, and G.I. Bell. 1990. Human facilitative glucose transporters. Isolation, functional characterization, and gene localization of cDNAs encoding an isoform (GLUT5) expressed in small intestine, kidney, muscle, and adipose tissue and an unusual glucose transporter pseudogene-like sequence (GLUT6). *J. Biol. Chem.* 265:13276-13282.

Kellerer, M., R. Lammers, A. Fritsche, V. Strack, F. Machicao, P. Borboni, A. Ullrich, and H.U. Häring. 2001. Insulin inhibits leptin receptor signalling in HEK293 cells at the level of janus kinase-2: a potential mechanism for hyperinsulinaemia-associated leptin resistance. *Diabetologia*. 44:1125-1132.

Kenchiah, S., J.C. Evans, D. Levy, P.W. Wilson, E.J. Benjamin, M.G. Larson, W.B. Kannel, and R.S. Vasan. 2002. Obesity and the risk of heart failure. *N Engl J Med.* 347:305-313.

Kennedy, J.W., M.F. Hirshman, E.V. Gervino, J.V. Ocel, R.A. Forse, S.J. Hoenig, D. Aronson, L.J. Goodyear, and E.S. Horton. 1999. Acute exercise induces GLUT4 translocation in skeletal muscle of normal human subjects and subjects with type 2 diabetes. *Diabetes*. 48:1192-1197.

Kenny, H.C., and E.D. Abel. 2019. Heart Failure in Type 2 Diabetes Mellitus. *Circ. Res.* 124:121-141.

Kirchhofer, A., J. Helma, K. Schmidthals, C. Frauer, S. Cui, A. Karcher, M. Pellis, S. Muyldermans, C.S. Casas-Delucchi, M.C. Cardoso, H. Leonhardt, K.P. Hopfner, and U. Rothbauer. 2010. Modulation of protein properties in living cells using nanobodies. *Nat Struct Mol Biol.* 17:133-138.

Kitabchi, A.E., and E.A. Nyenwe. 2006. Hyperglycemic crises in diabetes mellitus: diabetic ketoacidosis and hyperglycemic hyperosmolar state. *Endocrinol Metab Clin North Am.* 35:725-751, viii.

Kitabchi, A.E., G.E. Umpierrez, J.M. Miles, and J.N. Fisher. 2009. Hyperglycemic crises in adult patients with diabetes. *Diabetes Care.* 32:1335-1343.

Klip, A., T.E. McGraw, and D.E. James. 2019. Thirty sweet years of GLUT4. *J. Biol. Chem.* 294:11369-11381.

Klip, A., T. Ramlal, D.A. Young, and J.O. Holloszy. 1987. Insulin-induced translocation of glucose transporters in rat hindlimb muscles. *FEBS Lett.* 224:224-230.

Koester, A.M., A. Geiser, P.R.T. Bowman, S. van de Linde, N. Gadegaard, N.J. Bryant, and G.W. Gould. 2022a. GLUT4 translocation and dispersal operate in multiple cell types and are negatively correlated with cell size in adipocytes. *Sci. Rep.* 12:20535.

Koester, Anna M., A. Geiser, Kamilla M.E. Laidlaw, S. Morris, Marie F.A. Cutiongco, L. Stirrat, N. Gadegaard, E. Boles, Hannah L. Black, Nia J. Bryant, and Gwyn W. Gould. 2022b. EFR3 and phosphatidylinositol 4-kinase IIIa

regulate insulin-stimulated glucose transport and GLUT4 dispersal in 3T3-L1 adipocytes. *Bioscience Reports*. 42.

Kohn, A.D., F. Takeuchi, and R.A. Roth. 1996. Akt, a Pleckstrin Homology Domain Containing Kinase, Is Activated Primarily by Phosphorylation. *JBC*. 271:21920-21926.

Kolb, H., and S. Martin. 2017. Environmental/lifestyle factors in the pathogenesis and prevention of type 2 diabetes. *BMC Med*. 15:131.

Koumanov, F., B. Jin, J. Yang, and G.D. Holman. 2005. Insulin signaling meets vesicle traffic of GLUT4 at a plasma-membrane-activated fusion step. *Cell Metab*. 2:179-189.

Kruger, M., K. Babicz, M. von Frieling-Salewsky, and W.A. Linke. 2010. Insulin signaling regulates cardiac titin properties in heart development and diabetic cardiomyopathy. *J Mol Cell Cardiol*. 48:910-916.

Kruhøffer, P., and C. Crone. 1972. Einar Lundsgaard, 1899-1968. *Ergeb. Physiol*. 65:1-14.

Kudo, T., K. Fukuchi, A.J. Annala, A.F. Chatziioannou, V. Allada, M. Dahlbom, Y.-C. Tai, M. Inubushi, S.-C. Huang, S.R. Cherry, M.E. Phelps, and H.R. Schelbert. 2002. Noninvasive Measurement of Myocardial Activity Concentrations and Perfusion Defect Sizes in Rats With a New Small-Animal Positron Emission Tomograph. *Circulation*. 106:118-123.

Kusumi, A., T.K. Fujiwara, T.A. Tsunoyama, R.S. Kasai, A.A. Liu, K.M. Hirose, M. Kinoshita, N. Matsumori, N. Komura, H. Ando, and K.G.N. Suzuki. 2020. Defining raft domains in the plasma membrane. *Traffic*. 21:106-137.

Kuzuya, A., K. Numajiri, M. Kimura, and M. Komiyama. 2008. Single-molecule accommodation of streptavidin in nanometer-scale wells formed in DNA nanostructures. *Nucleic Acids Symp Ser (Oxf)*:681-682.

Laakso, M. 2011. Heart in diabetes: a microvascular disease. *Diabetes Care*. 34 Suppl 2:S145-149.

Lau, K.S., E.A. Partridge, A. Grigorian, C.I. Silvescu, V.N. Reinhold, M. Demetriou, and J.W. Dennis. 2007. Complex N-glycan number and degree of branching cooperate to regulate cell proliferation and differentiation. *Cell*. 129:123-134.

Lauritzen, H.P.M.M. 2013. Insulin- and Contraction-Induced Glucose Transporter 4 Traffic in Muscle. *Exercise and Sport Sciences Reviews*. 41:77-86.

Lean, M.E., W.S. Leslie, A.C. Barnes, N. Brosnahan, G. Thom, L. McCombie, C. Peters, S. Zhyzhneuskaya, A. Al-Mrabeh, K.G. Hollingsworth, A.M. Rodrigues, L. Rehackova, A.J. Adamson, F.F. Sniehotta, J.C. Mathers, H.M. Ross, Y. Mcilvenna, R. Stefanetti, M. Trenell, P. Welsh, S. Kean, I. Ford, A. Mcconnachie, N. Sattar, and R. Taylor. 2018. Primary care-led weight management for remission of type 2 diabetes (DiRECT): an open-label, cluster-randomised trial. *The Lancet*. 391:541-551.

Lebeche, D., A.J. Davidoff, and R.J. Hajjar. 2008. Interplay between impaired calcium regulation and insulin signaling abnormalities in diabetic cardiomyopathy. *Nat Clin Pract Cardiovasc Med*. 5:715-724.

Lee, T.W., K.J. Bai, T.I. Lee, T.F. Chao, Y.H. Kao, and Y.J. Chen. 2017. PPARs modulate cardiac metabolism and mitochondrial function in diabetes. *J Biomed Sci*. 24:5.

Lelek, M., M.T. Gyparaki, G. Beliu, F. Schueder, J. Griffié, S. Manley, R. Jungmann, M. Sauer, M. Lakadamyali, and C. Zimmer. 2021. Single-molecule localization microscopy. *Nat Rev Methods Primers*. 1.

Levental, I., and E. Lyman. 2023. Regulation of membrane protein structure and function by their lipid nano-environment. *Nat. Rev. Mol. Cell Biol*. 24:107-122.

Li, C.H., L. Bai, D.D. Li, S. Xia, and T. Xu. 2004. Dynamic tracking and mobility analysis of single GLUT4 storage vesicle in live 3T3-L1 cells. *Cell Res.* 14:480-486.

Liao, R., and M. Jain. 2007. Isolation, culture, and functional analysis of adult mouse cardiomyocytes. *Methods Mol Med.* 139:251-262.

Lin, B.Z., P.F. Pilch, and K.V. Kandror. 1997. Sortilin is a major protein component of Glut4-containing vesicles. *J Biol Chem.* 272:24145-24147.

Linscheid, N., P.C. Poulsen, I.D. Pedersen, E. Gregers, J.H. Svendsen, M.S. Olesen, J.V. Olsen, M. Delmar, and A. Lundby. 2020. Quantitative Proteomics of Human Heart Samples Collected In Vivo Reveal the Remodeled Protein Landscape of Dilated Left Atrium Without Atrial Fibrillation. *Mol Cell Proteomics.* 19:1132-1144.

Linssen, P.B.C., M.G.J. Veugen, R.M.A. Henry, C.J.H. van der Kallen, A.A. Kroon, M.T. Schram, H.-P. Brunner-La Rocca, and C.D.A. Stehouwer. 2020. Associations of (pre)diabetes with right ventricular and atrial structure and function: the Maastricht Study. *Cardiovasc. Diabetol.* 19:88.

Liu, J., A. Kimura, C.A. Baumann, and A.R. Saltiel. 2002. APS facilitates c-Cbl tyrosine phosphorylation and GLUT4 translocation in response to insulin in 3T3-L1 adipocytes. *Mol Cell Biol.* 22:3599-3609.

Liu, S., P. Hoess, and J. Ries. 2022. Super-Resolution Microscopy for Structural Cell Biology. *Annu. Rev. Biophys.* 51:301-326.

Livingstone, R., N.J. Bryant, J.G. Boyle, J.R. Petrie, and G.W. Gould. 2022. Diabetes is accompanied by changes in the levels of proteins involved in endosomal GLUT4 trafficking in obese human skeletal muscle. *Endocrinol Diabetes Metab.* 5:e361.

Lizunov, V.A., I. Lisinski, K. Stenkula, J. Zimmerberg, and S.W. Cushman. 2009. Insulin regulates fusion of GLUT4 vesicles independent of Exo70-mediated tethering. *J. Biol. Chem.* 284:7914-7919.

Lizunov, V.A., K. Stenkula, A. Troy, S.W. Cushman, and J. Zimmerberg. 2013. Insulin regulates Glut4 confinement in plasma membrane clusters in adipose cells. *PLoS One*. 8:e57559.

Lizunov, V.A., K.G. Stenkula, I. Lisinski, O. Gavrilova, D.R. Yver, A. Chadt, H. Al-Hasani, J. Zimmerberg, and S.W. Cushman. 2012. Insulin stimulates fusion, but not tethering, of GLUT4 vesicles in skeletal muscle of HA-GLUT4-GFP transgenic mice. *Am J Physiol Endocrinol Metab*. 302:E950-960.

Ljubkovic, M., M. Gressette, C. Bulat, M. Cavar, D. Bakovic, D. Fabijanic, I. Grkovic, C. Lemaire, and J. Marinovic. 2019. Disturbed Fatty Acid Oxidation, Endoplasmic Reticulum Stress, and Apoptosis in Left Ventricle of Patients With Type 2 Diabetes. *Diabetes*. 68:1924-1933.

Lopaschuk, G.D., and W.C. Stanley. 1997. Glucose Metabolism in the Ischemic Heart. *Circulation*. 95:313-315.

Louch, W.E., K.A. Sheehan, and B.M. Wolska. 2011. Methods in cardiomyocyte isolation, culture, and gene transfer. *J Mol Cell Cardiol*. 51:288-298.

Lundsgaard, E. 1939. On the mode of action of insulin. *Upsala Läk.-Fören. Förh.*:143.

Lycas, M.D., and S. Manley. 2024. DNA-PAINT adaptors make for efficient multiplexing. *Cell Rep Methods*. 4:100801.

Macheda, M.L., D.J. Kelly, J.D. Best, and S. Rogers. 2002. Expression during rat fetal development of GLUT12 - a member of the class III hexose transporter family. *Anatomy and Embryology*. 205:441-452.

Maidorn, M., S.O. Rizzoli, and F. Opazo. 2016. Tools and limitations to study the molecular composition of synapses by fluorescence microscopy. *Biochem J*. 473:3385-3399.

Malide, D., G. Ramm, S.W. Cushman, and J.W. Slot. 2000. Immunoelectron microscopic evidence that GLUT4 translocation explains the stimulation of glucose transport in isolated rat white adipose cells. *J. Cell Sci.* 113:4203-4210.

Marfella, R., C. Amarelli, F. Cacciatore, M.L. Balestrieri, G. Mansueto, N. D'Onofrio, S. Esposito, I. Mattucci, G. Salerno, M. De Feo, M. D'Amico, P. Golino, C. Maiello, G. Paolisso, and C. Napoli. 2020. Lipid Accumulation in Hearts Transplanted From Nondiabetic Donors to Diabetic Recipients. *Journal of the American College of Cardiology.* 75:1249-1262.

Maria, Z., A.R. Campolo, and V.A. Lacombe. 2015. Diabetes Alters the Expression and Translocation of the Insulin-Sensitive Glucose Transporters 4 and 8 in the Atria. *Plos One.* 10:e0146033.

Martin-Fernandez, M.L., C.J. Tynan, and S.E. Webb. 2013. A 'pocket guide' to total internal reflection fluorescence. *J Microsc.* 252:16-22.

Mathur, A., Z. Ma, P. Loskill, S. Jeeawoody, and K.E. Healy. 2016. In vitro cardiac tissue models: Current status and future prospects. *Advanced Drug Delivery Reviews.* 96:203-213.

Mazella, J., N. Zsürger, V. Navarro, J. Chabry, M. Kaghad, D. Caput, P. Ferrara, N. Vita, D. Gully, J.-P. Maffrand, and J.-P. Vincent. 1998. The 100-kDa Neurotensin Receptor Is gp95/Sortilin, A Non-G-Protein-coupled Receptor. *Journal of Biological Chemistry.* 273:26273-26276.

McConnell, G. 2019. Video-rate gigapixel imaging of the brain. *Nat Photonics.* 13:732-734.

McConnell, G., and W.B. Amos. 2018. Application of the Mesolens for subcellular resolution imaging of intact larval and whole adult *Drosophila*. *Journal of Microscopy.* 270:252-258.

McConnell, G., J. Trägårdh, R. Amor, J. Dempster, E. Reid, and W.B. Amos. 2016. A novel optical microscope for imaging large embryos and tissue volumes with sub-cellular resolution throughout. *eLife*. 5:e18659.

McCormick, P.J., K. Dumaresq-Doiron, A.S. Pluviose, V. Pichette, G. Tosato, and S. Lefrancois. 2008. Palmitoylation controls recycling in lysosomal sorting and trafficking. *Traffic*. 9:1984-1997.

McHugh, K., A.D. DeVore, J. Wu, R.A. Matsouaka, G.C. Fonarow, P.A. Heidenreich, C.W. Yancy, J.B. Green, N. Altman, and A.F. Hernandez. 2019. Heart Failure With Preserved Ejection Fraction and Diabetes: JACC State-of-the-Art Review. *JACC*. 73:602-611.

Mikhaylova, M., B.M. Cloin, K. Finan, R. van den Berg, J. Teeuw, M.M. Kijanka, M. Sokolowski, E.A. Katrukha, M. Maidorn, F. Opazo, S. Moutel, M. Vantard, F. Perez, P.M. van Bergen en Henegouwen, C.C. Hoogenraad, H. Ewers, and L.C. Kapitein. 2015. Resolving bundled microtubules using anti-tubulin nanobodies. *Nat Commun*. 6:7933.

Miles, J.M., R.A. Rizza, M.W. Haymond, and J.E. Gerich. 1980. Effects of acute insulin deficiency on glucose and ketone body turnover in man: evidence for the primacy of overproduction of glucose and ketone bodies in the genesis of diabetic ketoacidosis. *Diabetes*. 29:926-930.

Morris, N.J., S.A. Ross, W.S. Lane, S.K. Moestrup, C.M. Petersen, S.R. Keller, and G.E. Lienhard. 1998. Sortilin is the major 110-kDa protein in GLUT4 vesicles from adipocytes. *J Biol Chem*. 273:3582-3587.

Morris, S., N.D. Geoghegan, J.B.A. Sadler, A.M. Koester, H.L. Black, M. Laub, L. Miller, L. Heffernan, J.C. Simpson, C.C. Mastick, J. Cooper, N. Gadegaard, N.J. Bryant, and G.W. Gould. 2020. Characterisation of GLUT4 trafficking in HeLa cells: comparable kinetics and orthologous trafficking mechanisms to 3T3-L1 adipocytes. *PeerJ*. 8:e8751.

Mueckler, M., C. Caruso, S.A. Baldwin, M. Panico, I. Blench, H.R. Morris, W.J. Allard, G.E. Lienhard, and H.F. Lodish. 1985. Sequence and structure of a human glucose transporter. *Science*. 229:941-945.

Mueckler, M., and B. Thorens. 2013. The SLC2 (GLUT) family of membrane transporters. *Mol. Aspects Med.* 34:121-138.

Murdolo, G., F. Angeli, G. Reboldi, L. Di Giacomo, A. Aita, C. Bartolini, and P. Vedecchia. 2015. Left ventricular hypertrophy and obesity: only a matter of fat? *High Blood Press Cardiovasc Prev.* 22:29-41.

Muretta, J.M., I. Romenskaia, and C.C. Mastick. 2008. Insulin releases Glut4 from static storage compartments into cycling endosomes and increases the rate constant for Glut4 exocytosis. *J Biol Chem.* 283:311-323.

Murphy, D.B. 2002. Diffraction and Interference in Image Formation. In *Fundamentals of Light Microscopy and Electronic Imaging*. John Wiley & Sons, Inc. 61-84.

Nakashima, N., P.M. Sharma, T. Imamura, R. Bookstein, and J.M. Olefsky. 2000. The tumor suppressor PTEN negatively regulates insulin signaling in 3T3-L1 adipocytes. *J Biol Chem.* 275:12889-12895.

Nakatsu, F., J.M. Baskin, J. Chung, L.B. Tanner, G. Shui, S.Y. Lee, M. Pirruccello, M. Hao, N.T. Ingolia, M.R. Wenk, and P. De Camilli. 2012. PtdIns4P synthesis by PI4KIIIalpha at the plasma membrane and its impact on plasma membrane identity. *J. Cell Biol.* 199:1003-1016.

Neubauer, S., M. Horn, M. Cramer, K. Harre, J.B. Newell, W. Peters, T. Pabst, G. Ertl, D. Hahn, J.S. Ingwall, and K. Kochsiek. 1997. Myocardial phosphocreatine-to-ATP ratio is a predictor of mortality in patients with dilated cardiomyopathy. *Circulation.* 96:2190-2196.

Neubauer, S., T. Krahe, R. Schindler, M. Horn, H. Hillenbrand, C. Entzeroth, H. Mader, E.P. Kromer, G.A. Riegger, K. Lackner, and et al. 1992. 31P magnetic resonance spectroscopy in dilated cardiomyopathy and coronary

artery disease. Altered cardiac high-energy phosphate metabolism in heart failure. *Circulation*. 86:1810-1818.

Neuhaus, M., C. Fryklund, H. Taylor, A. Borreguero-Muñoz, F. Kopietz, H. Ardalani, O. Rogova, L. Stirrat, S.K. Bremner, P. Spéjel, N.J. Bryant, G.W. Gould, and K.G. Stenkula. 2023. EHD2 regulates plasma membrane integrity and downstream insulin receptor signaling events. *Mol Biol Cell*. 34:ar124.

Nystrom, F.H., H. Chen, L.N. Cong, Y. Li, and M.J. Quon. 1999. Caveolin-1 interacts with the insulin receptor and can differentially modulate insulin signaling in transfected Cos-7 cells and rat adipose cells. *Mol Endocrinol*. 13:2013-2024.

O'Connell, T.D., M.C. Rodrigo, and P.C. Simpson. 2007. Isolation and culture of adult mouse cardiac myocytes. *Methods Mol Biol*. 357:271-296.

Ogurtsova, K., J.D.d.R. Fernandes, Y. Huang, U. Linnenkamp, L. Guariguata, N.H. Cho, D. Cavan, J.E. Shaw, and L.E. Makaroff. 2017. IDF Diabetes Atlas: Global estimates for the prevalence of diabetes for 2015 and 2040. *Diabetes Research and Clinical Practice*. 128:40-50.

Oreña, S.J., A.J. Torchia, and R.S. Garofalo. 2000. Inhibition of glycogen-synthase kinase 3 stimulates glycogen synthase and glucose transport by distinct mechanisms in 3T3-L1 adipocytes. *J Biol Chem*. 275:15765-15772.

Ovesný, M., P. Křížek, J. Borkovec, Z. Svindrych, and G.M. Hagen. 2014. ThunderSTORM: a comprehensive ImageJ plug-in for PALM and STORM data analysis and super-resolution imaging. *Bioinformatics*. 30:2389-2390.

Pan, X., N. Zaarur, M. Singh, P. Morin, and K.V. Kandror. 2017. Sortilin and retromer mediate retrograde transport of Glut4 in 3T3-L1 adipocytes. *Mol Biol Cell*. 28:1667-1675.

Parameswaran, S., S. Kumar, R.S. Verma, and R.K. Sharma. 2013.

Cardiomyocyte culture – an update on the in vitro cardiovascular model

and future challenges. *Canadian Journal of Physiology and Pharmacology*. 91:985-998.

Pike, L.J. 1992. Phosphatidylinositol 4-Kinases and the Role of Polyphosphoinositides in Cellular Regulation. *Endocrine Reviews*. 13:692-706.

Planinc, I., P. Garcia-Canadilla, H. Dejea, I. Ilic, E. Guasch, M. Zamora, F. Crispi, M. Stampanoni, D. Milicic, B. Bijmens, A. Bonnin, and M. Cikes. 2021. Comprehensive assessment of myocardial remodeling in ischemic heart disease by synchrotron propagation based X-ray phase contrast imaging. *Sci Rep*. 11:14020.

Ploug, T., B.v. Deurs, H. Ai, S.W. Cushman, and E. Ralston. 1998. Analysis of GLUT4 Distribution in Whole Skeletal Muscle Fibers: Identification of Distinct Storage Compartments That Are Recruited by Insulin and Muscle Contractions. *The Journal of Cell Biology*. 142:1429-1446.

Pop-Busui, R., A.J. Boulton, E.L. Feldman, V. Bril, R. Freeman, R.A. Malik, J.M. Sosenko, and D. Ziegler. 2017. Diabetic Neuropathy: A Position Statement by the American Diabetes Association. *Diabetes Care*. 40:136-154.

Popov, D. 2010. Endothelial cell dysfunction in hyperglycemia: Phenotypic change, intracellular signaling modification, ultrastructural alteration, and potential clinical outcomes. *International Journal of Diabetes Mellitus*. 2(3):189-195.

Powell, T., and V.W. Twist. 1976. A rapid technique for the isolation and purification of adult cardiac muscle cells having respiratory control and a tolerance to calcium. *Biochem Biophys Res Commun*. 72:327-333.

Pulit, S.L., C. Stoneman, A.P. Morris, A.R. Wood, C.A. Glastonbury, J. Tyrrell, L. Yengo, T. Ferreira, E. Marouli, Y. Ji, J. Yang, S. Jones, R. Beaumont, D.C. Croteau-Chonka, T.W. Winkler, G. Consortium, A.T. Hattersley, R.J.F. Loos, J.N. Hirschhorn, P.M. Visscher, T.M. Frayling, H. Yaghoobkar, and C.M.

Lindgren. 2019. Meta-analysis of genome-wide association studies for body fat distribution in 694 649 individuals of European ancestry. *Hum Mol Genet.* 28:166-174.

Purcell, S.H., L.B. Aerni-Flessner, A.R. Willcockson, K.A. Diggs-Andrews, S.J. Fisher, and K.H. Moley. 2011. Improved Insulin Sensitivity by GLUT12 Overexpression in Mice. *Diabetes.* 60:1478-1482.

Raja, M., and R.K.H. Kinne. 2020. Mechanistic Insights into Protein Stability and Self-aggregation in GLUT1 Genetic Variants Causing GLUT1-Deficiency Syndrome. *J. Membr. Biol.* 253:87-99.

Randle, P.J., P.B. Garland, C.N. Hales, and E.A. Newsholme. 1963. THE GLUCOSE FATTY-ACID CYCLE ITS ROLE IN INSULIN SENSITIVITY AND THE METABOLIC DISTURBANCES OF DIABETES MELLITUS. *The Lancet.* 281:785-789.

Rattigan, S., G.J. Appleby, and M.G. Clark. 1991. Insulin-like action of catecholamines and Ca²⁺ to stimulate glucose transport and GLUT4 translocation in perfused rat heart. *Biochimica et Biophysica Acta (BBA) - Molecular Cell Research.* 1094:217-223.

Reinhardt, S.C.M., L.A. Masullo, I. Baudrexel, P.R. Steen, R. Kowalewski, A.S. Eklund, S. Strauss, E.M. Unterauer, T. Schlichthaerle, M.T. Strauss, C. Klein, and R. Jungmann. 2023. Ångström-resolution fluorescence microscopy. *Nature.* 617:711-716.

Ren, W., U.S. Jhala, and K. Du. 2013. Proteomic analysis of protein palmitoylation in adipocytes. *Adipocyte.* 2:17-28.

Renier, N., Z. Wu, David J. Simon, J. Yang, P. Ariel, and M. Tessier-Lavigne. 2014. iDISCO: A Simple, Rapid Method to Immunolabel Large Tissue Samples for Volume Imaging. *Cell.* 159:896-910.

Riehle, C., and E.D. Abel. 2016. Insulin Signaling and Heart Failure. *Circ Res.* 118:1151-1169.

Ries, J., C. Kaplan, E. Platonova, H. Eghlidi, and H. Ewers. 2012. A simple, versatile method for GFP-based super-resolution microscopy via nanobodies. *Nat. Methods*. 9:582-584.

Röder, P.V., B. Wu, Y. Liu, and W. Han. 2016. Pancreatic regulation of glucose homeostasis. *Experimental & Molecular Medicine*. 48:e219-e219.

Rooney, L.M., J. Christopher, B. Watson, Y.S. Kumar, L. Copeland, L.D. Walker, S. Foylan, W.B. Amos, R. Bauer, and G. McConnell. 2024. Printing, Characterizing, and Assessing Transparent 3D Printed Lenses for Optical Imaging. *Adv. Mater. Technol.*

Rossiter, J.L., L.J. Redlinger, G.R. Kolar, W.K. Samson, and G.L.C. Yosten. 2022. The actions of C-peptide in HEK293 cells are dependent upon insulin and extracellular glucose concentrations. *Peptides*. 150:170718.

Rubler, S., J. Dlugash, Y.Z. Yuceoglu, T. Kumral, A.W. Branwood, and A. Grishman. 1972. New type of cardiomyopathy associated with diabetic glomerulosclerosis. *Am J Cardiol*. 30:595-602.

Rust, M.J., M. Bates, and X. Zhuang. 2006. Sub-diffraction-limit imaging by stochastic optical reconstruction microscopy (STORM). *Nat. Methods*. 3:793-795.

Saisho, Y. 2014. Importance of Beta Cell Function for the Treatment of Type 2 Diabetes. *J Clin Med*. 3:923-943.

Saltiel, A.R. 2021. Insulin signaling in health and disease. *J. Clin. Investig.* 131:e142241.

Sano, H., S. Kane, E. Sano, C.P. Mîinea, J.M. Asara, W.S. Lane, C.W. Garner, and G.E. Lienhard. 2003. Insulin-stimulated phosphorylation of a Rab GTPase-activating protein regulates GLUT4 translocation. *J Biol Chem*. 278:14599-14602.

Sarma, S., R.J. Mentz, M.J. Kwasny, A.J. Fought, M. Huffman, H. Subacius, S. Nodari, M. Konstam, K. Swedberg, A.P. Maggioni, F. Zannad, R.O. Bonow,

and M. Gheorghiade. 2013. Association between diabetes mellitus and post-discharge outcomes in patients hospitalized with heart failure: findings from the EVEREST trial. *Eur J Heart Fail.* 15:194-202.

Sato, A., H. Kawano, T. Notsu, M. Ohta, M. Nakakuki, K. Mizuguchi, M. Itoh, T. Suganami, and Y. Ogawa. 2010. Antiobesity effect of eicosapentaenoic acid in high-fat/high-sucrose diet-induced obesity: importance of hepatic lipogenesis. *Diabetes.* 59:2495-2504.

Savova, M.S., L.V. Mihaylova, D. Tews, M. Wabitsch, and M.I. Georgiev. 2023. Targeting PI3K/AKT signaling pathway in obesity. *Biomed Pharmacother.* 159:114244.

Schaeffer, P.J., J. Desantiago, J. Yang, T.P. Flagg, A. Kovacs, C.J. Weinheimer, M. Courtois, T.C. Leone, C.G. Nichols, D.M. Bers, and D.P. Kelly. 2009. Impaired contractile function and calcium handling in hearts of cardiac-specific calcineurin b1-deficient mice. *Am J Physiol Heart Circ Physiol.* 297:H1263-1273.

Schermelleh, L., A. Ferrand, T. Huser, C. Eggeling, M. Sauer, O. Biehlmaier, and G.P.C. Drummen. 2019. Super-resolution microscopy demystified. *Nat. Cell Biol.* 21:72-84.

Schindelin, J., I. Arganda-Carreras, E. Frise, V. Kaynig, M. Longair, T. Pietzsch, S. Preibisch, C. Rueden, S. Saalfeld, B. Schmid, J.-Y. Tinevez, D.J. White, V. Hartenstein, K. Eliceiri, P. Tomancak, and A. Cardona. 2012. Fiji: an open-source platform for biological-image analysis. *Nat. Methods.* 9:676-682.

Schmidl, S., S.A. Tamayo Rojas, C.V. Iancu, J.Y. Choe, and M. Oreb. 2020. Functional Expression of the Human Glucose Transporters GLUT2 and GLUT3 in Yeast Offers Novel Screening Systems for GLUT-Targeting Drugs. *Front. Mol. Biosci.*:598419.

Schnitzbauer, J., M.T. Strauss, T. Schlichthaerle, F. Schueder, and R. Jungmann. 2017. Super-resolution microscopy with DNA-PAINT. *Nat. Protoc.* 12:1198-1228.

Sevilla, L., E. Tomàs, P.n. Muñoz, A. Gumà, Y. Fischer, J. Thomas, B. Ruiz-Montasell, X. Testar, M. Palacín, J. Blasi, and A. Zorzano. 1997. Characterization of Two Distinct Intracellular GLUT4 Membrane Populations in Muscle Fiber. Differential Protein Composition and Sensitivity to Insulin. *Endocrinology.* 138:3006-3015.

Sharma, S., J.V. Adroge, L. Golfman, I. Uray, J. Lemm, K. Youker, G.P. Noon, O.H. Frazier, and H. Taegtmeyer. 2004. Intramyocardial lipid accumulation in the failing human heart resembles the lipotoxic rat heart. *The FASEB Journal.* 18:1692-1700.

Shewan, A.M., B.J. Marsh, D.R. Melvin, S. Martin, G.W. Gould, and D.E. James. 2000. The cytosolic C-terminus of the glucose transporter GLUT4 contains an acidic cluster endosomal targeting motif distal to the dileucine signal. *The Biochemical journal.* 350 Pt 1:99-107.

Shewan, A.M., R.K. McCann, C.A. Lamb, L. Stirrat, D. Kioumourtzoglou, I.S. Adamson, S. Verma, D.E. James, and N.J. Bryant. 2013. Endosomal sorting of GLUT4 and Gap1 is conserved between yeast and insulin-sensitive cells. *J. Cell Sci.* 126:1576-1582.

Shi, J., and K.V. Kandror. 2005. Sortilin is essential and sufficient for the formation of Glut4 storage vesicles in 3T3-L1 adipocytes. *Dev Cell.* 9:99-108.

Shi, J., and K.V. Kandror. 2007. The luminal Vps10p domain of sortilin plays the predominant role in targeting to insulin-responsive Glut4-containing vesicles. *J Biol Chem.* 282:9008-9016.

- Shimomura, O., F.H. Johnson, and Y. Saiga. 1962. Extraction, purification and properties of aequorin, a bioluminescent protein from the luminous hydromedusan, *Aequorea*. *J. Cell. Comp. Physiol.* 59:223-239.
- Simpson, I.A., D.R. Yver, P.J. Hissin, L.J. Wardzala, E. Karnieli, L.B. Salans, and S.W. Cushman. 1983. Insulin-stimulated translocation of glucose transporters in the isolated rat adipose cells: characterization of subcellular fractions. *Biochim Biophys Acta.* 763:393-407.
- Slot, J.W., H.J. Geuze, S. Gigengack, D.E. James, and G.E. Lienhard. 1991a. Translocation of the glucose transporter GLUT4 in cardiac myocytes of the rat. *PNAS.* 88:7815-7819.
- Slot, J.W., H.J. Geuze, S. Gigengack, G.E. Lienhard, and D.E. James. 1991b. Immuno-localization of the insulin regulatable glucose transporter in brown adipose tissue of the rat. *J. Cell Biol.* 113:123-135.
- Sofroniew, N.J., D. Flickinger, J. King, and K. Svoboda. 2016. A large field of view two-photon mesoscope with subcellular resolution for in vivo imaging. *Elife.* 5.
- Sowa, G., M. Pypaert, and W.C. Sessa. 2001. Distinction between signaling mechanisms in lipid rafts vs. caveolae. *Proc Natl Acad Sci U S A.* 98:14072-14077.
- Speakman, J., C. Hambly, S. Mitchell, and E. Król. 2007. Animal models of obesity. *Obes. Rev.* 8:55-61.
- Stanley, W.C., F.A. Recchia, and G.D. Lopaschuk. 2005. Myocardial Substrate Metabolism in the Normal and Failing Heart. *Physiological Reviews.* 85:1093-1129.
- Stenkula, K.G., and C. Erlanson-Albertsson. 2018. Adipose cell size: importance in health and disease. *Am. J. Physiol. - Regul.* 315:R284-R295.

Stenkula, K.G., V.A. Lizunov, S.W. Cushman, and J. Zimmerberg. 2010. Insulin controls the spatial distribution of GLUT4 on the cell surface through regulation of its postfusion dispersal. *Cell Metab.* 12:250-259.

Stuhlinger, M.C., F. Abbasi, J.W. Chu, C. Lamendola, T.L. McLaughlin, J.P. Cooke, G.M. Reaven, and P.S. Tsao. 2002. Relationship between insulin resistance and an endogenous nitric oxide synthase inhibitor. *JAMA.* 287:1420-1426.

Sun, X.J., P. Rothenberg, C.R. Kahn, J.M. Backer, E. Araki, P.A. Wilden, D.A. Cahill, B.J. Goldstein, and M.F. White. 1991. Structure of the insulin receptor substrate IRS-1 defines a unique signal transduction protein. *Nature.* 352:73-77.

Sun, Y., P.J. Bilan, Z. Liu, and A. Klip. 2010. Rab8A and Rab13 are activated by insulin and regulate GLUT4 translocation in muscle cells. *Proc Natl Acad Sci U S A.* 107:19909-19914.

Suzuki, K., and T. Kono. 1980. Evidence that insulin causes translocation of glucose transport activity to the plasma membrane from an intracellular storage site. *PNAS.* 77:2542-2545.

Sych, T., K.R. Levental, and E. Sezgin. 2022. Lipid-Protein Interactions in Plasma Membrane Organization and Function. *Annu. Rev. Biophys.* 9:135-156.

Symons, J.D., and E.D. Abel. 2013. Lipotoxicity contributes to endothelial dysfunction: a focus on the contribution from ceramide. *Rev Endocr Metab Disord.* 14:59-68.

Taegtmeyer, H. 1985. Carbohydrate interconversions and energy production. *Circulation.* 72:lv1-8.

Taylor, E.B., D. An, H.F. Kramer, H. Yu, N.L. Fujii, K.S.C. Roeckl, N. Bowles, M.F. Hirshman, J. Xie, E.P. Feener, and L.J. Goodyear. 2008. Discovery of

TBC1D1 as an Insulin-, AICAR-, and Contraction-stimulated Signaling Nexus in Mouse Skeletal Muscle*. *JBS*. 283:9787-9796.

Taylor, M., T.R. Wallhaus, T.R. Degrado, D.C. Russell, P. Stanko, R.J. Nickles, and C.K. Stone. 2001. An evaluation of myocardial fatty acid and glucose uptake using PET with [18F]fluoro-6-thia-heptadecanoic acid and [18F]FDG in Patients with Congestive Heart Failure. *J Nucl Med*. 42:55-62.

Teo, Z.L., Y.C. Tham, M. Yu, M.L. Chee, T.H. Rim, N. Cheung, M.M. Bikbov, Y.X. Wang, Y. Tang, Y. Lu, I.Y. Wong, D.S.W. Ting, G.S.W. Tan, J.B. Jonas, C. Sabanayagam, T.Y. Wong, and C.Y. Cheng. 2021. Global Prevalence of Diabetic Retinopathy and Projection of Burden through 2045: Systematic Review and Meta-analysis. *Ophthalmology*. 128:1580-1591.

Todaro, G.J., and H. Green. 1963. Quantitative studies of the growth of mouse embryo cells in culture and their development into established lines. *J Cell Biol*. 17:299-313.

Todd, J.A. 2010. Etiology of type 1 diabetes. *Immunity*. 32:457-467.

Trachanas, K., S. Sideris, C. Aggeli, E. Poulidakis, K. Gatzoulis, D. Tousoulis, and I. Kallikazaros. 2014. Diabetic cardiomyopathy: from pathophysiology to treatment. *Hellenic journal of cardiology*. 55:411-421.

Trimble, W.S., and S. Grinstein. 2015. Barriers to the free diffusion of proteins and lipids in the plasma membrane. *J. Cell Biol*. 208:259-271.

Trybus, M., A. Hryniewicz-Jankowska, K. Wójtowicz, T. Trombik, A. Czogalla, and A.F. Sikorski. 2023. EFR3A: a new raft domain organizing protein? *Cell Mol Biol Lett*. 28:86.

Tsampasian, V., D. Cameron, R. Sobhan, G. Bazoukis, and V.S. Vassiliou. 2023. Phosphorus Magnetic Resonance Spectroscopy ((³¹P MRS) and Cardiovascular Disease: The Importance of Energy. *Medicina (Kaunas)*. 59:174.

- Tsien, R.Y. 1998. The green fluorescent protein. *Annu. Rev. Biochem.* 67:509-544.
- Tycko, J., V.E. Myer, and P.D. Hsu. 2016. Methods for Optimizing CRISPR-Cas9 Genome Editing Specificity. *Mol Cell.* 63:355-370.
- Ueda-Wakagi, M., K. Hayashibara, T. Nagano, M. Ikeda, S. Yuan, S. Ueda, Y. Shirai, K.I. Yoshida, and H. Ashida. 2018. Epigallocatechin gallate induces GLUT4 translocation in skeletal muscle through both PI3K- and AMPK-dependent pathways. *Food Funct.* 9:4223-4233.
- Uhlig, M., W. Passlack, and J. Eckel. 2005. Functional role of Rab11 in GLUT4 trafficking in cardiomyocytes. *Mol Cell Endocrinol.* 235:1-9.
- UNESCO. 2021. UNESCO Recommendation on Open Science.
- Uusitupa, M. 2002. Lifestyles matter in the prevention of type 2 diabetes. *Diabetes Care.* 25:1650-1651.
- Vahouny, G.V., R.W. Wei, A. Tamboli, and E.N. Albert. 1979. Adult canine myocytes: isolation, morphology and biochemical characteristics. *J Mol Cell Cardiol.* 11:339-357.
- Valli, J., A. Garcia-Burgos, L.M. Rooney, E.O.B. Vale de Melo, R.R. Duncan, and C. Rickman. 2021. Seeing beyond the limit: A guide to choosing the right super-resolution microscopy technique. *J. Biol. Chem.* 297:100791.
- van Bilsen, M., P.J.H. Smeets, A.J. Gilde, and G.J. van der Vusse. 2004. Metabolic remodelling of the failing heart: the cardiac burn-out syndrome? *Cardiovasc. Res.* 61:218-226.
- van de Linde, S. 2019. Single-molecule localization microscopy analysis with ImageJ. *J. Phys. D: Appl. Phys.* 52:203002.
- van de Linde, S., A. Löschberger, T. Klein, M. Heidbreder, S. Wolter, M. Heilemann, and M. Sauer. 2011. Direct stochastic optical reconstruction microscopy with standard fluorescent probes. *Nat. Protoc.* 6:991-1009.

Voigt, F.F., D. Kirschenbaum, E. Platonova, S. Pagès, R.A.A. Campbell, R. Kastli, M. Schaettin, L. Egolf, A. van der Bourg, P. Bethge, K. Haenraets, N. Frézel, T. Topilko, P. Perin, D. Hillier, S. Hildebrand, A. Schueth, A. Roebroek, B. Roska, E.T. Stoeckli, R. Pizzala, N. Renier, H.U. Zeilhofer, T. Karayannis, U. Ziegler, L. Batti, A. Holtmaat, C. Lüscher, A. Aguzzi, and F. Helmchen. 2019. The mesoSPIM initiative: open-source light-sheet microscopes for imaging cleared tissue. *Nat Methods*. 16:1105-1108.

Wang, W., P.A. Hansen, B.A. Marshall, J.O. Holloszy, and M. Mueckler. 1996. Insulin unmasks a COOH-terminal Glut4 epitope and increases glucose transport across T-tubules in skeletal muscle. *JCB*. 135:415-430.

Wardzala, L.J., S.W. Cushman, and L.B. Salans. 1978. Mechanism of insulin action on glucose transport in the isolated rat adipose cell. Enhancement of the number of functional transport systems. *J. Biol. Chem*. 253:8002-8005.

Wardzala, L.J., and B. Jeanrenaud. 1981. Potential mechanism of insulin action on glucose transport in the isolated rat diaphragm. Apparent translocation of intracellular transport units to the plasma membrane. *J. Biol. Chem*. 256:7090-7093.

Ware, B., M. Bevier, Y. Nishijima, S. Rogers, C.A. Carnes, and V.A. Lacombe. 2011. Chronic heart failure selectively induces regional heterogeneity of insulin-responsive glucose transporters. *Am J Physiol Regul Integr Comp Physiol*. 301:R1300-1306.

Waring, M.J., D.M. Andrews, P.F. Faulder, V. Flemington, J.C. McKelvie, S. Maman, M. Preston, P. Raubo, G.R. Robb, K. Roberts, R. Rowlinson, J.M. Smith, M.E. Swarbrick, I. Treinies, J.J. Winter, and R.J. Wood. 2014. Potent, selective small molecule inhibitors of type III phosphatidylinositol-4-kinase alpha- but not beta-inhibit the phosphatidylinositol signaling cascade and cancer cell proliferation. *ChemComm*. 50:5388-5390.

Westermeier, F., J.A. Riquelme, M. Pavez, V. Garrido, A. Diaz, H.E. Verdejo, P.F. Castro, L. Garcia, and S. Lavandero. 2016. New Molecular Insights of Insulin in Diabetic Cardiomyopathy. *Front Physiol.* 7:125.

Whicher, C.A., S. O'Neill, and R.I.G. Holt. 2020. Diabetes in the UK: 2019. *Diabetic Medicine.* 37:242-247.

Wieczorke, R., S. Dlugai, S. Krampe, and E. Boles. 2003. Characterisation of mammalian GLUT glucose transporters in a heterologous yeast expression system. *Cell. Physiol. Biochem.* 13:123-134.

Willig, K.I., B. Harke, R. Medda, and S.W. Hell. 2007. STED microscopy with continuous wave beams. *Nat. Methods.* 4:915-918.

Winder, W.W., and D.G. Hardie. 1996. Inactivation of acetyl-CoA carboxylase and activation of AMP-activated protein kinase in muscle during exercise. *Am J Physiol.* 270:E299-E304.

Wollman, A.J.M., D. Kioumourtzoglou, R. Ward, G.W. Gould, and N.J. Bryant. 2022. Large scale, single-cell FRET-based glucose uptake measurements within heterogeneous populations. *iScience.* 25:104023.

Wright, J.J., J. Kim, J. Buchanan, S. Boudina, S. Sena, K. Bakirtzi, O. Ilkun, H.A. Theobald, R.C. Cooksey, K.V. Kandrор, and E.D. Abel. 2009. Mechanisms for increased myocardial fatty acid utilization following short-term high-fat feeding. *Cardiovasc Res.* 82:351-360.

Wu, X., and H.H. Freeze. 2002. GLUT14, a duplicon of GLUT3, is specifically expressed in testis as alternative splice forms. *Genomics.* 80:553-557.

Yan, Q., Y. Lu, L. Zhou, J. Chen, H. Xu, M. Cai, Y. Shi, J. Jiang, W. Xiong, J. Gao, and H. Wang. 2018. Mechanistic insights into GLUT1 activation and clustering revealed by super-resolution imaging. *PNAS.* 115:7033-7038.

Yang, J., and G.D. Holman. 2005. Insulin and Contraction Stimulate Exocytosis, but Increased AMP-activated Protein Kinase Activity Resulting

from Oxidative Metabolism Stress Slows Endocytosis of GLUT4 in Cardiomyocytes. *Journal of Biological Chemistry*. 280:4070-4078.

Zeng, G., F.H. Nystrom, L.V. Ravichandran, L.N. Cong, M. Kirby, H. Mostowski, and M.J. Quon. 2000. Roles for insulin receptor, PI3-kinase, and Akt in insulin-signaling pathways related to production of nitric oxide in human vascular endothelial cells. *Circulation*. 101:1539-1545.

Zeng, W., I. Jacobi, D.J. Beck, S. Li, and H.A. Stone. 2015. Characterization of syringe-pump-driven induced pressure fluctuations in elastic microchannels. *Lab Chip*. 15:1110-1115.

Zhao, F., D. Cambié, V. Hessel, M.G. Debijs, and T. Noël. 2018. Real-time reaction control for solar production of chemicals under fluctuating irradiance. *Green Chemistry*. 20:2459-2464.

Zimmermann, M., L. Beer, R. Ullrich, D. Lukovic, E. Simader, D. Traxler, T. Wagner, L. Nemeč, L. Altenburger, A. Zuckermann, M. Gyöngyösi, H.J. Ankersmit, and M. Mildner. 2017. Analysis of region specific gene expression patterns in the heart and systemic responses after experimental myocardial ischemia. *Oncotarget*. 8:60809-60825.

Zisman, A., O.D. Peroni, E.D. Abel, M.D. Michael, F. Mauvais-Jarvis, B.B. Lowell, J.F. Wojtaszewski, M.F. Hirshman, A. Virkamaki, L.J. Goodyear, C.R. Kahn, and B.B. Kahn. 2000. Targeted disruption of the glucose transporter 4 selectively in muscle causes insulin resistance and glucose intolerance. *Nat Med*. 6:924-928.

Zuppinger, C. 2019. 3D Cardiac Cell Culture: A Critical Review of Current Technologies and Applications. *Frontiers in Cardiovascular Medicine*. 6:87.